(1)

AGARD-CP-426

AGARD-CP-426

AGARD CONFERENCE PROCEEDINGS No.426

Aerospace Materials Process Modelling

DISTRIBUTION AND AVAILABILITY
ON BACK COVER

AGARD-CP-426

NORTH ATLANTIC TREATY ORGANIZATION

ADVISORY GROUP FOR AEROSPACE RESEARCH AND DEVELOPMENT

(ORGANISATION DU TRAITE DE L'ATLANTIQUE NORD)

AGARD Conference Proceedings No.426

AEROSPACE MATERIALS PROCESS MODELLING

Papers presented at the 65th Meeting of the Structures and Materials Panel of AGARD, held in Çeşme, Turkey, 2–4 October 1987.

THE MISSION OF AGARD

According to its Charter, the mission of AGARD is to bring together the leading personalities of the NATO nations in the fields of science and technology relating to aerospace for the following purposes:

- Recommending effective ways for the member nations to use their research and development capabilities for the common benefit of the NATO community;
- Providing scientific and technical advice and assistance to the Military Committee in the field of aerospace research and development (with particular regard to its military application);
- Continuously stimulating advances in the aerospace sciences relevant to strengthening the common defence posture;
- Improving the co-operation among member nations in aerospace research and development;
- Exchange of scientific and technical information;
- Providing assistance to member nations for the purpose of increasing their scientific and technical potential;
- Rendering scientific and technical assistance, as requested, to other NATO bodies and to member nations in connection with research and development problems in the aerospace field.

The highest authority within AGARD is the National Delegates Board consisting of officially appointed senior representatives from each member nation. The mission of AGARD is carried out through the Panels which are composed of experts appointed by the National Delegates, the Consultant and Exchange Programme and the Aerospace Applications Studies Programme. The results of AGARD work are reported to the member nations and the NATO Authorities through the AGARD series of publications of which this is one.

Participation in AGARD activities is by invitation only and is normally limited to citizens of the NATO nations.

Published August 1988

ISBN 92-835-0476-3

Printed by Specialised Printing Services Limited
40 Chigwell Lane, Loughton, Essex IG10 3TZ

PREFACE

In recent years there has been a significant increase in the effort of developing process models for aerospace materials. Many factors have been responsible for this. Aerospace materials technology is changing very rapidly with the introduction of expensive and sophisticated materials. In addition the shorter life cycle from design to application is inconsistent with the traditional trial-and-error approaches formerly used.

The AGARD Structures and Materials Panel Specialists' Meeting on Aerospace Materials Process Modelling was organized to assess how developments in analytical process modelling can both lower costs and increase reliability in manufacture of components; to review recent work in this field; and to identify directions for future research. The meeting limited its discussions to modelling the behaviour of metallic materials, and in particular the forming of components such as castings and forgings.

Dr Gary L.Denman
Chairman, Sub-Committee on
Aerospace Materials Process Modelling

***

L'effort de développement consacré à la modélisation des procédés d'élaboration des matériaux aérospatiaux s'est accentué sensiblement au cours des dernières années. Plusieurs facteurs sont à l'origine de cette tendance. La technologie des matériaux aérospatiaux est en pleine évolution, suite à l'arrivée sur le marché de matériaux sophistiqués et de coût élevé. En outre, le raccourcissement du cycle entre la conception et l'application ne correspond plus aux méthodes classiques par approches itératives employées dans le passé.

Une réunion de spécialistes du Panel AGARD des Structures et Matériaux portant sur la modélisation des procédés d'élaboration des matériaux aérospatiaux fut organisée. Elle avait pour but d'évaluer dans quelle mesure les développements dans le domaine de la modélisation analytique pouvaient, d'une part, amener une diminution de coût de fabrication des composants, et d'autre part, une meilleur fiabilité, de passer en revue les réalisations récents dans ce domaine et d'indiquer des futures voies de recherche.

Les discussions furent limitées à la modélisation due comportement des matériaux métalliques dans un environnement donné, et notamment le formage de composants tels que les pièces moulées et les pièces forgées.

Dr Gary L.Denman
Chairman, Sub-Committee on
Aerospace Materials Process Modelling

STRUCTURES AND MATERIALS PANEL

Chairman: Professor Paolo Santini
Dipartimento Aerospaziale
Universita degli Studi di Roma
"La Sapienza"
Via Eudossiana, 16
00185 Roma — Italy

Deputy Chairman: Prof. Dr-Ing Hans Försching
Direktor der DFVLR Institut für
Aeroelastik
Bunsenstrasse 10
D-3400 Göttingen — Germany

AEROSPACE MATERIALS PROCESS MODELLING

SUB-COMMITTEE AND PROGRAMME CHAIRMAN

Chairman: Dr Gary L.Denman
Director Materials Laboratory
AF Wright Aeronautical Laboratories
AFWAL/ML
Wright-Patterson AFB
OH 45433-6533, USA

SMP MEMBERS

Dr H.J.G.Carvalhinhos — PO
Dr P.Costa — FR
Mr D.Coutsouradis — BE
Prof. A.Deruyttere — BE
Prof. J.S.L.Leach — UK
Mr O.Sensburg — GE
Col S.Signoretti — IT
Dr W.Wallace — CA
Mr H.Zocher — GE

HOST MEETING COORDINATOR

Colonel D.Kaya
Ministry of Defence — ARGE
R & D Department
Ankara — Turkey

The Panel wishes to express its thanks to the AGARD Turkish National Delegates for the invitation to hold this Meeting in Turkey.

PANEL EXECUTIVE

Mr M.C.McConnell

AGARD-OTAN
7, rue Ancelle
92200 Neuilly sur Seine
France
Tel: (Paris) (1) 47.38.57.90 Telex: 610176

From USA & Canada
AGARD-NATO
Attn: SMP Executive
APO New York 09777

CONTENTS

PROCESSING SCIENCE AND MATERIALS DEVELOPMENT

Harold L. Gegel
Air Force Systems Command, Aeronautical Systems Division
Air Force Wright Aeronautical Laboratories/Materials Laboratory (AFWAL/MLLM)
Wright-Patterson Air Force Base, Ohio 45433-6503 USA

SUMMARY

The development of advanced technologies for the fabrication of close-tolerance parts, in conjunction with the development of advanced materials, plays a key role in the design and manufacturing of affordable aerospace systems. New process and product-design concepts must be evolved in parallel with the development of advanced materials for future systems in order to exploit the achievements being made in materials science and to tailor specific properties while simultaneously producing controlled geometrical shapes. A scientific description of production equipment and, in general, physical objects, media, fields, and interface and material-related phenomena requires theoretical models which are capable of predicting the response of the fabricating system to the initial inputs. The design of a product and the corresponding manufacturing process generally requires both deterministic models and expert systems which utilize designer intuition and logic in finding acceptable solutions. This paper reviews some of the recent developments in process modeling as related primarily to metalworking systems and how they aid in the understanding of the role of computer and human expertise in modern computer-aided engineering (CAE).

INTRODUCTION

A technological revolution is in progress throughout the industrial world. Many corporations are implementing the just-in-time production philosophy which emphasizes the total life-cycle costs of the system and its components. Manufacturing is moving toward a flexible environment wherein many different products can be made on the same day to customer order, eliminating expensive inventory. This concept offers a dual advantage--the ability to produce according to need while reducing industry costs.

The ultimate flexible factory is not yet a reality. Creating this factory requires full understanding of how to integrate new technology into the particular manufacturing enterprise. The cornerstone of this understanding is an organized and comprehensive design system along with a methodology which makes it relatively easy for a designer to search for solution principles during the conceptual stage of design.

In the search for solutions and in the analysis of system properties, it is often useful to create a model of the system for studying its behavior by means of computer simulation or physical-modeling techniques. These design methodologies frequently lead to new sub-solutions and the introduction of early optimizations. One of the important goals of any manufacturing organization is to determine the optimum means for producing defect-free parts on a repeatable basis. The optimization criteria vary depending upon the manufacturing goals, the overall system requirements, and the product specifications. Establishing appropriate criteria requires in-depth views--global and local--of manufacturing processes. From an optimization point of view, manufacturing processes require a determination of the material-flow mechanics for achieving a proper process design and developing a rational strategy for process control.

Flexible manufacturing requirements are forcing manufacturing technologists to seek a scientific description of mechanics, physical objects, media, fields, and interface and material phenomena in order to simulate the entire manufacturing process in the computer and obtain near-optimal solutions for producing the required product qualities. The objective is to avoid costly build-and-test design on the shop floor, which prevents the use of manufacturing equipment and eliminates flexibility.

Mathematical modeling of physical space-time phenomena is the foundation of any theoretical interpretation of a given manufacturing process, and heuristic modeling or artificial intelligence (AI) makes it possible to handle the fuzzy domains of manufacturing which require human judgement for decision making.

The incorporation of theoretically and physically correct notions into a model of a unit process must be linked to laboratory tests on physical scale models as well as to special observations on natural phenomena in the production environment. Building a model means establishing a complete set of relationships suitable for describing a broad class of operations such as conventional forging, hot die forging, precision forging, and isothermal forging, which, as a rule, are inhomogeneous and transient over a large volume of workpiece material.

In such a general formulation, experience, common sense, and intuition can aid in supplying the minimally necessary mathematical and physical assumptions. Different types of models and knowledge are required for describing the domain of design and manufacturing.

TYPES OF MODELS

Three general types of models required for linking design with manufacturing are

- Domain Independent - Meta Systems
- Domain Dependent - Knowledge-Based Expert Systems
- Deterministic - Mathematical Models

Meta Systems

Meta-system models can also be thought of as meta-knowledge models--which are models of knowledge about knowledge. Meta-system knowledge (1-2) can be procedural, judgmental, or both. It directs the processing of factual knowledge, procedural knowledge (algorithms, operations), and judgement knowledge (heuristics, beliefs). Meta-knowledge models have the ability to

- Control pattern-directed actions
- Exhibit dynamic, self-modifying flexible behavior
- Anticipate unexpected developments
- Deal with uncertainties (fuzzy knowledge)
- Utilize open-ended solution space
- Control the "explosion" of information created by engineering design tools

Knowledge used in engineering design and manufacturing, in general, is not uniform in kind or applicability. It may be very high level knowledge as in the conceptual stages of design where the engineer is presented with differing and often conflicting options, particularly between requirements related to disparate goals such as maintainability, reliability, performance and producibility. Chandrasekaran (3) has categorized this type of knowledge as creative knowledge. Engineers use creative knowledge to accomplish such tasks as defining the minimum physical assumptions necessary for creating a mathematical model of a given unit process, evaluating initial design options, and initiating a new production line. Other classes of knowledge defined by Chandrasekaran include innovative knowledge, which is not so general as creative knowledge but still involves considerable decision making, and routine knowledge, which is knowledge enabling engineers to perform the daily tasks of engineering and manufacturing.

Meta-system-information models are essential for making use of the overlapping types of engineering design knowledge in a cooperative way. In summary, meta systems organize information, automatically propagate information, dynamically change data bases, facilitate incremental design, provide immediate feedback of potential errors, monitor and control the design process, provide instantaneous visibility of information, provide a uniform user interface to design tools and knowledge, and automatically record information.

Knowledge-Based Expert Systems

Knowledge-Based Expert Systems (KBES) are applications-oriented or domain-dependent models (2). Expert programs generally embody the knowledge of more than one expert in the particular field, and they are constructed in consultation with these experts. Knowledge engineers (computer scientists) mediate in the modeling of information from various experts (engineers, technologists). KBES, a sub-discipline of artificial intelligence (AI), have been in various stages of development for over 30 years. Some are now being used as consultative systems in the areas of geology, medicine, engineering, and computer science (2). These systems offer great promise in the area of CAD/CAM/CAE technologies for increasing the productivity of engineers and for raising engineering design to a new paradigm. A representative sample of KBES systems currently in use can be found in The Handbook of Artificial Intelligence (2), and a partial list of expert systems now being used by U. S. manufacturing industries is given in a paper by King, Brooks, and Schaefer (4).

Mathematical Models

Engineering design is based on utilizing a number of concepts which describe the general characteristics of the object (part, assembly, system) and phenomena such as chemical reactions, material flow, heat flow, vibration, and turbulence in various media. These phenomena are presented as mathematical abstractions or models. They are developed through the use of intuition, common sense, and experience by means of axioms, formulas, and various mathematical relations that enable the researcher or engineer, at least in principle, to determine the characteristics of the phenomena by means of logically developed operations, experimental observations, or a combination of these.

Manufacturing and design problems are formulated, described, and solved by introducing models which reflect the basic and important properties of the substance (workpiece material) and unit process (forging, extrusion, injection molding). A number of basic concepts are introduced axiomatically as primary and others as secondary or derived concepts expressed in certain ways through the primary relationships. Among the primary relationships described mathematically are

- Force Equilibria
- Momentum Balance
- Energy Balance
- Conservation of Mass or Volume
- Continuity
- Material Flow Laws

Secondary concepts such as a the intrinsic workability of the material can be incorporated as a non-holonomic constraint or inequality of certain process parameters such as strain rate (die velocity) and die/workpiece temperatures.

For full modeling of a manufacturing process, a systems approach must be used, as shown in Fig. 1. As indicated in this figure, models describing the equipment characteristics, the material system, and the process-control system are required for satisfying the

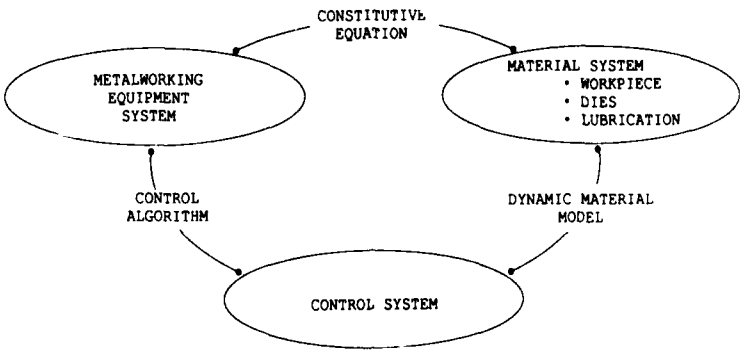

Figure 1 - Schematic Representation of Systems Approach.

manufacturing specifications. Given the existence of models for the process equipment and its control system, material models known as constitutive equations are required for providing the additional knowledge needed for making the physical and mathematical link between these systems. The material-behavior models, i.e., the constitutive equation and dynamic material model (intrinsic workability), must be determined experimentally. These models express how the workpiece material responds to the demands of the process, while the model based on a continuum-mechanics description of the unit process describes the demands of the process. Thus, the component models of the various sub-systems are combined into an overall simulation model for establishing the optimum processing conditions needed to satisfy the goals of the manufacturing and product specifications.

INTERRELATIONS BETWEEN THE VARIOUS MODELS

Because the knowledge required for making manufacturing decisions varies both in type and application, the three different types of models previously described must be used in cooperation for designing and intelligently operating an actual manufacturing system. Figure 2 shows the relationship between the different types of models. In this figure a KBES is viewed also as a tool, as any other design or diagnostic tool (for example, a finite-element program for fluid flow, plastic flow, or heat flow) would be. The meta system organizes, integrates, and controls the evolution and propagation of knowledge for the entire system. It resides above the operating system of the computer and gives it a degree of intelligence. Several of these systems (TRIAD, TEIRESIAS, and KI-Shell™) have been developed (5,6) for assisting human experts in making decisions and for monitoring the performance of expert systems. Meta systems assist in knowledge acquisition and in modifying the rules and concepts used to make predictions as part of their model-based understanding process. The meta system assists the designer by acquiring information from a data base and making it available to the designer at the exact moment it is required in the design life cycle. This system can be thought of as a life-cycle assistant for design projects where several different design tools must be utilized. The "assistant," which is schematically shown in Fig. 3, provides an interface which supports the use of tools according to the specific policies of the manufacturing enterprise, releasing the designer from the burden of implementing these policies. It assists the user in dealing with enterprise-, task-, and system-related questions. The following typifies the questions to be addressed by the designer when confronted with the diversity of knowledge which must be brought into play for efficient development of the product:

- Enterprise Related:

  What results should be reported in the case of successful/unsuccessful task completion?

  What possible conclusions can be drawn from the summary reports thus far?

- Task Related:

  What task should be performed next?

  What is the input/output and command sequence for the tool?

  What are the constraints on this task?

  What should be done if the task succeeds or fails?

  What are the options at this point?

  What decisions were previously made which affect the current task?

- System Related:

  What tools are available for a task?

  What queries make sense at this point?

  How is the tool invoked?

  What parameters are required for this tool?

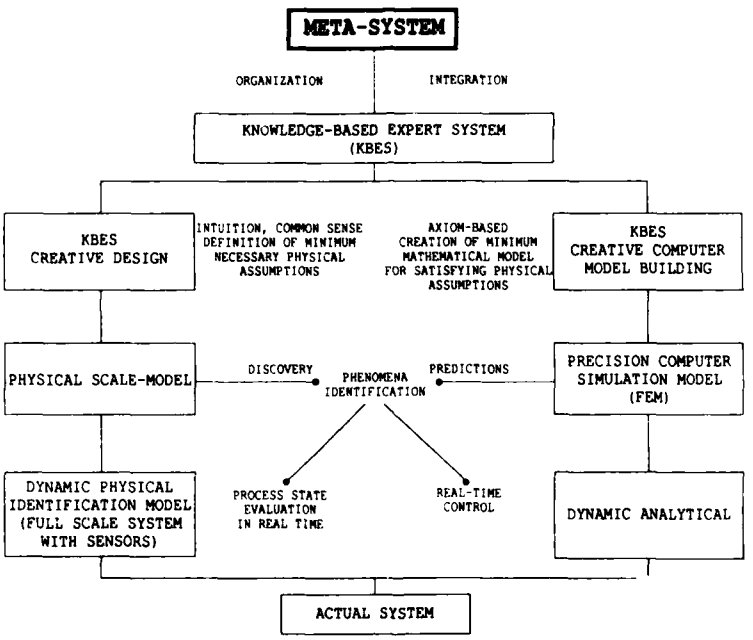

Figure 2 - Representation of Various Systems Used in Manufacturing Design.

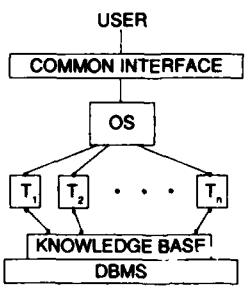

Figure 3 - Schematic Representation of Approach to Knowledge-Based Integration for Life-Cycle Assistance.

In summary, the assistant monitors and mediates between the user, design tools, and information which is needed for supporting the design life cycle. It 1) enforces the policies by which design team members move from one task to another, 2) assists with a task by bringing to the user's attention task-specific constraints and means of addressing them, 3) understands the complementary roles of users and tools in problem solving during the course of the design life cycle, and 4) eliminates the need to know tool-specific details such as input/output formats, cryptic commands and parameters, and which tool to utilize. Thus, the three types of models, when used in cooperation, form the basis for an intelligent computer-integrated-engineering (CIE) design methodology for design problems whose physical phenomena may be represented by partial differential equations. This methodology incorporates optimization techniques and the human decision-making procedure into an interactive design system which also utilizes designer intuition and logic in the design process.

Physical-scale modeling and computer-simulation modeling (Fig. 2) are used in parallel to identify the important characteristic phenomena associated with the particular material process manufacturing system. The computer-simulation model is generally based on an advanced numerical method such as the finite-element or finite-difference method. These methods allow the designer to build models which are very complete in process detail. Their major drawback is the amount of CPU time which is required for a given simulation. Other more approximate methods (7-10) are available for solving manufacturing problems and are generally part of the numerical-method repertoire available to the designer as a discrete tool. These tools are particularly valuable in the conceptual-design stage when possible process-design alternatives are being investigated. Generally, these approximate methods fall into the following categories: 1) the slab method which restricts the change of stress to only one direction, 2) the uniform-deformation-energy method which neglects redundant work, 3) the slip-line field solution which is limited to rigid-plastic materials under plane-strain conditions, and 4) the bounding methods which provide fairly good estimates of the upper and lower limits of the deformation force but cannot provide details of local stress and strain distributions (8). The boundary integral method is now being developed for treating three-dimensional flow problems in an approximate way. This numerical method will find increasing use as a conceptual design tool for introducing optimization at an early stage.

The dynamic analytical model is generally a second-order differential equation which adequately describes the performance of the whole system, and it is used to maintain any prescribed performance of the unit process. Real-time experimental data generated from a full-scale dynamic physical model (production equipment with sensors) are used in combination with the dynamic analytical model to evaluate the process state and to identify the possibility of faulting. Thus, qualitative and quantitative information is organized and integrated in an intelligent way for designing and controlling the actual system. A specific example for the case of solidification modeling and control is shown in Fig. 4. Figure 5 shows where expert systems might be used to support the design life cycle for the case of investment casting.

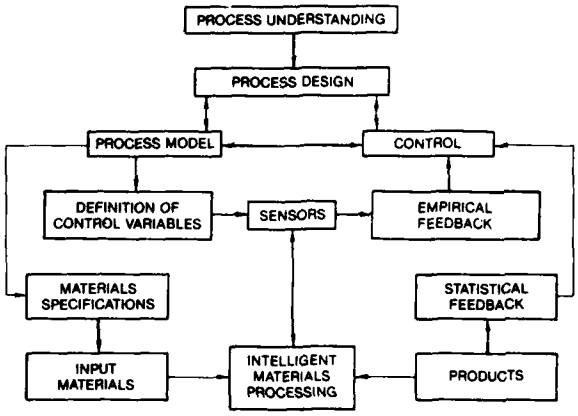

Figure 4 - Flow Diagram for Solidification Process Control Modeling.

A decision tree for a typical forging enterprise is shown in Fig. 6. It defines the various tasks, their interrelationship, and the analytical tools which are available to the design engineer for solving the enterprise's forging-process problems. Since this decision tree is a template of the thought processes of several forging design engineers, the KI-Shell™ represents a synthesis of data-modeling and artificial-intelligence techniques.

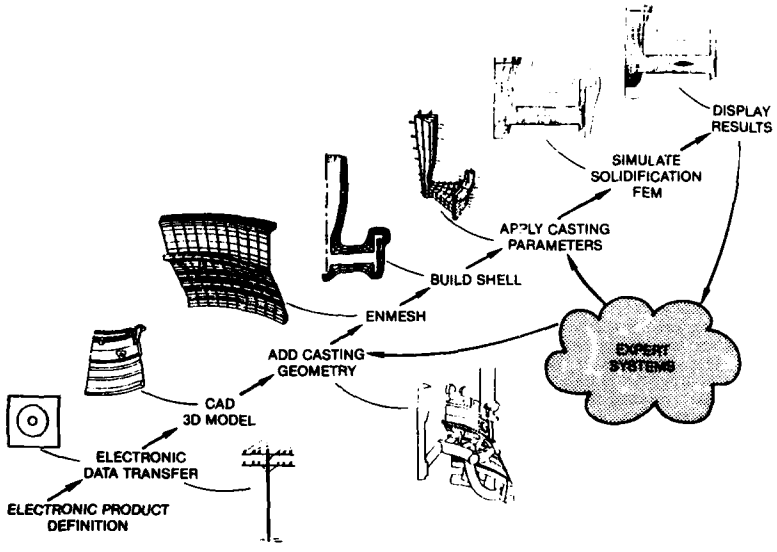

Figure 5 - Expert-Systems Applications in Process Modeling.

ANALYTICAL TOOLS REQUIRED FOR MODELING

Advanced Structural Materials

Most numerical methods that have been developed for modeling unit processes are based upon the fundamental time-dependent characteristics of material behavior. For example, materials have been classified as having elastic, viscoelastic, elastic-plastic, elastic-viscoplastic, and fluid-like characteristics. Approximations of these different types of behavior have been made to take into account both material characteristics and the nature of the shape-making process. An example is the rigid-plastic and rigid-viscoplastic finite-element program, ALPID (11), which is a generalized finite-element program for solving highly nonlinear plasticity problems common to most metalworking processes. Because the plastic strain is so large relative to the elastic deformation, the elastic characteristics of the workpiece material are neglected. This physical approximation solves several fundamental numerical and practical problems; by way of illustration, it eliminates the difficulty in obtaining numerical convergence during transitioning from elastic to plastic states while predicting accurate load and maintaining a high degree of accuracy in plastic-strain predictions. On the practical side, this approximation significantly reduces computation time and costs.

A number of analytical tools which are useful in modeling advanced structural materials are

- Elastic-Plastic Finite-Element Module
- Viscoplastic Finite-Element Module
- Elastic-Viscoplastic Finite-Element Module
- Fluid-Flow Finite-Element Module
- Heat-Transfer Finite-Element Module
- Mass-Transport Module for Fluid Flow by Seepage/Capillary Action
- Interface Modules for Superposing Chemical Reactions and Phase Transformations on Material Flow
- Distribution Function for Describing Whisker-Orientation Variation

ILLUSTRATIONS OF UNIT-PROCESS MODELING

ALPID Forging Simulations

Rib-Web Forging. The simulation of a titanium alloy is shown in Fig. 7; it was made to investigate the possibility of defect generation due to improper die design. These isothermal predictions substantiated the intuition and experience of titanium forging designers. The defect that would have formed in the actual forging was a lap. Other simulations for nonisothermal forging of the same titanium alloy showed that temperature gradients exacerbated the problem, indicating that this die design was very poor.

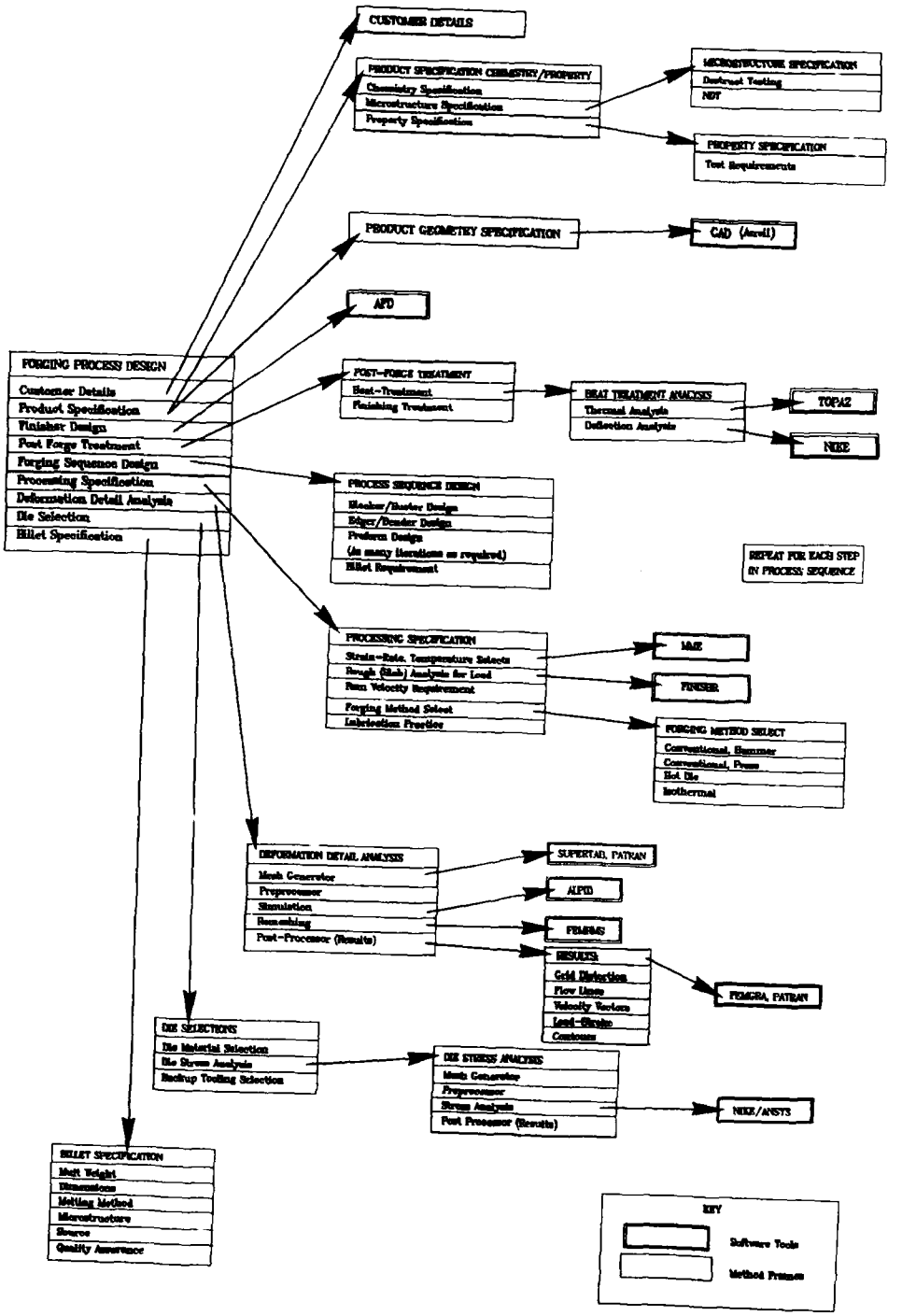

Figure 6 - Form Tree of Process Design.

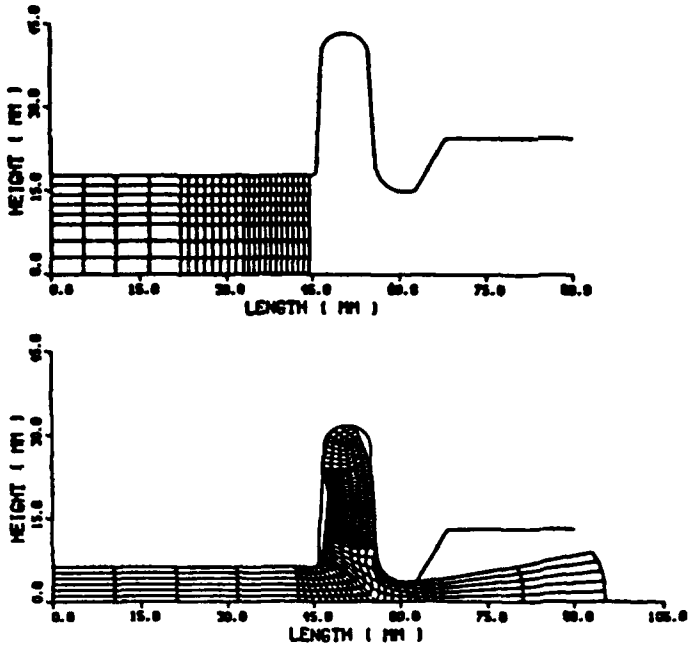

Figure 7 - Metal-Flow Simulation With ALPID during Rib-Web Forging.

3-D Wedge Deformation by Forging. Metal flow during a three-dimensional (3-D) deformation process is illustrated in Fig. 8. The 3-D shape changes which occur during forging were accurately predicted by the ALPID model. Careful examination of the deformation steps reveals that the specimen bulges at the anticipated locations and rotates at the thin side of the tapered wedge. This simulation represents one of the first attempts to model 3-D metal flow during open die forging.

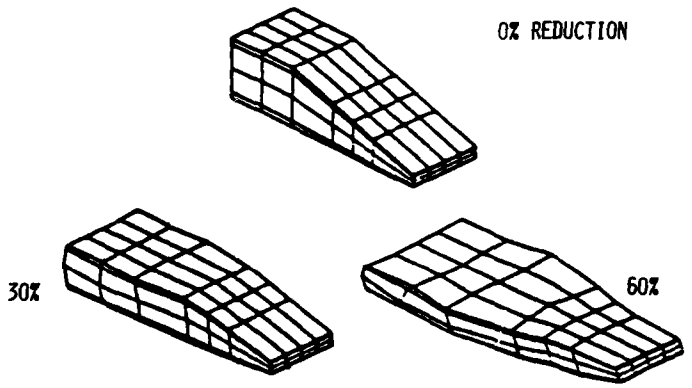

Figure 8 - Wedge Deformation Simulated by 3-D Finite-Element Method (Friction: m = 0.4).

Powder Consolidation

The ALPID thermoviscoplastic finite-element program was modified to accommodate the change in constitutive properties as a function of density increase during hot isothermal compaction of particulate materials. A schematic diagram of simple die pressing is shown in Fig. 9. Figure 10 illustrates the ALPID-predicted density distribution, indicated by solid contour lines, along with an experimental validation of the predictions, indicated by dashed contour lines.

Only one-fourth of the cylinder is shown in the simulation due to the geometrical symmetry of the process. Excellent agreement between predicted and observed results should be noted.

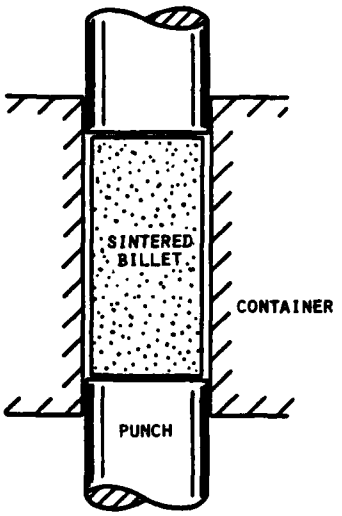

Figure 9 - Schematic Diagram of Simple Die Pressing.

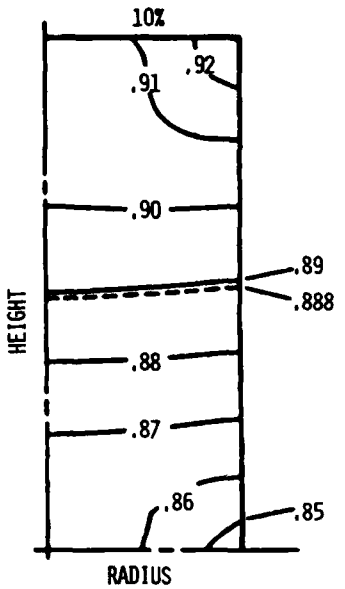

Figure 10 - Density Distribution Predicted by ALPID During Simple Die Pressing (Friction Factor, 0.2; Initial Relative Density, 0.8).

Sheet-Metal Forming

Stretch Forming of a Hemisphere. A punch stretch forming operation is shown schematically in Fig. 11 for a titanium sheet-metal alloy designated as Ti-6Al-4V. The simulations were made to predict the location of material thinning due to friction, temperature, and strain-rate distribution. The prediction in Fig. 12 was found to be in exact agreement with actual observations.

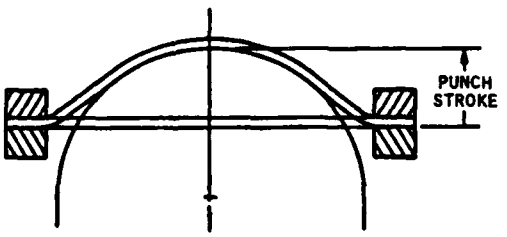

Figure 11 - Schematic Diagram of Stretch Forming of a Hemisphere (Friction = 0.3).

3-D Square-Cup Drawing. A schematic of the process for square-cup drawing of an aerospace structural aluminum alloy is presented in Fig. 13, and the 3-D ALPID-predicted results are given in Fig. 14. Because ALPID is a rigid-thermoviscoplastic finite-element model, springback predictions must be added through an elastic finite-element model. The springback analysis is always conducted after the plastic forming has occurred in a modular fashion. This methodology simplifies the problem formulation and reduces the total computation time.

Heat-Flow Modeling

Heat-flow analysis is frequently coupled with various types of material-flow models to predict the effect of temperature gradients on the possible field quantities. It has been applied for predicting shape distortions and residual stresses as a result of heat-treatment cycles. Heat-flow models can also be used independently to predict temperature gradients; and, for the case of solidification modeling where the solidification time is long, heat-flow analysis is conducted to evaluate the potential for solidification shrinkage. Most conventional solidification analyses are three dimensional, whereas the heat-flow analyses coupled with material flow are generally carried out for the two-dimensional cases because of the large amount of CPU time required. A typical heat-flow simulation is shown in Fig. 15 for an aluminum die casting. CAST3 was used (12) for this simulation.

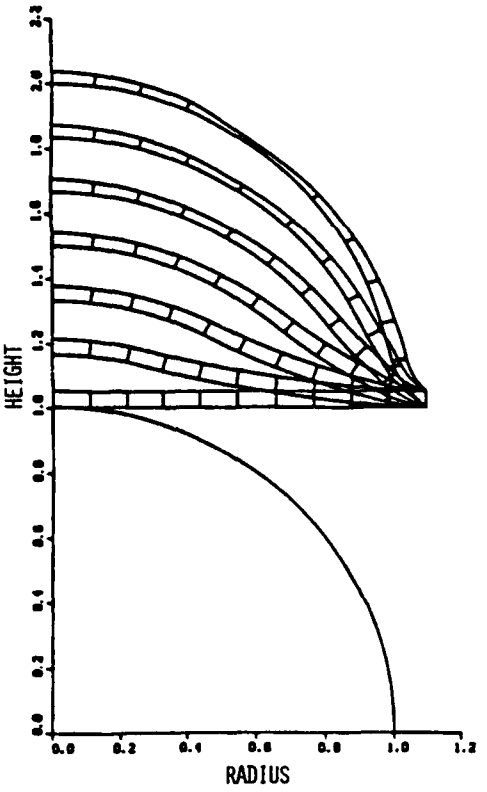

Figure 12 - Simulation of Various Stages in Stretch Forming of a Hemisphere.

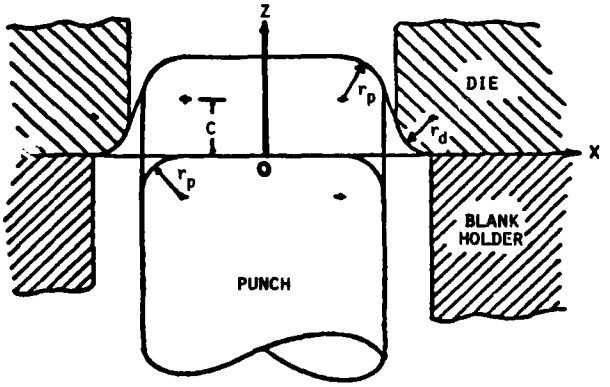

Figure 13 - Schematic Process Sketch of Square-Cup Drawing.

GENERAL- AND SPECIAL-PURPOSE APPLICATION CODES

Large general-purpose codes evolved over the years as different models became available, but the smaller special-purpose application packages were developed for the purpose of solving problems in a particular domain. The general-purpose packages are usually considered to be more difficult to use because of their generality. They usually consist of building blocks which must be integrated in order to develop a finite-element model of a specific manufacturing application such as sheet-metal forming, forging, or casting.

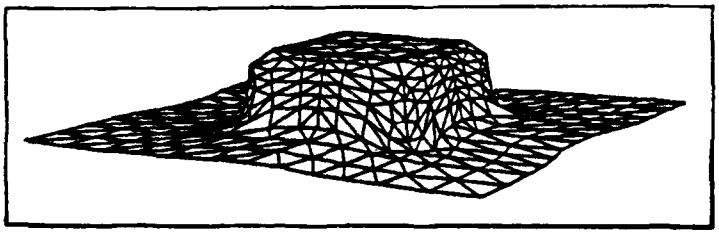

Figure 14 - Square-Cup Drawing Process Simulated by Three-Dimensional Sheet Program.

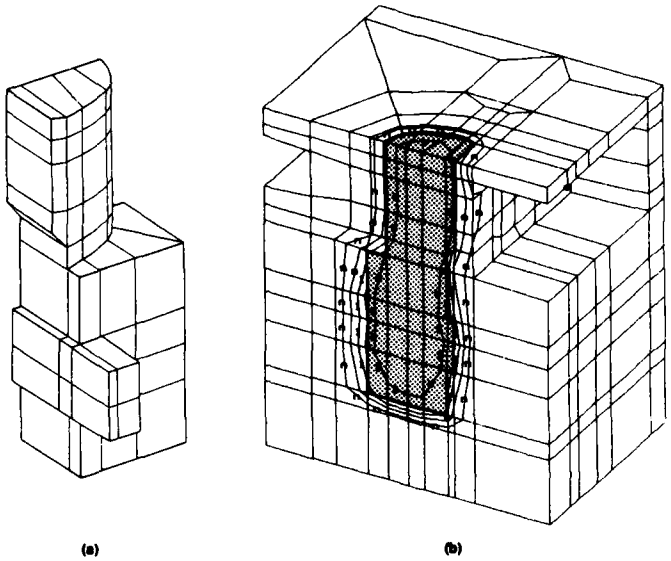

Figure 15 - Three-Dimensional FEM Simulation of Aluminum Die Casting in Iron Mold Showing Temperature Contours. (a) Part Geometry, (b) Solidifying Aluminum and Mold.

In principle, this appears to be an ideal situation; however, in practice, the building-block approach to modeling can be a barrier to its implementation in vendor organizations. Experience, for example, in comparing ALPID with certain commercial packages shows that ALPID can be at least four times as efficient for a complex net-shape forging problem and as much as two times as efficient for a simple upsetting problem with equivalent accuracy. Creating the finite-element model with the smaller-size programs similar to ALPID has also been found to be easier, especially for the novice engineer.

The more-generalized finite-element packages require the user to be more knowledgeable about finite-element procedures, including details concerning specific building blocks. Small vendor organizations often lack the financial or human resources required to dedicate a person to such a specialized field. Also, most vendor organizations have no need for the entire analysis capabilities offered by the commercial general-purpose codes. The smaller application packages were developed to circumvent these difficulties and to permit solutions to more complicated industrial problems, which involve such process attributes as heat transfer, chemical reactions, and phase changes.

ECONOMICS OF PARALLEL PROCESSING

A major barrier to the implementation of process-modeling methodologies as a routine design tool in vendor and manufacturing industries in the U. S., and probably throughout the world, is the overall cost. Two major cost factors in process design by computer simulation are 1) the efficiency of the designer in performing the design tasks, and 2) the cost of computation or CPU time. The first cost driver has already been discussed somewhat, but it should be placed in perspective again. The designer, in order to be efficient, should have a design system which assists him in solving the problem. The designer should be able to think about the design-problem solution rather than how the tools needed for each design task can be invoked. The system should allow the designer

to retrieve information easily from a repository regardless of the data-base structure or hardware system. Similarly, it should be possible to propagate the information generated during the design life cycle easily and automatically to other levels of design where it may be needed. The design system should have the capability for combining tools and dissociating them in such a way that the cryptic procedures are transparent to the designer. The time constant for invoking the tools and carrying out the numerical and symbolic computations should be as short as possible.

The purpose of integrating the tools used by a given enterprise with a KI-Shell™ is, in general, to enhance not only the performance of the designer but also the design and business policies of the particular enterprise. Minimizing the total clock time for numerical and symbolic processing depends on having a proper computer architecture in a workstation environment.

Recent advances in very large scale integrated circuit (VLSIC) technology have made it feasible to build large complex computers and perform scientific computations at interactive speeds, and drastic reduction in hardware costs have made parallel computers such as the NCUBE and the Intel hypercube available to many users at affordable prices. However, since commercial products must be general purpose to permit them to be marketed in different areas of application, algorithms must be developed and existing algorithms restructured for the architecture if these computers are to be used in a specific application. Optimal performance can be attained only when the architecture is tailored to the computational requirements of the applications as has been done in the areas of computer vision and digital signal processing.

An increase in speed of computation by parallelism can be achieved at different levels of computation, resulting in three classes of parallel architectures--namely, multiprocessors, attached computational arrays (high-performance math processors), and pipelined vector processors. Multiprocessors consist of a number of inexpensive processors running in parallel which share data either through shared memory or by explicit message passing. The processor interconnection scheme is a crucial parameter affecting the performance of a multiprocessor. The hypercube architecture falls in the message-passing multiprocessor category. A number of research and commercial multiprocessors have been implemented. Attached-array processors are specialized hardware units consisting of multiple arithmetic units which are tailored to perform specific computations very swiftly using internal parallelism and pipelining. Systolic arrays have been proposed for computations; these must be used as a coprocessor to a general-purpose host computer and are not yet available as commercial products. Finally, vector CPU's such as CRAY-1 are designed for fast arithmetic operations on data arranged in arrays. These systems are too expensive to be used as a CPU for a workstation.

During the U. S. Air Force effort to build a powerful workstation for supporting cost-effective design, these three classes of computers were evaluated; it was determined that the hypercube architecture would provide the most computational power for the cost, and a prototype system was built and demonstrated. The powerful workstation consisted of a DEC Microvax-II host computer for input/output processing and an Intel hypercube system with vector processing at each node. The design tools were integrated with a KI-Shell™. This approach allowed the designer to do a global (design-in-the-large) analysis of the problem based on an embedded methodology for an extrusion enterprise in this particular case, and detailed design was accomplished with finite-element modeling using the high-speed capabilities of the hypercube computer. Computational speed-up ranged from 30 to 100 times, depending on the size and complexity of the design problem and the number of available processors. The more complex the design problem, the larger the speed-up observed. This experience indicates that three-dimensional finite-element analysis will become affordable for the various classes of metal-deformation problems. Much fundamental work remains to be done in the development of a powerful workstation for process and product design. Proper architectures must be developed which optimize both numerical and symbolic processing since the design process is heuristic, deterministic, and data-base driven. The new workstation architectures should have features which allow 1) reconfiguration for implementing different processor interconnection topologies of different steps of computation to provide swift routing of data between processors and memories, 2) vector VLSIC coprocessors to speed up vectorizable segments of the code, and 3) shared memory for fast access to global data.

MATERIAL-BEHAVIOR MODELING

Success in the use of process simulation as a manufacturing design tool depends strongly upon good material models and physical-property data for the mathematical model. Incorporating the behavior of the workpiece material under processing conditions has been severely neglected in past approaches to designing unit processes; in many cases, constitutive equations were used as a matter of convenience. Classical workability analysis has served as a qualitative guideline at best (13).

The traditional approach to describing material workability is inadequate since the effects of poor die design cannot be separated from the inability of the material to satisfy the demands of the process. The ability to define the intrinsic workability of any material would be a direct step toward achieving near-optimal design by process modeling. The traditional approach to process modeling is, in effect, only process diagnostics because the resulting solution is entirely dependent upon the initial boundary conditions selected for the modeling. This solution is called an admissible solution, and it does not necessarily represent the actual material behavior during processing.

Interpretation of the results is based entirely upon the past experience of the designer. Process design by this approach may require as many as 15 to 20 simulations and a good guess.

Recently, a new scientific approach to describing the intrinsic workability of any workpiece material being subjected to large nonlinear plastic deformations as a function of temperature and time has been developed. Gegel (14,15), Prasad, et al. (16), and Gegel, et al. (17), developed a method called Dynamic Material Modeling which describes the mechanical and microstructural stability of a material system as a function of time. They view the workpiece material as a stochastic dynamic system and model it using control-theory methodologies. Because it is impossible to predict a priori how the various time-dependent deformation processes will combine to provide the degrees of freedom required for irreversible plastic flow, the workpiece is treated as a black box and modeled as input and output functions. A constitutive equation is developed in terms of state variables, and it is expressed as $\bar{\sigma} = \bar{\sigma}(T, \ln\dot{\bar{\varepsilon}}, t)$, where $\bar{\sigma}$ is the effective flow stress, $\ln\dot{\bar{\varepsilon}}$ the logarithm of the effective strain rate, T the absolute temperature, and t time. Information regarding the stability of the system as a function of time is derived from this equation by applying the Lyapounov (18) axiom. Figure 16 is a graphical representation for Ti-6242 alloy for a time which corresponds to an effective strain of 0.6. Figure 17 is a processing map for 2024 aluminum alloy containing ∿ 20 volume percent SiC whiskers for a time which is equivalent to 0.3 effective strain. These are composite maps which show both mechanical and metallurgical stability. The boundaries surrounding the stable region are the stationary states for the system at some particular time t, and they represent the set of catastrophy points for the system. A catastrophy point represents a singularity such as a first-order phase transformation, crack nucleation, or the onset of a plastic instability. This information has been incorporated into the ALPID finite-element program by Malas (18) as a nonholonomic constraint to optimize workability and as a system parameter for controlling the evolution of microstructure. The nonholonomic constraint procedure is schematically shown in Fig. 18.

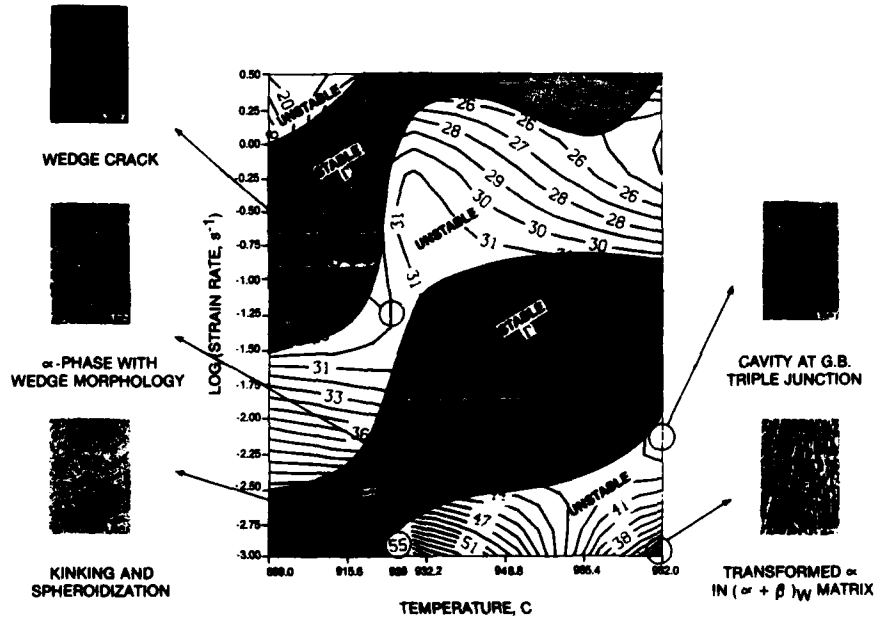

Figure 16 - Processing Map for Ti-6242 β Preform.

An important point should be made concerning material properties. A limiting factor to the application of process-simulation techniques for routinely designing new fabrication processes will be the lack of a validated material data base. Information such as constitutive equations, intrinsic workability maps, effective heat-transfer coefficients, interface parameters for friction analysis, and heat-capacity data for the workpiece and die materials and their coefficients of expansion must be developed and validated for a certified design data base. This area of research appears to be one where the NATO countries could effectively cooperate to establish a data base and standard test and analysis methodologies.

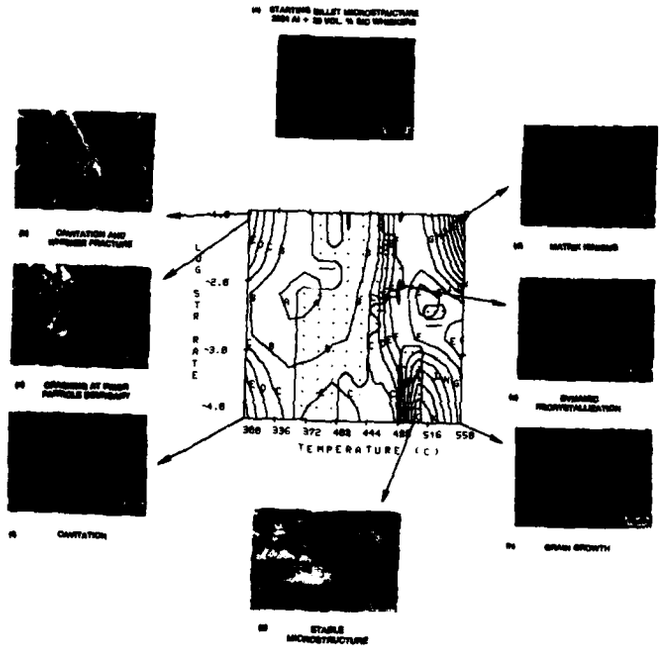

Figure 17 - Processing Map for 2024 Aluminum Alloy with SiC Whiskers.

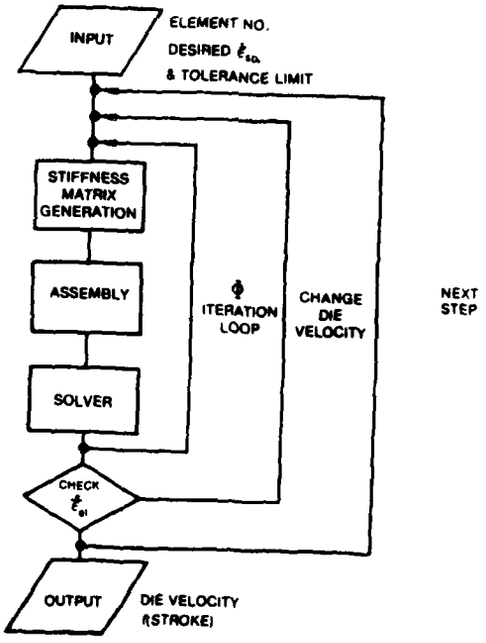

Figure 18 - Schematic Diagram of Nonholonomic-Constraint Procedure.

REFERENCES

1. Ramanathan, J., Demion, S., McKnight, W., and Li, C., "Opportunities and Approaches for using Artificial Intelligence Techniques in Practical Software Engineering Environments," Technical Report TRIAD-7, Dept CIS, The Ohio State University, Columbus, OH, 1984.

2. Barr, A., and Feigenbaum, E. A., The Handbook of Artificial Intelligence, Vol. II, Heuris Tech Press, Stanford, CA, and William Kaufmann, Inc., Los Angeles, CA, 1982.

3. Chandrasekaran, B., "Expert Systems: Matching Techniques to Tasks," Annual Report for Research on Distributed Knowledge Base Systems for Diagnosis and Information Retrieval, Air Force Office of Scientific Research, Bolling Air Force Base, Washington, D.C., November 1983.

4. King, M. S., Brooks, S. L., and Schaefer, R. M., "Knowledge-Based Systems: How Will They Affect Manufacturing in the 80's?," Computers in Engineering 1985, Vol. 2, The American Society of Mechanical Engineers, New York, NY, 1985, pp. 383-390.

5. Ramanathan, J., and Venugopal, V., "Tool Integration in Life Cycle Support Environments," Proceedings National Computer Conference, AFIPS, 1987.

6. Ramanathan, J., and Venugopal, V., "Knowledge-Based Assistance for Design in the Large," UES-KIC Technical Report KICTR-871, Universal Energy Systems, Knowledge Integration Center, Columbus, OH, 1987; Ramanathan, J., Ashok, V., et al., "Knowledge-Based Monitor and Repository for Life-Cycle Assistance," UES-KIC Technical Report KICTR-872, Universal Energy Systems, Knowledge Integration Center, Columbus, OH, 1987.

7. Pittman, J. F. T., Wood, R. D., Alexander, J. M., and Zienkiewicz, O. C., Numerical Methods in Industrial Forming Processes - Proceedings of An International Conference Held at The University College, Swansea, Pineridge Press Ltd., West Cross, Swansea, U. K., 1982.

8. Thomsen, E. G., Yang, C. T., and Kobayashi, S., Mechanics of Plastic Deformation in Metal Processing, The Macmillan Company, New York, NY, and Collier-Macmillan Ltd, London, U. K., 1965.

9. Altan, T., Oh, S.I., and Gegel, H. L., Metal Forming - Fundamentals and Applications, The American Society for Metals, Metals Park, OH, 1983.

10. Gunasekera, J. S., Gegel, H. L., Malas, J. C., Doraivelu, S. M., and Morgan, J. T., "Computer-Aided Process Modeling of Hot Forging and Extrusion of Aluminum Alloys," Annals of the CIRP, Vol. 31, Techniche Rundschau, Berne, Switzerland, 1982, pp. 132-135.

11. Oh, S. I., "Finite Element Analysis of Metal Forming Processes with Arbitrarily Shaped Dies," International Journal of Mechanical Science, Vol. 24, 1982, p. 479.

12. Samonds, M., et al., "Finite Element Modeling of Solidification in Sand Casting Employing an Implicit-Explicit Algorithm," Applied Mathematical Modeling, Vol. 9, 1985, pp. 170-174.

13. Dieter, L. E., "Bulk Workability Testing," Metals Handbook, Mechanical Testing, Vol. 8, American Society for Metals, Metals Park, OH, 1985, pp. 573-597.

14. Gegel, H. L., in Proceedings of Symposium on Experimental Verification of Process Models 1981, Chen, C. C., ed. (Metals Congress, September 21-23, 1981, Cincinnati, OH, 1981), American Society for Metals, Metals Park, OH, 1983, pp. 32.

15. Gegel, H. L., "Synthesis of Atomistics and Continuum Modeling to Describe Microstructure," Computer Simulation in Materials Science, Arsenault, R. J., Beeler, J. R., Jr., and Esterling, D. M., eds., American Society for Metals International, Metals Park, OH, 1987, pp. 291-344.

16. Prasad, Y. V. R. K., et al., "Modeling of Dynamic Materials Behavior in Hot Deformation; Forging of Ti-6242," Metallurgical Transactions, Vol. A15, 1984, p. 1883.

17. Gegel, H. L., et al., "Materials Modeling and Intrinsic Workability for Simulation of Bulk Deformation," Advanced Technology of Plasticity, Vol. 2, Lange, K., ed., Springer-Verlag, Berlin, 1987, pp. 1243.

18. Malas, J. C., Thermodynamic and Continuum Approach to the Design and Control of Precision Forging Processes, Masters Thesis, Wright State University, Dayton, OH, 1985.

ACKNOWLEDGMENTS

Special thanks go to Mr. J. C. Malas and Dr. S. M. Doraivelu for helpful discussions during the preparation of this paper and to Ms. M. Whitaker for editorial assistance and preparation of the manuscript.

Modelling of Deformation and Microstructural Changes in P/M René 95 Under Isothermal Forging Conditions

by

O. Alniak*, D.D. Morphy**, T. Terada**, A.K. Koul** and J-P. Immarigeon**

* Kara Harp Okulu, Teknik Bölüm
Military Academy, Technical Division
Ankara, Turkey

**National Aeronautical Establishment
National Research Council of Canada
Ottawa, Ontario, Canada, K1A 0R6

SUMMARY

The changes in microstructure induced by forging and their influence on flow strength in hot isostatically pressed P/M René 95 as revealed by constant true strain compression tests under simulated isothermal forging conditions are discussed. Results are presented for initially fine (7 μm) and coarse (50 μm) grained compacts tested at temperatures of 1050, 1075 and 1100°C and at strain rates in the range from 10^{-4} s^{-1} to 1 s^{-1}. Under these test conditions, both the fine and coarse grained compacts recrystallize and their grain size is refined during flow. This grain refinement gives rise to softening in both materials. Ultimately, their microstructures transform into the same equiaxed fine grained microduplex structure at which point their flow strength becomes identical. Continued deformation at that point produces no further change in grain size or flow strength. Under this steady state regime of deformation, the microduplex grain size and flow strength are independent of the original microstructure but are conditioned by the strain rate at a given temperature. The steady state grain size increases whereas the steady flow strength decreases with a decrease in strain rate and/or an increase in temperature. It is shown how changes in microstructure and flow strength during isothermal forging can be modelled in P/M René 95 compacts by means of established deformation models for predicting peak flow strength, using the steady state deformation data as a boundary condition for the evolution of microstructure and flow strength and a model for deformation-induced recrystallization during forging that has been recently developed for this class of materials.

SYMBOLS

ϵ	true strain, ln(h/ho) where ho is initial specimen height
$\dot{\epsilon}$	true strain rate
$\dot{\epsilon}_S$	strain rate in soft regions of model material
$\dot{\epsilon}_R$	strain rate in hard regions of model material
F	volume fraction of soft recrystallized material
σ	flow stress
σ_p	peak flow strength
σ_{ss}	steady state flow strength
σ_o	back stress due to intragranular γ'
σ_i	internal stress due to grain boundary ledges
m	strain rate sensitivity of flow strength
p	grain size sensitivity of flow strength
Q	activation energy
R	gas constant
T	absolute temperature in K
$C(S, \dot{\epsilon})$	structure and strain rate dependent time constant
t	time
n	time exponent
A, A'	experimentally established material constants
$\dot{\epsilon}_{gbs}$	rate equation for grain boundary sliding
$\dot{\epsilon}_{gbs/AV}$	ibid. (Ashby and Verall mechanism)
$\dot{\epsilon}_{gbs/G}$	ibid. (Gittus mechanism)
$\dot{\epsilon}_{mdg}$	rate equation for intragranular flow by dislocation creep (motion of dislocation within grains)
D_V	volume diffusion coefficient
D_B	grain boundary or interphase boundary diffusion coefficient
Γ	grain boundary energy
b	Burgers' vector
μ	shear modulus
k	Boltzmann's Constant
λ	initial grain size
d	as-worked steady state grain size
N	number of steady state grain layers in partially recrystallized spherical grain model.

See also Table IV

1. INTRODUCTION

One of the major materials engineering breakthroughs of the early seventies was the development of powder processed nickel-base superalloys for use in gas turbine engines[1]. It was then demonstrated that practically unworkable high strength nickel-base superalloys could be made readily forgeable by a combination of rapid solidification and isothermal metalworking technologies[2]. This allowed the production of high strength powder processed discs for use in high performance aero engines. Powder metallurgy superalloy technology is by now well established and powder processed parts are used both in military and civilian engines[3].

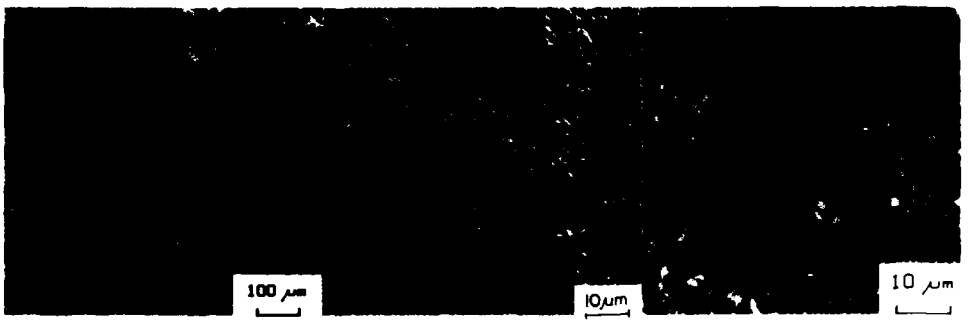

Figure 1. Examples of necklace microstructures (a) and (b) in isothermally forged P/M MarM200 and (c) P/M 713LC compacts showing partial recrystallization of initially coarse-grained microstructures after forging at sub-solvus temperatures. (after Immarigeon et al., Refs. 10 and 15).

In this technology, high strength alloys are first atomized from the melt into a powder which is subsequently consolidated into fully dense compacts by hot extrusion or hot isostatic pressing(4). The high rates of solidification achieved during atomization result in powders containing fine-grained particles of uniform composition. Consolidation produces compacts which have excellent mechanical properties and can be used in the as-consolidated condition in some applications. The as-consolidated compacts can also be further processed by forging to optimize their mechanical properties. This is done normally at slow strain rates, typically in the range between 10^{-3} and 10^{-1} s^{-1}, under isothermal or near isothermal forging conditions(5).

The extent to which microstructure and therefore mechanical properties can be controlled in these materials by thermomechanical treatments is quite remarkable. These alloys are multiphase materials that contain a large volume fraction of an intermetallic compound called γ'. The γ' is a metastable ordered phase which precipitates during cooling from high temperatures and its morphology controls mechanical properties. Above a certain temperature, called the γ' solvus temperature, this phase is unstable and ultimately goes into solid solution. During working at temperatures below the γ' solvus temperature, the presence of the γ' promotes recrystallization and prevents grain growth. Fine grained microstructures with superior low cycle fatigue (LCF) properties can therefore be obtained by mechanical working at sub-solvus temperatures whereas coarse grained microstructures with superior creep properties can be obtained by heat treatment above the γ' solvus temperature where grain growth can virtually proceed unimpeded. A wide range of in-between microstructures, including the so-called necklace structures produced by forging a coarse grained compact at sub-solvus temperatures, is also possible(6). Necklace structures offer excellent combinations of LCF and crack propagation resistance(7) which may be desirable in some applications.

There is much interest in the forging industry in the development of techniques for predicting microstructures in forgings in order to optimize the mechanical properties of forged components(8,10). In recent years, powerful computer techniques and numerical procedures have been developed for the analysis of large strain plasticity problems(11). Those that rely on the finite element method have evolved to the point where they can be used to predict microstructures in forgings so long as there are means available to describe the evolution of microstructure and its influence on flow characteristics during forging(12). This requires data on flow strength and its relationship to microstructure at forging temperatures and strain rates(13).

Extensive work has been conducted at the NAE to study the forging behaviour of P/M superalloys(14-18) and, recently, a model was proposed for deformation-induced recrystallization and necklace formation in these materials(19). In the proposed model, partially recrystallized material characteristic of a necklace structure of the type shown in Fig. 1 is regarded as a composite material consisting of hard unrecrystallized and soft recrystallized regions. Variations in flow strength during forging are ascribed to changes in the volume fraction F of recrystallized material.

The rate equation for the deformation of partially recrystallized composite material is written in terms of those for the recrystallized and unrecrystallized regions as

$$\dot{\epsilon} = F\,\dot{\epsilon}_S + (1 - F)\,\dot{\epsilon}_H \qquad (1)$$

where the rate equations for the soft and hard regions, $\dot{\epsilon}_S$ and $\dot{\epsilon}_H$ may be viewed as constitutive relations that relate flow strength to strain rate and temperature within each region. Both relations are of the general form

$$\dot{\epsilon} = A\,\lambda^p\,(\sigma - \sigma_0)^{1/m}\,\exp\left(\frac{-Q}{RT}\right) \qquad (2)$$

where A is material constant, λ is the grain size, σ is the flow stress, σ_0 is a microstructure dependent parameter, p and m are numerical exponents that depend on the mechanism of deformation , Q is the activation energy for the deformation mechanism, T is the absolute temperature and R is the gas constant.

The volume fraction F of recrystallized material is described in the proposed model by an Avrami type relation of the form

$$F = 1 - \exp\left(-C(S,\dot{\epsilon})\,t^n\right) \qquad (3)$$

where C is a parameter conditioned by the instantaneous microstructure and strain rate, t is the time and n is a

Table I. Chemical composition of the commercially procured René 95 powder used in this study (Wt.%)

C	Mn	Si	Cr	Ni	Co	Fe	Mo	W	Nb	Ti	Al
.059	.03	.02	13.18	Bal	7.60	.09	3.48	3.38	3.39	2.59	3.44

B	Zr	S	P	O	N
.012	.05	.001	.003	84ppm	26ppm

numerical exponent whose value can vary from 1 to 4 depending on the nature of the nucleation and growth of the recrystallized grains. The model has been shown to be consistent with the forging behaviour of both coarse and fine-grained P/M 713LC compacts.[19]

The purpose of the work described in this paper was to assess the applicability of these concepts to the modelling of flow stress and microstructural changes in P/M René 95 during isothermal forging. To this end, compacts were prepared from a commercially procured P/M René 95 powder and their forging characteristics under isothermal forging conditions were evaluated by compression testing.

2. EXPERIMENTAL MATERIAL

The commercially procured -150 mesh argon atomized powder used in this study was a low carbon version of the standard René 95 alloy with a very fine grain size of the order of 1 to 5 microns. The chemical composition of the powder and its mesh size distribution are given in Tables I and II respectively. Fully dense compacts of the powder were produced by hot isostatic pressing at sub-solvus temperatures in order to obtain a fine-grained microstructure. The powder was first encapsulated in 304 stainless steel cans and degassed at 350°C under a vacuum of 6×10^{-6} mbar for at least eight hours prior to compaction. The cans were then sealed off by tungsten inert gas welding and subsequently hot isostatically pressed (HIPed) in the NAE HIP facility. A dual-stage HIP cycle was used that has been shown to minimize MC carbide precipitation at prior particle boundaries (PPB)(20). Details of the HIP consolidation conditions are given in Table III.

Table II. Mesh size distribution of the commercially procured René 95 powder used in this study

Mesh Size	+140	-140 +200	-200 +270	-270 +325	-325 +400	-400
% fraction	0	12.6	19.4	10.0	9.3	48.7

The compacts were produced in the form of round bars 30 cm long by 2 cm in diameter from which cylindrical compression test pieces were machined as detailed under section 3. The microstructures at the ends of the as-hipped bars were compared in terms of second phase volume fraction, morphology and distribution and in terms of grain size. They were found to be identical, a reflection of a good temperature uniformity within the HIP vessel. A typical as-hipped microstructure is shown in Fig. 2. It consists primarily of a fine-grained microduplex structure with a uniform dispersion of a few apparently undeformed powder particles that have retained an as-cast fine-grained dendritic structure. The presence of the γ' phase during consolidation has minimized growth of the fine as-atomized grains. It also has promoted recrystallization and the formation of the microduplex structure. The latter consists of coarse primary γ' in a fine grained γ matrix. The primary γ' size is close to that of the γ grain size and this gives the structure its microduplex appearance. The material also contains a large volume fraction of uniformly distributed intragranular cooling γ' which was formed during slow cooling in the HIP press from the HIP temperature.

Table III. Hot isostatic pressing conditions used for consolidating the René 95 powder*

Temperature °C ± 0.5%	Time hrs	Argon Pressure MPa
950	3	193
plus 1120	2	207

* γ' solvus temperature approximately 1160°C

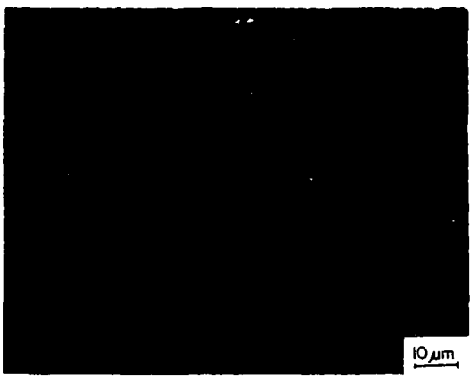

Figure 2. Typical microstructure of the experimental P/M René 95 compacts produced by hot isostatic pressing at sub-solvus temperatures exhibiting a uniform dispersion of a few undeformed powder particles (arrows ⟹) in a fine grained microduplex matrix (arrows ▶—). (Details of consolidation conditions are given in Table III.)

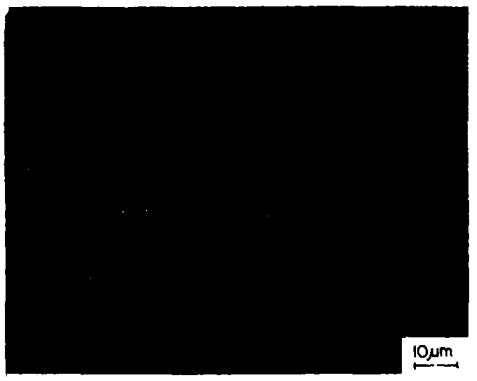

Figure 3. Microstructure of the hipped P/M René 95 compacts after a grain coarsening treatment of 2 hours at a super-solvus temperature of 1200°C followed by slow cooling showing preferential precipitation of coarse γ' at grain boundaries and prior particle boundaries (arrows ⟹) and a dispersion of fine cooling γ' in the grains interiors (arrow ▶—).

The hot working characteristics of the experimental material were evaluated in the as-hipped fine-grained condition typified by Fig. 2 and in a grain coarsened condition obtained by heat treatment of the as-hipped material above its γ' solvus temperature. The microstructure produced by this treatment is shown in Fig. 3. By dissolving the γ', the fine as-hipped grains were allowed to grow and a coarse grained structure was obtained. The heat treatment employed consisted of 2 hours at 1200°C followed by slow cooling in the furnace. This slow cooling was applied to simulate cooling in the HIP press and thereby produce a cooling γ' morphology similar to that which would have been obtained in compacts produced by consolidation above the γ' solvus temperature.

As compared to the as-hipped fine-grained material, Fig. 2, the grain size after heat-treatment, Fig. 3, is large approaching the powder particle size. The grain boundaries have obviously not migrated past the PPB's probably due to the pinning effects of the MC carbides and/or other segregated compounds or elements that are known to be present along these boundaries[21,22]. During slow cooling from the solutioning temperature some preferential agglomeration of the γ' has occurred along the grain boundaries. This makes the PPB stand out and enhances the particulate appearance of the microstructure since many of the grain boundaries coincide with PPB's. There is also some evidence of γ' cellular growth in the vicinity of PPB's that has also been caused by slow cooling.

While it is evident that the grain size is far from being uniform, either in the as-hipped or grain-coarsened material, an average mean linear intercept grain size was established in each case for the purpose of the analysis. The measured grain sizes averaged 7 μm and 50 μm for the as-hipped and the grain-coarsened compacts respectively.

3. EXPERIMENTAL METHOD

The isothermal forging characteristics of the compacts were evaluated by means of carefully controlled uniaxial compression tests using a high temperature test rig developed by NAE for isothermal forging studies[23]. The induction heated rig, which is shown with its peripheral equipment in Fig. 4 and in cross section in Fig. 5, allows compression tests to be conducted in a controlled atmosphere at temperatures up to 1200°C and at constant true strain rates anywhere between 5×10^{-5} and $5\ s^{-1}$. In this rig, the compression test piece can be quenched within seconds of the end of the test, which allows as-worked microstructures to be preserved for metallographic studies. The rig is used with a universal testing machine which is interfaced to a dedicated minicomputer used for test management and data acquisition.Details of this apparatus have been published elsewhere[23,24].

In this study, compression tests were conducted at 1050, 1075 and 1100°C and at strain rates in the range from $10^{-4}\ s^{-1}$ to $1\ s^{-1}$, using small cylindrical compression test pieces with the geometry and dimensions shown in Fig. 6. Test temperatures were kept constant to within ±2°C and were controlled with calibrated thermocouples embedded in the compression tooling. Test strain rates were maintained constant to within better than ±3% of the preset rates using an analogue function generator to control the motion of the MTS hydraulic actuator and a high temperature displacement transducer to measure the gap between the compression dies[25]. The specimens were heated in the rig and soaked at the test temperature for 20 minutes prior to testing. A lubricant consisting of a mixture of boron nitride powder and a boro-silicate glass frit was used to reduce friction at the interface between the specimen end faces and the compression tooling. This proved reasonably effective in preventing barelling of the specimen and in ensuring homogeneity of the deformation as evidenced by the uniform spread of the lubricating groves machined in the specimen end faces and by the absence of barelling. This is demonstrated in Fig. 7 after a true strain of 1.2 corresponding to a 70% reduction in height of the compression test piece.

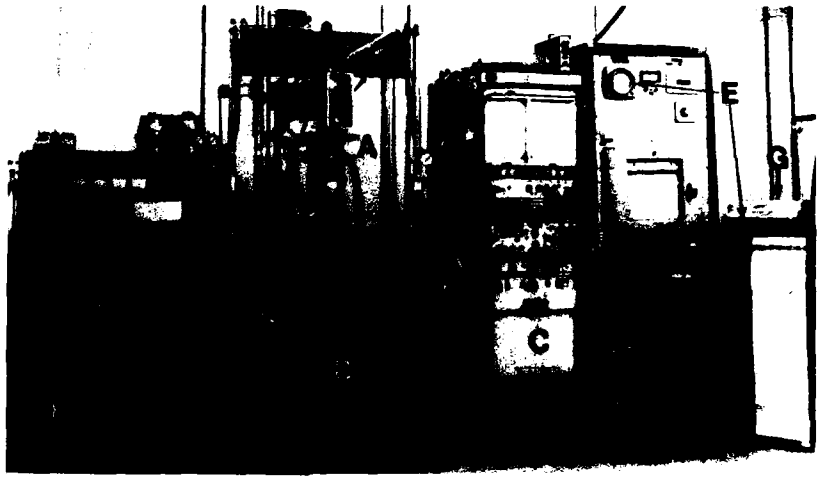

Figure 4. NAE's high temperature compression test rig for isothermal forging studies showing
A Induction-heated furnace and compression tooling
B Servo-controlled hydraulic test frame
C Computer interfaced servo-controller
D Analog function generator for constant true strain rate control
E Temperature controller and multi pen-recorder
F Induction generator for high temperature furnace
G Inert gas drying and deoxidation train
(after Gautron et al. Ref. 24)

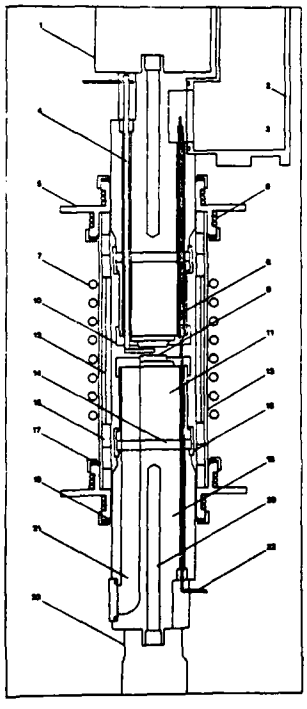

1	Load cell	-
2	Window	Plexiglass
3	Displacement transducer housing	aluminum
4	Quenching actuator	TZM
5	Collar	304 SS
6	Cooling coil	copper
7	Induction coil	copper
8	Transducer probes	alumina
9	Compression dies	silcon nitride
10	Collar	TZM
11	Anvil	TZM
12	Susceptor	301 SS
13	Furnace retort	quartz
14	Thermal insulating plate	cotronic 902
15	Thermal insulating collar	asbestos
16	Collar	304 SS
17	O-ring	viton
18	Anvil support	347 SS
19	O-ring	viton
20	Internal cooling passages	-
21	Quenching chute	-
22	Type K thermocouple	inconel sheathed
23	Hydraulic actuator	-

Figure 5. Schematic cross section of NAE's high temperature compression test rig identifying the key components of the compression train and the materials used in each case. (after Gautron et al. Ref. 24).

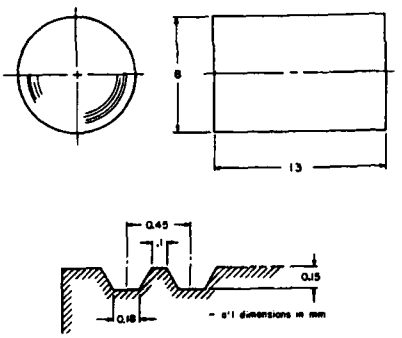

Figure 6. Details of the geometry and dimensions of the compression specimens showing the fine grooves machined in their end faces to retain the high temperature lubricant used in this work to reduce friction and promote uniaxiality of deformation.

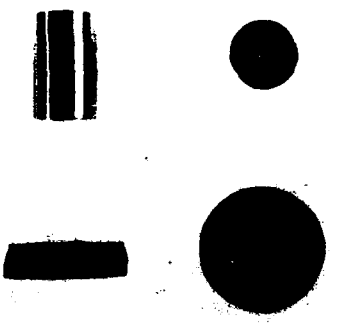

Figure 7. Compression specimens before and after testing. The uniform expansion of the lubricating grooves in the end faces of the test piece and the relative absence of barelling after a true strain of 1.2 are typical of the tests conducted in this work.

Two types of tests were performed in this study, one where the strain rate was maintained constant throughout the test and several specimens were deformed to the same strain of 1.2, and the other where the strain rate was increased in a stepwise manner, while keeping the total accumulated strain as small as possible to minimize changes in microstructure. In the first case, the test parameters were varied to establish the strain rate and temperature dependence of flow strength and to evaluate the effects of strain rate and temperature on the as-worked microstructure. In the second case, where the strain rate was incrementally increased by a factor of around three in a stepwise manner, a single specimen was used to establish the strain rate and temperature dependence of flow strength at constant structure.

4. RESULTS AND DISCUSSION

The bulk of the experimental work was conducted on the as-hipped fine grained compacts since the deformation data for fine grained microstructures is needed to model deformation in both fine and partially recrystallized coarse-grained compacts as will be explained later. The constant true strain rate compression flow curves for the as-hipped material are shown in Fig. 8. The data indicate that the flow stress reaches its maximum value in the early stages of deformation for most test conditions. The material subsequently softens with increasing strain at all but the slowest strain rates, where the flow stress appears independent of strain, although there is some evidence of hardening during flow at the highest temperature (1100°C) and slowest strain rate (10^{-4} s^{-1}) examined.

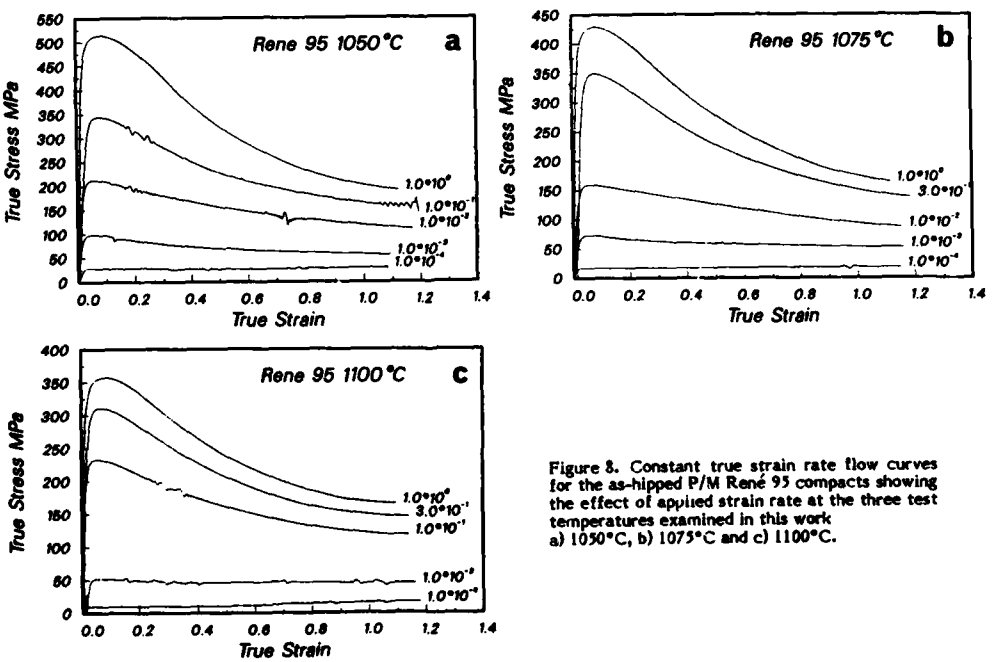

Figure 8. Constant true strain rate flow curves for the as-hipped P/M René 95 compacts showing the effect of applied strain rate at the three test temperatures examined in this work
a) 1050°C, b) 1075°C and c) 1100°C.

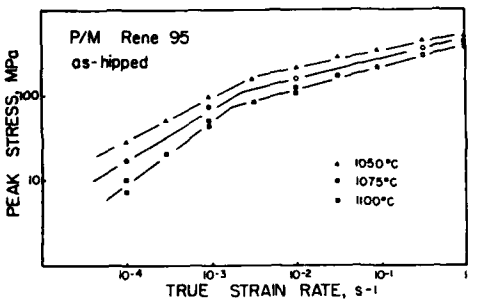

Figure 9. Variation in the peak flow strength of the hipped P/M René 95 fine grained compacts as a function of strain rate (log.log plot).

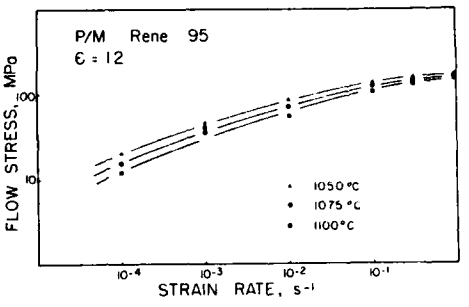

Figure 10. Variation in flow stress of the P/M René 95 compacts at a strain of 1.2 as a function of strain rate at the three test temperatures.

4.1 Strain Rate Dependence of Flow Strength

The effects of strain rate, $\dot{\epsilon}$, on the peak flow strength, σp, of the fine-grained as hipped material are illustrated in Fig. 9. A discontinuity in the strain rate sensitivity, the slopes m of the isothermal curves in Fig. 9 where

$$m = \frac{d \ln \sigma p}{d \ln \dot{\epsilon}} \qquad (4)$$

occurs at intermediate strain rates between 10^{-3} and 10^{-2} s^{-1} at all test temperatures. Below the transition strain rates, the strain rate sensitivity is high, increasing from 0.5 at 1050°C to 0.66 at 1100°C, while above the transition strain rates, it is low, of the order of 0.20 to 0.25 and is not as nearly dependent on temperature as it is below the transition strain rates. This behaviour is generally consistent with fine grain superplasticity and can be attributed to a change in deformation mechanism as the strain rate is raised from below to above the transition strain rate[26-29]. After a true strain of 1.2, the apparent strain rate sensitivity of the flow stress is greatly reduced relative to that for peak flow strength, decreasing from approximately 0.3 at the lower strain rates to approximately 0.1 at the higher strain rates, as shown in Fig. 10.

4.2 Temperature Dependence of Flow Strength

A selected number of flow curves from Fig. 8 are reproduced in Fig. 11 to illustrate the effects of temperature on flow strength at identical strain rates. The temperature dependence of flow strength is marginally higher for the peak flow strength than it is after a strain of 1.2. This effect can also be noted by comparing the data shown in Figs. 9 and 10.

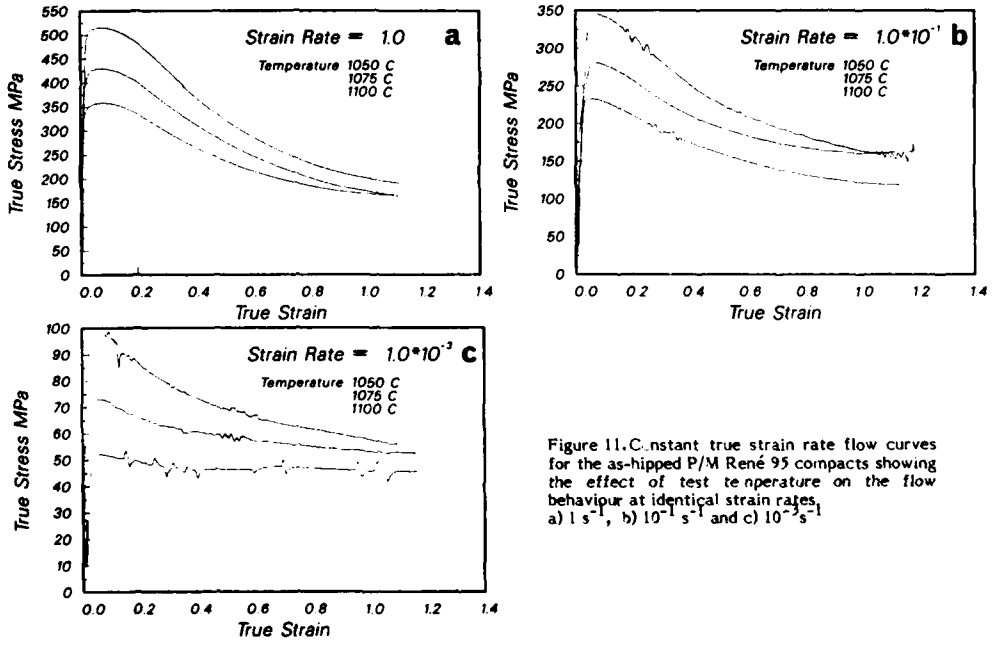

Figure 11. Constant true strain rate flow curves for the as-hipped P/M René 95 compacts showing the effect of test temperature on the flow behaviour at identical strain rates a) 1 s^{-1}, b) 10^{-1} s^{-1} and c) 10^{-3} s^{-1}

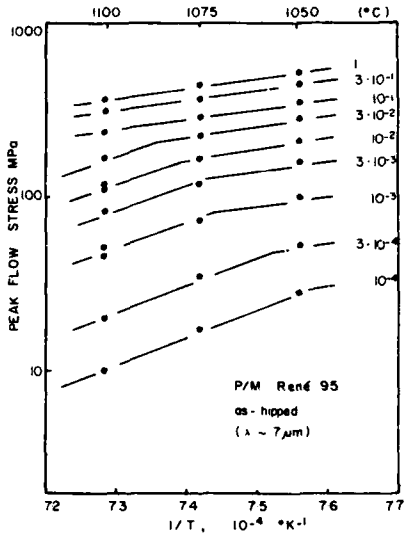

Figure 12. Temperature dependence of peak flow strength at constant strain rates for the hipped P/M René 95 fine grained compacts showing a discontinuity in the temperature dependence of flow strength over the range of test temperatures examined. (See text for details.)

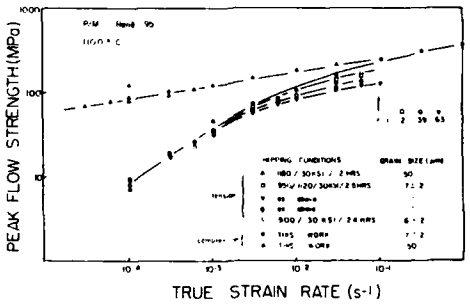

Figure 13. Comparison of peak flow strengths for P/M René 95 compacts with different microstructures as a function of strain rate at 1100°C. (See text for details.)

The temperature sensitivity of the peak flow strength ($d \ln\sigma_p / d\ 1/T$) obtained by plotting log flow stresses at constant strain rates against the inverse of the absolute temperature exhibits a discontinuity which shifts to higher temperatures as the strain rate is increased, as shown in Fig. 12. This discontinuity is consistent with the change in deformation mechanism indicated by Fig. 9. Activation energies for the respective mechanisms can be calculated on the basis of the data contained in Fig. 12 from the relation (c.f.eq.2)

$$Q = \frac{R}{m} \frac{d \ln \sigma_p}{d\ 1/T} \qquad (5)$$

where R is the gas constant and m is the strain rate sensitivity given by Equation 4. The significance of these calculated quantities is however questionable since the γ' volume fraction is not constant over the range of temperature considered and therefore the microstructure varies from one temperature to another. True activation energies require that calculations be made based on constant structure data and this is not the case for the data shown in Fig. 12.

4.3 Microstructure Dependence of Flow Strength

The coarse grained compact had a higher initial flow strength (peak flow strength) than the fine grained as hipped material at all temperatures and strain rates examined in this work. This is shown in Fig. 13 which compares peak flow strength for the two materials at 1100°C. The data presented in Fig. 13 also include some tensile test results from earlier NAE work for fine and coarse-grained compacts of comparable grain sizes that were produced by Hipping a different batch of René 95 powder[30]. Considering the differences in materials and test methods employed, the correlation between tensile and compression data for both coarse and fine grained materials is quite good. At higher strain rates, the apparent difference between tensile and compressive flow strength for the fine grained compacts can be attributed to microstructural differences caused by the test techniques employed. The tensile data were generated by the stepped strain rate test technique with which an increasing amount of strain accumulates with increasing number of test steps. When the accumulated strain is small, typically less than 0.2, the microstructural changes are minimal and the tensile and compressive flow strength are nearly identical. In contrast, when the accumulated strain is large, the microstructural changes become increasingly significant and tensile and compressive flow strength data tend to deviate. In these compacts, when the total accumulated strains were of the order of 0.4 and 0.6 the corresponding tensile flow strengths were 20 and 30% lower than the compressive flow strength respectively, Fig. 13. It is therefore important that, in order to establish strain rate and temperature sensitivities of flow strength the data should be generated at constant structure.

It was found that, at all strain rates and temperatures, the difference in flow strength between the coarse and fine grained compacts gradually decreased as the amount of applied strain was increased. For instance, at 1100°C and 10^{-3} s^{-1} the peak flow strength for the 50 μm grain size material was roughly three times higher than that for the 7 μm grain size compact, Fig. 14a. However, after a strain of 1.2, the difference in flow strength for the two materials was reduced to less than 20%. This convergence of flow strength with increasing strain, can be attributed to the microstructure evolving in each case towards the same fine grained microduplex structure, as indicated by Fig. 14b. This is clearly demonstrated in Fig. 15 which compares the as-worked microstructures for the two materials after a true strain of 1.2 at 1100°C and 10^{-3} s^{-1}. The initially coarse grained material shows partially recrystallized regions of fine microduplex grains, Fig. 15a, of a size similar to that observed in the as-worked fine grained (7 μm) compact. The initially fine grained (7 μm) material appears fully recrystallized and shows little evidence of prior powder particles. Its

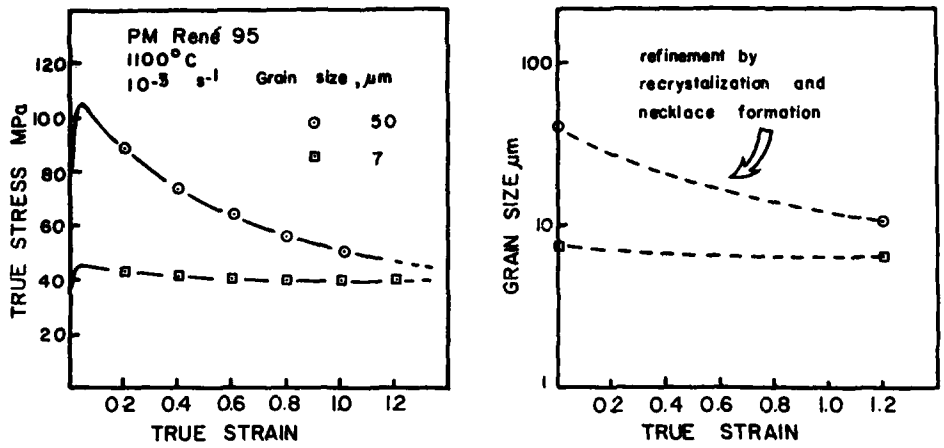

Figure 14. Comparison of a) the flow curves for initially coarse and fine grained compacts of hipped P/M René 95 deformed under the same test conditions (1100°C, 10^{-3} s^{-1}) and b) the associated refinement in grain size revealed by metallography.

microstructure is equiaxed microduplex with a γ' particle size similar to the γ matrix grain size. Some grain refinement has occurred during flow although in this case the decrease in grain size was rather minimal, down from 7 to approximately 6 μm as indicated in Fig. 14b.

4.4 Changes in Microstructure Induced by Working

Metallography of as-worked microstructures for both coarse (50 μm) and fine (7 μm) grained compacts revealed that their average grain size was refined during flow at all test temperatures and strain rates examined in the work with the exception of the initially fine grained material at the slowest strain rate (10^{-4}) and 1100°C, when marginal coarsening of the microduplex grain size was noted. This is shown in Fig. 16 which compares the soaked and as-worked microstructures for the as-hipped material after a strain of 1.2 at a selected number of strain rates and temperatures. The micrographs indicate that remnants of the as-cast dendritic structure associated with undeformed powder particles present in the as-hipped material (Fig. 2) are entirely eliminated within a strain of 1.2 at the highest strain rates and test temperatures. The micrographs also reveal that the as-worked microduplex grain size is influenced by the deformation conditions, decreasing with an increase in strain rate and/or a decrease in temperature at equivalent applied strain. After a strain of 1.2, the variations in average microduplex grain sizes (measured as mean linear intercepts)as a function of strain rates at the three test temperatures are compared in Fig. 17.

It was also noted that a regime of deformation develops at high strains during which there is no further change in the microduplex grain size with continued straining at constant strain rates and temperature. Within this regime, the flow stress also remains nearly constant. Evidence to this effect is provided in Fig. 18 which compares the flow curves

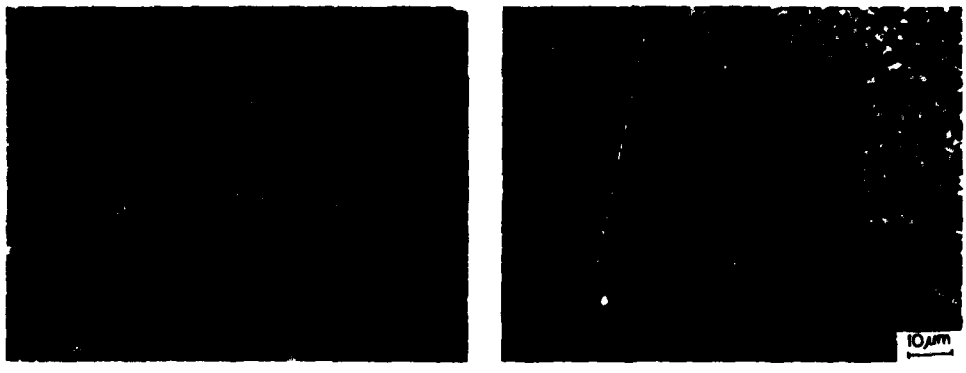

Figure 15. Microstructures after deformation to a strain of 1.2 at 1100°C and 10^{-3} s^{-1} in a) initially coarse-grained and b) initially fine-grained P/M René 95 compacts. The necklace structure in a) is typical of coarse-grained P/M superalloys after forging at sub-solvus temperatures. (c.f. Fig. 1).

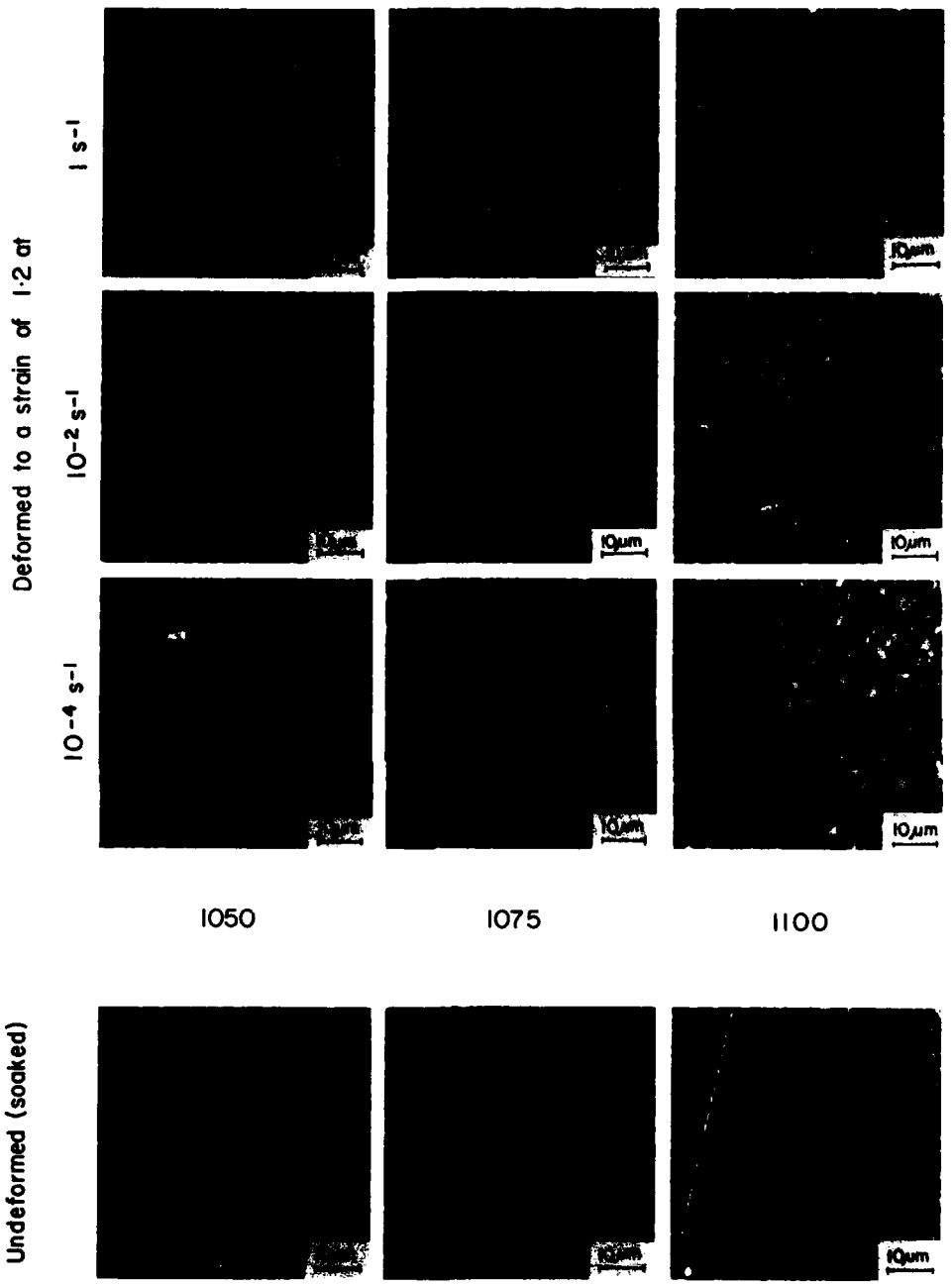

Figure 16. Effects of forging temperature and strain rate on the microstructure of the as-hipped fine-grained P/M René 95 compacts after a true strain of 1.2 corresponding to a 70% reduction in height of the compression test piece. The microstructures of undeformed specimens soaked for 20 minutes at the three test temperatures are also shown for comparison.

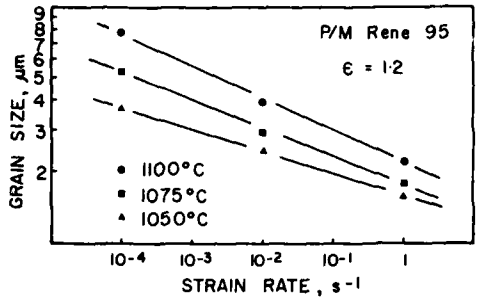

Figure 17. Variation in as-worked microduplex grain size as a function of strain rate at the three test temperatures after a true strain of 1.2 for initially fine grained (approximately 7 μm) P/M René 95 compacts. Grain sizes are mean linear intercepts derived from Fig. 16.

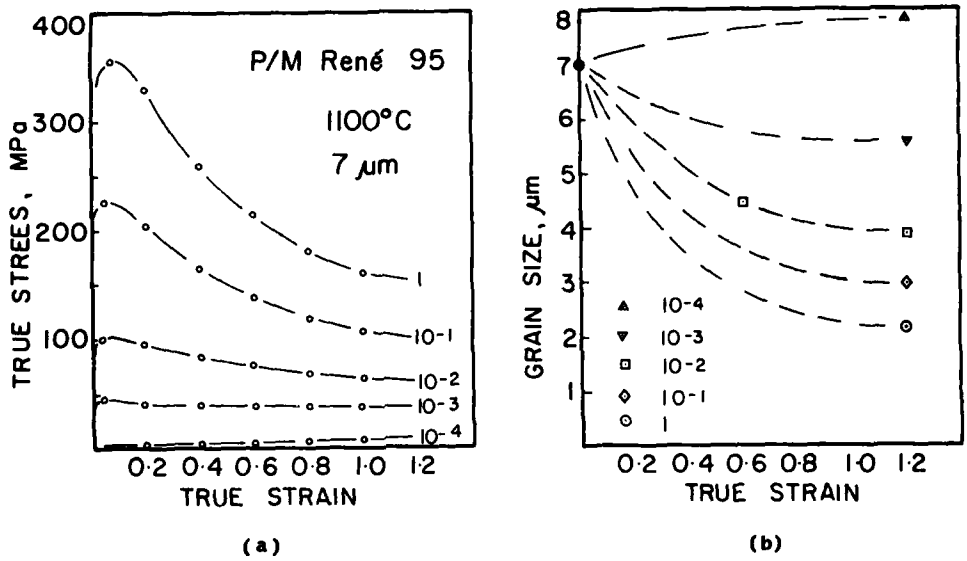

Figure 18. Effects of strain rate at 1100°C on a) the flow curves and b) the evolution in microduplex grain size during deformation for the initially fine-grained P/M René 95 compacts.

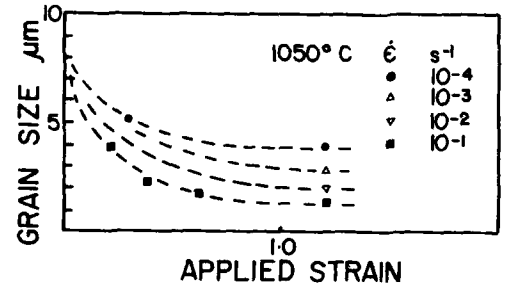

Figure 19. Effect of strain and strain rate on the evolution of grain size during constant true strain rate deformation of fine-grained P/M 713 LC compacts at 1050°C (1323K)(after Ref. 19).

of the as-hipped material and the corresponding as-worked grain sizes after a strain of 1.2 over a wide range of strain rates at 1100°C. The steady state regime of flow is established within true strains of less than 1.2 at strain rates below 10^{-2} s^{-1} at this test temperature. At higher strain rates, strains larger than 1.2 are apparently required to achieve steady state. However, the measured flow stresses and grain sizes at strains of 1.2 must be close to their expected steady state values since the softening rates are rapidly decreasing and the flow stresses are approaching a constant value at that point, Fig. 18. A steady state regime of deformation has already been reported for a similar material (Hipped 713LC). The microstructural evidence available in this case is shown for comparison in Fig. 19. At 1050°C the steady state is established in P/M 713LC within a strain of 1.2 at strain rates below 10^{-1} s^{-1}.

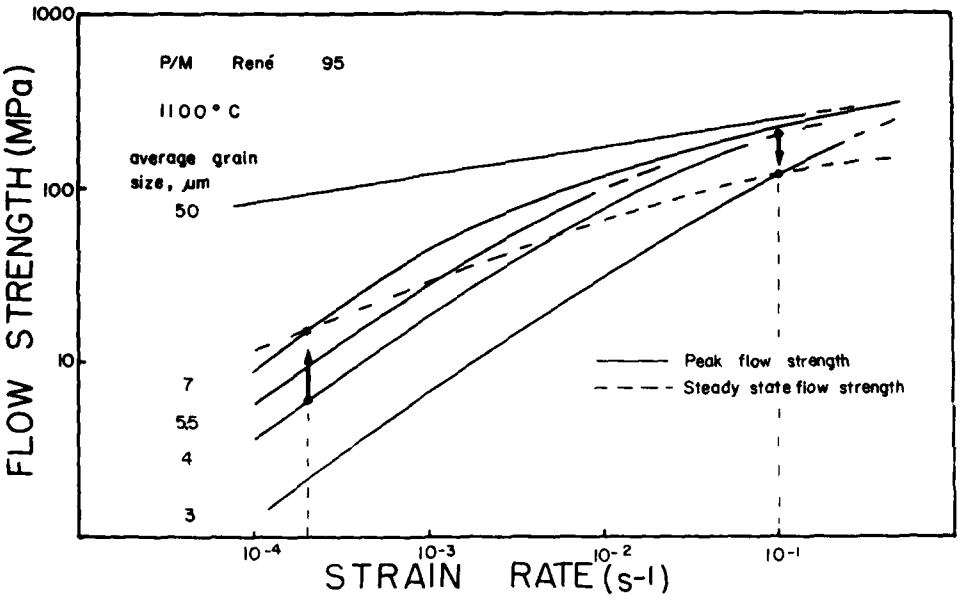

Figure 20. Deformation map for P/M René 95 at isothermal forging temperatures and strain rates obtained by superposition of peak flow strength data at constant grain size (solid lines) and steady state data (broken line). The steady state data provides a boundary condition for the evolution of microstructure and changes in flow strength during flow. (See text for details). The peak flow strength data for the 50 and 7 μm grain size compacts are derived from Figs. 10 and 13 respectively while the data for the 4 μm grain size material was obtained by an interrupted test method that involved prestraining the fine grained as-hipped material to refine its grain size from 7 to 4 μm. This was achieved by deforming the as-hipped material to a strain of 0.7 at 3×10^{-2} s^{-1}. At that point, the test was interrupted and immediately followed by a stepped strain rate test to establish the strain rate dependence of flow strength at 4 μm. The lines for other grain sizes were obtained by interpolation from the data contained in Fig. 17. Finally, for the steady state data line, it was assumed that the measured flow strengths at strains of 1.2, Fig. 10, provide good approximation of steady state flow stresses over the whole range of strain rates considered.

4.5 Deformation Phenomenology

Several conclusions can be drawn from the above observations regarding the flow behaviour and microstructural evolution in PM René 95 under isothermal forging conditions.

1) At typical isothermal forging rates and temperatures, the grain size of Hipped P/M René 95 is refined during flow.

2) The grain refinement in both coarse and fine grained compacts causes flow softening.

3) A steady state regime of deformation ultimately develops at high strains during which the flow strength and grain size undergo no further change with continued straining at constant strain rate and temperature. The flow strength at a strain of 1.2 and the corresponding as-worked microstructures may be viewed as steady state quantities at least to a first approximation for modelling purposes.

4) The steady state flow stress and steady state grain size are independent of the initial microstructure but are each conditioned by the applied strain rate and the forging temperature.

5) The steady state grain size increases with a decrease in strain rate and/or an increase in forging temperature whereas the steady flow stress increases with an increase in strain rate and/or a decrease in forging temperature.

The phenomenology of steady state is fundamental to the isothermal forging deformation model which has already been proposed for this class of materials [19]. According to the model, steady state flow provides a boundary condition for the evolution of both the microstructure and flow strength during deformation and can be used to predict the magnitude and direction of change in grain size and flow strength for a given microstructure as a function of strain rate. This is demonstrated for P/M René 95 in Fig. 20 where peak flow strength data for different initial grain sizes (solid lines) are combined with steady state data (broken line) over a wide range of strain rates at 1100°C. The figure, which may be viewed as a deformation map, indicates for instance that at 2×10^{-4}, s^{-1}, a compact with a 4 μm grain size will harden during flow as its grains grow from 4 to 7 μm, while at 10^{-1}, s^{-1}, the same compact will soften as its grain size is refined down to 3 μm. Whether the grains grow or are refined during flow depends on the relative size of the starting and the steady state grain sizes and this is dictated by the applied strain rate and temperature[18].

Although the changes in grain size are not dramatic in Fig. 20, the difference between peak and steady state flow strengths at a given strain rate can be quite significant. This is indicative of a strong grain size dependence of flow strength in fine-grained materials at these high temperatures and slow forming rates and arises because of the contribution of grain boundary sliding mechanisms during deformation[13]. This contribution is large enough when the grain size is sufficiently fine, typically below 10 μm, to confer superplastic characteristics to as-hipped superalloy compacts[15-18].

4.6 Deformation Modelling

In accordance with the deformation map of Fig. 20, the grain size of the as-hipped (7 μm) and grain coarsened (50 μm) compacts are refined and their flow strength is reduced at all rates of interest to isothermal forging. In order to model these changes, it is important to understand how the refinement of the grains occurs in each case. Metallography reveals that the mechanisms involved are identical in both materials. While these mechanisms are not entirely understood, both deformation induced recrystallization and redistribution of the γ' phase are believed to contribute to the transformation. There is evidence to show that recrystallization starts along the grain boundaries of the original grains and progresses by the addition of new grains at the interface between the previously recrystallized fine grained portions of the original grains and their unrecrystallized interiors. As the strain increases, the volume fraction of recrystallized material also increases until the original grains are entirely consumed. In the case of the initially coarse grained (50 μm) material the process gives rise at intermediate strains to a necklace structure of the type shown in Fig. 15a. In the case of the initially fine grained material the difference between the initial and steady state grain sizes is small over the entire range of strain rates examined and consequently the original grains are entirely consumed without forming a well defined necklace structure, Fig. 15b

In order to model these deformation-induced changes in flow strength and microstructure as a function of deformation conditions, it is necessary to predict the flow strength for partially recrystallized material and the rate of recrystallization. Mathematical treatment of these problems requires:

1) a rate equation for partially recrystallized material, and
2) a kinetic relationship for deformation-induced recrystallization.

How these relationships can be formulated in the case of P/M René 95 is explained below.

4.6.1 Flow Strength Predictions

Following the model for deformation induced recrystallization in P/M 713 LC[19], the partially recrystallized P/M René 95 compacts can be viewed as composite materials consisting of soft recrystallized grains and hard unrecrystallized regions corresponding to the interiors of the original grains. As the volume fraction of the recrystallized material increases with strain, the flow strength of the compacts is increasingly influenced by flow localization within the fine recrystallized regions. The contribution from grain boundary sliding towards overall deformation becomes increasingly prominent and ultimately dominates once the transformation is complete.

The rate equation for peak flow strength prior to the onset of grain refinement in both coarse and fine grained compacts can be written in terms of those for grain boundary sliding, (gbs) and intragranular flow, (mdg) as:

$$\dot{\epsilon} = \dot{\epsilon}_{gbs} + \dot{\epsilon}_{mdg} \tag{6}$$

where $\dot{\epsilon}$ is the applied strain rate and $\dot{\epsilon}_{gbs}$ and $\dot{\epsilon}_{mdg}$ are the strain rates due to gbs and mdg respectively. In the coarse grained compacts, the strain contribution from gbs is initially small because of a large initial grain size and the rate equation reduces to

$$\dot{\epsilon} = \dot{\epsilon}_{mdg} \tag{7}$$

In the fine grained compacts, the contribution from each deformation mechanism depends on the initial grain size and the applied strain rate. At slow strain rates, the contribution from gbs dominates whereas at high strain rates it becomes negligible. This gives rise to the discontinuity from high to low strain rate sensitivity for fine-grained materials as indicated in Fig. 9. At high strain rates, the rate equation for the fine grained material also reduces to Eq. 7 while at low strain rates it reduces to

$$\dot{\epsilon} = \dot{\epsilon}_{gbs} \tag{8}$$

At strain rates of interest to isothermal forging both gbs and mdg contribute to the deformation and the rate equation is that given by Eq. 6.

The $\dot{\epsilon}_{mdg}$ component in Eq. 6 can be represented by a dislocation glide/climb controlled creep equation of the form

$$\dot{\epsilon}_{mdg} = A' \frac{D_v \mu b}{kT} \left(\frac{\sigma - \sigma_o}{\mu} \right)^4 \tag{9}$$

where σ_o is a back stress due to intragranular γ' precipitates, A' is an experimentally determined material constant and other symbols have their usual meaning (see SYMBOLS section).

The $\dot{\epsilon}_{gbs}$ component in Eq. 6 can be represented by atomistic models for describing superplastic flow where sliding along the grain boundaries may be controlled by diffusion flow accommodation within the grain interiors, as in Ashby and Verrall's model[31], or by dislocation climb within the boundary planes, as in Gittus's model[32].

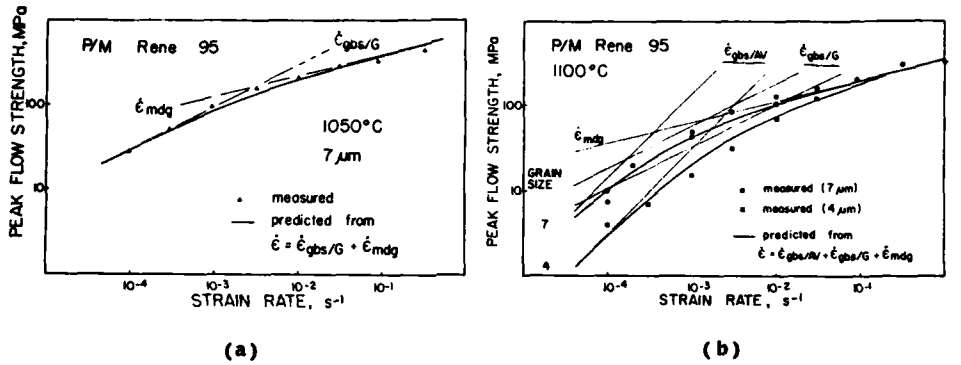

Figure 21. Comparison of experimentally established peak flow strengths for the as-hipped P/M René 95 compacts with predictions based on superposition of intragranular deformation and grain boundary sliding mechanisms
a) at 1050°C assuming that a mechanism of the type proposed by Gittus[32] predominates at low strain rates.
b) at 1100°C assuming that both the Gittus and Ashby and Verall[31] contribute to deformation.

In the case of Ashby and Verrall's model the rate equation is given by:

$$\dot{\epsilon}_{gbs/AV} = \frac{100\,\Omega}{kT\,\lambda^2}\left(\sigma - \frac{0.72\,\Gamma}{\lambda}\right) D_v \left(1 + \frac{3.3\,\delta}{\lambda}\frac{D_B}{D_v}\right) \qquad (10)$$

whereas for Gittus's model:

$$\dot{\epsilon}_{gbs/G} = 53.4\,\frac{D_B \mu b}{kT}\left(\frac{b}{\lambda}\right)^2 \left(\frac{\sigma - \sigma_i}{\mu}\right)^2 \qquad (11)$$

where λ is the grain size, Γ is the grain boundary energy and $0.72\Gamma/\lambda$ and σ_i are threshold stresses arising from fluctuations in the grain boundary area and grain boundary ledges respectively[31,32].

Predictions of peak flow strength in P/M 713 LC compacts of different grain sizes, based on the superposition of a dislocation creep model (Eq. 9) with the Gittus model for grain boundary sliding (Eq. 11), have been shown to closely approximate the experimental data at 1050°C[33] and correctly predict the strain rate sensitivity of flow strength ($m \simeq 0.5$) at slow strain rates. In P/M René 95, the superposition of these two equations also describes peak flow strength and its strain rate sensitivity ($m = 0.5$) at 1050°C reasonably well as shown in Fig. 21a. However, at 1100°C, this superposition does not adequately predict the peak flow strength or its strain rate sensitivity at slow strain rates. In this case, the strain rate sensitivity m is greater than 0.5, of the order of 0.66 (c.f. Fig. 9), and falls in between the values predicted by Eqs. 8 and 9.

It has however been suggested that superplastic flow can arise from the simultaneous operation of a number of mechanisms[29]. It is therefore quite possible that at 1100°C both the Ashby and Verrall and the Gittus mechanisms are contributing to flow at the lower strain rates. This is not totally unexpected since the contribution from diffusional flow accommodation in the grain interiors can be expected to increase as the forging temperature is increased from 1050°C to 1100°C. Therefore, it is suggested that at 1100°C, the variation in peak flow strength can be described by superposition of Eq. 7, 8 and 9 where

$$\dot{\epsilon} = \dot{\epsilon}_{mdg} + \dot{\epsilon}_{gbs/G} + \dot{\epsilon}_{gbs/AV} \qquad (12)$$

That this is indeed the case is shown in Fig. 21b where the magnitude of peak flow strength and its strain rate and grain size dependences are closely approximated by Eq. 12. The parameters and constants used in calculating the peak flow strength values in Fig. 21 are given in Table IV. In the discussion that follows on deformation at 1100°C, any reference to $\dot{\epsilon}_{gbs}$ will be assumed to represent a combination of $\dot{\epsilon}_{gbs/AV}$ and $\dot{\epsilon}_{gbs/G}$.

Again following the approach used to model necklace growth in P/M 713LC compacts[19], the deformation-induced recrystallization is assumed to proceed by the addition of concentric layers of steady state grains of diameter d, starting along the boundaries of the original grains of diameter λ in the manner shown schematically in Fig. 22. As the strain increases, more layers are added until the original grains are entirely consumed. In initially coarse grained material, several layers of steady state grains may be needed to complete the transformation whereas in initially fine grained compacts (typically less than 10 μm, one or less layer may be required depending on the sizes of the original and the recrystallized steady state grains, Fig. 22b. In this approach, a spherical grain model is used and it is assumed that the size of the recrystallized grain is dictated by strain rate (and temperature) in accordance with the experimental data shown in Fig. 17.

Table IV: Values of Material Parameters and Physical Constants Used in Calculations

Symbol	Parameter	Units	Value
A'	Power law creep constant	-	see Note 1
A' (1323K)	Power law creep constant at 1323K	-	4.7×10^{3}
A' (1373K)	Power law creep constant at 1373K	-	9.3×10^{3}
b	Burgers Vector	m	1.7×10^{-10}
k	Boltzmann's Constant	MNm/K	1.38×10^{-29}
μ	Shear modulus	MN/m^2	see Note 2
μ (1323K)	Shear modulus at 1323K	MN/m^2	5.0×10^{4}
μ (1373K)	Shear modulus at 1373K	MN/m^2	3.5×10^{4}
D_V	Volume diffusion coeff.	m^2/s	see Note 3
D_V (1323K)	Volume diffusion coeff. at 1323K	m^2/s	1.1×10^{-17}
D_V (1373K)	Volume diffusion coeff. at 1373K	m^2/s	3.2×10^{-17}
σ_i	Back stress due to grain boundary ledges	MN/m^2	< 1 [19]
D_B	Boundary diffusion coeff.	m^2/s	see Note 4
D_B (1323K)	Boundary diffusion coeff. at 1323K	m^2/s	2.1×10^{-11}
D_B (1373K)	Boundary diffusion coeff. at 1373K	m^2/s	3.6×10^{-11}
Ω	Atomic volume	m^3	1.1×10^{-29}
δ	Boundary thickness $\sim 2b$	m	3.0×10^{-10}
Γ	Boundary energy	J/m^2	0.1
R	Gas constant	J/mol/K	8.3143
Q_V	Activation energy for volume diffusion	KJ/mol/K	318
Q_B	Activation energy for boundary diffusion	KJ/mol/K	159

Note 1

For microduplex material, $\sigma_o = 0$ and $\dot{\epsilon} = A' D_v \frac{\mu b}{kT} \left(\frac{\sigma}{\mu} \right)^4$

or $A' = \frac{\dot{\epsilon}}{D_v} \frac{kT}{\mu b} \left(\frac{\sigma}{\mu} \right)^{-4}$

Substituting an experimentally determined σ_p value at appropriate test temperature and applied true strain rate, A' values at 1323K and 1373K can be calculated.

Note 2

$$\mu = \mu_o \left(1 + \frac{T-300}{T_M} \cdot \frac{TM}{\mu o} \frac{d\mu}{dT} \right)$$

where μ_o is the shear modulus at 300K and T_M is the melting temperature. For René 95 $\mu_o = 3.49 \times 10^5$ MN/m^2, $T_M = 1600K$ and $\frac{TM}{\mu o} \frac{d\mu}{dT} = -1.34$.

Note 3

$D_v = D_o \exp(-Q_V/RT)$ where D_o for Ni, for the temperature range of interest, equals $4.0 \times 10^{-5} m^2/s$ and Q_V is 318 KJ/Mol/K.

Note 4

$D_B = D_o \exp(-Q_B/RT)$ where D_o for Ni, for the temperature range of interest equals 4.0×10^{-5} m^2/s and Q_B is 159 KJ/mol/K.

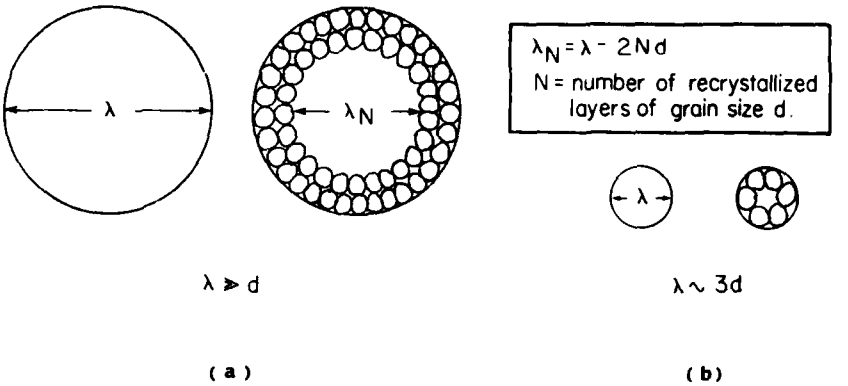

Figure 22. Single grain model with diameter λ used for modelling deformation induced recrystallization during isothermal forging in P/M René 95 compacts illustrating the concentric layerwise build up of steady state grains of diameter d with increasing deformation in
a) initially coarse grained compact, $\lambda \gg d$
b) initially fine grained compact, $\lambda \approx 3d$

The rate equation for partially recrystallized material can then be written as

$$\dot{\epsilon} = F(\dot{\epsilon}_{mdg} + \dot{\epsilon}_{gbs})_d + 1 - F(\dot{\epsilon}_{mdg} + \dot{\epsilon}_{gbs})\lambda_N \qquad (13)$$

where F is the volume fraction of recrystallized material, and λ_N is the average diameter of the unrecrystallized portions of the spherical model grain and is given by

$$\lambda_N = \lambda - 2Nd \qquad (14)$$

where N is the number of steady state grain layers and can be a non-integer for modelling purposes.

4.6.2 Recrystallization Kinetics

As explained elsewhere, the kinetics of deformation-induced recrystallization can be described by adapting Cahn's treatment of transformation kinetics for grain boundary nucleated reactions(19). In this adaptation, a reduced effective grain size equal to the size of the untransformed portions of the original grains is used to describe recrystallization events beyond site saturation of the original grain boundaries. For the spherical grain model shown in Fig. 22, the reduced effective grain size, λ_N, gradually decreases as the number of recrystallized grain layers increases in accordance with Eq. 14. Also, the nucleation and growth rates of new grains are asumed to be conditioned by the strain rate within the untransformed portions of the original grains which provides the driving force for additional recrystallization. For P/M 713 LC compacts the recrystallization kinetics were best described by assuming that the transformation is growth controlled in which case the adapted Cahn treatment takes the form:

$$F = 1 - \exp\left[\frac{-12K}{\lambda_N}\dot{\epsilon}_g\left(\frac{\epsilon}{\dot{\epsilon}}\right)\right] \qquad (15)$$

where K is material constant which can be determined experimentally from flow data at slow strain rates(19).

The coupling of Eqs. (13) and (15) forms the deformation model and can be viewed as a constitutive relation capable of treating microstructure as a dynamic variable of the deformation process. The model can therefore be used to predict changes in microstructure as a function of deformation conditions.

Eq. 13 reduces to a fourth order polynomial in stress which can be solved for any given value of F, i.e. at any stage of transformation. The calculated stress can then be used to estimate the effective strain rate $\dot{\epsilon}_g$ from Eq. 9 assuming that the recrystallized and unrecrystallized regions of the original grains carry the same stress(19). This calculated effective strain rate is in turn used to predict the rate of transformation with continued deformation through Eq. 15. By repeating this procedure in a stepwise fashion changes in flow strength and microstructure can be determined for the spherical grain model. Experimental verification of this model was, however, beyond the scope of this study.

Using Eqs. 13 and 15 in conjunction with numerical procedures for metalworking analysis, based on the finite element method, the local variations in microstructure within a forging, caused by strain and strain rate gradients, can also be predicted. It has been suggested that such predictions could be used to tailor microstructure in superalloy disc forgings to component design requirements(10).

5. CONCLUSIONS

This paper has shown that a recently proposed methodology for modelling forging deformation and microstructural evolution in P/M superalloys under isothermal forging conditions is applicable to P/M René 95 compacts. This methodology assumes that several mechanisms contribute towards overall deformation and uses established models for each of the mechanisms to formulate a rate equation for predicting flow strength. It also uses an Avrami type relationship, with steady state flow data as boundary conditions, to predict changes in microstructure as a function of initial microstructure and applied strain rate. The rate equation in combination with the Avrami type relationship forms a microstrucure dependent constitutive relation which can be used to predict microstructural gradients within forgings.

Peak flow strength data for the initial microstructure, plus steady state flow strength and grain size data are the only experimental quantities required to use this model. The former can be obtained on a single specimen by a stepped strain rate test, while the latter can be generated by conventional constant true strain rate compression tests using four to five specimens, one per strain rate condition. However, to generate the steady state data, it is necessary to conduct the tests on initially fine-grained material ($< 10\ \mu m$) since only in this case can the steady state be established within the strain limits of compression testing.

REFERENCES

(1) J-P. Immarigeon, The Superalloys, Materials for Gas Turbine Hot Section Components, Canadian Aeronautics and Space Journal, Vol. 27, No. 4, December 1981, pp. 336-350.

(2) M.M. Allen, R.L. Athey and J.B. Moore, Application of Powder Metallurgy to Superalloy Forging, Metals Engr. Quart. Vol. 10, No. 1, Feb. 1970, pp. 20-30. See also J.B. Moore and F. L. Athey, US Patent No. 3,519,504, 1970.

(3) R.H. Dreshfield and H.R. Gray, P/M Superalloys, A Troubled Adolescent, Proc. Seminar on P/M Superalloys, Current and Future, 1984 Int. Powder Metallurgy Conf. Toronto, Canada, (1984) pp. 1-20.

(4) J-P. Immarigeon and W. Wallace, Trends in Superalloy Powder Processing, Metal Powder Report, Vol. 38, No. 10, October 1983, pp. 537 - 541.

(5) T.E. Howson, W.H. Couts Jr. and J.E. Coyne, High Temperature Deformation Behaviour of P/M René 95, Proc. 5th Int. Conf. on Superalloys - 1984, Eds. by M. Gell et al. Pub. TMS-AIME, 1984, pp. 275-284.

(6) G.H. Gessinger, Powder Metallurgy of Superalloys, Butterworth, London, 1984, p. 121, 154.

(7) M. Jeandin, Necklace Structure Obtained by Forging Astroloy Super-Solidus Sintered Preforms, Jour. of Material Science, Vol. 17, 1982, pp. 2902 - 2908.

(8) T. Altan, G.D. Laboti and V. Nagpal, Application of Process Modelling in Massive Forming Processes, in Process Modelling, Fundamentals and Applications to Metals, Eds. T. Altan, H. Burte, H. Gegel and A. Male, Pub. ASM, Metals Park, Ohio, Materials/Metalworking Technology Series, 1983, pp. 77-99.

(9) J.F. Thomas Jr., Flow Based Analyses of Metal Deformation Processes: An Overview, AGARD Lecture Series No. LS-137 on Process Modelling Applied to Metal Forming and Thermomechanical Processing, October 1984, Pub. AGARD-NATO, paper No. 1, pp. 1-1/1-18.

(10) J-P. Immarigeon, D. Morphy and A.K. Koul, Selective Thermomechanical Treatments for Dual Property P/M Superalloy Disc Forgings, in Ref. 3, pp. 97 - 120.

(11) N. Rebelo, Numerical Methods in Metalforming and Finite Element Simulation of Forging Processes in Ref. 9, papers 6 and 7, pp. 6-1/7-16.

(12) S. Brown and L. Anand, An Internal Variable Constitutive Model for the Hot Working of Metals, Proc. Symp on Computer Modelling of Fabrication Processes and Constitutive Behaviour of Metals, May 1986, Eds. J.J.M. Too et al., Pub. CANMET-EMR, Ottawa, Canada, in press, 1987.

(13) J-P. Immarigeon, The Role of Microstructure in the Modelling of Plastic Flow in P/M Superalloys at Forging Temperatures and Strain Rates, in Ref. 9, paper 4, pp. 4-1/4-30.

(14) W. Wallace, J-P. Immarigeon, J.M. Trenouth and B.D. Powell, Control of Grain Structure During Superalloy Powder Processing, AGARD Conference Proceedings No. 200, on Advanced Fabrication Techniques in Powder Metallurgy and Their Economic Implications, April 1976, Paper No. 9, pp. 1-13, Also published as NRC, NAE LTR-ST-812, November 1975.

(15) J-P. Immarigeon, W. Wallace and G. Van Drunen, The Hot Working Behaviour of Mar-M200 Superalloy Compacts, Proc. 3rd International Symposium, on Superalloys - Metallurgy and Manufacture, Claitor's Publishing Division, Baton Rouge, 1976, pp. 463 - 472. Also published as NRC, DME/NAE Quarterly Bulletin, 1, 1977, pp. 1 - 12.

(16) A.Y. Kandeil, J-P. Immarigeon, W. Wallace and M.C. de Malherbe, Flow and Fracture Behaviour of Mar-M200 Powder Compacts During Isothermal Forging, Metal Science, Vol. 14, No. 10, 1980, pp. 493 - 499.

(17) A.Y. Kandeil, J-P. Immarigeon, W. Wallace and M.C. de Malherbe, Thermomechanical Processing of a Nickel-Base Superalloy Compact, High Temperature Technology, Vol. 1, No. 4, 1983, pp. 201 - 207.

(18) J-P. Immarigeon and P.H. Floyd, Microstructural Instabilities During Superplastic Forging of a Nickel-Base Superalloy Compact, Met. Trans., Vol. 12A, 1981, pp. 1177-1186.

(19) A.K. Koul and J-P. Immarigeon, Modelling of Plastic Flow in Coarse Grained Nickel-Base Superalloy Compacts under Isothermal Forging Conditions, Acta Metallurgica, Vol. 35, No. 7, 1987, pp. 1791 - 1805.

(20) Z.M. Fu, P. Au, D. Morphy, A.K. Koul and J-P. Immarigeon, Influence of Microstructure on High Temperature LCF Life in P/M René 95, Proc. 5th Int. Conf. on Mechanical Behaviour of Materials, Beijing, China, June 87, in press.

(21) R. Thamburaj, A.K. Koul, W. Wallace and M.C. de Malherbe, Prior Particle Boundary Precipitation in P/M Superalloys, Modern Developments in Powder Metallurgy, Vol. 15-17, Pub. MPIF, Princeton, N.J., 1985, pp. 635 - 673.

(22) C. Marques, G. L'Esperance and A.K. Koul, Prior Particle Boundary Precipitation in P/M Superalloys, to be published; also C. Marques, M.Eng Thesis, Ecole Polytechnique, Montreal, Canada 1986.

(23) J-P. Immarigeon, A.Y. Kandeil, W. Wallace and M.C. de Malherbe, A Hot Compression Testing Apparatus for the Study of Isothermal Forging, J. Testing and Evaluation, Vol. 8, No. 6, November 1980, pp. 273 - 281.

(24) S. Gautron, G. L'Esperance and J-P. Immarigeon, Isothermal Forging Behaviour of Ti 6242, to be published; also S. Gautron, Forgeage isotherme de l'alliage Ti 6242, M. Eng. Thesis, Ecole Polytechnique, Montreal, Canada, 1984.

(25) J-P. Immarigeon, P. Adams and R. Kulchyski, Analog Function Generator for Constant True Strain Rate during Uniaxial Compression with an MTS Testing Machine, NAE-NRC Report LTR-ST-786, Ottawa, Canada, 1975.

(26) J.W. Edington, K.N. Melton and C.P. Cutler, Superplasticity, Progress in Material Science, Vol. 21, 1976, pp. 61 - 158.

(27) T.G. Langdon, Experimental Observations in Superplasticity in Proc. Symp. on Superplastic Forming of Structural Alloys, Ed. N.E. Paton and C.H. Hamilton, TMS AIME, 1982, pp. 27 - 40.

(28) H.J. McQueen and B. Baudelet, Comparison and Contrast of Mechanisms, Microstructures, Ductilities in Superplasticity and Dynamic Recovery and Recrystallization, Proc. 5th ICSMA, Aachen, August 1979, ed. Haasen et al., Pergamon Press, 1979, pp. 329 - 336.

(29) K.A. Padmanabhan and G.J. Davies in Superplasticity, Pub. Springer-Verlag Berlin, 1980.

(30) Z.M. Fu, D. Morphy, T. Terada and J-P. Immarigeon, Tensile Deformation Behaviour of P/M René 95 at 1100°C, to be published.

(31) M.F. Ashby and R.A. Verrall, Diffusion Accommodated Flow and Superplasticity, Act. Metallurgica, Vol. 21, Feb. 1973, pp. 149-163.

(32) J.H. Gittus, Theory of Superplastic Flow in Two Phase Materials: Roles of Interphase-Boundaries, Dislocation Ledges and Diffusion, Trans. ASME, July 1977, pp. 244-251.

(33) J-P. Immarigeon and A.K. Koul, Flow Behaviour of Nickel-Base Superalloys at Isothermal Forging Temperatures and Strain Rates, Proc. Int. Conf. on Strength of Metals and Alloys, Montreal, Aug. 1985, ICSMA 7, eds. H.J. McQueen et al., Pub. Pergamon Press, Oxford, 1986, Vol. 3, pp. 2073 - 2078.

ACKNOWLEDGEMENTS

One of the authors, Colonel O. Alniak wishes to express his gratitude to the Department of National Defence of Canada for the granting of a NATO Fellowship, to the Turkish Armed Forces for their permission and support to hold this Fellowship, and to Dr. W. Wallace for providing access to NAE's experimental facilities and for his constant encouragement in completing the project. Special thanks are also due to Ms. S. Taylor of NAE for her expedient processing of the manuscript.

PREDICTION OF TEMPERATURE DISTRIBUTION IN AXISYMMETRIC EXTRUSION

by

S. Onurlu
Marmara Research Institute
Materials Research Department
P.O. Box 21, Gebze, 41401 Kocaeli-TURKEY

SUMMARY

In extrusion, the knowledge of temperature distribution is helpful in selecting process variables such as speed, initial temperetures and cooling conditions to optimize the process. This study describes a computer-aided numerical technique for the calculation of temperature distribution in the billet, extruded product and tools. The model is based upon Avitzur's spherical velocity field and extended to include transient heat conduction, heat generation and mass transport effects on the basis of local temperatures and strain-rates.The finite difference formulation of the problem considers the heat generation and conduction in each time step of the solution. A computer program is developed to solve the problem.Temperature distributions are calculated as a function of time. Predicted temperatures for the extrusion of aluminium alloys AA 2014 and AA 2024 are compared with experimental data.

NOMENCLATURE

c	specific heat
D/Dt	material derivative
k	thermal conductivity
m	shear factor
$\dot{q}$	heat generation rate
r,Φ,Ψ	spherical coordinates
r_f	radius of inner boundary of the deformation zone
$S^{i,j}$	surface area of element (i,j)
$T^{i,j}$	temperature of element (i,j) at the beginning of time increment Δt
$T^{i,j}$	temperature of element (i,j) at the end of time increment δt
$V^{i,j}$	volume of element (i,j)
v_f, v_o	exit speed of the extruded product, ram speed
v_f	speed of an element in the deformation zone
Δt	time increment
Δv	velocity discontinuity
$\nabla 2$	Laplacian operator
$\hat{\epsilon}$	effective strain-rate
ρ	density
$\bar{\sigma}$	effective stress

INTRODUCTION

Extrusion has become an economically important metal forming process in the last three decades. As a result of technological advances gained in aerospace industry there has been an increasing demand for the extruded products of high-strength light alloys. In order to use the extrusion process more effectively numerous investigations have been carried out concerning process, tooling and metal flow.

In extrusion,temperatures developed due to heat generation greatly influence tool life and the properties of the final product, and, most significantly, determine the maximum deformation speed which can be used for producing sound products. Therefore, it is essential to optimize the process variables so that the productivity of the process can be increased. The first step to determine the optimum process variables is to know the temperature distribution in material and tooling during extrusion. In this study, a computer-aided numerical technique is developed for the prediction of temperature distribution in the billet, product and tools during extrusion.

When a material is extruded, the plastic deformation energy, the shearing energy at the boundaries of the deformation zone and the friction energy dissipated at the tool-material interface contribute to temperature rise in the product. This non-steady-state temperature rise - which affects the properties of the extruded product - can be controlled by appropriate selection of process parameters such as ram speed,initial temperatures of the billet and tooling etc. The principles of isothermal extrusion and practical measures for its realization have been discussed by many investigators[1-5].

Several attempts have been made to predict the temperature distribution in extrusion. Akeret [6] has analysed the transient heat transfer and temperature distribution in direct extrusion using a numerical method which assumes that the billet is composed of cells of constant temperature. Altan and Kobayashi [7] have developed a numerical method to predict the temperature distribution during extrusion through conical dies. In their study,the heat generation and transportation were regarded as occurring instantaneously,

followed by an interval in which conduction takes place as for a stationary medium.They used visioplasticity data to determine the velocity field. Dalheimer [8] extended this technique to calculate temperatures in extrusion through flat-faced dies and used theoretically determined velocity and stress distributions for the calculation of the heat generation. The boundary of the deformation zone was determined by visioplasticity experiments. Altan and others [9] have attempted to calculate velocity and temperature distributions in axisymmetric extrusion, deriving a simplified version of the method introduced by Lambert and Kobayashi [10] for obtaining upper-bound velocity fields without discontinuities. The heat generation and heat conduction were considered to take place consecutively, as in the study of Altan and Kobayashi [7]. The method of the latter was applied to predict the temperature distribution in the extrusion of aluminium through flat-faced dies.

METHOD OF ANALYSIS

In extrusion through a flat-faced die, heat is generated by the deformation in the material, shearing at the deformation-zone boundaries and friction at the tool-material interface. Some of the heat generated is transported with the flowing material, some is transmitted to the punch, container and die, and some increases the temperature of the billet. Thus, the problem is complex, involving simultaneous heat generation, transportation and conduction. A numerical method of solution has therefore been developed. This finite difference method considers the effects of heat generation, conduction and mass transport on basis of local temperatures and strain-rate in each time increment of the solution.The following assumptions are made:

(a) Axial symmetry.
(b) Steady-state material flow.
(c) Constant material thermal properties.
(d) Von Mises material.

The kinematically admissible spherical velocity field with discontinuities described by Avitzur [11] is used for calculating the strain-rates in the deformation zone. The dead-metal zone angle is determined by a minimization of power, assuming constant flow stress. The grid system used for the finite difference formulation of the problem is illustrated in Fig.1. In this Eulerian grid system, the deformation zone is defined in spherical coordinates and the other regions in cylindrical coordinates. At the mesh points of the deformation zone, the heat generation rate is calculated by

$$\dot{q} = \bar{\sigma}\,\dot{\bar{\varepsilon}} \tag{1}$$

assuming that all of the plastic deformation energy is converted into heat. According to Avitzur's velocity field the effective strain-rate at each mesh point is given by

$$\dot{\bar{\varepsilon}} = 2\, v_f\, r_f^2\, \frac{1}{r^3} \sqrt{1 - \frac{11}{12}\sin^2\theta} \tag{2}$$

For each volume element, a mean value of effective strain-rate is obtained by integrating Eq. (2) between the boundaries of the element. For the flow stress of the material a relationship of the type $\bar{\sigma} = f(\bar{\varepsilon},T)$ is used. The heat generated by shearing is calculated by

$$\dot{q} = \int_s \Delta v\, \bar{\sigma}\, \frac{1}{\sqrt{3}}\, ds \tag{3}$$

at the boundaries of the deformation zone and

$$\dot{q} = \int_s v_o\, m\, \bar{\sigma}\, ds \tag{4}$$

at the billet-container interface. At the die-product interface, heat generation due to friction is neglected. The general form of the heat transfer equation is given by

$$k\,\nabla^2 T + \dot{q} = \rho\, c\, DT/Dt \tag{5}$$

The finite difference formulation of Eq.(5) in spherical coordinates (Fig.2)is written as follows

$$\left\{ 1 + \frac{\Delta t}{\Delta V_{i,j}} \frac{k}{\rho\, c} \left(\frac{S_{i,j+1}}{r_i\, \Delta\theta_j} + \frac{S_{i,j-1}}{r_i\, \Delta\theta_{j-1}} + \frac{S_{i+1,j}}{\Delta r_i} + \frac{S_{i-1,j}}{\Delta r_{i-1}} \right) - \Delta t\, v_r \frac{S_{i,j}}{\Delta V_{i,j}} \right\} T_{i,j}$$

$$+ \left(\Delta t\, v_r \frac{S_{i,j}}{\Delta V_{i,j}} - \frac{\Delta t}{\Delta V_{i,j}} \frac{k}{\rho\, c} \frac{S_{i+1,j}}{\Delta r_i} \right) T_{i+1,j} - \frac{\Delta t}{\Delta V_{i,j}} \frac{k}{\rho\, c} \left(\frac{S_{i,j+1}}{r_i\, \Delta\theta_j} T_{i,j+1} \right.$$

$$\left. + \frac{S_{i,j-1}}{r_i\, \Delta\theta_{j-1}} T_{i,j-1} + \frac{S_{i-1,j}}{\Delta r_{i-1}} T_{i-1,j} \right) = T'_{i,j} + \frac{\Delta t}{\rho\, c}\, \dot{q}_{i,j} \tag{6}$$

Eq. (6) is derived by using central difference for the spatial derivatives and backward difference for the time derivatives [12]. The finite difference expression of Eq. (5) in cylindrical coordinates is derived by a similar approach [13]. The heat generation rate per unit volume is considered to be constant at each time increment of solution and therefore small time increments are chosen for better approximation of the temperatures. The temperature distribution after time increment Δt is calculated by solving the set of finite difference equations obtained for the entire grid system. Calculated temperatures are assigned as the initial temperature distribution for the next time increment of solution and the repetition of the sequence gives the temperature distribution as a function of time. The numerical procedure has been computerized in FORTRAN IV. The block diagram of the computer program is given in Fig.3.

EXPERIMENTAL

The experimental work was conducted on an ENEFCO 5 MN extrusion press equipped with direct extrusion tools. Rod extrusions were performed at a ram speed of 5 mm/s using an extrusion ratio of 16:1 and billets of AA 2014 and 2024. The billets were homogenized at 490°C for 18 hr and air-cooled before being machined to 78 mm diameter and 150 mm length. They were then heat-treated at 495°C for 5 hr and quenched. Initial billet temperatures were selected to be 350°C for both alloys. The container temperature was maintained at 300°C.

Extrusion pressure, ram displacement and temperature at two points within the die were recorded during extrusion. K-type (chromel-alumel) sheathed thermocouples were used in temperature measurements. Two thermocouple holes were drilled into the die and the tips of the thermocouples were ensured to remain in contact with the base of the holes. The locations of the die thermocouples are shown in Fig.4. The work of Sheppard [14] has indicated that the temperature rise at the die surface approximates closely to the temperature rise at the surface of the extruded product. It was therefore decided to insert thermocouple 1 as close to the die-bearing surface as possible. The thermocouple tips are denoted by points 1 and 2 in Fig.4.

Extruded rods were quenched after extrusion by passing through a pipe placed 25 cm from die-exit. Low-pressure water was circulated inside the pipe. Thus, an amount of heat was lost from the product by convection which was taken into account in theoretical calculations.

RESULTS AND DISCUSSION

The temperatures at points 1 and 2 in the die that were measured during the extrusion of AA 2014 and AA 2024 alloys are compared with the predictions of the finite difference model. The grid system is composed of 122 mesh points. The finite difference mesh is established in such a way that points 1 and 2 are mesh points.

The measured and predicted temperatures of points 1 and 2 for the extrusion of AA 2014 and AA 2024 are shown as a function of ram displacement in Fig.5 and Fig.6, respectively. As mentioned before, point 1 is very close to die-bearing surface and temperature rise at point 1 approximates to the temperature rise at the surface of the extruded product. The experimental data and predicted temperatures at point 1 are generally in good agreement. The predicted temperatures get slightly higher than the measured temperatures towards the end of extrusion, the difference being 5°C for AA 2014 and 18°C for AA 2024 at the end of extrusion.

Point 2 is located at a distance of 10 mm from point 1. As seen in Fig.5, predicted temperatures at this point for the extrusion of AA 2014 are consistently higher, but the curve indicates acceptable agreement with the experimental results.The maximum variation between theory and experiment is 18°C, which occurs at the end of extrusion. For the extrusion of AA 2024, as can be seen in Fig.6, the theory predicts the temperature of point 2 to within ± 10°C.

In extrusion experiments it was observed that the selected ram speed could not be realized at the start of extrusion. Although the ram speed is selected to be 5 mm/s, the speed drops to 2.5 mm/s. The displacement vs. time record has revealed that this drop of speed lasts approximately 5 seconds corresponding to upsetting period. This fact is considered in the prediction of temperature distribution. Fig.7 shows the predicted surface temperature of the extruded rod at the die-exit for both alloys. The upsetting period is clearly reflected in the curves. Attention should be paid to starting temperatures when analyzing the curves. Although it is stated that initial billet temperatures are 350°C, starting temperatures below 350°C are observed in Fig.7. This is attributed to the fact that a heat loss to the die and container exists prior to extrusion, and this heat transfer is taken into account in the finite difference model. The predicted surface temperature for AA 2024 alloy is considerably higher than that for AA 2014 alloy.The difference in surface temperatures is 35°C at the end of extrusion.

In order to provide an economical production in extrusion, the extrusion speed should be selected as high as possible. Extrusion speed is governed by two limits. One is the load limit, i.e. the press capacity, and the other is the metallurgical limit, where the alloy starts to tear. If the exit temperature is too close to the solidus temperature of the

alloy, the surface tears and becomes unacceptable.Therefore, the temperature rise in the product should be estimated as close as possible for the optimization of the process. AA 2xxx and AA 7xxx series alloys classified as difficult to extrude, are widely used in aerospace industry. The working range of these alloys is very limited because they have relatively higher flow stresses and lower solidus temperatures. The prediction of temperature rise is of particular importance for alloys that are difficult to extrude.

The results of present work are also evaluated in terms of temperature rise. Assuming that temperature rise in the die at point 1 approximates closely to the temperature rise at the surface of the extruded product, measured and predicted temperature rise (ΔT) for each alloy is given in Table-1.

Table-1

Alloy	Measured ΔT in die at point 1, ^{o}C	Predicted ΔT at product surface, ^{o}C
AA 2014	121	114
AA 2024	124	147

The temperature rise is underestimated for AA 2014 alloy and overestimated for AA 2024 alloy by the theory.However, it can be said that predicted temperature rise for both alloys are acceptable to sufficient accuracy for engineering purposes. If a more accurate comparison is going to be made, thermocouple 1 can be placed at die-bearing surface.

CONCLUSIONS

1. The present model can be adequately used for predicting the temperature distribution in the billet and tooling for axisymmetric extrusion. However, additional work is necessary covering a range of extrusion ratios to verify further the model.

2. The temperature rise occuring during extrusion can also be predicted using the present numerical method, but the calculation will require a considerable computer time compared with analytical methods.

3. The model, in its present form, is limited to axisymmetric rod extrusion. The model can be adapted to different section geometries by modifying the finite difference formulation.

4. Since the computerized method of analysis developed in this study considers the process variables, it can also be used in the analysis and optimization of the extrusion process.

REFERENCES

1. A.J.Bryant, "Metallurgical Investigation of Defects in Hot Extruded Aluminium Alloys", Z.Metallkunde, Vol.62, 1971, pp.701-705.
2. K. Laue, "Isothermes Strangpressen", Z.Metallkunde, Vol.51, 1960, pp.491-495.
3. K. Laue and H. Stenger, "Strangpressen", Aluminium Verlag GMBH, Düsseldorf, 1976.
4. D. Ruppin and W. Strehmel, "Axiale Temperaturprofile in Strangpressbolzen aus Aluminium Werkstoffen", Aluminium, Vol.51, 1975, pp.585-588.
5. D. Ruppin and W. Strehmel, "Direktes Strangpressen mit Konstanter Austrittstemperatur-Einsatz Variabler Pressgeschwindigkeit", Vol.53, 1977, pp.543-548.
6. R. Akeret, "A Numerical Analysis of Temperature Distribution in Extrusion", J.Inst. Met., Vol.95, 1967, pp.204-211.
7. T. Altan and S. Kobayashi, "A Numerical Method for Estimating the Temperature Distribution in Extrusion through Conical Dies", Trans. ASME, J.Eng. Ind., Paper. 67-Prod 8, 1967.
8. R. Dalheimer, "Beitrag zur Frage den Spannungen, Formanderungen und Temperaturen beim Axialsymmetrischen Strangpressen",Ph.D. Thesis, Technical University of Stuttgart, W.Germany, 1970.
9. T. Altan, C.H. Lee and N. Akgerman, "Approximate Calculation of Velocity and Temperature Distribution in Axisymmetric Extrusion and Drawing", Proc. NAMRC, Ontario, May 14-15, 1973.
10. E.R. Lambert and S. Kobayashi, "A Theory on the Mechanics of Axisymmetric Extrusion through Conical Dies", J.Mech.Eng.Sci., Vol.10, 1968, pp. 367-380.
11. B. Avitzur, "Metal Forming: Processes and Analysis", McGraw-Hill, New York, 1968.
12. R.S. Varga, "Matrix Iterative Analysis", Prentice-Hall, New Jersey, 1962.
13. B. Altan, M. Gevrek and S. Onurlu, "A Finite Difference Solution of a Transient Heat Conduction Problem in Spherical Coordinates", Proc. 2. Symp. on Numerical Analysis and Applications, METU, Ankara, Feb. 11-15, 1985.
14. T.Sheppard and D.Raybould, "On Load and Temperature Rise During the Extrusion of Superpure Al, Al-Zn, and Al-Zn-Mg Alloys", J.Inst. Metals, Vol. 101, 1973, pp.33-44.

ACKNOWLEDGEMENTS

The author wishes to thank Prof.Dr.Ş.Güleç, Head of Materials Research Department, Marmara Research Institute, Gebze, for supporting the research. He is also grateful to Dr.M.Gevrek and Dr.B.Altan for theoretical and experimental help.

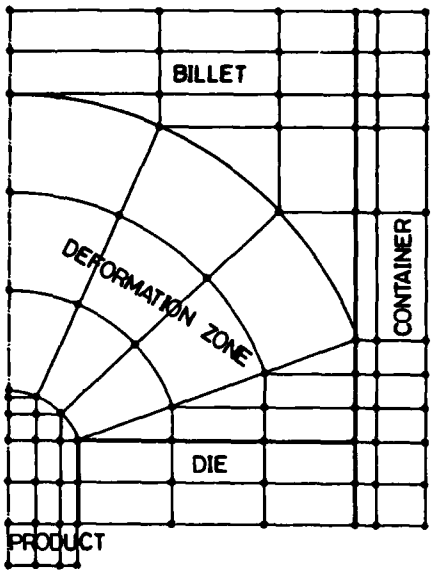

Fig.1. Grid system.

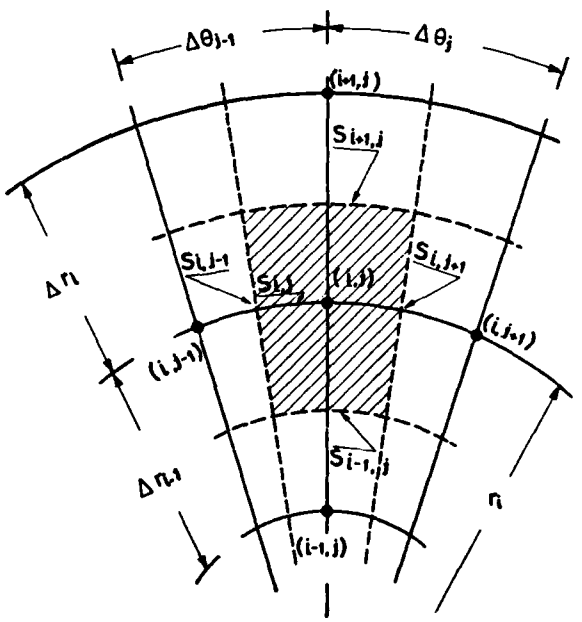

Fig.2. Volume element in spherical coordinates.

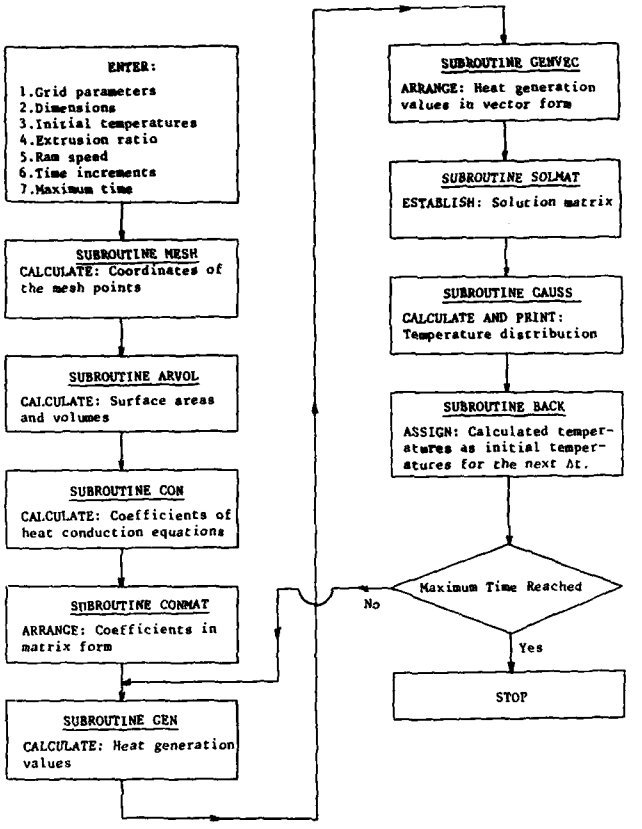

Fig.3. Block diagram of the computer program.

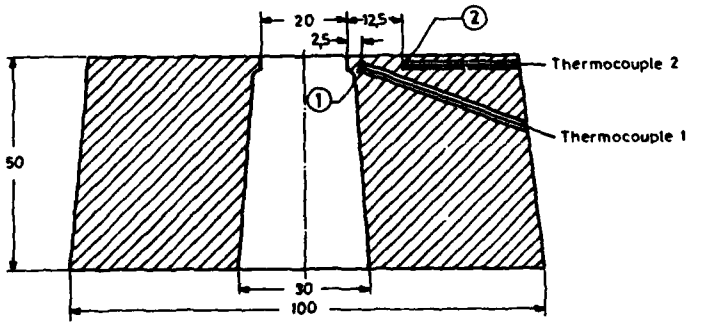

Fig.4. Locations of the die thermocouples.

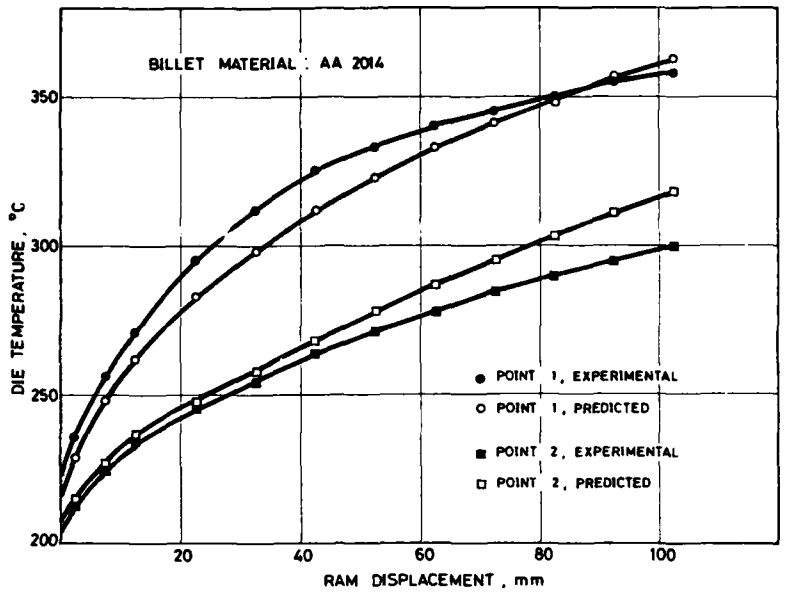

Fig.5. Measured and predicted temperatures at points 1 and 2 in the die for AA 2014. Extrusion ratio=16:1.

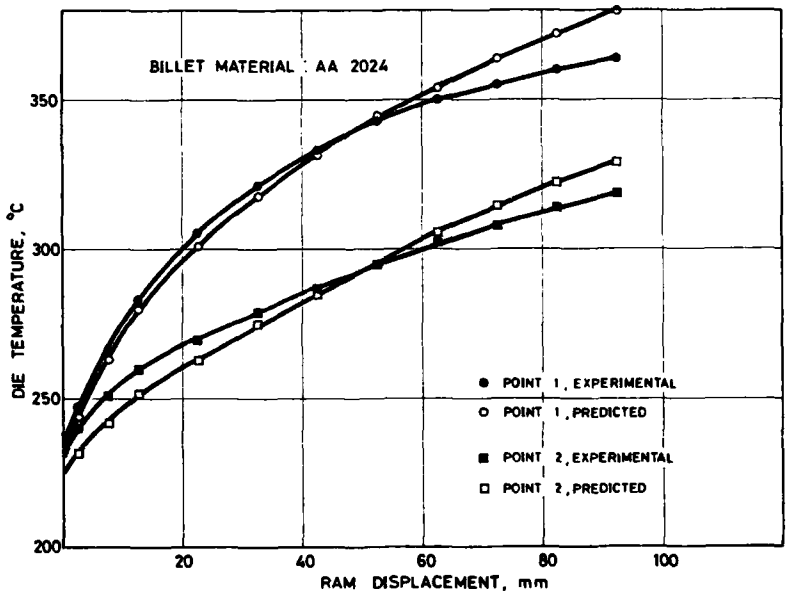

Fig.6. Measured and predicted temperatures at points 1 and 2 in the die for AA 2024. Extrusion ratio=16:1.

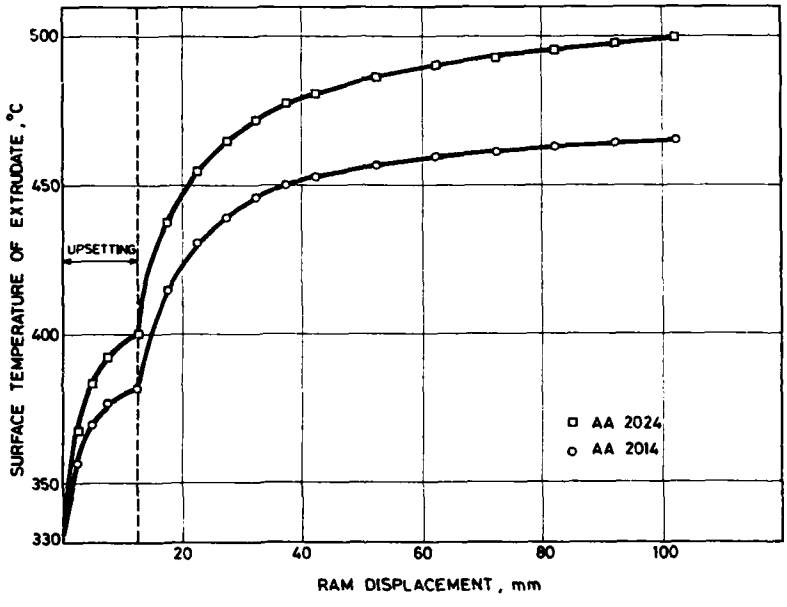

Fig.7. Predicted surface temperature of the extruded rod at the die-exit.

METALLURGICAL MODELLING OF SUPERALLOY DISC ISOTHERMAL FORGINGS

by

R.W.Evans
Reader in Materials Engineering
University College of Swansea
Singleton Park
Swansea SA2 8PP
UK

SUMMARY

The metallurgical structure of superalloy aeroengine disc forgings is a complex function of the forging operation parameters and the post forging heat treatment. It is often desirable to obtain certain specific structures in parts of the disc which are, for instance, resistant to crack propagation and this has traditionally been accomplished by means of a series of production trials. This expensive and time consuming procedure can be considerably shortened if the development of microstructure during the forging can be accurately modelled by a suitable computer code. The paper describes such a model and its use in the design of isothermal forged components.

The model described is a fully thermally coupled visco-plastic finite element algorithm. It treats nodal velocities as the basic unknowns and both the mesh geometry and the various metallurgical structural terms are updated by a single step Euler scheme. Facilities are available for ensuring that surface nodes follow die shapes after impingement, that flow is incompressible and that suitable surface friction forces are applied. Throughout the whole forging process (which may involve the re-meshing of severely distorted elements), the metallurgical history of elements is retained so that the effects of subsequent heat treatments can be assessed.

An example is given of the modelling of an axisymmetric isothermal superalloy disc forging. The evolution of structure is followed and the model used to show how the forging process may be optimized to produce the required structures both in terms of die design and forging press operation.

1. INTRODUCTION

Turbine discs in modern jet engines see extreme conditions of stress and temperature in service and yet are critical components both for the efficient operation and structural integrity of the engine. In particular, discs must resist both creep and fatigue failure, and this ability has been achieved by a combination of good metallurgical practice during manufacture and an understanding of the best structures, particularly with regard to grain size distribution. Thus, defects are only tolerated within very fine limits and the metallurgical structures are such as to resist crack propagation. This often requires a mixed grain size (the 'necklace' structure) and the structure must be produced during the manufacturing operations.

Discs are generally hot forged and hence in superalloys it is dynamic recrystallization during deformation as well as subsequent quenching which govern grain structure. The correct structures can only be obtained by a close control of the forging process and, in the past, this has required the production of many trial forgings with different press conditions and die geometries. This expensive and time consuming procedure can be circumvented if the forging process can be computer modelled in such a way as to follow the development of microstructures as well as the general flow patterns and die loadings. The forging parameters can then be optimized in such a way as to produce the desired structure in only a limited number of trials. This paper describes a model which has been developed for axi-symmetric forgings in superalloys. The model is applicable to fast and slow forgings and to hot and cold die practice, but the present work describes its use for isothermal slow rate conditions. The material considered is a particular disc superalloy but the general methodology is applicable to other alloys of the same generic class.

2. THE GENERAL PROBLEM

The general forging problem is illustrated in Figure 1. A volume of metal V at some initial temperature is forged between dies represented by W. In some cases the velocity of the dies is specified and in others the total die forces are given, or occasionally a mixture of both boundary conditions. The material in V undergoes strain by a visco-plastic flow process and since the plastic strains which ensue are large, elastic effects during the forging can be ignored. However, during eventual release of the forging loads, when strains are small, elastic effects become important and have to be calculated. Surfaces of the work-piece such as Ω are in contact with the dies whereas surfaces such as S are free to move. There are restrictions to movement over surfaces Ω and these can be either of the sticking or slipping friction kinds. The whole deformation process is transient so that not only does the shape of the deforming body change with time but also the extents of the surfaces Ω and S and possibly their frictional conditions.

As well as the deformation process being transient, time dependent changes generally occur in the thermal fields. Thus it is possible that the dies and workpiece may not be initially at the same temperature so that conduction across Ω changes temperatures. Similarly surfaces of the type S will lose heat by radiation and convection. During straining, considerable internal work is generated within the workpiece and at the frictional interface, and most of this is immediately converted into heat. Since deformation is inhomogeneous, so is heat generation, and a full transient heat flow analysis is required.

If these conditions fully summarize the forging process then the numerical techniques available make the solution of the boundary and initial value problem relatively simple. However, further complications are introduced by the physical deformation properties of the forged material. Thus the flow stress of the material will be dependent not only on strain but also on strain rate so that the flow is strongly non-linear. This necessitates the use of iterative procedures to solve the forging problem. In addition, the flow properties will generally be very temperature dependent and since the deformation itself generates heat and leads to temperature change the whole problem is strongly coupled. This coupling is not only thermal. At the microstructural level, the material may undergo various metallurgical changes during and immediately after forming, and it is important to be able to predict such changes. Not only are such changes strain, strain rate and temperature sensitive but they alter the flow stress, thus leading to further coupling.

The techniques described here for numerical analysis of this complex process are based on finite element methods. The above description of a transient process, where importance centres on the current strain rates, strains, temperatures and microstructures of individual parts of the body, dictates the use of a Lagrangian meshing scheme for solution. Thus finite element nodal points are considered to be attached to the forged material and move with it. As positions are incremented with respect to time, they carry with them the history of the element with respect to strain and temperature and this allows the progressive change in the microstructure to be assessed during forging. The general philosophy of the finite element scheme is illustrated in Figure 2. The model begins by assigning nodal co-ordinates and temperatures within the forging and guessing nodal velocities. The true velocities are then calculated in an iterative manner by the visco-plastic mechanical model and on convergence, the current stresses, strain rate, heat evolution rates and temperature change rates are determined. The nodal positions and temperatures are then updated by a Euler scheme with a suitable time step. The new nodal positions and temperatures are then used as the starting points for a second iteration and the process continued until the required forging strain is achieved. Since a Lagrangian scheme is used a check can be kept on metallurgical changes. Each of these components of the model will now be described. In the analysis presented, repeated subscripts i and j imply summation over the co-ordinate directions i and j, and subscripts following a comma imply partial differentiation.

3. THE CONSTITUTIVE EQUATION AND METALLURGICAL STRUCTURE EVOLUTION

The constitutive equation for metal flow is central to the development of a realistic model. Hot forged metals may be considered as having mechanical properties which are governed by a visco-plastic flow rule. The current stress state does not govern the current state of strain but only the current strain rate. Then, as a general formulation, the stress tensor, σ_{ij} is

$$\sigma_{ij} = f(\dot{\varepsilon}_{ij}, T, s_1, s_2, \ldots s_n) \tag{1a}$$

where $\dot{\varepsilon}_{ij}$ is the strain rate tensor, and s_1, s_2, ... s_n are suitable structural parameters such as grain size, dislocation density, defect structure and so on. For the constitutive model to be complete, the growth of each of these structural parameters with deformation must be known so that equation 1a must be supplemented by a further equation set of the form

$$\frac{ds_l}{d\varepsilon} = g_l(\dot{\varepsilon}_{ij}, T, s_1, \ldots, s_l, \ldots, s_n) \tag{1b}$$

with one such equation for each of the parameters $l = 1,n$. If the full equation set is known, then it provides not only a method of relating σ_{ij} to $\dot{\varepsilon}_{ij}$ but also, through the integration of equation 1b a means of tracing metallurgical structure development through the forging. Unfortunately, the complete material behaviour as outlined in equation 1 is rarely known, and more empirical methods must be used. Thus, for instance, many of the structural parameters are strongly strain dependent and, at least for superalloys, can be replaced simply by strain. This procedure will be referred to more fully in section 5.

It is generally accepted that material behaviour is closely described by the Levy-Mises equations so that

$$\dot{\varepsilon}_{ij} = \lambda \sigma'_{ij} \tag{2}$$

where λ is a suitable (non-constant) proportionality factor and σ'_{ij} is the deviatoric stress defined as

$$\sigma'_{ij} = \sigma_{ij} - p \qquad (i = j)$$

$$\text{and} \quad \sigma'_{ij} = \sigma_{ij} \qquad (i \neq j) \tag{3}$$

and p is the mean stress $\frac{1}{3}(\sigma_{ii})$. λ is a function of the current stress and strain rate state and equation 2 can be written conveniently as

$$\dot{\varepsilon}_{ij} = \frac{3}{2}\frac{\bar{\dot{\varepsilon}}}{\bar{\sigma}}\sigma'_{ij} \tag{4}$$

where $\bar{\dot{\varepsilon}}$ and $\bar{\sigma}$ are the effective strain rate and effective stress respectively. These are defined as

$$\bar{\sigma} = \sqrt{\left(\frac{3}{2}\sigma_{ij}\sigma_{ij}\right)}$$

$$\bar{\dot{\varepsilon}} = \sqrt{\left(\frac{2}{3}\dot{\varepsilon}_{ij}\dot{\varepsilon}_{ij}\right)} \tag{5}$$

With these rearrangements, the constitutive equation 1a can now be regarded as a relationship between the effective strain rates and stresses

$$\bar{\sigma} = h(\bar{\dot{\varepsilon}}, T, s_1, \ldots, s_l, \ldots s_n) \tag{6}$$

4. MECHANICAL MODEL

4a. General

The material in the forging zone is assumed to flow according to equation 4 and elastic deformation is assumed unimportant. At some stage in the quasi-static process a boundary value problem has to be solved with the initial conditions of inhomogeneous strain and temperature throughout the body being known. On some part of the surface Ω in contact with the dies the velocities, u, will be prescribed whereas on the remainder of the contact surface Ω_σ the traction F will be specified. Equilibrium and compatibility equations with respect to stress and strain will be satisfied.

Neglecting body and material convective forces, the equilibrium equations become

$$\sigma_{ij,j} = 0 \tag{7}$$

and for an arbitrary perturbation of the velocity field

$$\int_V \sigma_{ij,j}\, \delta u_i \, dV = 0 \tag{8}$$

By using the divergence theorem, symmetry of the stress tensor and imposing $\delta u_i = 0$ on essential boundary conditions the virtual work statement is obtained.

$$\int_V \sigma_{ij}\, \delta\dot{\varepsilon}_{ij}\, dV - \int_{\Omega_F} F_i\, \delta u_i \, d\Omega_F = 0 \tag{9}$$

For hot deforming metal, there is no change in volume so that the material must remain incompressible. Thus equation 9 becomes

$$\int_V \sigma'_{ij}\, \delta\dot{\varepsilon}_{ij}\, dV + \int_V p\, \delta\dot{\varepsilon}_{ii}\, dV - \int_{\Omega_F} F_i\, \delta u_i \, d\Omega_F = 0 \tag{10}$$

$$\text{subject to the constraint} \qquad \int_V \dot{\varepsilon}_{ii}\, dV = 0 \tag{11}$$

and where σ'_{ij} and $\dot{\varepsilon}_{ij}$ are related through equation 4.

4b. Discretization

It is assumed that the body is divided into finite elements connected only at the nodal points. In the programme suite the elements are eight-noded quadratic iso-parametric elements. At the elemental level, the velocity field, [u], is approximated by

$$[u] = [N]^T [\upsilon] \tag{12}$$

where [υ] is the vector of nodal point velocities and [N] the shape function matrix. In vector form, the strain rate tensor becomes

$$[\dot{\varepsilon}] = [B][\upsilon] \tag{13}$$

where [B] contains the necessary spatial derivatives of the shape functions. The effective strain is given by

$$\bar{\dot{\varepsilon}} = ([\varepsilon]^T [D]^T [\varepsilon])^{\frac{1}{2}} = ([\upsilon]^T [B]^T [D]^T [D][B][\upsilon])^{\frac{1}{2}} = ([\upsilon]^T [P]^T [P][\upsilon])^{\frac{1}{2}} \tag{14}$$

Substitution into equations 10 and 11 and assembling over all m elements yields

$$\sum_1^m \left[\int_V \frac{\bar{\sigma}}{\bar{\dot{\varepsilon}}} [P][\upsilon] dV - \int_\Omega [N][F] d\Omega + \int_V \frac{\zeta}{2} \dot{\varepsilon}_{ii}\, dV \right] = 0 \tag{15}$$

$$\text{and} \quad \int [\upsilon]^T [B]^T [C]\, dV = 0 \tag{16}$$

The last term in equation 15 ensures that the material remains incompressible and corresponds to the penalty function method of ensuring the constant volume constraint.[9] Equation 15 represents a non-linear set in the nodal velocities and these must be solved iteratively for given element geometry.

4c. Boundary Conditions

If sticking friction of boundary nodes is assumed, then boundary conditions present no difficulty since they are merely ascribed the relevant die velocity. Under slipping friction conditions the situation is not so straightforward. The application of a Coulomb friction condition leads to unsymmetric matrices and, instead, a friction factor defined by

$$\tau = \frac{m}{2}\bar{\sigma} \tag{17}$$

is used where τ is the shear friction stress. Difficulty arises when a point of reversal of velocity between die and workpiece creates a singularity. Since the point of reversal is not known in advance the abrupt change which occurs during iteration leads to ill-conditioning. To avoid this, equation 17 has been replaced by a arc tangent function[8], yielding

$$\tau = \frac{m\bar{\sigma}}{2}\left[\frac{2}{\pi}\tan^{-1}\frac{\upsilon_R}{a\,|\upsilon|}\right] \tag{18}$$

where υ_R is the relative velocity between die and workpiece, a is a constant and υ the die velocity.

A further restriction is placed on surface nodal velocities by the necessity of ensuring that those nodes in compressive contact with the dies move in a direction parallel to the dies. In the forging model, die profiles are defined in a linear piece-wise fashion so that if a node is in contact with a die facet which makes an angle ϕ with the radial direction, then its velocities in the radial and axial directions must be confined to be in the ratio $1:\cot\phi$.

4d. Updating

For the general forging analysis, the above mechanical scheme must be supplemented by a transient thermal analysis to determine temperature change rates. This must take into account the internal heat evolution rate $\alpha\bar{\varepsilon}\bar{\sigma}$ where $\alpha \sim 0.95$. However, for the present isothermal examples, no detailed analysis will be given.

At any one updating point the isothermal model presents values of the nodal velocities. The nodal co-ordinates can now be updated by a simple one-step Euler scheme so that

$$x_i^{(t+1)} = x_i^{(t)} + v_i^{(t)}\Delta t \tag{19}$$

Δt must be chosen with due regard to the following criteria.

1) The time stepping scheme must be numerically stable and Δt must be sufficiently small to maintain as a reasonable approximation the small strain analysis outlined in section 4a. Experience shows that this can be done by limiting the maximum element strain per increment to less than 0.05.

2) During an updating step, the velocity of a node already in contact with the die may be such that it is in danger of leaving a linear die facet and joining the next die facet. The time step must be chosen so that the node only just enters the new linear die facet.

3) During an update, the nodal velocity of a surface node not already in contact with the die may make it pierce a die facet. The time step must then be chosen to allow the node to just touch the die facet.

After a series of time steps, some elements may become sufficiently distorted to yield difficulty either with accuracy or in inverting the Jacobean matrices for the iso-parametric representation. If this occurs, the mesh must be re-drawn. The current information about strain, temperature and metallurgical structure must then be interpolated onto the new mesh. Routines within the programme must allow this re-meshing to be done automatically using the element quadratic shape functions as interpolating polynomials.

5. A PRACTICAL CONSTITUTIVE RELATIONSHIP

The mechanical and microstructural data required for the relationships presented in section 3 can only be obtained by recourse to experimental work. The section describes such experimentation and its analysis for one disc superalloy.

Mechanical testing has been carried out by the compression of glass lubricated cylindrical specimens in a hot die furnace. The tests are true constant strain rate tests and the relevant true strain curves can be calculated from the load-displacement values. Each test is carried out at constant strain rate and temperature and a range of tests (usually covering temperatures between 900°C and 1150°C and strain rates between $10^{-4}s^{-1}$ and $100s^{-1}$) is required. A typical set of stress-strain curves are shown in Figure 3. For superalloys, all the curves show the same shape. There is a reasonably distinct yield stress (σ_1) followed by a period of work hardening to a maximum stress at a stress and strain value σ_2, ε_2. This is followed by a period of softening or constant stress which has a stress value of σ_3 at some large strain (say $\varepsilon = 0.4$). The work hardening section of the curve is well represented by a second order polynomial in strain whereas the softening portion is reasonably linear. Thus, for a variety of initial conditions, stress-strain curves can be defined by the quantities σ_1, σ_2, σ_3 and ε_2. If these have a systematic variation with strain rate and temperature then they form a good basis for a mechanical constitutive relationship. Various relationships have been proposed but the most satisfactory appears to be

$$\sigma = \frac{1}{\alpha}\sinh^{-1}\left[\left\{\frac{\dot{\varepsilon}}{A}\exp\left(\frac{Q}{RT}\right)\right\}^{\frac{1}{n}}\right] \tag{20}$$

Figure 4 shows a typical fit for σ_2 and σ_1. Thus each of the stresses σ_1, σ_2 and σ_3 can be represented by equation 20 with different values of the constants α, A, Q and n. There is considerable evidence for steels[9] and for superalloys that ε_2, the strain at maximum stress, is related to testing conditions by an equation of the form

$$\varepsilon_2 = B\,\dot{\varepsilon}^m \exp\left(\frac{H}{RT}\right) \tag{21}$$

and Figure 5 shows a typical fit. Although knowledge of all the various constants described allows any stress-strain curve to be constructed, this is not a full constitutive equation since it does not prescribe the path to be followed in moving from one stress-strain curve to another. This would normally be achieved by a knowledge of structural parameters. However, careful experimentation using strain rate and temperature change testing suggests that these structural parameters can be replaced with good accuracy by the quantity strain (i.e. a strain-hardening rule). It is then sufficient to note, finally, that the compressive strain, strain rate and stress are numerically equal to the effective strain, strain rate and stress. All parameters may be grain size dependent but this effect seems to be small in superalloys.

Although the replacement of structural terms by strain in the mechanical equation of state is a considerable convenience, it has the disadvantage of removing the possibility of using the constitutive equation to follow structural evolution. This information must now be obtained by separate experimentation. The forged structures of the specimens deformed to a strain of 0.5 in the tests described above can be investigated since they are quenched after forging within 2 seconds. The structures show a systematic variation with testing conditions. There is always a degree of dynamic recrystallization leading to a reduction in grain size from the initial ASTM 1. The fraction of recrystallization increases with increasing strain rate at constant temperature and with increasing temperature at constant strain rate (Figure 6). In addition the recrystallized grain size changes with testing conditions, higher temperatures giving larger grain sizes. An analysis of the results suggests that for a strain of 0.5, the recrystallized grain size M (ASTM number) is given by (Figure 7)

$$M = C\,\dot{\varepsilon}^p \exp\left(\frac{F}{RT}\right) \tag{22}$$

The information contained in the tests described above does not yield direct knowledge of the kinetics of the dynamic recrystallization process. Such data can be obtained from tests to smaller overall strain and a series of such tests are illustrated in Figure 8. Several conclusions can be drawn from these tests. For all tests conducted at strains less than the strain maximum, ε_p, no recrystallization is ever observed. For strain greater than ε_p, there is always recrystallization and except for strains very close to ε_p, the grain size of the dynamically recrystallized regions is reasonably constant and equal to that described by equation 22. The volume fraction recrystallized at strain ε is a function only of ε - ε_p so that the important variable in the kinetics of recrystallization is strain and not time. This is supported by the fact that volume fractions recrystallized at a strain of 0.5 increase with strain rate even though times for deformation decrease. Several possibilities are now available to describe the kinetics of recrystallization. Detailed experiments on partially recrystallized material suggest that once recrystallization has commenced, then new grains can appear anywhere in the structure (i.e. in recrystallized or non-recrystallized areas) and on this basis it is possible to define an instantaneous rate of recrystallization with respect to strain, dr/dε, which is a function of the current temperature and strain rate only. The variation is given by (Figure 9)

$$r = \frac{dr}{d\varepsilon} = D\,\dot{\varepsilon}^q \exp\left(\frac{G}{RT}\right) \tag{23}$$

At any time step updating, the forging model can now calculate changes in metallurgical structure. Thus at the start of an increment the volume fraction recrystallized will be f_1 and at the end f_2, where

$$f_2 = 1 - (1 - f_1)\exp(-r\dot{\varepsilon}\Delta t) \tag{24}$$

where r is given by equation 23. The volume fraction (f_2 - f_1) will have grain size given by equation 22 so that the current grain size distribution can also be updated. If the volume fraction of grains of size M = i [i = 0 → 14] is h_i at the start of an increment then

$$\sum_{i=0}^{14} h_i = 1$$

At the end of an increment where there has been a volume fraction recrystallized equal to $\Delta f (= r\dot{\varepsilon}\Delta t)$ at grain size ASTM = M, the grain size distribution will be g_i where

$$g_i = h_i(1 - \Delta f) \qquad i \neq M$$

$$g_i = h_i(1 - \Delta f) + \Delta t \quad i = M \tag{25}$$

6. EXAMPLE FORGING

This section describes results from a modelling of a typical disc forging. The piecewise linear die representation and the initial billet mesh geometry are shown in Figure 10. The forging has a volume of 0.0075m³ and is conducted isothermally at 1050° C. Various mesh deformation stages and microstructure development are shown in Figure 11. As with any finite element model, there is far more information (with respect to stress, die loads, grain size distribution etc.) available than summarized in the figures, but several points are of interest. It is clear that die geometry has a marked effect on dynamic recrystallization. Thus die corners which are convex to the die interior markedly increase recystallization compared to the average values, whereas die corners which are concave have the reverse effect.

7. CONCLUSIONS

The model described in the paper has been applied to a wide range of forgings in several different superalloys, and has been shown to yield good predictions of forging flow, die load and metallurgical structure. It has the advantage that the coding has been written especially to run on micro-computers and the whole analysis can be run on a desk-top PC with a minimum of 512k RAM. If the computer contain a Maths processor then each time step takes, on average, 30 minutes, and the example forging was completed in 23 increments. The use of larger computers is, of course, quite possible and this will increase the speed of calculation.

8. REFERENCES

1. Zienkiewicz, O.C. and Godbole, P.N., 'Flow of Plastic and Viscoplastic solids with Special Reference to Extrusion and Forging Processes', Int. J. Num. Meth. in Eng., 8, 1974, 3-16.
2. Kobayashi, S., 'Thermoplastic Analysis of Metal Forming by the Finite Element Method', Numerical Analysis of Forming Processes, Ed. J.J. Pittman, O.C. Zienkiewicz, R.D. Wood and J.M. Alexander, Wiley, Chichester, 1984, 45-71.
3. Sellars, C.M., 'Physical Metallurgy of Hot Working', Hot Working and Forming Processes, Ed. C.M. Sellars and G.J. Davies, Metals Society, London, 1980, 3-16.

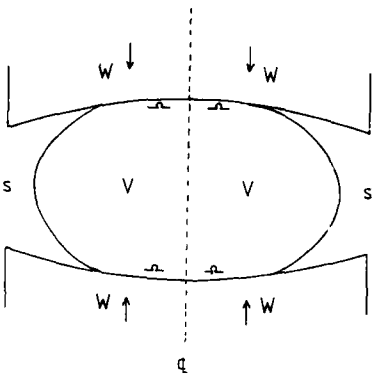

Figure 1. Schematic Forging Process

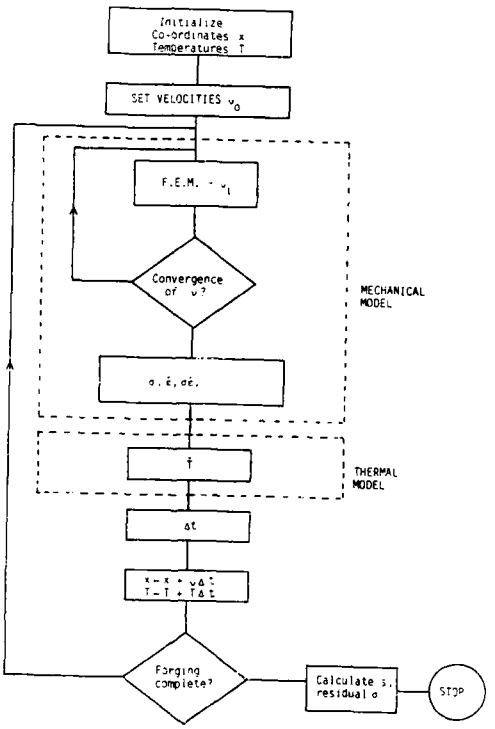

Figure 2. General Modelling Scheme

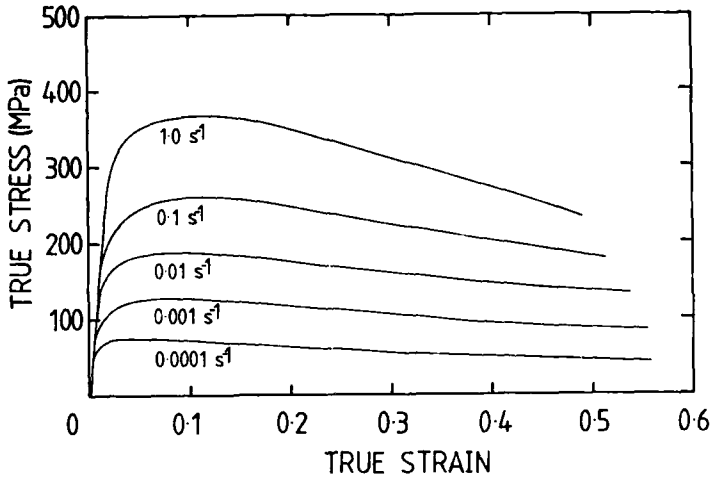

Figure 3. Compressive stress/strain curves at constant temperature

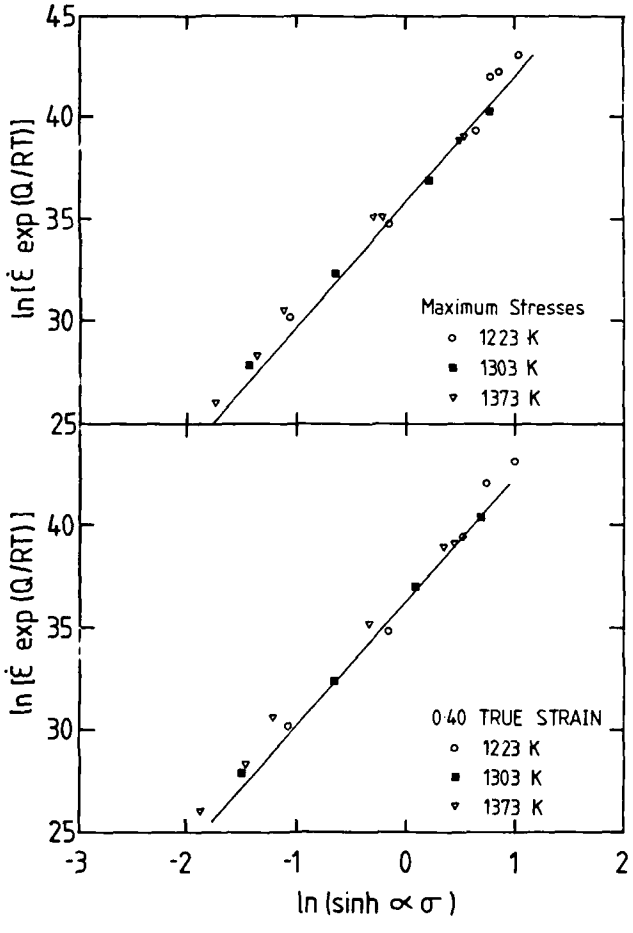

Figure 4. Variation of stress (σ) with temperature (T) and strain rate ($\dot{\varepsilon}$)

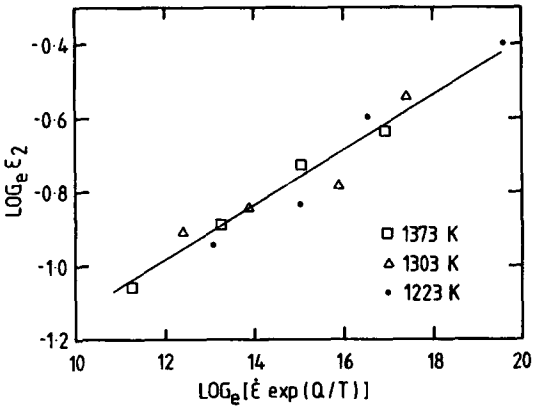

Figure 5. Variation of strain to maximum stress (ε_2) with strain rate ($\dot{\varepsilon}$) and temperature (T)

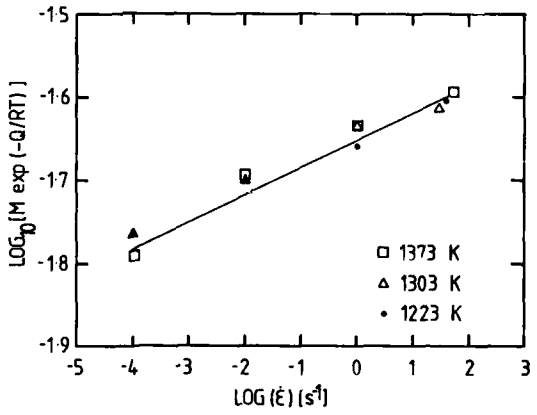

Figure 7. Variation of ASTM grain size (M) with temperature (T) and strain rate ($\dot{\varepsilon}$) at a strain of 0.5

(a)

(b)

(c)

Figure 6. Microstructures of specimens tested to strains of 0.50 at constant strain rate and various temperatures. a = 950°C. b = 1030°C, c = 1100°C.

0.1 mm

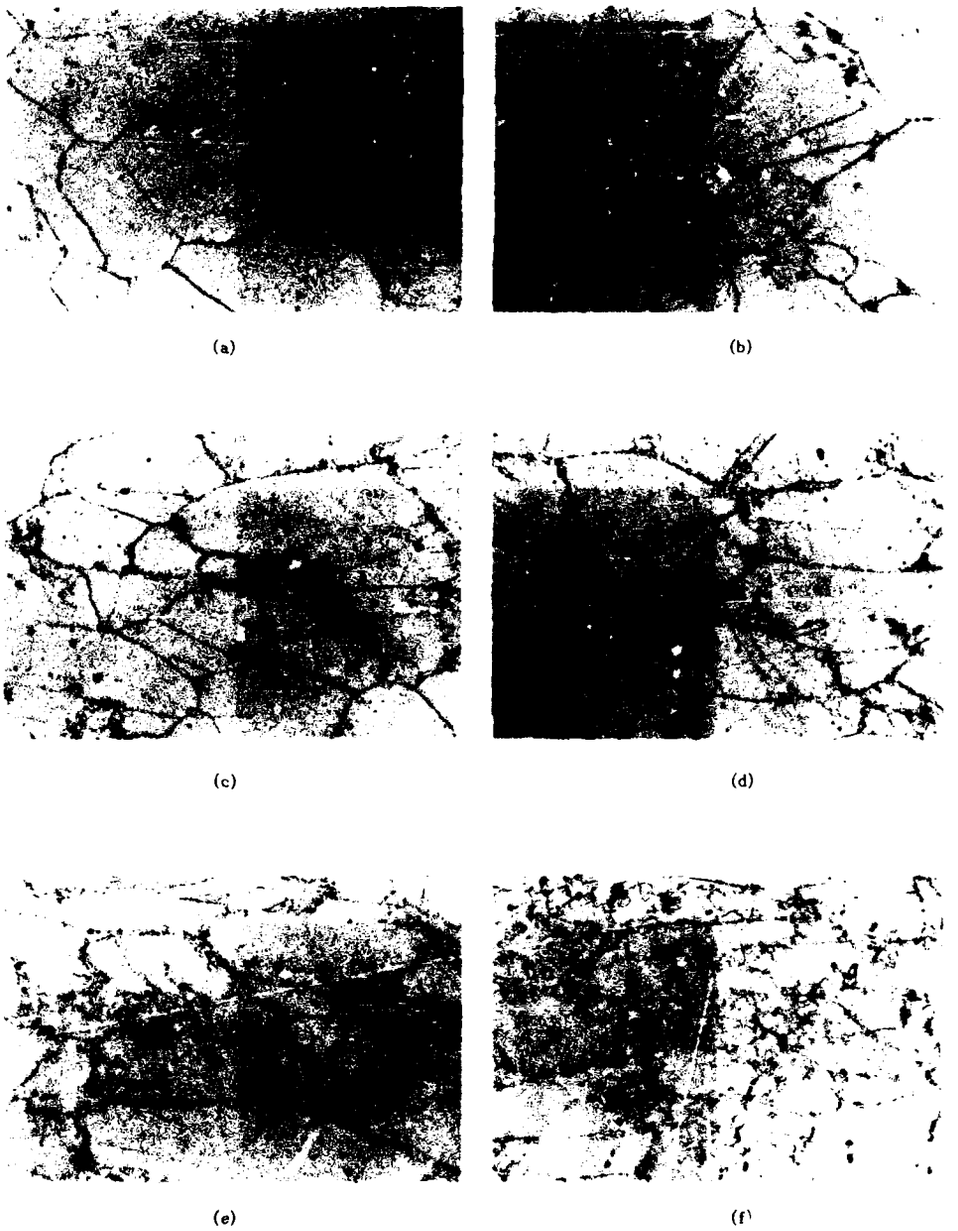

Figure 8. Microstructures of specimens tested to various strains at constant temperature and strain rate. a = 0.05 strain, b = 0.10, c = 0.20, d = 0.30, e = 0.40, f = 0.50. 0.05 mm

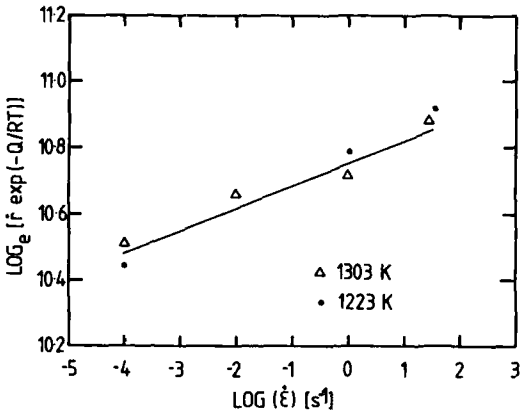

Figure 9. Variation of recrystallization rate ($\dot{r}$) with temperature (T) and strain rate ($\dot{\varepsilon}$)

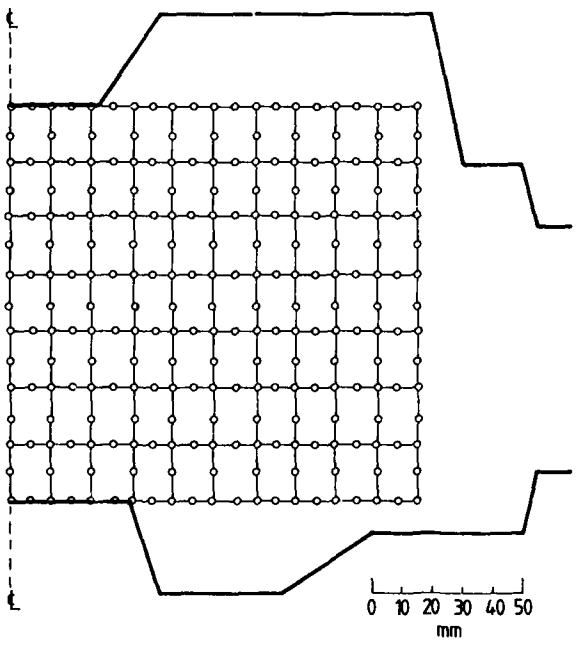

Figure 10. Initial die and billet mesh geometry for axisymmetric disc forging

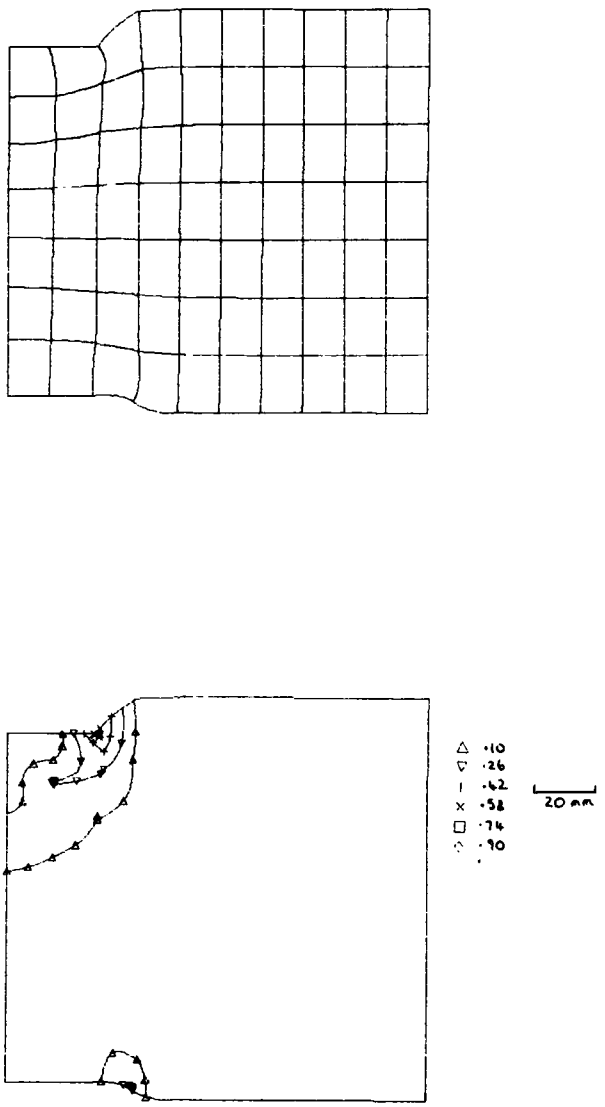

Figure 11a. Forged billet showing mesh geometry and volume fraction recrystallization.

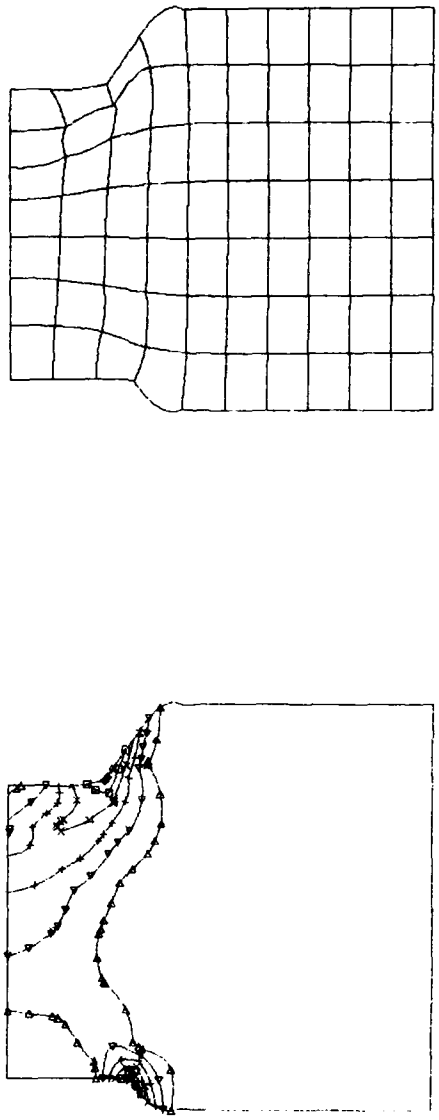

Figure 11b. Forged billet showing mesh geometry and volume fraction recrystallization.

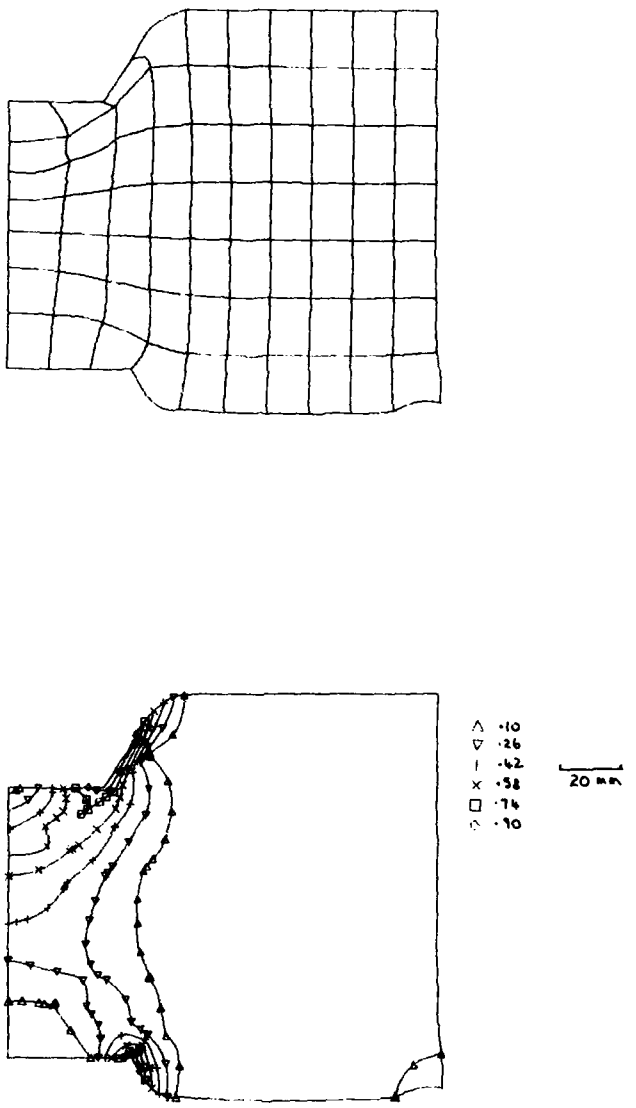

Figure 11c. Forged billet showing mesh goemetry and volume fraction recrystallized.

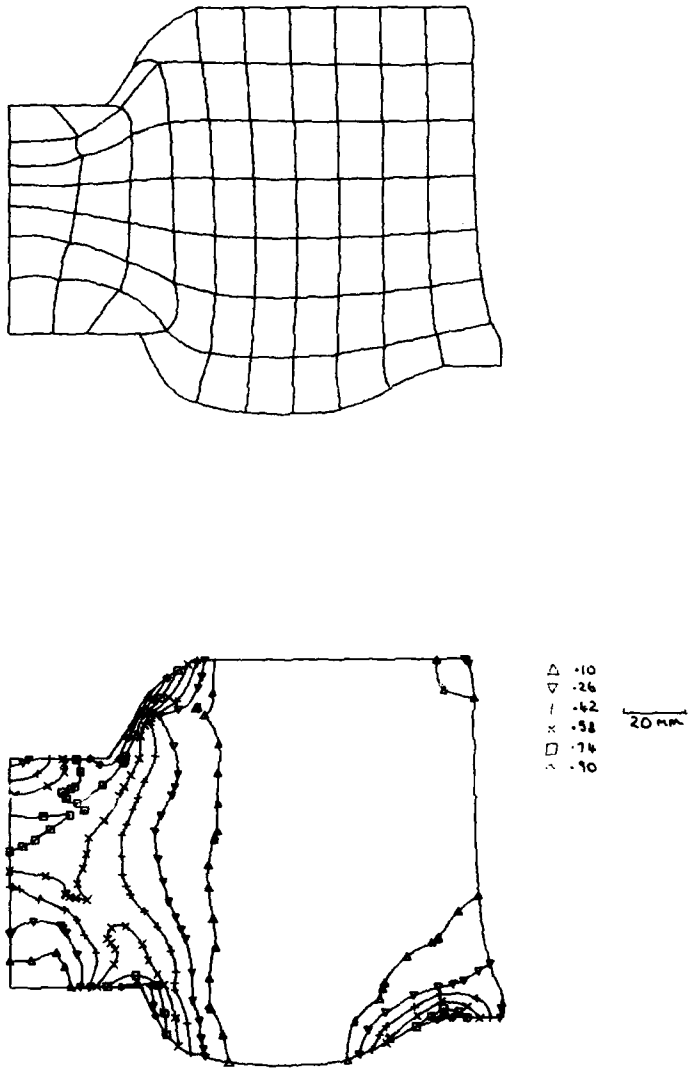

Figure 11d. Forged billet showing mesh geometry and volume fraction recrystallized.

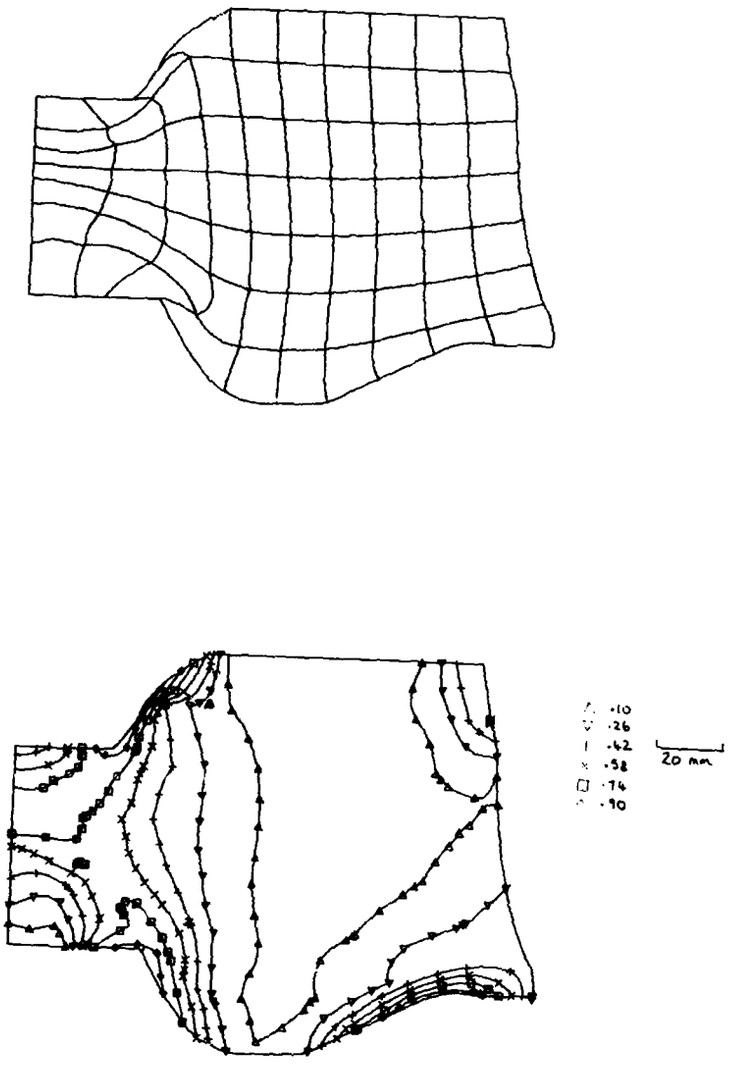

Figure 11e. Forged billet showing mesh geometry and volume fraction recrystallized.

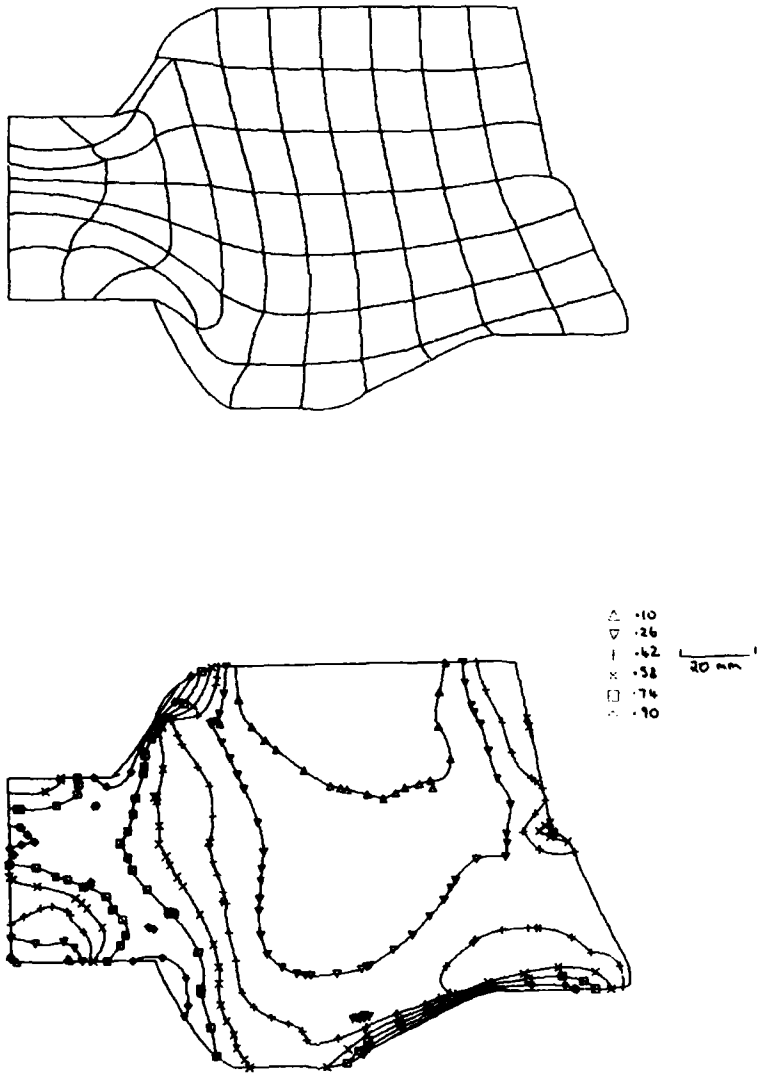

Figure 11f. Forged billet showing mesh geometry and volume fraction recrystallization.

A COMPUTER PROGRAM SIMULATING THE HOT FORGING OF METAL POWDER

E. WEY, C. LEVAILLANT and J.L. CHENOT
Centre d'Etude de Mise en Forme des Matériaux
Ecole Nationale Supérieure des Mines
Sophia Antipolis
06560 VALBONNE, FRANCE

ABSTRACT

A computer program for the simulation of hot forging of metal powder was developed using finite element technique. The constitutive equation for powder behaviour includes viscoplastic effects and porosity. The relationship between flow stress σ_{eq} and equivalent strain rate $\dot{\varepsilon}_{eq}$ is :

$$\sigma_{eq} = K (\rho \dot{\varepsilon}_{eq})^m$$

And the law used in our model follows the tensorial relationship :

$$\underline{\underline{\sigma}} = \frac{\sigma_{eq}}{\rho \dot{\varepsilon}_{eq}} \left(\frac{2}{3c} \underline{\underline{\dot{e}}} + \frac{1}{9f} \operatorname{tr} \underline{\underline{\dot{\varepsilon}}} \, \underline{\underline{1}} \right)$$

where ρ is the relative density and c and f are coefficients depending on ρ.

This model involves also unilateral contact conditions and friction with the dies. A remeshing module permits the calculation of very large deformation with complex dies.

This simulation program is applied to the forging of an automotive part. The simulation allows to optimize the dies geometry to achieve complete densification and good strain range everywhere in the worked piece.

1. INTRODUCTION

The powder route is now a way often used to form parts with new materials or with improved metallurgical properties. The hot forging process applied to powder compacts is interesting in many ways :

- the compacted preform is heated and rapidly forged in a closed die to full densification and final shape ;
- productivity can be large ;
- the microstructural characteristics of the initial powder are maintained.

A computer program simulating the hot forging of metal, FORGE2, was developped in the CEMEF laboratories [1,2]. This program is now industrialy used to optimise the forging sequences for two dimensional or axisymmetrical cases (no geometrical defects like folding, good die filling, homogeneous total strain, ...). The aim of this paper is to present the constitutive equations applied to the simulation of the hot metal powder flow and densification and the characterization method. These equations are used into a modified version of FORGE2. Two forging examples with an aluminium powder are then studied to demonstrate the validity and possible use of the program.

2. CONSTITUTIVE EQUATIONS

2.1. Rheology

The classical approach to study the rheological behaviour of dense and incompressible materials is to apply the Von Misès plasticity theory. It allows to determine an equivalent stress σ_{eq} associated with the flow of the material. The relationship between the equivalent strain rate $\dot{\varepsilon}_{eq}$ and the equivalent stress σ_{eq} is the rheological law.

During the forging of a powder material, that material flows to fill the dies while its density increases. For that reason, the equivalent stress must be a function of the density variations and must reduce to the classical dense expression when the material is fully compacted. Many approaches have been developed to describe the plastic deformation of powder material at a microscopic level, but they do not allow a mechanical formulation suitable for the simulation of material forming.

A new approach has been defined [3,4]. The material is considered as an homogeneous medium caracterized by its relative density ρ instead of an heterogenous set of individual particles and pores. We define an equivalent stress with the isotropic invariants of the Cauchy stress tensor :

$$\sigma_{eq}^2 = \frac{3}{2}\, c(\rho)\ \underline{\underline{s}} : \underline{\underline{s}} + f(\rho)\ (tr\underline{\underline{\sigma}})^2 \qquad (1)$$

where :
- $\underline{\underline{\sigma}}$: Cauchy stress tensor ;
- $\underline{\underline{s}}$: deviatoric part of $\underline{\underline{\sigma}}$;
- ρ : relative density is the ratio of the apparent density to the theoretical density of the material ,
- c,f : rheological coefficients depending on ρ caracterizing the material

The plastic strain rate will be deduced from a potential ϕ' depending on $\underline{\underline{\sigma}}$, ρ and temperature θ :

$$\dot{\underline{\underline{\varepsilon}}} = \frac{\partial \phi'}{\partial \underline{\underline{\sigma}}} \qquad (2)$$

ϕ' is supposed to depend only on σ_{eq} defined by (1) and θ

$$\phi'(\sigma_{eq},\ \theta) \qquad (3)$$

We can now write :

$$\dot{\underline{\underline{\varepsilon}}} = \lambda\ \frac{\partial \sigma_{eq}}{\partial \underline{\underline{\sigma}}} = \frac{\lambda}{\sigma_{eq}}\ (\frac{3c}{2}\ \underline{\underline{s}} + f\ tr\ \underline{\underline{\sigma}}\ \underline{\underline{1}}) \qquad (4)$$

where : $\lambda = \dfrac{\partial \phi'}{\partial \sigma_{eq}}$

It is possible to define also an equivalent strain rate $\dot{\varepsilon}_{eq}$ by duality with the equivalent stress, using the egality of the plastic deformation power :

$$\underline{\underline{\sigma}} : \dot{\underline{\underline{\varepsilon}}} = \rho\ \sigma_{eq}\ \dot{\varepsilon}_{eq} \qquad (5)$$

Using (5) with (4) and (1), we obtain

$$\lambda = \rho\ \dot{\varepsilon}_{eq} \qquad (6)$$

$$\dot{\varepsilon}_{eq}^{\,2} = \frac{1}{\rho^2}\ (\frac{2}{3c}\ \dot{\underline{\underline{e}}} : \dot{\underline{\underline{e}}} + \frac{1}{9f}\ (tr\dot{\underline{\underline{\varepsilon}}})^2) \qquad (7)$$

where $\dot{\underline{\underline{e}}}$ is the deviatoric part of $\dot{\underline{\underline{\varepsilon}}}$.

The volume conservation implies that the densitification rate can be expressed by :

$$\frac{\dot{\rho}}{\rho} = -\ tr\ \dot{\underline{\underline{\varepsilon}}} \qquad (8)$$

When the full density is reached, the equivalent stress (1) must reduce to a classical Von Mises criterion, implying that :

$$c(1) = 1 \quad \text{and} \quad f(1) = 0$$

A minimul value of the relative density exists. It depends on the particles morphology. At that level, the particles are just in contact, and any applied stress leads to an irreversible deformation, thus :

$$c\ (\rho_{mini}) \gg 1 \text{ and } f\ (\rho_{mini}) \gg 1$$

To summarize, we can say that, for powder material, the deformation mode is a mixing of pure deformation as for dense material and densification under isostatic pressure.

For the simulation of hot forging, we use the viscoplastic potential ϕ (dual of ϕ') :

$$\phi = \frac{K}{m+1}\ (\rho\ \dot{\varepsilon}_{eq})^{m+1} \qquad (9)$$

thus :

$$\underline{\underline{\sigma}} = \frac{\partial \phi}{\partial \dot{\varepsilon}} = \frac{\sigma_{eq}}{\rho \dot{\varepsilon}_{eq}}\ (\frac{2}{3c}\ \dot{\underline{\underline{e}}} + \frac{1}{9f}\ tr\ \dot{\underline{\underline{\varepsilon}}}\ \underline{\underline{1}}) \qquad (10)$$

$$\sigma_{eq} = K(\rho\dot{\varepsilon}_{eq})^m \text{ or } \rho\dot{\varepsilon}_{eq} = A\ \sigma_{eq}^{\,n}$$

The knowledge of the $c(\rho)$ and $f(\rho)$ functions enables then the determination of the powder rheological behaviour.

2.2. Friction

Friction is the key controlling phenomenon for die filling. In order to simulate that aspect, the friction is introduced in the model with a shear stress $\underline{\tau}$ on the product/tool interface. By analogy with the viscoplastic potential, we can define a friction potentiel such as :

$$\phi_f = \frac{\alpha}{p+1} \|\underline{V}_g\|^{p+1} \tag{11}$$

where $\underline{V}_g$ is the relative sliding velocity

Thus :
$$\underline{\tau} = - \frac{\partial \phi_f}{\partial \underline{V}_g} = -\alpha \|\underline{V}_g\|^{p-1} \underline{V}_g \tag{12}$$

3. TIME AND SPACE DISCRETIZATION

During forging, inertial forces can be neglected and the transient phenomenon is then studied as a sequence of quasi-stationnary states. At each time increment, on a well known geometry, the problem consists in calculating the velocity field by solving the equilibrium equation together with the behaviour law and the friction law. This set of equations is condensed into a variational principle wich allows the velocity field V to be calculated from a family of fields satisfying the boundary conditions. The problem consists in minimizing the functional

$$\Phi(\underline{V}) = \int_{\Omega} \phi(\underline{V})\, d\Omega + \int_{\Gamma} \phi_f(\underline{V})\, d\Gamma \tag{13}$$

with respect to V. The minimization is achieved on the domain Ω by the finite element method. The Ω domain is discretized into finite elements. Thus, to obtain the minimum of the functional, we have to solve a set of non-linear algebraic equations. That is done by the classical iterative Newton-Raphson method.

The discretized geometry at time $t+\Delta t$ is updated as a fonction of the geometry at time t and the velocity field V_t at this time with an explicit integration scheme :

$$\underline{X}_{t+\Delta t} = \underline{X}_t + \underline{V}_t \Delta t \tag{14}$$

Finally, for the forging problem, we have to introduce the contact evolution. This involves two main parts :
- a material point comes into contact during the time step ;
- a point previously in contact becomes free.

For the first problem, the difficulty lies in the explicit time integration scheme, wich allows the material point to penetrate the die. To avoid this, the penetrating point is projected orthogonally onto the die surface. For the second problem, a condition on the normal contact stress is used. If we have a compressive stress, the material point is restricted to slide on the die. There is separation for a traction stress.

4. POWDER CHARACTERIZATION METHOD [5,6]

4.1. Basic equations

To determine the powder material rheology, laboratory mechanical tests are conducted for simple geometry parts using homogeneous strains and stresses assumptions. Cylinder densification can be considered in the following three cases :

a) Hot Isostatic Pressing (HIP)

The densification rate $\dot{\rho}$ can be expressed as a function of the applied pressure P by :

$$\dot{\rho} = 3\, \rho\, A\, (f)^{\frac{n+1}{2}}\, P^n \tag{15}$$

b) Uniaxial closed die pressing

In this case, the densification rate is related to the axial strain rate V/h (V:ram velocity, h:cylinder height), assuming that friction can be neglected. Thus :

$$\dot{\rho} = \rho\, V/h = \rho A \left(\frac{9\ cf}{4f+c}\right)^{\frac{n+1}{2}} \rho^n \qquad (16)$$

c) Cylinder upsetting (assuming no barelling)

For this test, both load and diameter can be measured during upsetting at constant ram velocity V. Thus, two relations are obtained, one for the upsetting pressure P and the other one for the apparent Poisson's ratio $\nu = \dot{\varepsilon}_{rr}/\dot{\varepsilon}_{zz}$ ($\dot{\varepsilon}_{rr}$: radial strain rate, $\dot{\varepsilon}_{zz}$: axial strain rate).

$$\frac{V}{h} = A\,(c+f)^{\frac{n+1}{2}}\,\rho^n \qquad (17)$$

$$\nu = \frac{2f-c}{2(c+f)} \qquad (18)$$

4.2. Experimental procedure

The viscous flow law can be determined in some cases on fully densified specimens (if available) by simple tensile or torsion testing at various strain rates. If the full density cannot be achieved, the flow law can be fitted directly on non dense specimens, together with c and f functions. Typical experimental procedure involves series of tests on cylindrical specimens with various initial relative density ρ_0. The test must be stopped before a to large increase in relative density, in order to get rheological characteristics for the ρ_0 value.

For HIP, the pressure P is the imposed parameter, whereas for uniaxial closed die or free compression, it is the ram velocity V. Series of test with various P or V must be carried out. The slope of the $\dot{\rho}$ vs. P or V vs. P logarithmic plots gives n value. A can be determined by plotting $\dot{\rho}/\rho_0\rho^n$ (for HIP) or $V/h\ P^n$ (for uniaxial compression) as a function of ρ_0 and extrapolating this curve to $\rho_0=1$. From these rheological parameters A and n, equation (15) gives $f(\rho_0)$ for HIP whereas equation (16) gives only a relation between $c(\rho_0)$ and $f(\rho_0)$. It appears that neither HIP nor closed die compression can give the whole set of material parameters. Cylinder upsetting with apparent Poisson's ratio measurement, if possible, is the most attractive test method because it enables to identify all parameters using equations (17) and (18).

The variations of the c and f fonctions with relative density are generally well described by an hyperbolic law with an asymptote for a minimum density ρ_{mini} :

$$c = 1 + K_1 \frac{1-\rho}{\rho-\rho_{mini}} \qquad (19)$$

$$f = K_2 \frac{1-\rho}{\rho-\rho_{mini}} \qquad (20)$$

Thus, we have the relationship :

$$c = 1 + \beta\, f$$

Our results on different materials tend to indicate that the β factor would be a constant depending essentially on powder morphology and granulometry.

4.3. Discussion of the assumptions

The principle of the simple method here exposed is that the material is and remains homogeneous throughout the tests and is submitted to a simple stress state constant in all specimen (pure isostatic pressure with absence of friction). That can be not verified for particular conditions. In these cases, the computer simulation can be used to fit A, n, K_1, K_2 and ρ_{mini} parameter on experimental results themselves.

5. NUMERICAL SIMULATION

5.1. Cylindrical sample

The specimen geometry (initial $\varnothing_0$=88 mm, h_0=30 mm and final form $\varnothing_f$=116 mm, h_f=17mm) is given on figures 1 and 2 with the initial mesh and the deformed one. The material constants used for the forging computation are listed below (for an Al-4%Cu-5i Mg alloy at 500 °C) :

- K = 54.5 (units : MPa, seconds)
- m = p = 0.074 • α = 10.9
- ρ_{mini} = 0.64 • K_1 = 4.37 • K_2 = 0.36

The initial relative density is 0.80 and the upper die speed is assumed to be constant equal at 360 mm/sec. The total forging time is 0.036 sec.

Figure 3 shows a comparison on relative density evolution at the sample center as a function of time. Experimental evolution is almost linear throughout the forging. Computation results are in good agreement with experiment.

Figure 4a represented the contour lines of the computed relative density at 85 % of the total die displacement. When comparing with experimental gammametry data (figure 4b), it appears that computation predicts the correct density distribution, with underdensification in the peripheral zone of the sample.

Figure 5 shows the evolution of the forging load. The computed load is in good agreement with experiment between 0.02 and 0.032 sec. Initial discrepancy can be attributed to mechanical clearances compensation. On the actual forging press, the speed decreases rapidly at the end of the forging pass instead of the constant speed in the computation. That explains the final computed rapid evolution.

5.2. Connecting rod

The model is now applied to the case of a preform presenting some variation in the forging direction. It is the AA section of a connecting rod (figure 6), with the plane strain assumption. Figure 7a represents the initial mesh and the upper die and figure 7b represents the deformed mesh at the end of the forging (die displacement = 2.16 mm and forging time = 0.006 sec). In this case, deformation and homogeneous densification are simultaneously researched.

The observation of the contour lines of the relative density at time 0.031 sec (figure 8) and time 0.0054 sec (figure 9) indicates that the densification is obtained by material flow from the lowest section aera towards the other section via the joining radius. It leads to inhomogeneous particle deformation. Particle major axis is given by the Grain Aspect Ratio :

$$GAR = (1 + \varepsilon xx) / (1 + \varepsilon yy) \qquad (21)$$

x horizontal axis
y vertical axis

In the fillet zone, the particle major axis is parallel to the forging direction (GAR<1) and perpendicular (GAR>1) on both sides (figure 10).

The simulation program predicts here a weakness possibility in the fillet zone of the connecting rod with that forging preform.

6. CONCLUSION

We have described here the powder hot forging process through a viscoplastic model wich takes into account both densification and material flow. It is based on a yield criterion for porous material depending on relative density.

A computer program, based on the finite element method, allows the simulation of the powder forging process. That program will conduct to powder preform optimization in order to improve the mechanical characteristics of the forged parts.

REFERENCES

[1] Y. GERMAIN : Modélisation par éléments finis d'écoulement viscoplastique avec frottement ; these de docteur ingénieur ; Ecole Nationale Supérieure des Mines de Paris ; 14 juin 1985 (in French)

[2] Y. GERMAIN, J.L. CHENOT, P.E. MUSSEN : Finite element analysis of shaped lead-tin disk forging ; proceedings of NUMIFORM 86

[3] M. ABOUAF : Modélisation de la compaction de poudres métalliques frittées , Doctorat es-Sciences ; Université scientifique et médicale et Institut polytechnique de Grenoble ; May 1985 (in French)

[4] M. ABOUAF, J.L. CHENOT : A numerical model for hot deformation of metal powders. Journ. of theorical and applied Mechanics Vol. 5. n°1. 1986 pp. 121-140 (in French)

[5] C. LEVAILLANT, J.L. GUERBES, C. LAUGEE, P. AMOUROUX : Modelling of aluminium alloy powder hot forging process in view of computer aided design of preform. Second Int. Conf. on Advanced Technology of Plasticity. Stuggart. F.R.G. Aug. 1987. K. Lange. Ed. Springer Verlag pp. 953-960

[6] C. LEVAILLANT, H.J. BRAUDEL, F. WEY : Mise en Forme de poudres métalliques - Rapport ARMINES-AFME March 1986 (in French).

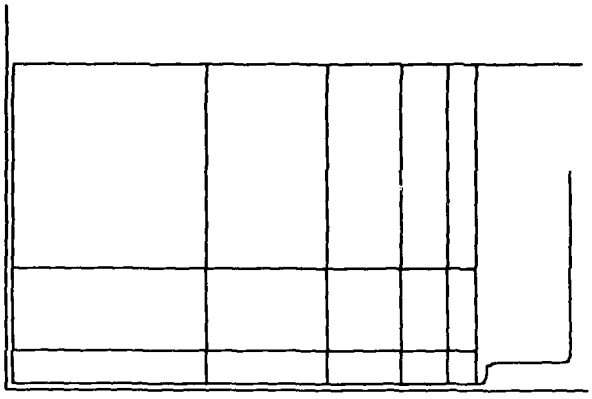

Figure 1 - Cylinder upsetting - Initial mesh and dies

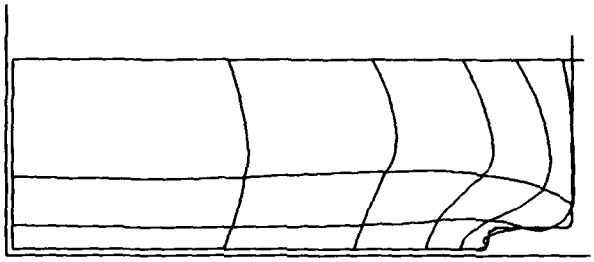

Figure 2 - Cylinder upsetting - Deformed mesh and dies

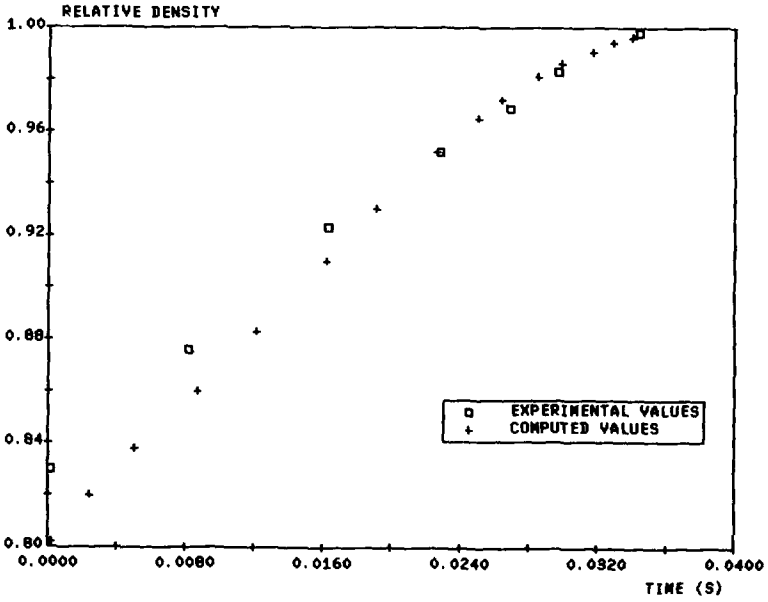

Figure 3 - Cylinder upsetting - Relative density evolution at the center

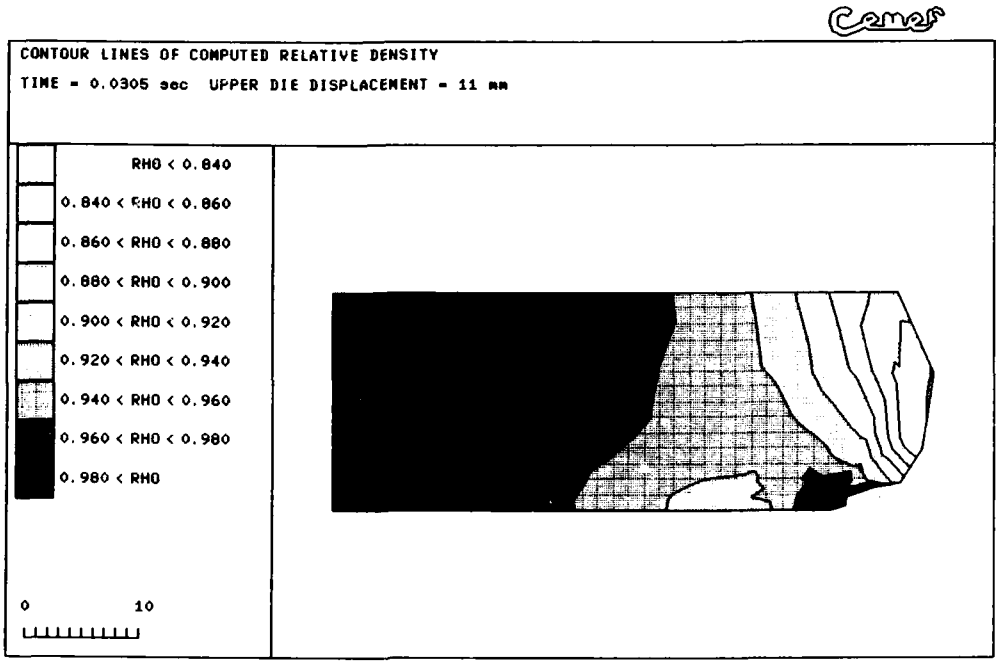

Figure 4a - Cylinder upsetting - Computed relative density

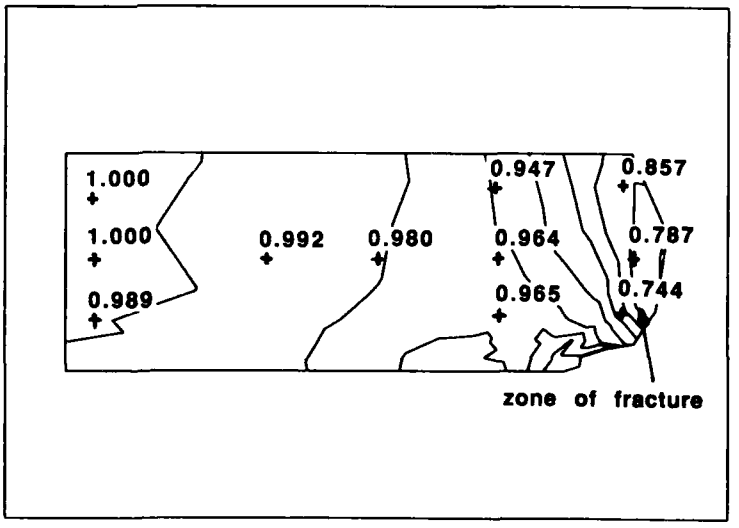

Figure 4b - Cylinder upsetting - Measured relative density

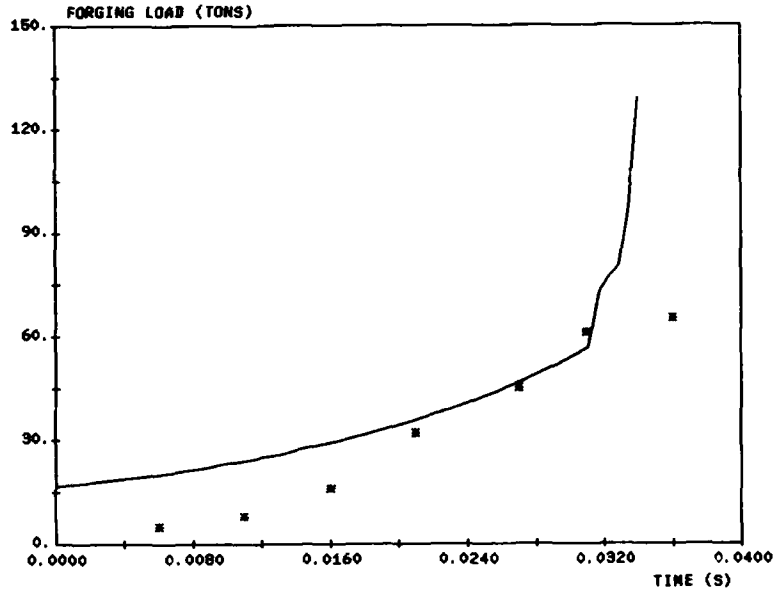

Figure 5 - Cylinder upsetting - Forging load evolution

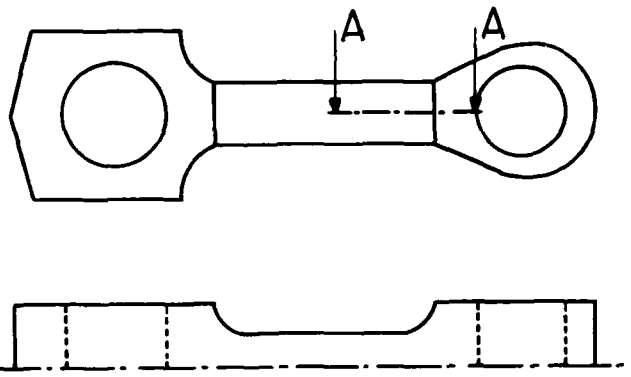

Figure 6 - Connecting rod - Studied section

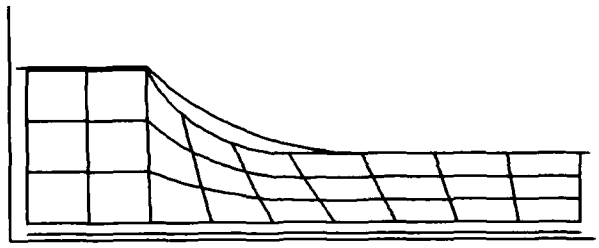

Figure 7a - Connecting rod - Initial mesh and die

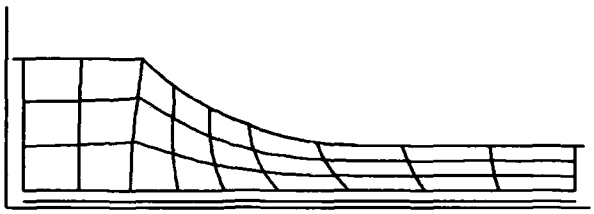

Figure 7b - Connecting rod - Deformed mesh and die

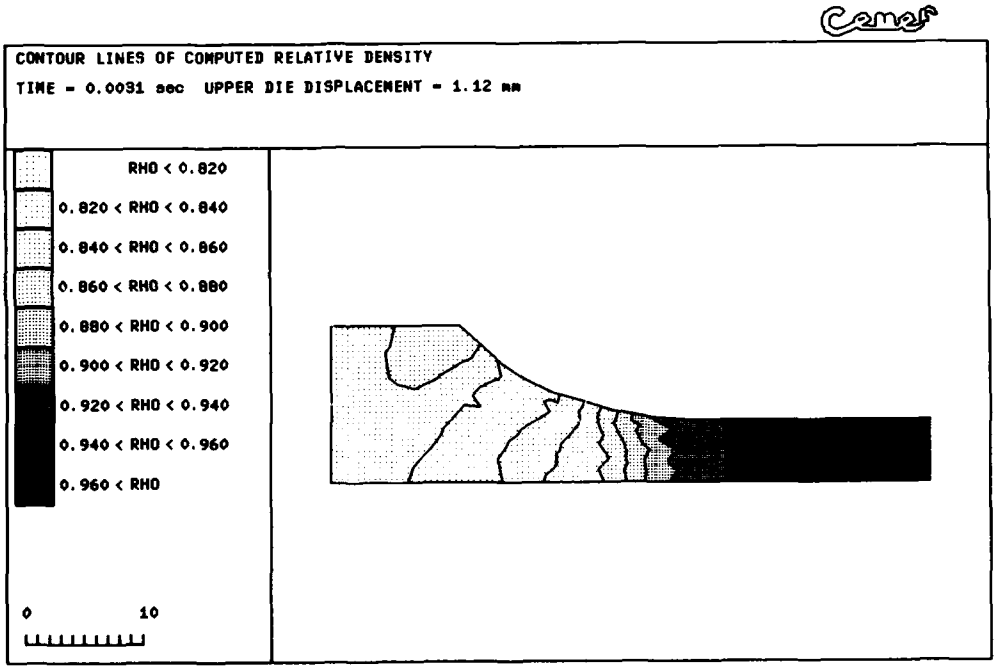

Figure 8 - Connecting rod - Computed relative density at mid forging

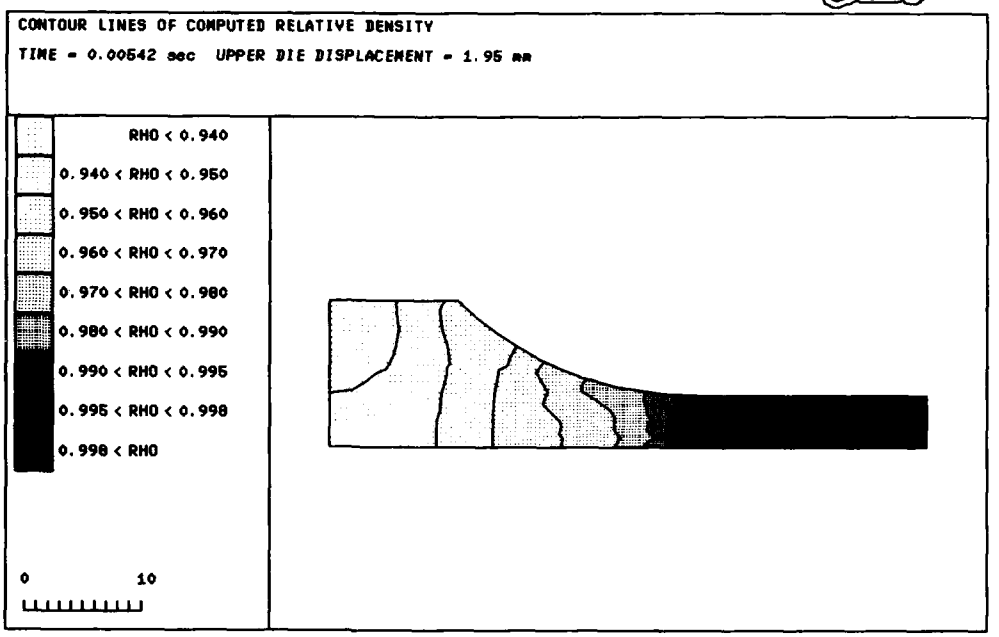

Figure 9 - Connecting rod - Computed relative density near end of forging

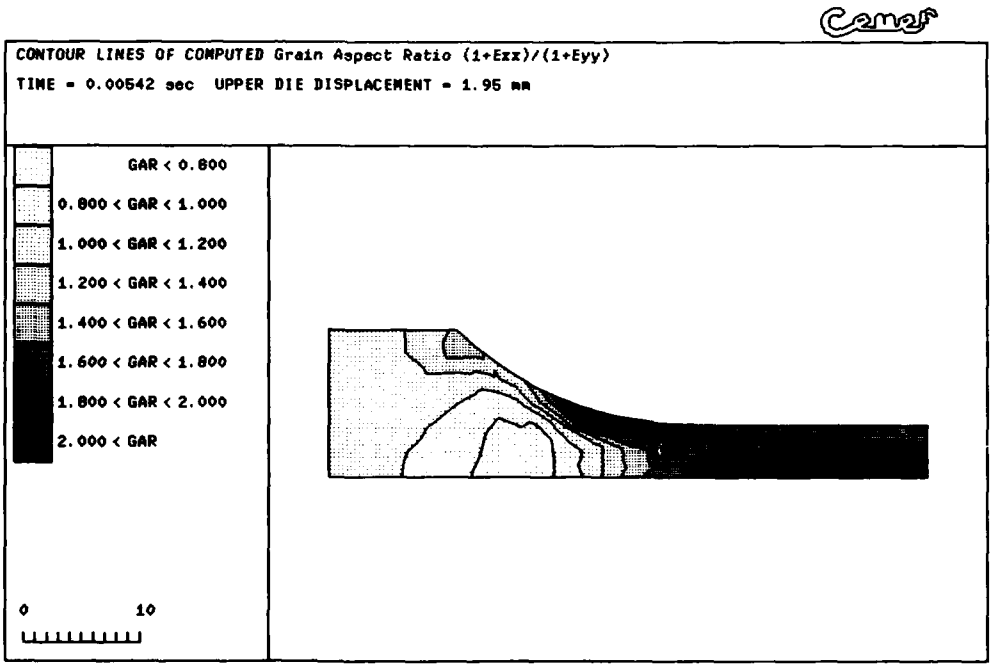

Figure 10 - Connecting rod - Grain aspect ratio at the end of forging

MICROSTRUCTURES, FLOW PROPERTIES AND PROCESSING OF Ti6242 ALLOY

by

Alpay Ankara
Chairman
Department of Metallurgical Engineering
Middle East Technical University
Ankara 06531, Turkey

and

Taylan Altan
Ohio State University
Engineering Research Center
Baker Building, 1971 Neil Avenue
Columbus, OH 43210-1271, USA

SUMMARY

This paper reviews the physical phenomena that occurs during metal deformation process of Ti 6242 alloy. Data on flow properties is obtained by compression tests. The paper covers also the flow stress variations with the type of equipment used, deformation heating, effects of temperature, strain, strain rate and microstructural variations.

1. INTRODUCTION

A large number of aerospace components are manufactured by means of one or more material-deformation processes followed by heat treatment and machining. This is the case especially for highly stressed critical jet enginee and airframe parts such as disks, blades, and structural ribweb type components. The manufacturing cost of these components, used in aerospace systems, continues to rise. Therefore, innovations are being sought to reduce the processing and life cycle costs of such products while improving material utilization and properties. Such innovations can be achieved by the combined application of materials science, mechanics, and mechanical engineering disciplines to develop advanced metal processing techniques, more productive and less costly than the state-of-the-art methods.

Recognizing the need for innovative techniques in deformation processing, the U.S. Air Force initiated an effort on processing research and development (1). This effort includes an appropriate combination of basic and applied research, a coordinated application of materials data, process analysis, computer-aided simulation of metal flow, and equipment behavior (2). This new approach is expected to encourage innovative approaches for the future application and development of metal forming technology.

In order to implement the computer-aided design and manufacturing (CAD/CAM) approach, detailed mathematical models of the workpiece material, the forming process, and the workpiece-tool interface conditions are required. However, these models did not exist in a sufficiently complete form. Hence, the overall objective of this program has been to develop and verify the required models and integrate them to form an interactive computer program for process design. The process models have been developed to a level of sophistication sufficient to allow the control of microstructure and properties in addition to the shape of the finished part. Although the methodology is generally applicable to a range of deformation processes, the validation and application has been restricted to the forging process for a Ti-6Al-2Sn-4Zr-2Mo (designated as Ti-6242 here after) turbine compressor disk.

This program has been conducted by a team of investigators from various universities and companies in the following five phases:

Phase I- Material Behavior Under Processing Conditions
Phase II- Process Modeling for Disk Type Forging
Phase III- Interface Effects
Phase IV- Integration of Material and Process Models
Phase V- Property/Microstructure Relationships on the Forged Disk

The results of this study have been applied extensively not only to forging of Ti-6242 but also to forming of various other alloys. This paper illustrates the methodology, developed in this U.S. Air Force study, as applied to Ti-6242 alloy.

2. MATERIAL CHARACTERIZATION

In massive forming processes the workability and flow stress data are important material variables which strongly dedends on microstructure of a given material composition. The size, shape and distribution of the phases is also of great importance in determining the mechanical properties of the formed product. In Ti-6242 forgings the microstructure of the alloy vary significantly with die temperature, strain rate, strain and final heat treatment.

To demonstrate the effect of preform microstructure and thermomechanical processing on final microstructure uniaxial compression tests were done. Data were obtained for strain of $\varepsilon \approx 0.7$ and strain rate of 2×10^{-1} sec in a pneumatic press and using SEM. Threedifferent sets of experiments were run to compare the final microstructures formed. These were

i) Heat treatment
ii) Hot forging
iii) Hot forging followed by heat treatment

i) Microstructures After Heat Treatment

1. Alpha-and-beta microstructure

Fig. 1. shows the as received microstructure of alpha-plus-beta alloy. Material has elongated alpha grains and transformed beta which consist of Widmanstatten alpha-and-beta phase.

Heat treatment of alpha-plus-beta alloy from 900°C to 980°C for times upto 8 hours are performed. The resulting microstructures for few characteristic samples are fiven in Figure 2. The time at a given temperature (upto 2 hours) did not effect the microstructure much. However, 8 hours of heat treatment resulted in pronounced coarsening of the Widmanstatten alpha in the tnasformed beta matrix. A similar effect on microstructure was found with increase of temperatures from 900°C to 980°C.

2. Beta microstructure

Fig. 3 exhibit the microstructures developed by heat treatment above beta-transus temperatures of 1010°C and 1040°C for times upto 8 hours. This treatment revealed only Widmanstatten or basketweave microstructures. Heat treatmenttime and temperature did not influence the morphology of the transformed phase, however, the beta grain size increased with heat treatment time and temperature.

ii) Microstructures After Hot Deformation

1. Alpha-plus-beta preform material

The microstructures developed by hot deformation of alpha-plus-beta preform material below beta-transus was characterized with larger amont of alpha phase and coarse Widmanstatten alpha precipitates in the transformed beta matrix as compared with non-deformed preforms. It is clear that the subtransus deformation leads to the development of equilibrium amounts of globular alpha.

However hot working temperatures close to beta-transus resulted in refined matrix phase, Figure 4 exhibits some microstructures hot deformed alpha-plus-beta preform.

2. Beta preform material

Figure 5 shows some examples of microstructures developed by deformation at temperatures of 1010°C to 1040°C. The microstructures developed in compression above beta- transus is characterized by large colonies of alpha needles.

iii) Hot Forging Followed by Heat Treatment

1. Alpha-plus-beta preform material

Figures 6 and 7 show examples of the microstructures developed by post defomation heat treatment from 900°C to 980°C for times upto 8 hours.

The increased amount of alpha phase and coarsening of Widmanstatten alpha is obvious. The residual hot work seems to assist the microstructure in attaining a microstructure close to equilibrium one. The transformed beta phase, either deformed or after post-deformation heat treatment (close to beta-transus) consists of both caurse and fine Widmanstatten alpha precipitates.

2. Beta-preform material

The microstructures developed by post deformation heat treatment below beta-transus for samples deformed at 1010°C and 1040°C is given Figure 8 , in general a coarsening of Widmanstatten or basketweave microstructures is obvious.

Heat treatments above the beta-transus results that the structure transforms to single phase bcc titanium and this phase reverts to fine acicular alpha precipitates in large previous beta grains during cooling. The above figures show microstructures developed by post deformation heat treatment in the beta phase field.

From the above data it is clear that a large variety of microstructures can be obtained by various thermomechanical processing, which in turn would determine the properties of the deformed product.

3. FLOW STRESS DATA

The flow stress data are most commonly obtained by conducting a uniform compression test (without barrelling) or a torsion test at the temperature and strain rate of interest (3).

A cam plastometer, if available, would provide a constant strain rate ($\dot{\varepsilon}$) during uniform compression tests. However, since cam plastometers are not readiliy available, a programmable high speed electrohydaraulic testing machine (for example an MTS) or a regular crank or eccentiric driven mechanical press can also be used for obtaining flow stres data via uniform compression tests.

The MTS machine is capable of monotonic or cyclic (0.0001 to 50 Hz) loading at cross head speeds of 2.5×10^{-5} to 50.8 cm/sec. (10^{-5} to 20 in./sec.). Using a custom made RC (Resistance-Capacitance) electrical circuit it is possible to provide an exponential signal to control the ram of the MTS to obtain a constant strain rate (within ± 3 percent variation) during compression testing. In an MTS machine, compression tests can be conducted at constant strain-rates from 10^{-3} to 10 $sec.^{-1}$. Usually a high temperature compression fixture, such as that show in Figure 9 is used for conducting hot isothermal compression test in the MTS(3).

The mechanical press can also be used to obtain flow stress data at nearly constant strain rates, in the range of $\dot{\bar{\epsilon}}$ = to 20 sec.$^{-1}$ (4). Data at various strain rates are obtained for a given press by slowing the flywheel to rotate at various speeds. For 50 percent reduction in height of the specimen, the strain rate during uniform compression tests in a mechanical press remains nearly constant up to a strain ϵ of approximately 0.4. Examples of $\bar{\sigma}$ - ϵ data, obtained in a mechanical press, are shown in Figures 10-13. These tests were conducted using a high-temperature fixture, similar to that of Figure 9. However, the mechanical press fixture did not have an integral furnace and was heated outside of the press prior to each compression test (4,5).

To demonstrate the ability to use various kinds of equipment for flow stress determination, data were obtained for the same material and microstructure (Ti-6242/equiaxed alpha microstructure) in a mechanical press and in MTS machine. These data are compared in Figure 11, which illustrates that there are small differences between these two test results. Observed differences are a result of test-to-test variations of specimen composition (which was slightly different for the two tests because specimens were cut from billets made from two different heats), lubrication, and specimen preheat temperature. The latter point may be particularly important in view of the great temperature dependence of the flow stress that many $\alpha + \beta$ titanium alloys, such as Ti-6242, exhibit at hot working temperatures. In view of the general agreement, however, it may be concluded that both the mechanical press and the MTS machine can be used for obtaining flow stress data by conducting uniform compression tests.

Flow stress data, available in the literature, are always given for a specific alloy, with known composition. However, often the microstructure and the heat treatment of the alloy prior to testing may influence significantly the magnitude and variation of $\bar{\sigma}$ - $\bar{\epsilon}$ curve. With titanium alloys and high temperature nickel alloys especially, the microstructure of the material before deformation influences considerably the flow stress as well as the flow instabilities occurring during plastic deformation. Examples are given in Figure 10 and 12, where the flow stress of Ti-6242 is depicted for an equiaxed alpha microstructure, Figure 10, and an acicular, or Widmanstatten, , alpha microstructure, Figure 12, deformed at the same test temperature and strain rate. These examples clearly illustrate the need for characterizing the microstructure in obtaining flow stress data for metals.

At a given temperature, the flow stress ($\bar{\sigma}$) may increase, remain constant of decrease with increasing strain ($\bar{\epsilon}$), depending upon the alloy and its microstructure. The decrease of $\bar{\sigma}$ with increasing $\bar{\epsilon}$ can often be explained to a large extent by the temperature increase which occurs during the compression test. The temperature increase due to heat generation, $\Delta\theta$, can be estimated from

$$\Delta\theta = \frac{\bar{\epsilon}\,\bar{\sigma}}{Jc\rho}\,\beta \qquad (1)$$

In equation (1), ρ is mass density, c is the specific heat, J is the mechanical equivalent of heat and β is the portion of mechanical energy transformed into heat; β is approximately 0.95. To demonstrate the effect of deformation heating on flow stress, a study was conducted, and the flow stress of various high temperature alloys was determined in compression. It was found that the $\bar{\sigma}$ - $\bar{\epsilon}$ curve for 403 stainless steel showed a gradual increase up to a flow stress plateau (the "saturation" stress) while that of Ti-6Al-2Sn-4Zr-2Mo showed a considerable decrease with increasing strain (4). Adiabatic temperature increases calculated with equation (1) showed that the temperatures of the samples increased about 125^{0}C for the titanium alloy and only about 30^{0}C for steel. Considering that the flow stress of titanium alloys is much more temperature dependent than that of steels, the drop in the $\bar{\sigma}$ - $\bar{\epsilon}$ curve for the titanium alloy was considered to be due largely to adiabatic heating.

A recent study explained this phenomenon more quantitatively (5). Figure 13 shows the $\bar{\sigma}$ - $\bar{\epsilon}$ curves for Ti-6242 (equiaxed alpha microstructure) obtained with the uniform compression test at the approximate strain rate of $\dot{\bar{\epsilon}}$ = 10 sec.$^{-1}$. (The findings for $\dot{\bar{\epsilon}}$ = 2 sec.$^{-1}$ were similar.) These data have been replotted in Figure 14 to show $\bar{\sigma}$ as a function of the "nominal" test temperature at given values of ϵ. It appears that $\bar{\sigma}$ is a function of $\bar{\epsilon}$ and temperature for a given $\dot{\bar{\epsilon}}$. After calculating the temperature rise due to plastic deformation, Equation (1), and replotting each $\bar{\sigma}$ data point at the adjusted temperature (=nomial temperature plus temperature increase due to deformation heating), the $\bar{\sigma}$ versus temperature behavior appears as in Figure 15. Because a single $\bar{\sigma}$ versus temperatre curve fits all of the test data (except that for $\bar{\epsilon}$ <0.1), it can be concluded that $\bar{\sigma}$ is independent of $\bar{\epsilon}$. In other words, a high strain-rate (> 1 sec.$^{-1}$), "isothermal" $\bar{\sigma}$ - $\bar{\epsilon}$ curve for this material would exhibit an initial zone of strain hardening followed by a plateau. This behavior is the same as that observed in low strain-rate, isothermal testing of similar equiaxed alpha titanium alloys and for many other materials at hot working temperatures.

4. PROCESS MODELING

The physical phenomena describing a forming operation are difficult to express with quantitative relationships. The metal flow, the friction at the die/material interface, the heat generation and transfer during plastic flow, and the relationships between microstructure/properties and process conditions are difficult to predict and analyze. Often in producing discrete parts, several forming operations (pre-forming) are required to transform the initial simple geometry into the final complex geometry without causing material failure or degrading material properties. Consequently, the most significant objective of any method of analysis is to assist the forming engineer in the simultion of metal flow or process modelling. This objective is best achieved by using reasonably accurate and inexpensive computer software that is developed for process modelling. Thus, forming experiments can be run on a computer by simulating the material flow at each stage of a forming operation. The results, i.e., position of material boundaries, strains, strain rates, stresses, and temperatures, can be displayed on a graphics terminal, and reviewed. If these results indicate that process conditions, e.g., deformation speed, initial material and die temperatures, lubrication, and die geometry, must be modified, this can also be done on the computer before the dies are manufactured and processing equipment is tied up for physical die try-outs. As a result, the number of expensive trial-and-error type experiments and the manufacturing costs can be reduced and part quality can be controlled.

In order to model a deformation process, it is necessary to have at least three types of information:

a) The mechanics of metal flow, (velocities, strains, strain rates, temperatures). For this purpose, an FEM based code, such as ALPID, must be available, (ALPID, i.e. Analysis for Large Plastic Incremental Deformation was developed specifically for forging analysis at Battelle Columbus Laboratories).

b) The boundary conditions. (Friction, heat transfer at material die interface).

c) The material responce (constitutive equations and workability in function of temperature).

Figure 16 shows the distorted grid pattern in the quarter section of the disk at various reductions in height. It is worth noting that once the metal in the rim region of the disk touches the die surface, the gap between the die corner and the workpiece grows. This behavior in metal flow did not change significantly with increasing friction. Further, the metal flow was nearly the same for both $\alpha+\beta$ and β preform microstructures. Thus, in order to obtain corner fill, the simulation was continued with trapped-dies (Figure 17). The corner fill is obtained within a few extra percent of reduction. However, the load required increases rather rapidly and as compared to open die forging, almost four times more force is required to nearly fill the die corner. These observations related to metal flow and forces were also made during the experiments.

In order to use the modeling of forging to control microstructure and thereby obtain desired properties, one must know the distribution of deformation parameters quantitatively. Therefore, the effective strain and effective strain rate distributions can be plotted. Thus, the program ALPID is capable of providing information required for control of microstructure/properties through processing.

The simulation of a disk forging with flash is shown in Figure 18 [6]. This figure illustrates the predicted deformation pattern in isothermal forging a titanium disk. The material near the flash or parting line requires greater degree of freedom to accommodate the complicated flow pattern near the flash zone. Therefore, two remeshing operations were necessary to achieve the final deformation shown in Figure 18. Through remeshing, (a) a new mesh is assigned to accommodate the complicated deformation pattern, and (b) the strain distribution is interpolated from the old on the new mesh. This remeshing procedure is extremely important for simulating practical forging operations where large deformations are present and the properties of the deforming material is determined by the amount of deformation imposed on the forged part.

Figure 19 shows the simulation of a rib-web type forging via ALPID (7). The material used in the simulation is Ti-6242 alloy and the forging was done isothermally at 900°C with a ram speed of 0.1 in/min. Figure 19 clearly shows the formation of a void which may lead to a lap type defect. ALPID simulation predicted that a lap did not develop in this particular process condition. This fact was also confirmed with experiments conducted using lead as a model material.

Recently ALPID has been expanded to simulate nonisothermal forging processes (8)..

CONCLUSIONS

Upset test have been used to asses the effects of microstructure, temperature, strain, strain rate and interface condition on the flow behaviour of Ti-6242 alloy. Based on observations of the evolving microstructure for the different thermomechanical processing and flow data, a model for plastic flow has been suggested. Based on this, a finite element model has been developed whicheven can predict microstructures in forgins for optimization of properties in forged Ti-6242 alloy.

ACKNOWLEDGEMENTS

The majority of the results, discussed in this paper, have been obtained at Battelle Columbus Laboratories under project conducted with U.S. Air Force funding. The authors gratefully acknowledge this support and thank their colleagues Drs. Oh and Semiatin of Battelle for supplying information used in preparing this paper. Part of the work which was done on microstructures at Middle East Technical University was supported by NATO under the AGARD Programme of Support to Turkey, Project T-4 (SMP/AST-02) Processing Science. This support is greatfully acknowledged.

REFERENCES

(1) Burte, H.M. and Gegel, H.L., "The Role of Process Modeling in the Future of Materials Science and Technology", Process Modelling, American Society for Metals Prak, Ohio 44073, 1980. p 1.

(2) Altan, T., Lahoti, G.D.,and Nagpal,V., "Systems Approach in Massive Forming and Application to Modeling of Forging Processes", J. Applied Metalworking, Vol. 1, 1979, p 1.

(3) Altan, T., Semiatin, S.L., and Lahoti, G.D., "Determination of Flow stress Data for Practical Metal Forming Analysis", Annals CIRP, Vol. 30, 1981, p 129

(4) Douglas, J. R., and Altan, T., "Flow Stress Determination for Metals at Forging Rates and Temperatures". ASME Transactions, J. Engr. for Industry, February 1975, p 66

(5) Semiatin, S. L., Lahoti, G. D., and Altan, T., "Determination and Analysis of Flow Stress Data for Ti-6242 at Hot Working Temperatures", Process Modeling: Fundamentals and Applications to metals

T. Altan, et al., ends., p 387, ASM, Metals Park, Ohio, 1980.

(6) Ficke, J. A., Oh, S. I., andMalas, J.: Analysis of Isothermal Forging a Titanium Disk With Flash Using ALPID. Proceedings of NAMRC XII, May 1984, p 166

(7) Wu, W. T., Oh, S. I., and Altan, T.: Investigation of Defect Formation in Rib Web Type Forging by ALPID. Proceedings of NAMRC XII, Michigan Tech. Univ. Houghton, MI, May 30, 1984, p 159

(8) Wu, W. T., and Oh, S.I;ALPID: A General Purpose FEM Code Simulation of Non-Isothermal Forming Processes. Proceedings of NAMRC XIII, Univ. of CA, Berkeley, May 1985, p 449

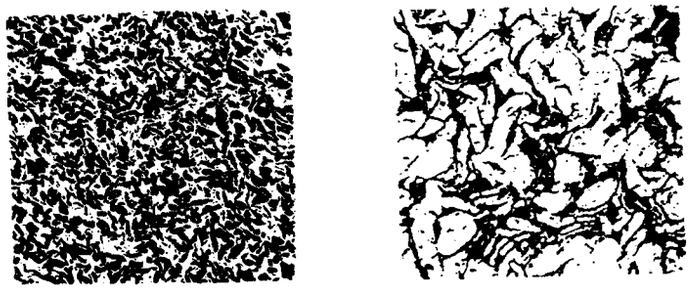

x280 x 1100

FIGURE 1. As received microstructure of Ti-6242

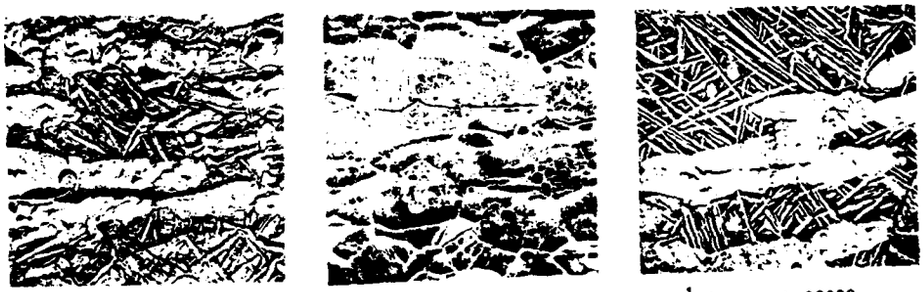

$\frac{1}{2}$ hours at 930°C 8 hours at 930°C $\frac{1}{2}$ hours at 950°C

8 hours at 950°C $\frac{1}{2}$ hours at 980°C 8 hours at 980°C

FIGURE 2. The microstructures of heat treated α + β alloy x 1100

8 hours at 1010°C

8 hours at 1040°C

FIGURE 3. The microstructure of heat treated β alloy x 1100

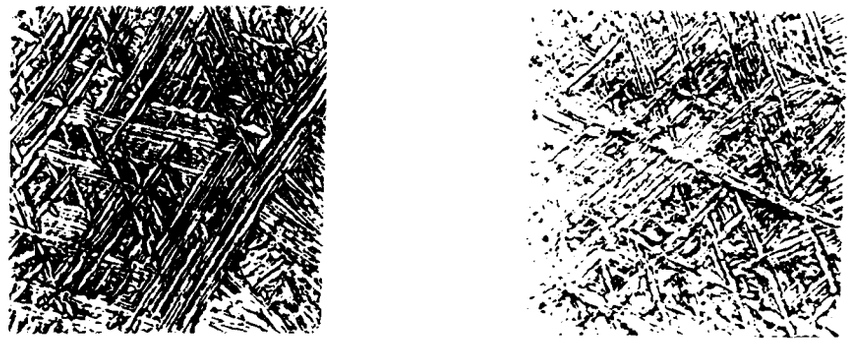

Deformed at 1010 °C

Deformed at 1040 °C

FIGURE 4. The microstructure of hot deformed α + β preform.
Deformed to ε = 0.7 x 1100

Deformed at 900 °C

Deformed at 980 °C

FIGURE 5. The microstructure of hot deformed β -preform.
Deformed to ε = 0.7 x 1100

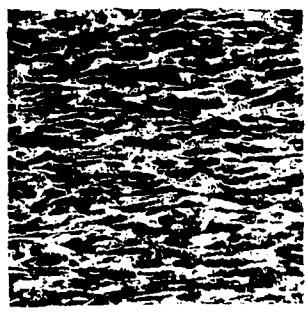

deformed at 900°C ×280
heat treatment 15 min

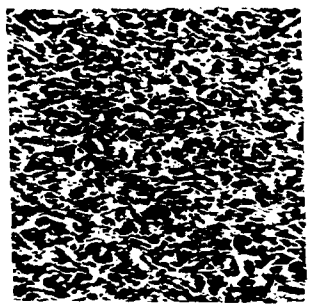

deformed at 930°C ×280
heat treatment 15 min

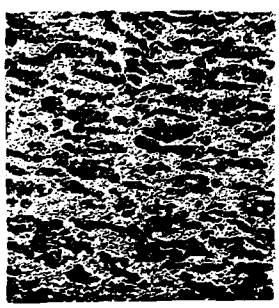

deformed at 980°C ×280
heat treatment 15 min

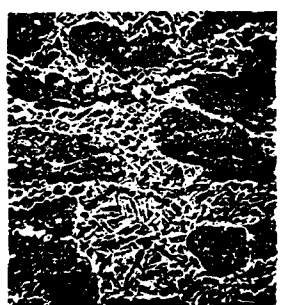

deformed at 980°C ×1100
heat treatment 15 min

deformed at 980°C ×1100
heat treatment 8 hours

FIGURE 6. The micro-structures of post deformation heat treatment at 900°C of α + β preform material for 15 min except last one which is 8 hours

heat treatment 15 min

heat treatment 30 min

heat treatment 75 min

heat treatment 8 hours

FIGURE 7. The microstructure of post-deformation heat treatment at 980°C of α+β preform materials deformed at 980°C.

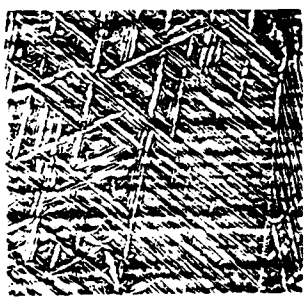

Heat treatment 15 min

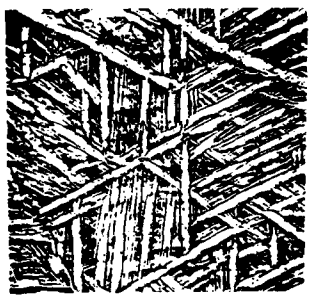

Heat treatment 30 min

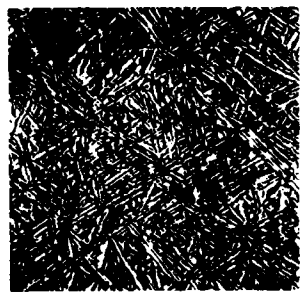

Heat treatment 8 hour

FIGURE 8. The microstructure of post-deformation heat treatment at 1040 of β - preform material.

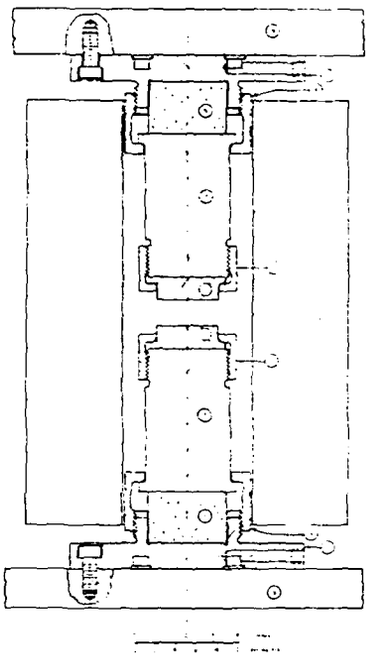

Figure 9 Hot-Isothermal Compression Test Fixture[12].

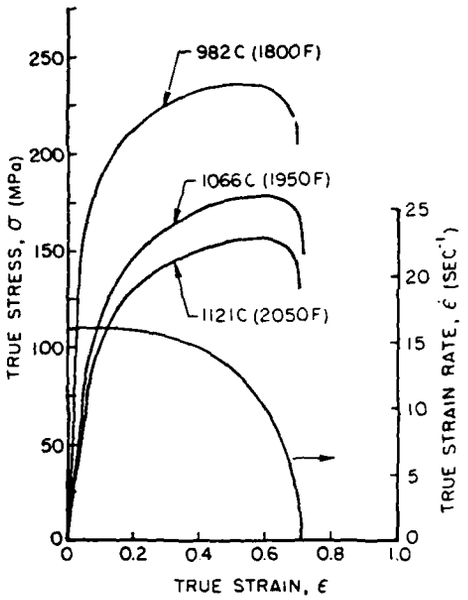

Figure 10(a) Example $\sigma - \varepsilon$ and $\dot{\varepsilon} - \varepsilon$ curves obtained from uniform compression tests conducted in a mechanical press.
(a) Material: Ti-6242, equiaxed alpha microstructure, initial test temperature = 913C.

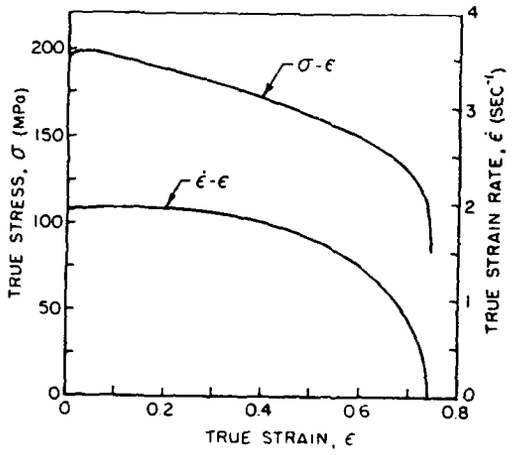

Figure 10(b) Example $\sigma - \varepsilon$ and $\dot{\varepsilon} - \varepsilon$ curves obtained from uniform compression tests conducted in a mechanical press.
(b) Material: 403 Stainless Steel, initial test temperatures = 982C, 1066C, 1121C.

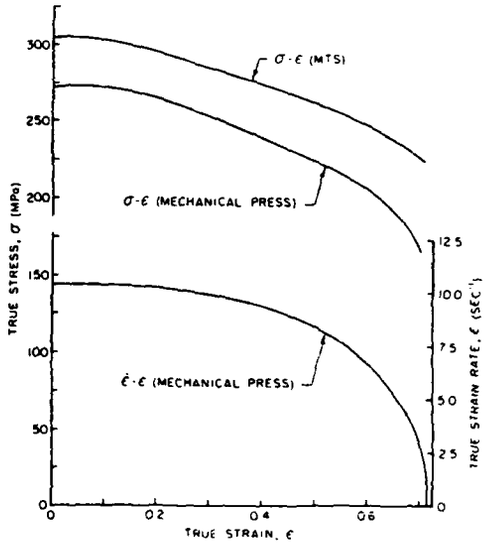

Figure 11 Comparison of stress-strain data obtained in a mechanical press and an MTS. Variation of strain rate with strain for mechanical press test is also shown.

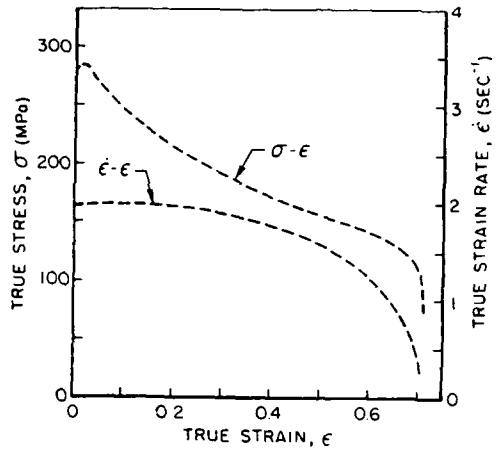

Figure 12 $\sigma - \dot{\varepsilon} - \varepsilon$ curves obtained from uniform compression tests conducted in mechanical press. (Material: Ti-6242, acicular alpha microstructure, initial test temperature = 913C).

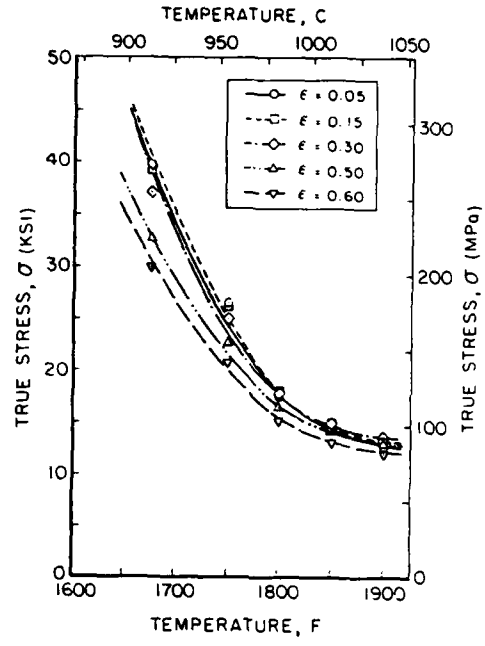

Figure 13 $\sigma - \varepsilon$ curve obtained from uniform compression tests conducted in a mechanical press. (Material: Ti-6242, equiaxed alpha microstructure; $\dot{\varepsilon} = 10$ sec^{-1})

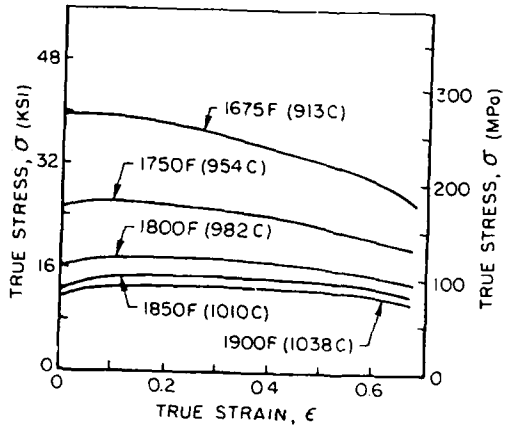

Figure 14 Flow stress data for Ti-6242 (equiaxed alpha microstructure) replotted to show stress as a function of temperature at different levels of strain ($\dot{\varepsilon} = 10$ sec^{-1})

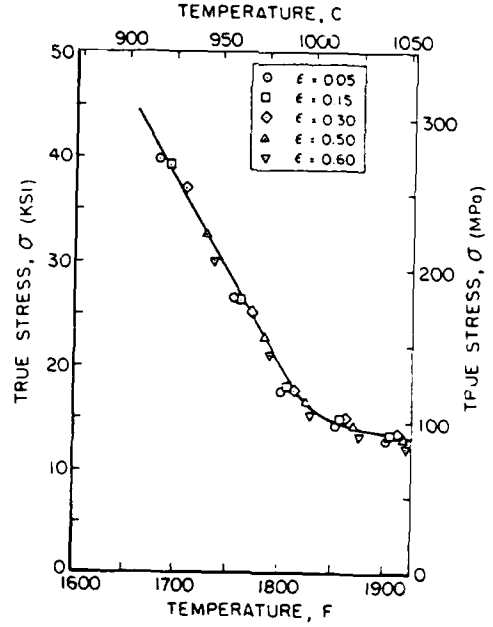

Figure 15 Flow stress data for Ti-6242 (equiaxed alpha microstructure) corrected for deformation heating effects ($\dot{\varepsilon} = 10$ sec^{-1})

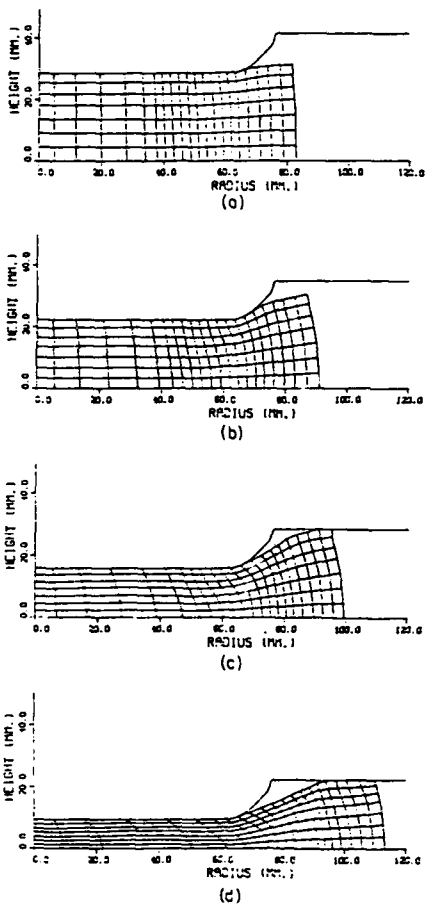

Figure 16 Predicted grid distortion for disk forging (Ti-6242-0.1Si, β-microstructure, m = 0.3, T = 900C) (a) 10% reduction in height, (b) 30%, (c) 50%, (d) 70%.

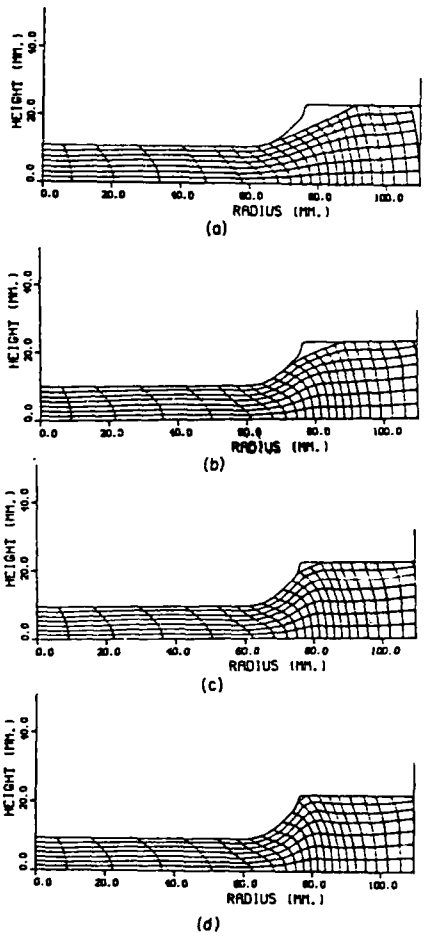

Figure 17 Grid distortion predicted for trapped die forging (Ti-6242-0.1Si, β-microstructure, m = 0.3, 900C) reduction: (a) 66%, (b) 69%, (c) 70%, (d) 70.25%.

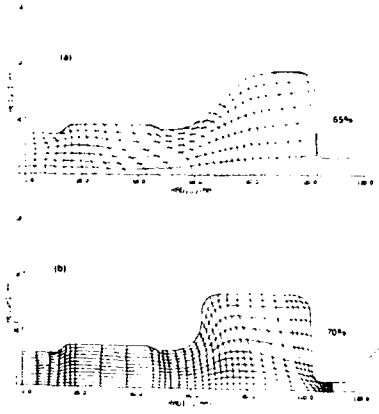

Figure 18 Grid Distortion in Forging a Ti Disk with Flash (a) Before First Remesh, and (b) At the End of Stroke (6).

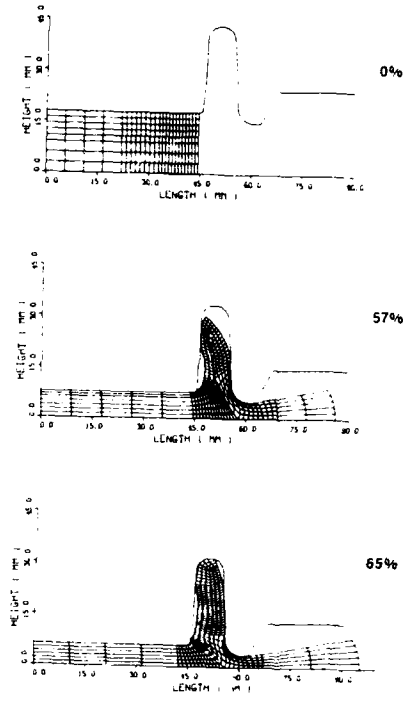

Figure 19 Metal Flow Simulation Via ALPID to Predict Potential Defect Formation in Isothermal Forging of Titanium Alloy (7).

PHYSICAL MODELING AND VISIOPLASTICITY STUDIES OF THE FORGING PROCESS

V. K. Jain
Mechanical Engineering Department
University of Dayton
Dayton, OH 45469

R. Srinivasan
Materials Science and Engineering
Wright State University
Dayton, OH 45435

SUMMARY

An analytical technique, which employs the approach of visioplasticity for evaluating large plastic strains such as those occurring in metalforming, is presented. The distortion of a quadrilateral element of a grid was tracked to compute strains during deformation. Here, two lines of a quadrilateral are used (length before and after deformation and direction cosines before deformation) to determine the true effective strain in the element. Although the method can be applied to any mode of deformation, its application to plane-strain deformation is considered. The method has been verified by application to basic cases of deformation such as uniaxial compression, tension, pure shear, and rotation of elements. Wedge testing was used for verification of the analytical results of a visco-plastic finite-element program ALPID which was developed to simulate metal flow in deformation processes such as forging and extrusion. Wedge-shaped specimens were machined from plates of 1100-F and 6061-T6 aluminum, and grids were engraved on the meridian plane by means of a CNC engraver. The specimens were annealed and compressed in a channel-shaped segmented die at room temperature. The undeformed and deformed grids were digitized, and true effective strains were computed and displayed as contour plots along with the ALPID-generated values. The results indicate that the strains predicted by ALPID are very near the experimental ones. Minor differences in the strain values are attributed to unavoidable experimental errors.

1. INTRODUCTION

The flow behavior of metals in deformation processes is characterized by the constitutive equations which relate the flow stress to strain, strain rate, and working temperature. Recently a method has been developed for modeling the flow of metals in metalforming processes using rigid visco-plastic finite-element (FEM) (1,2) analysis. This method predicts the deformation behavior at node points of each element by the application of variational principles and provides a solution using the initial and boundary conditions. The analysis is called ALPID (Analysis of Large Plastic Incremental Deformation). A number of assumptions were made to develop this model which could affect the degree of accuracy of the predicted results. It is necessary that the validity of such a theoretical model be verified through physical modeling techniques; this provides feedback which aids in the refinement of the model and demonstrates the accuracy of the predictions.

In the area of metalworking, two methods can be used to design experiments. The first is to simulate, as closely as possible, a production metalforming process, viz., extrusion or forging on a laboratory scale, and monitor the pertinent parameters such as force, temperature, and ram velocity. The data from such a test can be analyzed and compared with those predicted by an analytical model. The second approach is to devise a laboratory test which is faster, easier, and less expensive than a subscale production test but verifies the accuracy of the analytical model. These requirements are met by a test which is commonly used by the forging industry and known as the wedge test. The plane-strain deformation is studied by compressing a wedge specimen in a channel-shaped die and the three-dimensional deformation by compressing the specimen between a flat die and a punch.

This paper discusses the development and verification of a technique for experimentally determining strains in a two-dimensional deformation process. Here, classical equations of the theory of elasticity relating strains and displacement were used. The technique was later applied to validate the predictions of a visco-plastic finite-element program ALPID.

2. COMPUTATION OF STRAIN FROM DIMENSIONS OF DEFORMED AND UNDEFORMED GRID MESH

2.1 Literature Review

In order to analyze the metal flow in deformation processing, it is necessary to determine the distribution of the effective strain in the deformed body. The formulas defining these strains are derived in terms of the position of an element before and after deformation with reference to some coordinate system. Thus, the strains are computed by measuring the distortion of some geometrical pattern, viz., a grid mesh or an array of circles. The choice of pattern depends upon various factors such as the type

and accuracy of the information sought, the material, and the extent of the specimen deformation.

In most metalforming processes, the resultant deformation may not be homogeneous. Deformation in such cases, however, is assumed to be homogeneous since the deformed material can be divided into a number of small regions of homogeneous deformation. The most commonly used method for computing strains is called visioplasticity (3-6). In order to analyze a plane-strain or axisymmetric metal-deformation process using this method, a grid of points is placed in the plane of deformation. The grid is photographed after each step during an incremental deformation. From the change in position of the grid nodes and the deformation time, the velocity of the grid points can be estimated. In the case of two-dimensional deformation, if V is the velocity of a node point and u and v its components in the coordinate directions, the strain-rate variation with position can be calculated as follows:

$$\dot{\epsilon}_x = \frac{\partial u}{\partial x}, \quad \dot{\epsilon}_y = \frac{\partial v}{\partial y}, \quad \text{and} \quad \dot{\epsilon}_{xy} = \frac{\partial u}{\partial y} + \frac{\partial v}{\partial x} \tag{1}$$

Childs (7) applied this method to the analysis of the flow of metal in hot extrusion of mild steel. A grid was applied on the meridian plane of a cylindrical billet before extrusion. The process was interrupted, and the changes in the grid pattern from the undeformed state to the deformed state (in the partially extruded billet) were used to characterize the deformation. In general, the method is tedious, and the establishment of a good reference coordinate system is difficult (8).

Sowerby, et al. (9), recently proposed a method of characterizing deformation in terms of the principal stretches of a grid. The stretch of a line element during deformation is the ratio of its final length to its initial length, and the principal stretch directions are those in which line elements undergo no rotation during deformation. For an orthogonal grid (Fig. 1), the principal stretches and stretch directions are

$$\lambda_{11}^2 = \frac{\lambda_a^2 + \lambda_b^2}{2} + \frac{\lambda_a^2 - \lambda_b^2}{2} \frac{1}{\cos 2\theta} \tag{2a}$$

$$\lambda_{22}^2 = \frac{\lambda_a^2 + \lambda_b^2}{2} - \frac{\lambda_a^2 - \lambda_b^2}{2} \frac{1}{\cos 2\theta} \tag{2b}$$

$$\tan 2\theta = - \frac{2\lambda_a \lambda_b \cos\phi}{\lambda_a^2 - \lambda_b^2} \tag{3}$$

where $\lambda_a = a'/a$,

$\lambda_b = b'/b$,

ϕ = angle between the deformed pair of grid lines,

θ = angle between the principal direction 1 and the x axis,

a,b = lengths of the undeformed line elements OA and OC, respectively, and

a',b' = lengths of the deformed line elements OA' and OC', respectively.

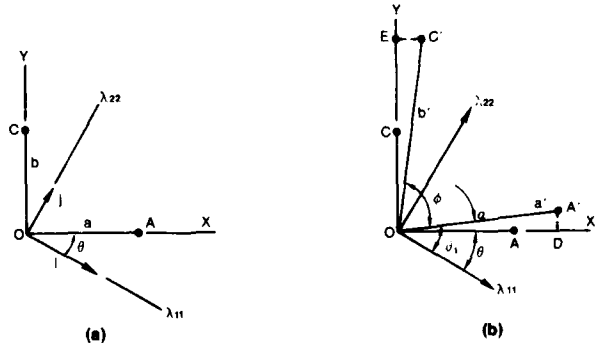

Figure 1 - (a) Undeformed Orthogonal Line Elements;
(b) Deformed State Following Homogeneous Strain.

For a nonorthogonal grid (Fig. 2), the principal stretches are given by

$$\lambda_{11}^2,\ \lambda_{22}^2 = \frac{\frac{1}{2}\left[(\lambda_a^2 + \lambda_b^2)\cos 2\theta \pm (\lambda_a^2 - \lambda_b^2)\right] - \lambda_a^2 \cos\xi \cos(\xi + 2\theta)}{\sin\xi \sin(\xi + 2\theta)} \tag{4}$$

$$\cos\phi = \frac{1}{\lambda_a \lambda_b}\left(\lambda_{11}^2 \cos\theta \cos\gamma + \lambda_{22}^2 \sin\theta \sin\gamma\right)$$

$$\cot(\xi + 2\theta) = \frac{2\lambda_a\lambda_b \cos\phi - (\lambda_a + \lambda_b)\cos\xi}{\sin\xi(\lambda_a^2 - \lambda_b^2)}$$

where ξ is the angle between line elements in the undeformed grid.

This method is recommended mainly for orthogonal grids (10) and requires that the angles ϕ and ξ be calculated at each grid point.

2.2 Theoretical Analysis

Consider a small element of a body, a corner of which is located at (x,y,z) and has lengths δx, δy, and δz parallel to the respective coordinate directions in the undeformed state (Fig. 3). During a deformation in which displacements in the body are given by u(x,y,z), v(x,y,z), and w(x,y,z), a line element of length δr (such as that represented by the diagonal AB of the element) deforms to length $\delta r'$ and position A'B'. Ford and

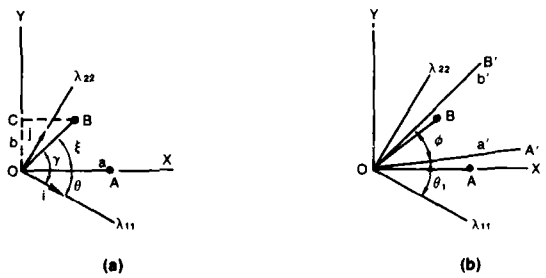

Figure 2 - (a) Undeformed Nonorthogonal Line Elements;
(b) Deformed State Following Homogeneous Strain.

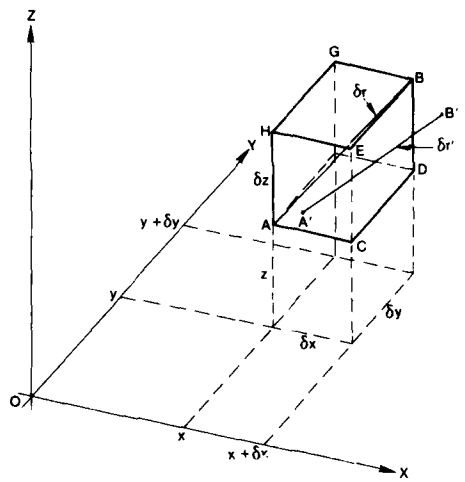

Figure 3 - Deformation of Line Element Due to Normal and Shear Strains (Ref. 11).

Alexander (11) showed that the engineering strain in AB (defined as $\delta r'/\delta r - 1$) is given by

$$\left(\frac{\delta r'}{\delta r}\right)^2 = (1 + 2e_{xx})\, \ell_r^2 + (1 + 2e_{yy})\, m_r^2 + (1 + 2e_{zz})\, n_r^2 + 2e_{xy}\, \ell_r\, m_r + 2e_{yz}\, m_r\, n_r + 2e_{zx}\, n_r\, \ell_r \tag{5}$$

where ℓ_r, m_r, and n_r are the direction cosine of the line element AB,

$$e_{xx} = \frac{\partial u}{\partial x} + \frac{1}{2}\left[\left(\frac{\partial u}{\partial x}\right)^2 + \left(\frac{\partial v}{\partial x}\right)^2 + \left(\frac{\partial w}{\partial x}\right)^2\right] \tag{6}$$

and

$$e_{xy} = \frac{\partial u}{\partial y} + \frac{\partial v}{\partial x} + \frac{\partial u}{\partial x}\frac{\partial u}{\partial y} + \frac{\partial v}{\partial x}\frac{\partial v}{\partial y} + \frac{\partial w}{\partial x}\frac{\partial w}{\partial y} \tag{7}$$

Other terms in Eq. (5) are defined in a similar manner. The above equation is general in that it can be applied to the analysis of two- and three-dimensional deformation. Here it will be used for the case of plane-strain deformation, where the displacement in the z direction is zero and Eq. (5) for this case reduces to

$$\left(\frac{\delta r'}{\delta r}\right)^2 = (1 + 2e_{xx})\, \ell_r^2 + (1 + 2e_{yy})\, m_r^2 + 2e_{xy}\, \ell_r\, m_r \tag{8}$$

Consider an orthogonal grid OABC deformed to O'A'B'C' (Fig. 4). Let ℓ_1, m_1 and ℓ_2, m_2 be the direction cosines of two line elements OB and OA, respectively. Using Eq. (8) on the line OB yields

$$\left(\frac{O'B'}{OB}\right)^2 = (1 + 2e_{xx})\,\ell_1^2 + (1 + 2e_{yy})\,m_1^2 + 2e_{xy}\,\ell_1\,m_1$$

or

$$\left(\frac{O'B'}{OB}\right)^2 = 1 + 2\ell_1^2\, e_{xx} + 2m_1^2\, e_{yy} + 2e_{xy}\,\ell_1\,m_1 \tag{9}$$

Similarly, for the line OA,

$$\left(\frac{O'A'}{OA}\right)^2 = 1 + 2\ell_2^2\, e_{xx} + 2m_2^2\, e_{yy} + 2e_{xy}\,\ell_2\,m_2 \tag{10}$$

For plane-strain plastic deformation, if ε_x and ε_y are the true strains in the x and y directions, respectively, then constancy of volume gives

$$\varepsilon_x = - \varepsilon_y \tag{11}$$

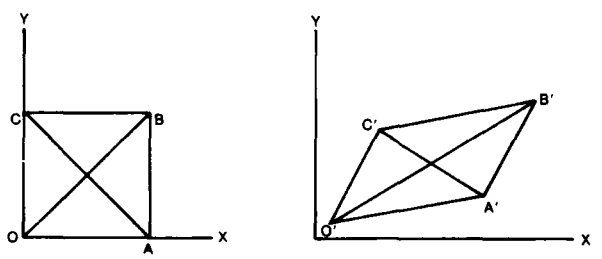

(a) (b)

Figure 4 - (a) Undeformed Orthogonal Grid;
(b) Deformed Grid Following Homogeneous Strain.

But $$\varepsilon_x = \ln(1 + e_x)$$

and $$\varepsilon_y = \ln(1 + e_y) \tag{12}$$

where e_x and e_y are the engineering strains related to e_{xx} and e_{yy}, respectively, by

$$e_x = \sqrt{1 + 2e_{xx}} - 1$$

and

$$e_y = \sqrt{1 + 2e_{yy}} - 1 \tag{13}$$

which yields

$$e_{yy} = - \frac{e_{xx}}{1 + 2e_{xx}} \tag{14}$$

Substitution of Eq. (14) into Eqs. (9) and (10) yields

$$\left(\frac{O'B'}{OB}\right)^2 = 1 + 2\ell_1^2 e_{xx} - 2m_1^2 \frac{e_{xx}}{1 + 2e_{xx}} + 2e_{xy} \ell_1 m_1 \tag{15}$$

$$\left(\frac{O'A'}{OA}\right)^2 = 1 + 2\ell_2^2 e_{xx} - 2m_2^2 \frac{e_{xx}}{1 + 2e_{xx}} + 2e_{xy} \ell_2 m_2 \tag{16}$$

The set of simultaneous equations, (15) and (16), results in a quadratic equation

$$A' e_{xx}^2 + B' e_{xx} + D' = 0 \tag{17}$$

where

$$A' = A_1C_2 - A_2C_1$$

$$B' = B_1C_2 - B_2C_1$$

$$D' = D_1C_2 - D_2C_1$$

$$A_1 = 4\ell_1^2; \quad A_2 = 4\ell_2^2$$

$$B_1 = 2\left[1 - \left(\frac{O'B'}{OB}\right)^2 + \ell_1^2 - m_1^2\right]; \quad B_2 = 2\left[1 - \left(\frac{O'A'}{OA}\right) + \ell_2^2 - m_2^2\right]$$

$$C_1 = 2\ell_1 m_1; \quad C_2 = 2\ell_2 m_2$$

$$D_1 = 1 - \left(\frac{O'B'}{OB}\right)^2 \quad ; \quad D_2 = 1 - \left(\frac{O'A'}{OA}\right)^2$$

Shear strain e_{xy} can be obtained by using either of the following modified forms of Eqs. (15) and (16):

$$A_1 e_{xx}^2 + B_1 e_{xx} + C_1(1 + 2e_{xx}) e_{xy} + D_1 = 0 \tag{18}$$

$$A_2 e_{xx}^2 + B_2 e_{xx} + C_2(1 + 2e_{xx}) e_{xy} + D_2 = 0 \tag{19}$$

The true effective and principal strains are given as:

$$\bar{\varepsilon} = \frac{2}{3} \sqrt{3\varepsilon_x^2 + \frac{3}{4} e_{xy}^2} \tag{20}$$

$$e_{1,2} = \frac{e_x + e_y}{2} \pm \sqrt{\left(\frac{e_x - e_y}{2}\right)^2 + \frac{1}{4}(e_{xy})^2} \tag{21}$$

$$\varepsilon_{1,2} = \ln(1 + e_{1,2}) \tag{22}$$

2.3 Application to the Cases of Basic Deformation

The equations developed above are applied to the following cases of basic deformation to demonstrate the strength and accuracy of the method:

(1) Simple compression of a square element
(2) Simple compression of a rectangular element
(3) Simple tension of a rectangular element
(4) Pure shear of a square element
(5) Pure rotation of a square element

In each case a representative orthogonal grid element is subjected to a known amount of homogeneous deformation, as summarized in Fig. 5. The corresponding strains are then calculated using the coordinates of the corners of the quadrilateral before and after the deformation, following the procedure outlined above. In each case two pairs (the two diagonals and a diagonal and a side of the element) of line elements are used to examine the effect of the choice of the pair on the strain values.

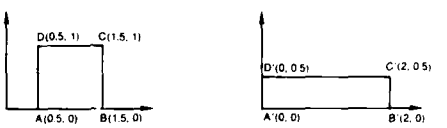

1. COMPRESSION: SQUARE TO RECTANGLE

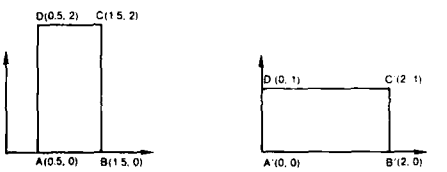

2. COMPRESSION: RECTANGLE TO RECTANGLE OF SAME ASPECT RATIO

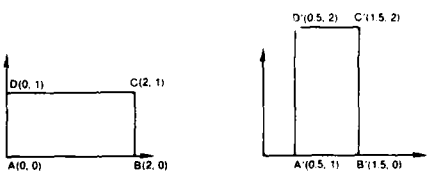

3. TENSION: RECTANGLE TO RECTANGLE

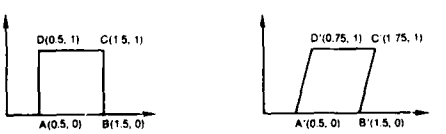

4. PURE SHEAR

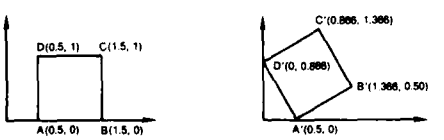

5. ROTATION OF ELEMENT

Figure 5 - Orthogonal Elements Subjected to Various Types of Simple Deformation.

Table I shows the calculated values of strains for the five cases of simple deformation (Fig. 5) using two pairs of line segments in the rectangular elements. The choice of the two diagonals, AC and BD, is more appealing, but the results obtained using this pair of line segments are not always correct. In general, two roots exist for Eq. (17), and one of the roots will be inadmissible. A computer program which uses only one of the roots may yield inaccurate results under certain circumstances; Example 2 (Case 4) in Table I is one such situation where a tall rectangle is compressed to a short rectangle having the same aspect ratio. Here, if the two diagonals are used, one of the roots will be zero and the other will provide the strain value. It may be difficult to decide which root should be used for further calculations. The other choice of line segments, diagonal AC and side AB, yields correct results in all cases. In fact, the strain being calculated is the strain in the triangle ABC. Thus, the analysis can be applied to triangular grids as well as to the conventional rectangular ones. Since the calculated values of the strains in each case are consistent with the amount of deformation provided, the accuracy of the method is verified.

Table I. Computed Values of True-Strain Components Using Different Pairs of Line Segments

Case	Line Segments	ϵ_x	ϵ_y	e_{xy}	$\bar{\epsilon}$
1a	AC, BD	0.6931	-0.6931	0	0.8002
1b	AC, AB	0.6931	-0.6931	0	0.8002
2a	AC, BD	0.6931	-0.6931	0	0.8002
2b	AC, AB	0.6931	-0.6931	0	0.8002
3a	AC, BD	-0.6931	0.6931	0	0.8002
3b	AC, AB	-0.6931	0.6931	0	0.8002
4a	AC, BD	0	0	0.25	0.144
4b	AC, AB	0	0	0.25	0.144
5a	AC, BD	0	0	0	0
5b	AC, AB	0	0	0	0

3 EXPERIMENTAL PROCEDURE

3.1 Development of Grid Mesh

Deformation in a body is characterized by the distribution of strain. The grid-deformation method of strain measurement involves applying a grid mesh on the surface or on an interior plane of a specimen. The grid may be defined as an array of lines or dots which indicate points in the specimen and is usually rectangular with dots or lines being repeated in two perpendicular directions. The distance between the discrete nodes on the grid before and after the deformation is measured, and the resulting data are analyzed. The grid method is an optical technique. Sighting of the grid is accomplished with or without photography. The accuray of the grid depends on the precision with which sighting can be carried out. Accuracy in the measurement of the grid does not lie in the precision of the measuring instrument but in the ability of the investigator to view the points clearly. If a dot or point (obtained by the intersection of two grid lines) is much larger than the resolution of the instrument, the resulting measurement will be inaccurate. The size of the point, therefore, plays an important role in the measuring process. Furthermore, a point under consideration should be clearly visible with the least amount of distortion before and after deformation has occurred.

A number of methods were used in attempts to apply a suitable grid pattern to the wedge-shaped specimens. These included photochemical etching and engraving techniques. The latter was accomplished by means of a CNC engraver and found to be accurate and appropriate for the case of interest here. A typical wedge-shaped specimen with engraved grid lines is shown in Fig. 6.

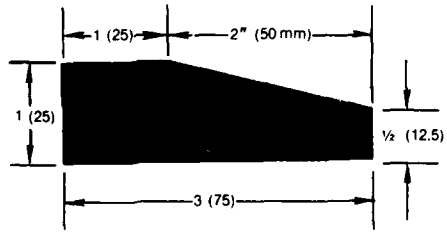

Figure 6 - Undeformed Wedge Specimen with Grids Engraved on Meridian Plane.

3.2 Segmented Die Design

In order to analyze the two-dimensional flow of metals and verify the ALPID code for complex deformation, wedge-shaped specimens (Fig. 6) with grids engraved on the meridian plane were compressed such that a range of strains varying from zero to 0.75 was obtained. Initially, a one-piece channel-shaped die with a punch was designed and fabricated for a 200-kip (0.89-MN) MTS testing machine. An aluminum specimen was compressed using this die. The compressed specimen could not be ejected undamaged from the die. The concept of segmented dies was, therefore, developed for convenient ejection of the specimens. These dies consist of several segments which are assembled to provide the same die cavity as that of the one-piece die and can be dismantled, after testing, to eject the workpiece. The major advantage of segmented dies is that through the use of different inserts, a new family of parts can be forged. The major drawback of these dies is that metal tends to extrude through the various joints of the die during deformation processing. The segments must, therefore, be held together with a pressure greater than the flow stress of the metal during deformation but be easy to disassemble after forging is complete.

The segmented die and punch designed and fabricated for this case (plane-strain wedge test) are shown in Figs. 7 and 8. The die has three main components, viz., the die base, two side plates which are fastened to the base by six 1/2-in.-diam. (12.5-mm) SAE Grade-8 bolts, and two restrainers (Fig. 7) bolted at the top of the side plates to minimize their expansion and, thus, metal extrusion through the joints during compression. The side plates are piloted with respect to the base by two 3/8-in. (9-mm) diam dowel pins. All components were machined from a 10-in.-diam. (250-mm) H-13 tool-steel bar, hardened to Rc 45-50 and ground to a surface finish of 16-μin. (0.4-μm) rms. The die and punch were coated with black oxide to prevent rusting, assembled as shown in Fig. 8, mounted on the MTS machine, and aligned in preparation for wedge testing.

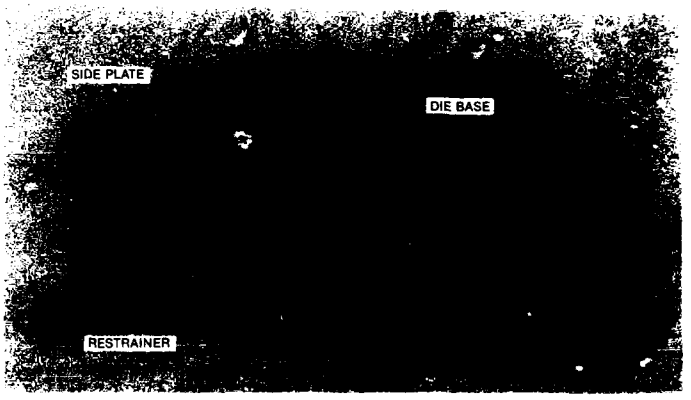

Figure 7 - Segmented-Die Components for Plane-Strain Wedge Test.

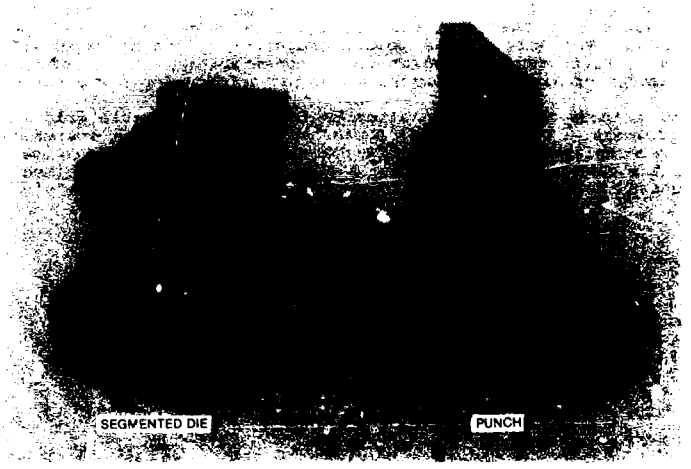

Figure 8 - Segmented Die and Punch for Two-Dimensional Wedge Test.

3.3 Compression of Wedge Specimens

In order to verify ALPID for a variety of materials and deformation spectra, specimens were machined from 1100-F and 6061-T6 aluminum. The specimens were then annealed. One 1100-O aluminum specimen was compressed to a deformation of 54.5% and three 6061-O aluminum specimens were compressed to height reductions of 14, 32, and 40% for this study.

Prior to actual compression of the wedge specimen, the punch, die, and specimen surfaces were coated with a graphite and molybdenum-disulfide-base spray lubricant to minimize friction along the sliding interfaces. The specimen was then mounted in the die, and the die segments were fastened together by means of the six bolts and restrainers. The duration of the test was determined by the extent of deformation, typically 250 sec. for a 50% reduction in height [0.5-in. (12.5-mm) ram displacement].

3.4 Digitizing Deformed and Undeformed Grids

The deformed specimens were cleaned with soap and methanol, to remove the thin film of lubricant, and then photographed. Due to the compression of the specimens, the horizontal grid lines became thin and the vertical ones, thick. The thin lines could not be effectively resolved by the camera due to reflection of light from the shiny surface of the aluminum specimen. The specimen surface was, therefore, coated with carbon black in order to print the deformed grid on 16 × 20 in. (400 × 500 mm) photographic paper for digitizing. The digitizing of deformed and undeformed grids, i.e., determination of the coordinates of the node points, was accomplished using a Tektronix 4954 digitizing tablet and 4010 terminal. Of the two types of digitizing devices available, the mouse with crosshairs, which is more accurate, was chosen for this study. The digitized data for the deformed and undeformed specimens were stored as files in the Prime-850 computer. The files containing the deformed and undeformed digitized data were used with a computer program to obtain the effective strains at various nodes.

3.5 Software Development

The analysis of grids to compute strain variations on the meridian plane involved three steps: digitization of the undeformed and deformed grids, calculation of the effective strain, and display of the effective strain as contour plots. A program, DIGIPLT, was employed on the Prime-850 computer to determine nodal coordinates of the undeformed and deformed grids using a Tektronix terminal and a digitizing tablet. The accuracy of the digitizing devices, verified using the grids shown in Fig. 6, was found to be within 0.005 in. (0.125 mm).

An analysis program was developed for calculating true effective and various strains from measurements of a deformed and an undeformed grid quadrilateral. The digitized data were used to determine the direction cosines of the undeformed line segments and the ratios of the corresponding deformed to undeformed line segments of the grid quadrilaterals. The true-effective-strain values were then determined from the above parameters using Eqs. (12) - (20). These values were smoothed using the least-squares formulas for third-degree, five-point analysis and stored in a file for plotting the strain contour maps. The decision to use five-point analysis for smoothing the data was arbitrary.

4. RESULTS AND DISCUSSION

A number of compression tests using 1100-O and 6061-O aluminum specimens (wedge shaped) were performed to verify the ALPID code. Figure 9 is a plot of ram travel versus

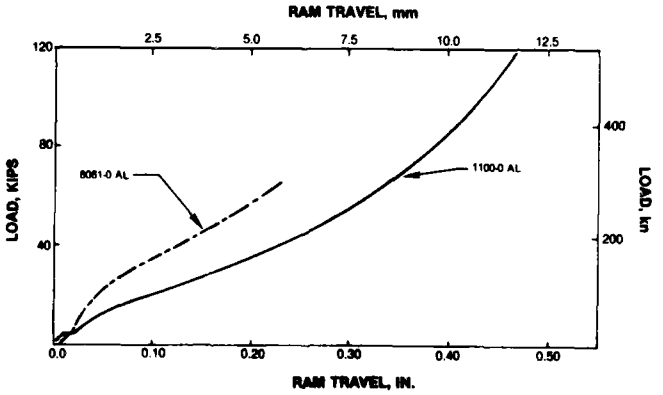

Figure 9 - Plot of Load vs. Ram Travel for Wedge Specimens Made from Two Materials.

compression load for the two materials. It can be seen that the load increases with the amount of deformation, but the rate of increase is larger for 6061 aluminum than for 1100 aluminum. The deformed grid meshes for the two materials for various amounts of deformation are shown in Figs. 10(a) - 13(a). The ALPID code was then used to generate the distorted grids [Figs. 10(b) - 13(b)] for both materials for the amount of deformation used in the experimental tests. It should be noted in Figs. 10 - 13 that the flow patterns as depicted by the two types of grid meshes are almost identical; the difference in flow behavior is attributed to the estimated value of the die-workpiece friction used to generate the ALPID simulations.

In order to quantify the verification of the ALPID code, the experimental and ALPID-generated values of effective true strain were used to plot the contour maps. Figures 14, 15, and 16 contain the maps for 14, 32, and 40% deformation of the 6061 aluminum specimens, respectively, and the maps for 1100-O aluminum are shown in Fig. 17. The ALPID-generated maps are very similar to the experimental ones.

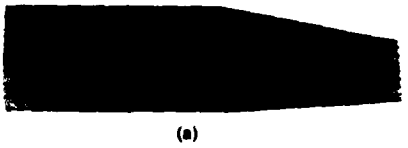

(a)

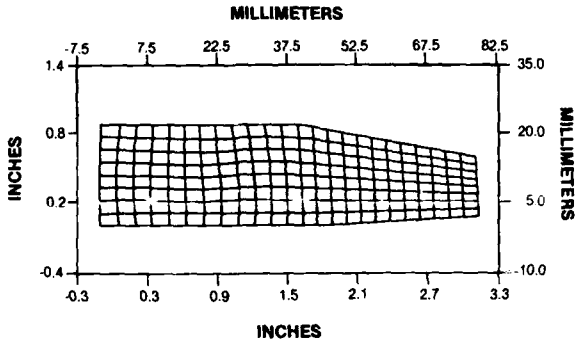

(b)

Figure 10 - Grid Patterns Showing Metal Flow in 6061-O Aluminum Wedge Specimen; Deformation 14%. (a) Experimental, (b) ALPID Simulation.

(a)

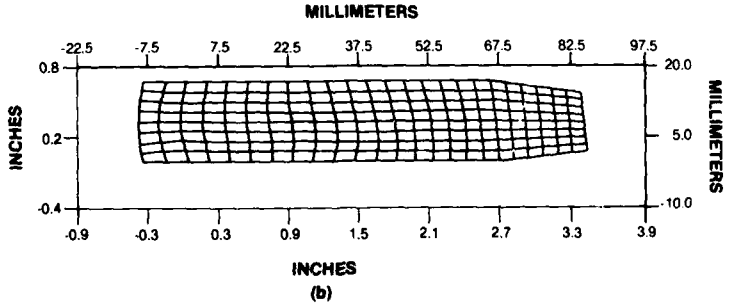

(b)

Figure 11 - Grid Patterns Showing Metal Flow in 6061-O Aluminum Wedge Specimen; Deformation 32%. (a) Experimental, (b) ALPID Simulation.

(a)

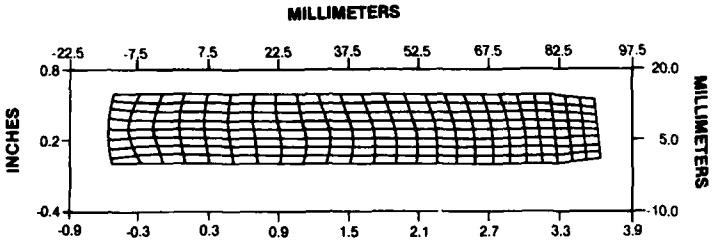

(b)

Figure 12 - Grid Patterns Showing Metal Flow in 6061-0 Aluminum Wedge Specimen; Deformation 40%. (a) Experimental, (b) ALPID Simulation.

(a)

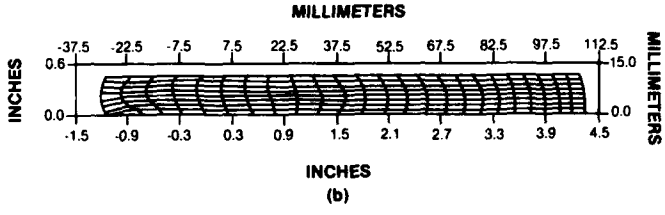

(b)

Figure 13 - Grid Patterns Showing Metal Flow in 1100-0 Aluminum Wedge Specimen; Deformation 54.5%. (a) Experimental, (b) ALPID Simulation.

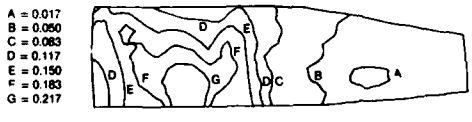

(a)

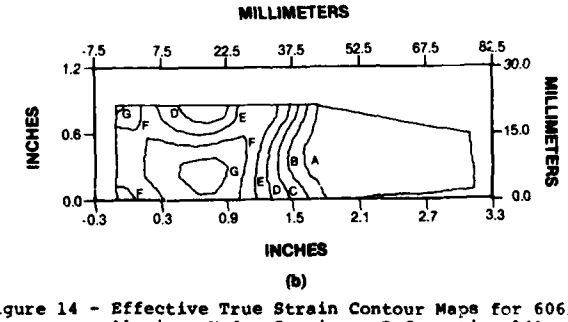

(b)

Figure 14 - Effective True Strain Contour Maps for 6061-0 Aluminum Wedge Specimen; Deformation 14%. (a) Experimental, (b) ALPID Simulation.

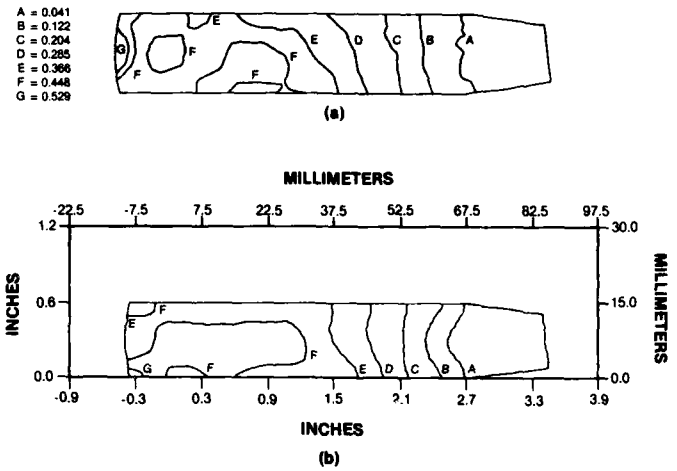

Figure 15 - Effective True Strain Contour Maps for 6061-0 Aluminum Wedge Specimen; Deformation 32%. (a) Experimental, (b) ALPID Simulation.

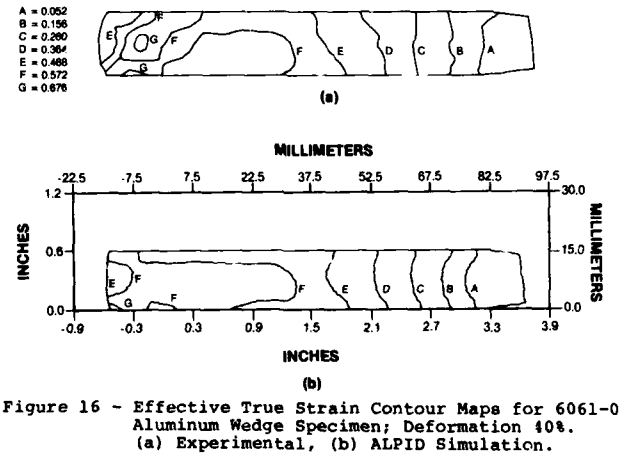

Figure 16 - Effective True Strain Contour Maps for 6061-0 Aluminum Wedge Specimen; Deformation 40%. (a) Experimental, (b) ALPID Simulation.

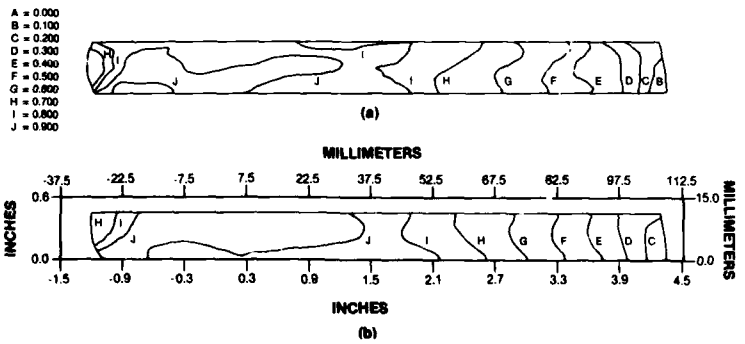

Figure 17 - Effective True Strain Contour Maps for 1100-0 Aluminum Wedge Specimen; Deformation 55%. (a) Experimental, (b) ALPID Simulation.

The reasons for the probable minor differences at some isolated locations in the experimental and ALPID-generated values of effective strains are listed below:

1. Error introduced in digitizing the deformed and undeformed grids on an electronic tablet.
2. Error in aligning the crosshairs of the cursor with the node points.
3. Error introduced in locating the grid node point precisely.
4. Distortion of the grid network during the printing process.
5. Undeformed grids not being identical on all specimens.
6. Imprecise constitutive equations for the materials under consideration.
7. Uncertainty in the estimation of the friction factor at the tool/specimen interfaces which may vary from specimen to specimen and with pressure and type of lubricant used.

5. CONCLUSIONS

The method for computing strains using the dimensions of a deformed and undeformed grid is valid. Any two line segments of a quaderilateral, preferably a diagonal and a side, can be used. This technique was applied to the verification of ALPID. It was found that the strain values predicted by ALPID were very near the experimental values and that the minor differences occurred due to a number of unavoidable experimental errors. The use of ALPID is, therefore, warranted for the modeling of metalworking processes and the design of forging dies.

REFERENCES

1. C. H. Lee and S. Kobayashi, "New Solutions to Rigid Plastic Deformation Problems Using a Matrix Method," Trans. ASME, J. Eng. Ind., 95 (1973) 865.
2. S. I. Oh, "Finite Element Analysis of Metal Forming Problems with Arbitrarily Shaped Dies," Int. J. Mech. Sci., 24 (1982) 479.
3. E. G. Thomsen, C. T. Yang, and S. Kobayashi, Plastic Deformation in Metal Processing, New York, NY, The Macmillan Company, 1965.
4. A. H. Shabaik and E. G. Thomsen, "A Theoretical Method for the Analysis of Metal-Working Problems," Trans. ASME, J. Eng. Ind., 90 (1968) 343.
5. A. H. Shabaik and E. G. Thomsen, "Computer Application to the Visioplasticity Method," Trans. ASME, J. Eng. Ind., 89 (1967) 339.
6. L. E. Farmer and P. L. B. Oxley, "A Computer-Aided Method for Calculating the Distributions of Strain Rate and Strain from an Experimental Flow Field," J. Strain Analysis, 11 (1976) 26.
7. T. H. C. Childs, "Metal Flow in the Hot Extrusion of Mild Steel," Met. Tech., 1 (1974) 305.
8. F. P. Chiang and P. Hareesh, "An Experimental Numerical Study of Cylindrical Extrusion Using Moiré Technique," in 13th NAMRC Proceedings, Dearborn, Michigan, NAMRIO, SME, 1985, p. 184.
9. R. Sowerby, E. Chu, and J. L. Duncan, "Determination of Large Strains in Metal Forming," J. Strain Analysis, 17 (1982) 95.
10. R. Sowerby and P. C. Chakravarti, "The Determination of the Equivalent Strain in Finite, Homogeneous Deformation Process," J. Strain Analysis, 18 (1983) 121.
11. H. Ford, Advanced Mechanics of Materials, New York, NY, Halsted Press, 1977.

ACKNOWLEDGEMENTS

The authors would like to thank the Air Force Wright Aeronautical Laboratories, Materials Laboratory, at Wright-Patterson Air Force Base (USA) for providing the support necessary to carry out this research. Thanks are also due to Mrs. M. Whitaker of Systems Research Laboratories for editorial assistance and preparation of the manuscript.

SUPERPLASTIC BEHAVIOUR OF SOME Ti-6Al-4V ALLOYS INVESTIGATED BY TORSION TESTING

Y. COMBRES, Ch. LEVAILLANT and F. MONTHEILLET*
Ecole Nationale Supérieure des Mines de Paris
CEMEF, Sophia-Antipolis
06565 VALBONNE Cedex FRANCE
* Ecole Nationale Supérieure des Mines de Saint-Etienne
Département Matériaux,
158 cours Fauriel
42023 SAINT-ETIENNE Cedex FRANCE

SUMMARY

Following the first demonstration of superplasticity in titanium alloys by LEE and BACKOFFEN in 1967 [1], increasing interest has been paid in technologies whereby superplastic forming of these alloys may be achieved. Numerous benefits from this process have been until now indicated including reduced costs, improved structural performances and large weight reductions. In fact, few metal working developments offer the opportunity of such wide-ranging implications in structural design as superplastic forming (SPF) combined or not with diffusion bounding (SPF/DB) to the aerospace industry. Because of the ability to form large complex structures, structure design methods are strongly modified.

While the potential advantages of these processes are impressive, it is nonetheless obvious that they are "high-tech" processes. Consequently, they require a great investment in the understanding of material and process interaction to achieve repeated success in their application. Obviously, it is well established now that, in SPF materials, slight variations of forming parameters can readily lead to either a success or failure for a given component. This fact promotes increased research in this area. These studies continue to address a range of titanium alloys but Ti-6Al-4V alloy has received the major part of the attention, at least in France. It has been widely used in the aerospace industry, and found to exhibit excellent superplastic properties in the conventionaly produced routes.

However, several microstructural features which can influence the superplasticity of this alloy can be found, due to variations from one heat to another. As an evidence of this, the work performed by PATUN and HAMILTON [2] clearly established that not only the average grain size $\bar{D}$ but also phase percentage, grain aspect ratio and grain size distribution have to be taken into account. The work done at the CEMEF since the last past 5 years was to compare different (from a microstructural point of view) Ti-6Al-4V alloys [3-7] and to set down their flow rules for further implementation in computer aided forming process design. Experiments were carried out on a torsion device. This technique for the SPF materials study is unusual compared with the large amount of works using tension and compression tests. Nevertheless, torsion testing is particularily well adapted to the simulation of forming processes such as rolling or forging. Finally, the present study is the complementary part of the modelling of isothermal forging or isothermal superplastic bulging carried out in our laboratory [8,9].

1. INTRODUCTION

Isothermal forging of Ti-6Al-4V alloy is now more and more used to form components encountered in aeronautic industry, not only for structural parts [10,11] but also for some engine components such as turbine discs. This process takes advantages from superplastic behaviour exhibited by the alloy in the 900-950 °C temperature and 10^{-3}-10^{-1} s^{-1} strain rate ranges. Such a behaviour leads to good formability which allows the use of complex shaped matrix and consequently near to the net shape forging in one operation. Nevertheless, very low forming strain rates usually lead to some problems : apart the low productivity, this process requires heated tools during all the operation (Hot Die Forging) and also an efficient protection against oxydation. Optimum SPF conditions (temperature, strain rate and initial microstructure) must be determined with accuracy.

Among the different ways to produce stock bars for isothermal forging, the most classic one is the ingot route (I.R.) [12,13]. The ingot is heavily rolled or extruded in the $\alpha+\beta$ range. High strains are achieved and microstructure is refined. Further thermal treatments are required to reach a fully recovered microstructure characterized by fine grains with a low dislocation density. This route produces flat parts or bars which can be hot die forged. Another way should be powder metallurgy (PM). Consolidation of powder using hot isostatic pressing (HIP) can lead to a fully dense material with low porosity density. It may also be produced close to the final shape parts. Sometimes, SPF should be done just after sintering for details that should not have been achieved by HIP and may avoid some further machining. Development of such a route needs prior investigation in order to know wether fully dense parts may exhibit superplastic properties.

In the present paper, the different routes are examined. Experiments are carried out in the same strain rate and temperature ranges so that comparison can be made. After describing the experimental procedure, the rheology is discussed in terms of stress-strain curves and strain rate sensitivity exponent. Microstructural evolutions are then compared and their interaction with rheology is underlined.

2. METALLURGY OF THE STUDIED ALLOYS

2.1. General characteristics

The Ti-6Al-4V alloy exhibits an α+β structure at room temperature. This is mainly due to the presence of vanadium which stabilizes the β phase at this temperature. The α phase crystallizes in a H.C.P. system with a ratio c/a of 1.587 which is lower than the theoretical value (1.63) and allows 5 slip systems instead of 1. This may explain the relative good ductility at this temperature. The α phase is either acicular or globular. Around 980 °C, the transformation α+β→β takes place. The β phase crystallizes in a B.C.C. system and when rapidly quenched, leads to an α' phase through a martensitic transformation. α' is more brittle than α and always exhibits a very thin needle structure.

The thermomechanical processes which have led to the three studied microstructures are presented below.

2.2. The equiaxed structure

The material was provided by Avions Marcel Dassault SA. Its chemical composition is given in table 1.

Al wt %	V wt %	C	Fe wt %	N_2	O_2	H_2
6.13	4.61	-	.32	-	-	-

Table 1

This material was prepared by the ingot route. After heavy straining in the α+β temperature range, rolled plates were subjected to thermal treatment. The subsequent microstructure exhibits a very fine average α grain size at room temperature of about 5 μm (figure 1). Such a fine structure is known to lead to superplastic behaviour [1,12,13]. It is labelled in the following : fine microstructure (FM).

2.3. The two acicular structures due to P.M.

The Ti-6Al-4V alloy was elaborated by CEZUS. Its chemical composition and mechanical properties are given in table 2.

Composition	Al wt %	V wt %	C ppm	Fe ppm	N_2 ppm	O_2 ppm	H_2 ppm
	6.17	3.95	210	1300	100	1650	13
Mechanical Properties	R(MPa)	R 0.2 (MPa)	Elongation (%)			Σ i	Hb Δ
	1033	961	16			462	321

Table 2

Powder was obtained by atomization under vacuum by the Centre d'Etudes Nucléaires de Grenoble, with the following conditions :

Pressure : 1.33 to 4 x 10^{-2} Pa
Accelerating voltage : 21.0 to 21.6 kV
Current load : .96 to .98 A
Screen diameter : 1.5 m

The particle size was included in the 100-630 μm range. A half part of the powder was annealed 5 hours at 1080 °C (i.e. above the β transus) in order to homogeneize chemical composition and obtain a change in the morphology of the sintered alloy. The specimens were machined from billets obtained by HIP with the following conditions : 950 °C - 4 hours - 10^8 Pa - inert atmosphere (Argon). Figures 2 and 3 show the corresponding microstructures. The first one, referred to as raw microstructure (RM), consists in fine acicular α phase with a grain aspect ratio (G.A.R.) of 9 (figure 2). The other one, labelled annealed microstructure (AM) consists in coarser lamellar α with a G.A.R. of 7.5 (figure 3). Such acicular morphologies are rather unusual for superplasticity (compare with figure 1).

According to the Ti-Al phase diagram, FM, RM and AM contain 80 % of α phase at room temperature. This percentage is far less important at elevated temperatures.

3. EXPERIMENTAL PROCEDURE

3.1. Torsion testing

A cylinder (radius R, length L) is submitted to a revolution rate $\dot{N}$. One head of the sample is fixed. For a number of revolutions N, a torque Γ is measured. The classical analysis of torsion testing [14] gives the strain rate $\dot{\bar{\varepsilon}}$ at the periphery (r=R).

- Figure 1 -

Micrograph showing the as received microstructure for the Ti-6Al-4V alloy usually used for SPF and labelled FM.
Initial grain size: 5 µm

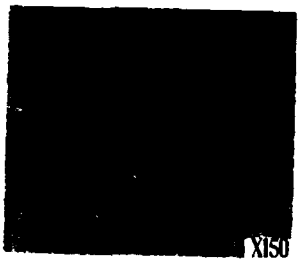

- Figure 2 -

Micrograph showing the as received acicular microstructure after PM+HIP'ing. Note the fine α needles. GAR = 9.
Labelled RM.

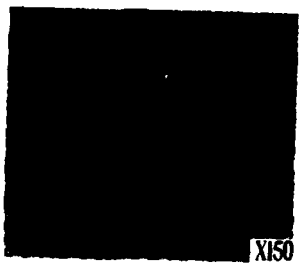

- Figure 3 -

Micrograph showing the influence of powder annealing. β grains coarsen whereas GAR of α needles decrease (GAR = 7.5).
Labelled AM.

$$\dot{\bar{\varepsilon}} = \frac{2\pi\dot{N}}{\sqrt{3}L} R \qquad (1)$$

and the equivalent strain at the outer radius :

$$\bar{\varepsilon} = \frac{2\pi N}{\sqrt{3}L} R \qquad (2)$$

According to the classical analysis, the main stress component is a shear stress $\sigma_{\theta z}$ (an axial stress σ_{zz} is also commonly observed, but it was found negligible [15]). Then the equivalent stress $\bar{\sigma}$ is given by :

$$\bar{\sigma} = \frac{\sqrt{3}\Gamma}{2\pi R^3}(3+\tilde{n}+\tilde{m}) \quad \text{where} \quad \tilde{n} = \left(\frac{\partial \ln \Gamma}{\partial \ln N}\right)_{\dot{N}} \quad \text{and} \quad \tilde{m} = \left(\frac{\partial \ln \Gamma}{\partial \ln \dot{N}}\right)_{N} \qquad (3)$$

The strain hardening index n and strain rate sensitivity exponent m can then be deduced from the following relationships :

$$n = \left(\frac{\partial \ln \bar{\sigma}}{\partial \ln \bar{\varepsilon}}\right)_{\dot{\bar{\varepsilon}}} = \tilde{n} + \left(\frac{\partial \ln(3+\tilde{n}+\tilde{m})}{\partial \ln N}\right)_{\dot{N}} \quad ; \quad m = \left(\frac{\partial \ln \bar{\sigma}}{\partial \ln \dot{\bar{\varepsilon}}}\right)_{\bar{\varepsilon}} = \tilde{m} + \left(\frac{\partial \ln(3+\tilde{n}+\tilde{m})}{\partial \ln \dot{N}}\right)_{N} \qquad (4)$$

3.2. Advantages and drawbacks of torsion compared with tension experiments

The main advantages are the following : at first, if $\dot{N}$ remains constant, whatever r is (between 0 and R), the strain rate $\dot{\bar{\varepsilon}}$ remains constant. In constant crossbeam rate tension experiments and especially with superplastic materials (i.e. large elongations), the strain rate does not keep a constant value. Secondly, the material flow is mechanically stable in torsion ; a large number of revolutions (esp. at high temperatures) can be achieved before flow localization. In tension, even with superplastic samples, necking occurs and the interpretation of the test is more difficult.

The main drawback is that the strain rate and strain are not homogeneous throughout the material. Both are functions of r and vary linearly from 0 to the values given by Eqs. (1) and (2). In tension, each cross section of the sample is submitted to the same strain and strain rate. Another point is that cavitation occurs very late in torsion because of the purely deviatoric stress state. The study of damage processes in the superplastic phenomenon requires triaxial depressive stress states such as those generally encountered in the neck of tensile specimens.

At last, superplasticity is known to strongly depend on microstructure. If microstructural evolution occurs during deformation, the problem of torsion test to assess material superplasticity is set down. In the general case, the microstructural effective parameter is the average grain size $\bar{D}$. Several studies of Ti-6Al-4V alloy have shown that the evolutions of $\bar{D}$ could be written in first approximation as function of time ($t = \bar{\varepsilon}/\dot{\bar{\varepsilon}}$) and temperature [16,17] between 10^{-4}-10^{-2} s^{-1}. Consequently, $\bar{D}$ should not depend on r during a torsion test, which justifies the use of the latter.

3.3. Experimental torsion procedure

The torsion experiments were carried out on an Instrument S.A. machine which is connected to a microcomputer in order to pilot the test and measure both the torque Γ and the axial force F. The heads of the specimen were fixed during the test and the rotation rate $\dot{N}$ was kept constant. It was possible to make it vary rapidly in order to impose jump tests. The specimen had 35 mm gauge length L and 3 mm radius R.

The FM was tested at 900, 927 and 950 °C in the 6×10^{-5}-10^{-3} s^{-1} strain rate range and this alloy should be considered as a reference material for superplasticity study. Both RM and AM were tested at 900 and 950 °C in the 10^{-5} - 10^{-3} s^{-1} strain rate range. The samples were kept 15 mm at the chosen temperature before testing. To prevent oxydation during experiments, high purity argon was circulated around the specimens in a quartz tube. Constant rate and jump tests were run in order to take into account the influence of microstructure on flow stress. Finally, specimens were deformed up to the maximal strain $\bar{\varepsilon}$=.04, to $\bar{\varepsilon}$=.5 and to $\bar{\varepsilon}$=1.

At the end of experiments, the samples were water quenched directly in the torsion device. The deformation structures developed during straining were studied using optical microscopy after polishing and etching in a 2 ml HF, 3 ml HNO_3, 95 ml H_2O solution [6].

4. RHEOLOGICAL RESULTS

4.1. The stress-strain curves

Figures 4 to 10 show the variations of the equivalent stress $\bar{\sigma}$ with equivalent strain $\bar{\varepsilon}$ for the three microstructures and the three temperatures investigated.

In the case of fine equiaxed grains (FM), when $\bar{\varepsilon}$ increases, the stress continuously increases over the strain rate and temperature ranges defined above. For large strains, the material tends more or less to a steady state. Strain hardening is larger for low strain rates (6×10^{-5} 2×10^{-4} s^{-1}) than for higher ones, so that the plateau value is reached later.

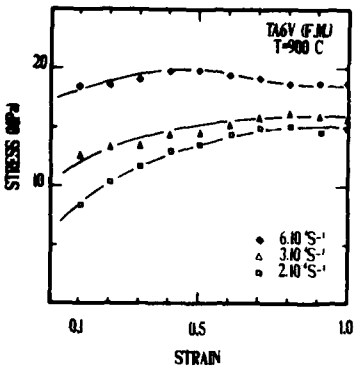

(4)

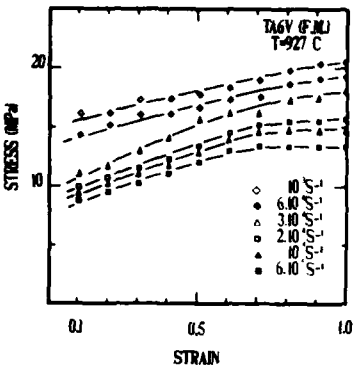

(5)

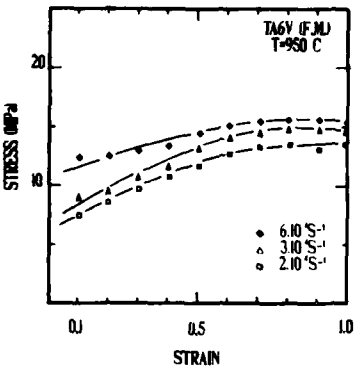

(6)

- Figures 4 to 10 -

Stress-strain curves for the following microstructures:

(4)-(6) : FM
(7)-(8) : Su
(9)-(10): Am

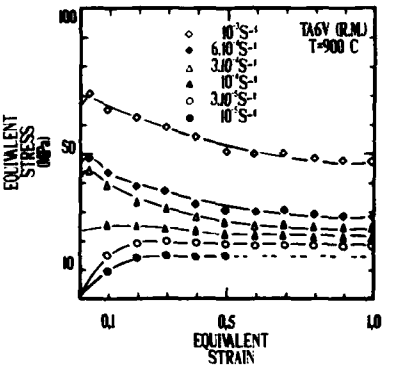

(7)

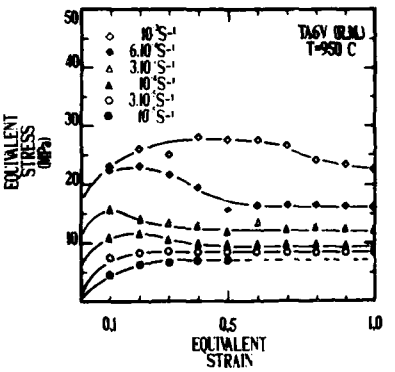

(8)

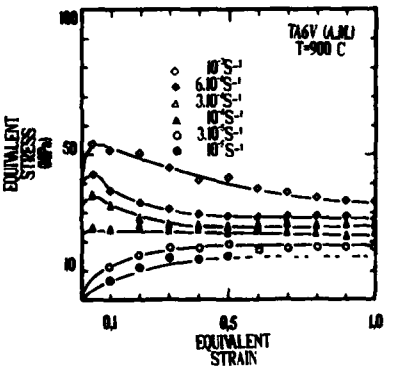

(9)

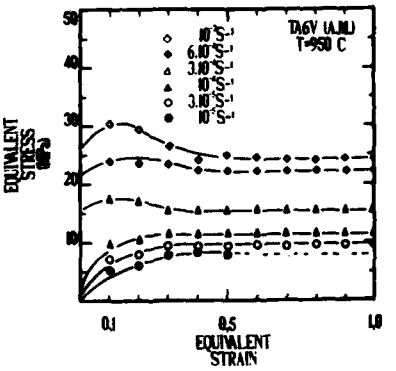

(10)

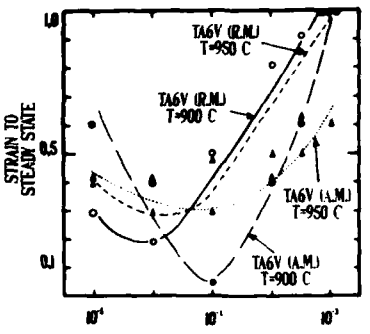

- Figure 11 -

Strain to steady-state function of T and $\dot{\bar{\varepsilon}}$ for RM and AM.

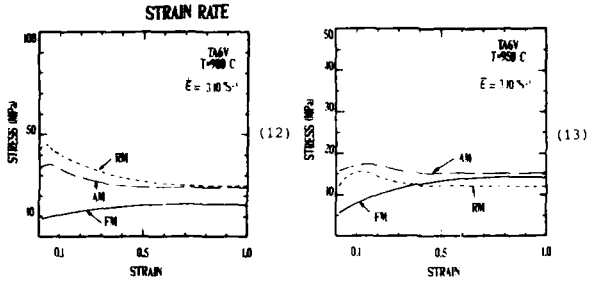

- Figures 12-13 -

Comparison of FM, RM and AM on a viewpoint of $(\bar{\sigma},\bar{\varepsilon})$ curves. $\dot{\bar{\varepsilon}} = 3\times10^{-4}\ s^{-1}$

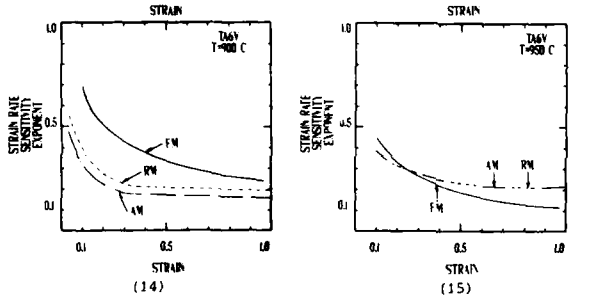

- Figures 14-15 -

Comparison of FM, RM and AM en a viewpoint of $(m,\bar{\varepsilon})$ curves.

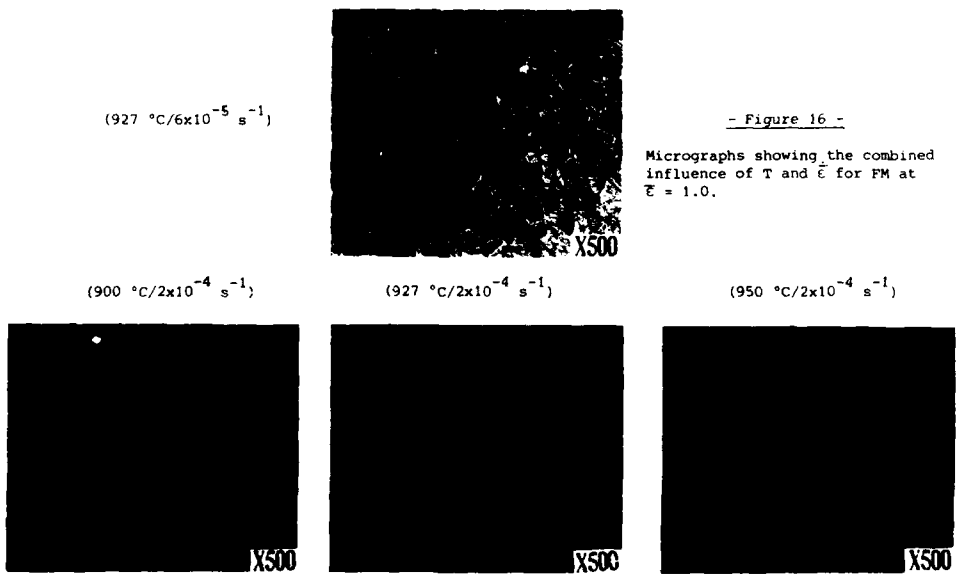

- Figure 16 -

Micrographs showing the combined influence of T and $\dot{\bar{\varepsilon}}$ for FM at $\bar{\varepsilon} = 1.0$.

For the acicular structure (RM and AM), two different types of behaviour can be distinguished. One is associated with large strain rates ($\dot{\bar{\varepsilon}}>3\times10^{-4}\ s^{-1}$) and consists in a short period of hardening (up to $\bar{\varepsilon}$=.04 at 900 °C and $\bar{\varepsilon}$ =.1 at 950 °C) followed by a progressive softening leading to a steady state. On the other hand, for low strain rates ($\dot{\bar{\varepsilon}}<10^{-4}\ s^{-1}$), the material first hardens and tends progressively to a steady state. Strain hardening becomes again larger when $\dot{\bar{\varepsilon}}$ increases to $10^{-4}\ s^{-1}$.

4.2. Influence of temperature

First, comparison of figures 4-6, 7-8 and 9-10 shows that when temperature is increased from 900 °C to 950 °C, the flow stress decreases. Calculation of the apparent activation energy Q for the steady state (i.e $\bar{\varepsilon}$ = 1.0) leads to the results given in table 3 (Q in kJoules/mole). These results are discussed later on.

Fine Equiaxed Microstructure	492
Acicular Raw Microstructure	747
Acicular Annealed Microstructure	595

Table 3 :

Apparent activation energy in the 1123-1173 K temperature range for steady state

For the acicular structures, when T increases, the steady state stress is divided by a factor 2 and the drop between peak stress and steady state one is smoothed. This should be attributed not only to the direct influence of temperature but also to the *decrease in α phase content from 46 % at 900 °C to 20 % at 950 °C* [6]. Since the α phase is 100 Hv harder than the β phase, this can account for a large part of the flow stress drop between the two temperatures. At last, figure 11 shows the determination of $\bar{\varepsilon}_{ss}$, the steady state deformation, as a function of $\dot{\bar{\varepsilon}}$ and T. When $\dot{\bar{\varepsilon}}$ increases, $\bar{\varepsilon}_{ss}$ first decreases, goes through a minimum value $\bar{\varepsilon}_{ss}^{m}$ and then increases. The evolution of $\bar{\varepsilon}_{ss}$ suggests to divide the strain rate range into low strain rates (associated with continuous hardening) and high ones (peak stress curves) so that $\bar{\varepsilon}_{ss}^{m}$ is rapidly reached for the transition strain rate (around 10^{-4} - 3 x $10^{-4}\ s^{-1}$). Annealing of the powder leads to a greater $\bar{\varepsilon}_{ss}^{m}$, thus to delay the steady state for high strain rates.

4.3. Comparison between acicular and equiaxed structures

The comparison is based on stress and m values. To simplify the discussion, m values were determined by linear regression for the three materials. Correlation was about .92 to .98 for low strains and greater than .98 for large strains. At last, comparison was made at $3\times10^{-4}\ s^{-1}$ which is well known to be in the superplastic strain rate range for both equiaxed structures [1,12,19-21] and acicular ones [7] and is related to the value of $\bar{\varepsilon}_{ss}^{m}$.

Figure 12 and 13 show the influence of the initial microstructure on stress. At 900 °C, RM and AM lead to the same ($\bar{\sigma}$, $\bar{\varepsilon}$) curve shape ; the peak stress is higher for RM but the steady state stresses have about the same value ; FM values of stresses are always far lower (-70 % at the begining, -40 % for large strains as compared with AM). At 950 °C, firstly, RM and AM exhibit the same peak stress curve shape but higher stresses are obtained with AM, so that the tendency is reverse as compared to 900 °C ; secondly, for low strains, FM values of stresses are lower than the others, but around $\bar{\varepsilon}$=.4 to .5 they exceed the RM ones.

The comparison of m values is given by figures 14 and 15. Whatever the temperature and the microstructure, *m values obtained by linear regression m(LR) always decrease* when $\bar{\varepsilon}$ increases. The maximum values of m decrease between 900 °C and 950 °C. At 900 °C, they are ordered as following m(FM)>m(RM)>m(AM). At 950 °C, FM and AM lead to nearly the same values ; for low strains, m(FM) is higher than the others but around $\bar{\varepsilon}$ = .3 to .4, it drops under m(RM or AM). This is to be closely related to the stress-strain curves comparison as shown in section 6.

5. MICROSTRUCTURAL EVOLUTIONS

5.1. The equiaxed structure

The observation of microstructural evolution using optical microscopy (at × 500 magnification) shows the following results. For a given value of $\bar{\varepsilon}$, the average grain size $\bar{D}$ decreases when $\dot{\bar{\varepsilon}}$ increases. For a fixed value of $\dot{\bar{\varepsilon}}$, $\bar{D}$ grows with an increasing strain (figure 16). When T increases, $\bar{D}$ increases, too. The micrographs of figure 16 enlighten the combined influence of T and $\dot{\bar{\varepsilon}}$ on microstructural changes.

5.2. The acicular structure

Figure 17 shows the microstructural evolution for AM at 900 °C. The conclusions can be extended to RM and 950 °C as well. Evolutions are presented for high strain rate ($6\times10^{-4}\ s^{-1}$) and low strain rate ($10^{-4}\ s^{-1}$).

5.2.1. Raw microstructure

Here again, as in part 4, the RM exhibits two different evolutions as for the associated ($\bar{\sigma}$,$\bar{\varepsilon}$) curves. For high strain rates, refinement of microstructure appears clearly between $\bar{\varepsilon}$ = .04 and $\bar{\varepsilon}$ = 1.0. The ex-β grain boundaries can be easily distinguished for low strains but not for large ones. The α needles appear to be broken

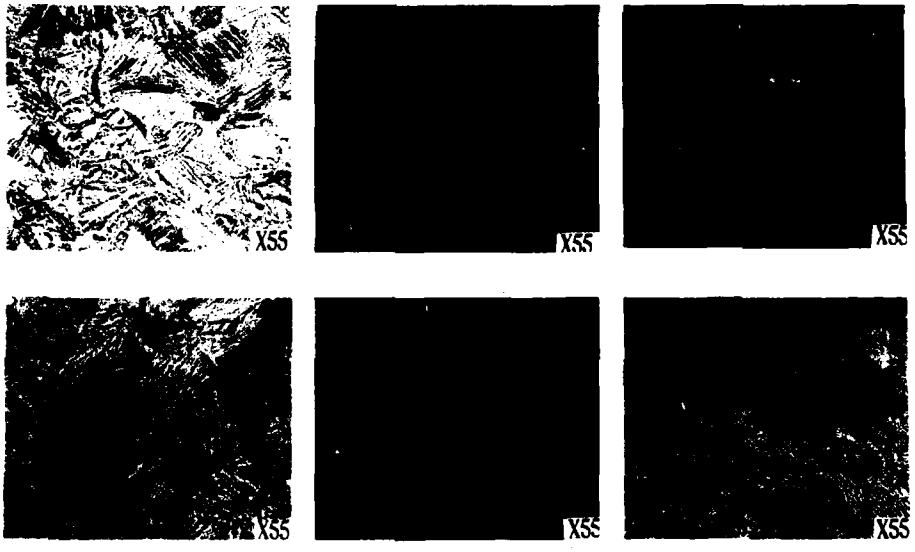

(a)

(b)

ε = .04 ε = .5 ε = 1.0

- Figure 17 -

Micrographs showing the influence of strain rate on acicular structures evolutions:case of AM at 900 °C.((a):6×10^{-4} ;(b):10^{-4} s^{-1})

- Figure 18 -

AM, 950 °C, 10^{-4} s^{-1} at total strain of 1.0. Formation of fine, equiaxed grains (arrowed) at the serrated boundaries of the elongated prior β grains.

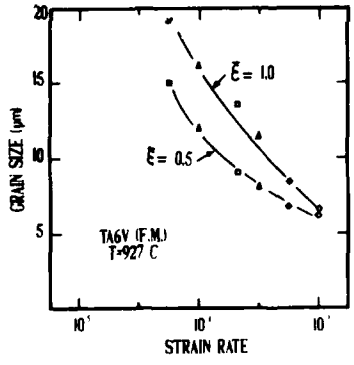

- Figure 19 -

FM: variations of $\bar{D}$ at 927 °C function of strain and strain rate.

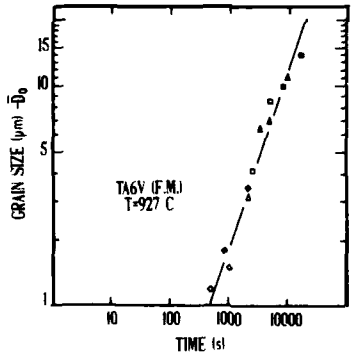

- Figure 20 -

FM: consistency of Eq.(5) at 927 °C.

at 900 °C, which indicates their presence at this temperature. The α phase is more and more globular as $\dot{\bar{\varepsilon}}$ decreases especially for the steady state. Of course, at 950 °C, the evolutions are rather similar. The main difference lies in the α percentage present after quenching : α grains are fewer according to the phase diagram. Consequently, the rapidly quenched β grains, presenting a martensitic structure α', clearly appear.

5.2.2. Annealed microstructure (figure 17)

One of the main consequences of powder annealing is the coarsening of both α needles (GAR decreases) and β grains (when discernable). All the tendencies already given for RM in 5.2.1. remain essentially valid. For high strain rates, α breaking is less significant as for RM and β grains can be easily distinguished. For the steady state, *no strain rate can lead to the same equiaxed structure of α as in RM.* Here again, when T increases to 950 °C, the β grains increase with a few broken α platelets. For low strain rates, new β grains appear at the boundary of elongated grains suggesting a recrystallization phenomenon (figure 18).

5.3. Modelling of structural evolutions

Figure 19 enlightens the evolutions of the FM average α grain size $\bar{D}$ as a function of strain rate for $\bar{\varepsilon}$=.5 and $\bar{\varepsilon}$=1 at T=927 °C. Assuming that it could be modelled by the following relationship :

$$\bar{D} = \bar{D}_0 + kt^l \quad (\bar{D}, \bar{D}_0 \text{ in } \mu m \ (\bar{D}_0 = 5\ \mu m), \ t \text{ in } s) \qquad (5)$$

calculations using linear regression have led to k=.0108 and l=.76 with a correlation coefficient of .98. Figure 20 shows the consistency of this relation (5) with the experimental data.

For the acicular structures, quantification of grain size appears to be difficult to carry out since β grain boundaries are not clearly revealed. Nevertheless, tendencies can be pointed out and are presented in figure 21 (see next page).

6. DISCUSSION

6.1. Comparison of rheological results with literature

Few studies have been done using torsion experiments on Ti-6Al-4V alloy. Nevertheless, MALCOR and MONTHEILLET [3-6] have already compared some equiaxed and acicular structures in the 800-1200 °C temperature and 5×10^{-3}-5 s^{-1} strain rate ranges. At first, comparing the two studies from the viewpoint of $(\bar{\sigma},\bar{\varepsilon})$ curves, the results are rather similar : for $\dot{\bar{\varepsilon}} > 5\times10^{-3}$ s^{-1}, (i.e. around the highest strain rates of the present study), acicular structures display a peak curve whereas the equiaxed one exhibits continuous hardening or a rapidly established steady state. Secondly, though the microstructures are quantitatively different, rheological results are still comparable. MALCOR and MONTHEILLET used a semi empirical law to describe the steady state. The hyperbolic sine SELLARS-TEGART relationship led to a very good agreement. Comparison with m and Q between the two studies gives (table 4) :

	Present study 900 - 950 °C 10^{-5} - 10^{-3} s^{-1}		MALCOR [6] 800 - 1200 °C 5×10^{-3}-5 s^{-1}	
	m*	Q (kJoules/mole)	m	Q (kJoules/mole)
Equiaxed FM	.19	492	.19	546
Acicular AM	.20	595	.23	600

Table 4

Comparison between [6] and the present study. (*) m values obtained by averaging the 900-950 °C values for steady state.

The AM, which is the more comparable to the acicular structure of [6], gives almost the same values for m and Q and may lead to similar behaviour and microstructural phenomena. For FM, if m is comparable, the slight drop in the Q value; between [6] and the present study (-10%) is consistent with the fact that the occurence of fine grained material superplastic behaviour is associated with lower activation energies. At last, the peak stress localization takes place nearly at the same strain in the two studies (between .04 and .1).

6.2. Comparison of microstructural evolutions with literature ones

Enhanced grain growth during superplastic flow is now well known since the studies of GHOSH and HAMILTON and ARIELI et al. [16,17]. FM microstructure in the superplastic range coarsens mostly because of grain boundary sliding (GBS) instead of dynamic recrystallization. For acicular microstructures, the present results are consistent with literature (MALCOR and MONTHEILLET [3,4,6]). High strain rate range corresponds to grain refinement whereas low strain rates lead to particle coarsening.

Several studies have shown dynamic recrystallization (DRX) of α phase in Ti-6Al-4V alloy [23-25]. Such a mechanism occurs for equiaxed structures as well as for acicular ones, for low strain rates (i.e. $\dot{\bar{\varepsilon}}<10^{-2}$ s^{-1}) and of course, seems to be more efficient at 900 °C than at 950 °C [25]. In fact, around the β transus (i.e. 950 °C) the α volume fraction is low and the grains behave like hard inclusions in a soft matrix (β). Such a

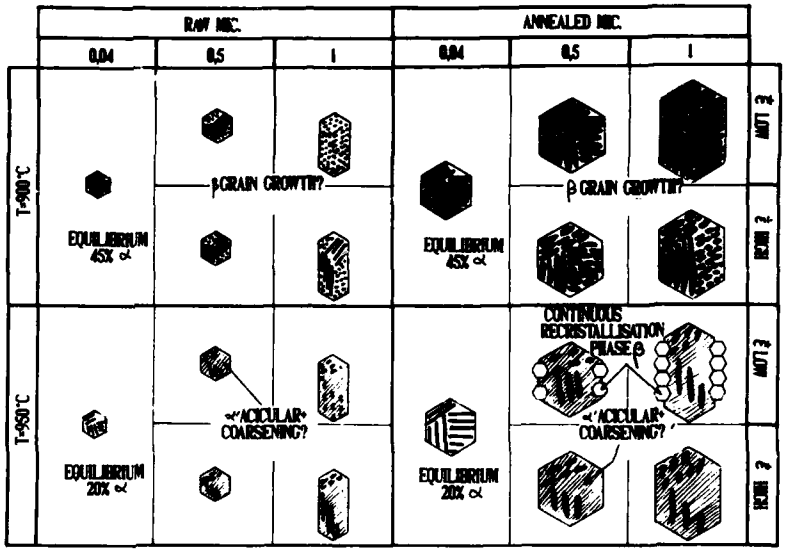

- Figure 21 -

Evolutions of acicular structures (RM & AM)

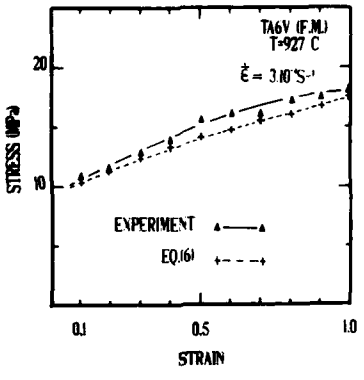

- Figure 22 -

Consistency of Eq.(6) for FM.

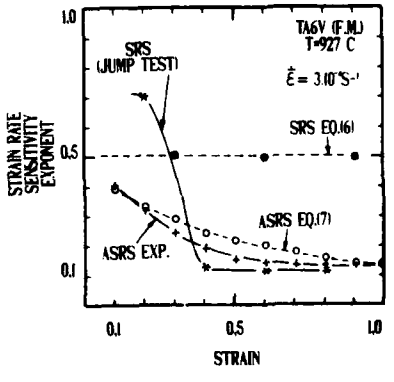

- Figure 23 -

SRS & ASRS evolutions for FM.

consideration is consistent with the idea that there is a critical α phase percentage below which the behaviour of β phase is predominant [4,6,26]. Estimations of transient α percentage (i.e. temperature) is about that of 927 °C for fine equiaxed and 950 °C for coarse lamellae structures from [4,6]. At 950 °C, α particles cannot be strained enough for DRX to take place [4]. The work performed by SHAKANOVA et al. [27] clearly shows that α DRX should take place in the investigated strain rate and temperature range for a sufficient imposed strain.

The fact that new β grains are produced during deformation has already been observed [4,6,22] in the 850-1100 °C temperature range below 1 s^{-1}. Some authors attributed such a phenomenon to DRX of β phase [22,27], some others to the continuous recrystallization (CRX) occurring by a progressive misorientation of subgrains during deformation [4,6,28,29]. Such a phenomenon is found in heavily strained high staking fault energy materials [30-33].

6.3. Influence of microstructural evolutions on rheology

6.3.1. Equiaxed structure

Enchanced grain growth during superplastic deformation leads to an apparent strain hardening [1,16,22,34]. As the average grain size increases, the flow stress increases and m decreases, too [1,2,7,17]. When strain hardening occurs, m determined by Eq. (4) should be called the apparent strain rate sensitivity (ASRS) [35]. Obviously, as structural evolutions are conditionning rheological ones, the strain rate sensitivity should be determined at constant structure. To a first approximation, $\bar{D}$ may represent the structure. Relation (5) allowed the choice of stresses at different strain rates, but same $\bar{D}$, to determine m_s, the S.R.S. exponent. At 927 °C, calculations using linear regression lead to $m_s = .5$ nearly constant with strain with a good correlation coefficient (>.999). Writting :

$$\bar{\sigma} = K \dot{\bar{\varepsilon}}^{m_s} \bar{D}^{p_s} \qquad \text{with} \quad m_s = .5 \tag{6}$$

similar calculation of p_s for 3×10^{-4} s^{-1}, lead to $p_s = 1.01$ (correlation .94) and $K = 102.25$ MPa $s^{-.5}$ μm^{-1}.

Such values of m_s and p_s are rather similar to those found in literature by ARIELI and ROSEN [36]. At last, using Eq. (5) and (6), the ASRS exponent m can be written as follow :

$$m = m_s + p_s \left(\frac{\partial \ln \bar{D}}{\partial \ln \dot{\bar{\varepsilon}}}\right)_{\bar{\varepsilon}} = m_s - p_s.1.\left(\frac{\bar{D}-\bar{D}_0}{\bar{D}}\right) \tag{7}$$

Figure 22 illustrates the consistency of Eq. (6) at 927 °C for the chosen strain rate of $3\times10^{-4}s^{-1}$. In the 10^{-4}-10^{-3} s^{-1} strain rate range, discrepencies still remain (max. 10%), but such a relationship gives a good approximation of reality. Figure 23 shows the differences between the experimental m(LR) ASRS and the one given by Eq. (7) ; agreement is rather good especially for large strains.

Nevertheless, such an agreement should not hide the limit of Eq. (6). The main assumption is that $\bar{D}$ should represent the structure. If a rapid variation in $\dot{\bar{\varepsilon}}$ during the test is asssumed to occur at a constant structure, jump tests should give a determination of m_s. Such tests were run and the same figure 23 shows that m_s decreases when $\bar{\varepsilon}$ increases (i.e the structure coarsens) as it has already been found [16]. Thus $\bar{D}$ is only a first order approximation of structure. At last, the knowledge of *m (ASRS) and* m_s (SRS) *are complementary.* If m_s determines the behaviour and the flow rule, m determines the ductility (i.e. the flow stability for a material in a given strain-strain rate state $(\bar{\varepsilon},\dot{\bar{\varepsilon}})$ to support further deformation given by $(\bar{\varepsilon}+\Delta\bar{\varepsilon}, \dot{\bar{\varepsilon}}+\Delta\dot{\bar{\varepsilon}})$).

6.3.2. The acicular structures

Modelling in the same way as 6.3.1. appears to be diffcult mainly because of grain size measurements. Nevertheless, a qualitative explanation can be proposed.

For low strain rates, the stress continuously increases. As the reference fine grained equiaxed alloy showed it, this phenomenon should be related to an increase of β size during deformation, especially around 950 °C. In fact, in the present case, at *900 °C, neither RM or AM clearly exhibit grain coarsening, mainly because of a large* α proportion, but it can be observed in the case of 950 °C. The fact that the structure coarsens leads to a less and less marked tendancy to superplasticity and is consistent with a decrease in m (ASRS) value.

In the high strain rate range, the softening is mainly due to the combined effect of both the fracture of α needles [4,6] and DRX of α phase [22,28] at 900 °C where α percentage is high. But at 950 °C, the material is mainly composed by 80 % of β phase. The strain induced softening is more characteristic of dynamic recovery (DR) at low strains and CRX at large strains.

6.4. Occurrence of superplasticity

At 950 °C, and 3×10^{-4} s^{-1}, above $\bar{\varepsilon}$=.5, FM stress exceeds RM one whereas m(FM) is lower than m(RM) (cf. part 4.3). In the superplastic range, large values of m are generally associated with low values of stress. The variations of m values with $\bar{\varepsilon}$ can be closely related to the stress ones (figures 13 and 15).

Fine grained structures are known to lead to a superplastic behaviour. GBS during deformation makes the grain coarsen. Consequently, m and m_s are high at the beginning of deformation. But superplastic behaviour is strongly grain size dependent, and is less marked for coarse structures. During a true constant strain rate path encountered in torsion experiments, m and m_s decrease. The SRS variations are not only due to microstructural changes but also to the involved mechanisms. Figure 23 clearly establishes that GBS first occurs ($m_s > m$) but is progressively replaced by a more classic behaviour characterized by grain work hardening (GWH) so that $m_s < m$. The transition should be given by conditions on critical values of strain rate as it was already done [37,38] or a critical value of $\bar{D}$: $\bar{D}_c$. Below $\bar{D}_c$, grain size is small enough to allow diffusion mechanisms to take place and lead to GBS ; above $\bar{D}_c$, diffusion is no more competitive as compared to dislocation creep and GWH occurs.

Such considerations can be extended to acicular structures as well, especially for low strain rates. Because of GBS, the delay at which GWH occurs may explain the limited RX phenoma (α DRX or β CRX) for which a minimal value of mechanical stored energy is required in the grain. For high strain rates, RX phenomena occur earlier (esp. β CRX) so that GBS may be established further for rather large strains. This could account for the fact that m (RM and AM) > m(FM) at 950 °C for $\bar{\varepsilon} > .5$.

7. CONCLUSIONS

Torsion experiments carried out by torsion testing on various microstructures of Ti-6Al-4V alloys, have shown results similar to tension studies in literature. The fine grained reference material clearly exhibited the well known dependence of strain rate on $(\bar{\sigma},\bar{D})$ couple, given by $\dot{\bar{\varepsilon}} \neq (\bar{\sigma}/\bar{D})^2$. If such a relationship accounts for stress and ASRS values, the consistancy should not hide its limits. The latter are mainly due to the fact that $\bar{D}$ may not represent the whole structure and should be chosen for a first order approximation of rheology. Despite all these restrictions, the use of the coupled relationships (5) + (6) should be made for implementation in computer aided simulation of forging [8] or bulging [9,39]. As compared to this reference material, PM + HIP'ed acicular structures exhibit similar behaviour with slight differences. For instance, strain induced RX may lead to structural refinements favourable to high strain rate sensitivity phenomena such as superplastic deformation [7]. The main problem for the development of PM+HIP+SPF route is the price of the powder and the cost of sintering operations even aided by predictive compressive computer calculations [40]. The future of acicular structures for superplasticity seems to be restricted to few applications. By all means, production of such parts appears to be more competitive using PM+Cold Compression + (Sintering and SPF) (if possible) or the IR+SPF.

8. REFERENCES

[1] D. LEE and W.A. BACKOFEN, Trans. of AIME, 239, 1034 (1967)
[2] N.E. PATON and C.H. HAMILTON, Metall. Trans., 10A, 241 (1979)
[3] J.G. MALCOR, Thesis, Ecole des Mines de Paris (1983)
[4] J.G. MALCOR and F. MONTHEILLET, Mem. Et. Sci. Rev. Metall., 81, 181 (1984)
[5] J.G. MALCOR and F. MONTHEILLET, Mem. Et. Sci. Rev. Metall., 80, 89 (1983)
[6] J.G. MALCOR and F. MONTHEILLET, Proceedings 4th RISØ Symposium, 399 (1983)
[7] Y. COMBRES, Ch. LEVAILLANT and F. MONTHEILLET, Proceedings of International Conference on Titanium Products and Applications, Eds. Titanium Development Association, 1163 (1986)
[8] Y. GERMAIN, Thesis, Ecole des Mines de Paris (1985)
[9] M. BELLET and J.L. CHENOT, Proceedings of International Conference on Titanium Products and Applications, Eds. Titanium Development Association, 1175 (1986)
[10] P. COMLEY , Proceedings of International Conference on Titanium Products and Applications, Eds Titanium Development Association, 1034 (1986)
[11] W. LEOUULTER, Proceedings of International Conference on Titanium Products and Application, Eds Titanium Development Association, 1107 (1986)
[12] W.D. GOODIN and J.K. LAYFIELD, Research and Technical Development, RaD Report n° 639A RMI Co, Niles Ohio USA (1985)
[13] J.L. BRANTHINGHAM and D.E. THOMAS, Proceedings of International Conference on Titanium Products and Applications, Eds Titanium Development Association, 1073 (1986)
[14] D.S. FIELDS and W.A. BACKOFEN, Proceedings ASTM, 57, 1259 (1957)
[15] F. MONTHEILLET, M. COHEN and J.J. JONAS, Acta. Metall., 32, 2077 (1984)
[16] A.K. GHOSH and C.H. HAMILTON, Metall. Trans., 10A, 699 (1979)
[17] A. ARIELI, B.J. McLEAN and A.K. MUKHERJEE, Proceeding of Titanium'80, 1047 (1980)
[18] R. CASTRO and L. SERAPHIN, Mem. Et. Sci. Rev. Metall., 63, 1025 (1966).
[19] C.H. HAMILTON and A.K. GHOSH, Proceedings of Titanium'80, 1001 (1980)
[20] Y. ITO and A. HASEGAWA, Proceedings of Titanium'80, 983 (1980)
[21] M.T. COPE and N. RIDLEY, Mater. Sci. and Technol., 2, 140 (1986)
[22] A. ROSEN, Final Scientific Report n° AFOSR-80-0132 (1981)
[23] B. HIDALGO-PRADA and A.K. MUKHERJEE, Annual Progress Report n° AFOSR-82-0081 (1985)
[24] C.C. CHEN and J.E. COYNE, Metall. Trans., 7A, 1931 (1976)
[25] M. MAJDIC and G. ZIEGLER, Z. Metallkunde, 65, 173 (1974)
[26] F. ABRASSART, Thesis, Ecole des Mines de Nancy (1972)
[27] G.V. SHAKANOVA, I.B. RODINA, F.V. TULYANKIN, A.L. PHILIPENKO, B.A. SHAKSHAGIN and N.V. BURHARINA, Proceedings of Titanium'80, 849 (1980).
[28] R.D. DOHERTY, Proceedings 1st RISØ Symposium, 57 (1980)
[29] B.A. COOKE and B. RALPH, Proceedings 1st RISØ Symposium, 211 (1980)
[30] Ch. PERDRIX, M.Y. PERRIN and F. MONTHEILLET, Mem. Et. Sci. Rev. Metall., 78, 309 (1982)
[31] F. MONTHEILLET, 24th Colloque de métallurgie, INSTN Saclay, 57 (1981)

[32] M.Y. PERRIN, Y. COMBRES, C. LEVAILLANT and F. MONTHEILLET, Proceedings 7th RISØ Symposium, 487 (1986)
[33] M.Y. PERRIN, Y. COMBRES, C. LEVAILLANT and F. MONTHEILLET, Proceedings 8th RISØ Symposium, 479 (1987)
[34] N.E. PATON and C.H. HAMILTON, Titanium Science and Technology, Eds. G. Lütjering, U. Zwiken and W. Bunk, Vol. 2, 649 (1985)
[35] G. GUREWITZ and A.K. MUKHERJEE, Mater. Sci. and Eng., 70, 191 (1985)
[36] A. ARIELI and A. ROSEN, Metall. Trans., 8A, 1591 (1977)
[37] A.K. GHOSH and R. RAJ, Acta Metall., 29, 607 (1981)
[38] A.K. GHOSH and R. RAJ, Acta Metall., 34, 447 (1986)
[39] M. BELLET, Y. COMBRES, C. LEVAILLANT and J.L. CHENOT (to be published)
[40] E. WEY, Ch. LEVAILLANT and J.L. CHENOT, incl. in this proceedings.

The authors gratefully aknowledge the Avions Marcel Dassault S.A. for providing the equiaxed microstructure alloy and mahining of samples, Cezus S.A. for the alloy atomized by the Centre d'Etudes Nucléaires de Grenoble which also performed annealing, HIP'ing and machining of acicular structure specimens.

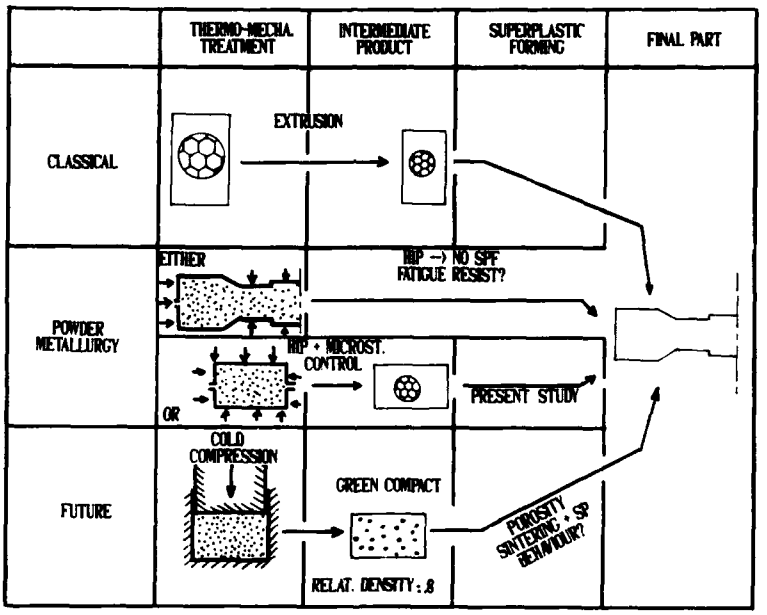

- Figure 24 -

LE MODELE DE FORGEAGE ISOTHERME FORGE 2

P.E. MOSSER - Section d'étude des procédés de forge
S.N.E.C.M.A. - Direction Technique
291, avenue d'Argenteuil
92234 GENNEVILLIERS FRANCE

Y. GERMAIN* - Centre d'Etude de Mise en Forme (CEMEF)
Ecole des Mines de Paris
06565 SOPHIA ANTIPOLIS FRANCE

* actuellement Ohio State University
Department of Metallurgical Engineering
COLUMBUS OHIO 43210-1179 USA

Résumé

Le logiciel FORGE 2 a été développé par le CEMEF sous les spécifications fonctionnelles de la SNECMA pour modéliser les écoulements de la matière au cours du forgeage isotherme de pièces axisymétriques. Il permet de prévoir les défauts de remplissage des matrices, la macro-et la microstructure métallurgique de la pièce forgée et les contraintes sur les outillages.

Après une présentation des fondements théoriques du modèle, on expose les bases d'une méthode d'identification du test de l'anneau pour une formulation de type fluide. Puis on montre un exemple d'utilisation de FORGE 2 pour la mise au point d'une gamme de forgeage isotherme d'un disque de turboréacteur. Cet exemple numérique est confronté avec des forgeages réels.

Summary

The finite element model FORGE 2 developped by CEMEF under SNECMA's specifications describes the metal flow during the isothermal forging of axisymmetric parts. It allows to predict the defects appearing during the deformation, the metallurgical structure of the forged part and the stresses on the die impression.

The theoretical aspects of the model are described here, as well as a method for identifying the friction factors in a fluid formulation. The usefullness of FORGE 2 is then shown by comparing the experimental and numerical forgings of a jet engine compressor disk.

1 - INTRODUCTION

Le forgeage isotherme est un procédé de forgeage où les matrices sont maintenues à la même température que la pièce à forger.

En s'affranchissant du refroidissement, il est possible de réaliser, à des vitesses de déformation faibles où les contraintes d'écoulement sont réduites, des bruts plus près des cotes de la pièce terminée. Néanmoins, au cours d'une telle opération, les écoulements de matière sont plus complexes et les concentrations de contraintes sur les gravures plus importantes qu'en forgeage conventionnel. Il devient nécessaire de pouvoir visualiser les écoulements et les contraintes, dès la préparation de la gamme de forge, afin de limiter la procédure d'essai classique et de garantir la durée de vie des matrices.

C'est pourquoi la SNECMA a décidé de se doter d'un logiciel d'aide à la préparation de gammes. Le CEMEF, laboratoire de l'Ecole des Mines de Paris, a développé FORGE 2 sous spécifications fonctionnelles SNECMA. Ce code de calcul y est maintenant opérationnel.

Cet article décrit les fondements du modèle élaboré à partir d'une formulation du type fluide. Une difficulté associée à une telle formulation est l'expression puis l'identification d'une loi de frottement. On présentera une méthode pour le dépouillement du test de l'anneau. Enfin la gamme de forgeage isotherme d'un disque de compresseur sera étudiée numériquement et corrélée sur des forgeages soit de pièces réelles en TA6V soit de pièces modèle en alliage Pb38-Sn62.

2 - DESCRIPTION DU LOGICIEL FORGE 2 [1]

2.1 - Comportement rhéologique du matériau

En forgeage à chaud, il est très difficile de mettre en évidence un seuil plastique. De plus, la compétition entre les mécanismes d'écrouissage et d'adoucissement (restauration ou recristallisation dynamique) induit une grande dépendance de la contrainte d'écoulement vis à vis de la vitesse de déformation. Ceci a conduit à faire le choix d'une formulation où le déviateur du tenseur de contraintes s est relié au déviateur du tenseur de vitesses de déformation $\dot{\varepsilon}$ par la loi de Von Mises généralisée :

$$s_{ij} = (\sigma / \dot{\varepsilon}) \dot{\varepsilon}_{ij}$$

La loi de comportement rhéologique du matériau exprime $\sigma = \sqrt{3/2\ s_{ij} : s_{ij}}$

par une loi en puissance de $\dot{\bar{\varepsilon}} = \sqrt{2/3\ \dot{e}_{ij} : \dot{e}_{ij}}$

$$\sigma = \sqrt{3}\ K\ (\sqrt{3}\ \dot{\bar{\varepsilon}})^m$$

Une telle loi peut être définie par morceaux pour mieux représenter le comportement d'un matériau réel sur un grand intervalle de vitesse de déformation.

2.2 - Loi de frottement

La forme générale de la cission de frottement est :

$$\tau = -\alpha |V_g|^{p-1} * V_g$$

où Vg désigne la vitesse de glissement de la pièce relativement à la matrice. Cette loi considère la couche lubrifiante comme une couche limite d'un matériau similaire à celui forgé. Il existe peu de données relatives à cette formulation. On donnera au paragraphe 3 une méthode d'identification des coefficients α et p.

2.3 - Principe variationnel

A un instant donné, le champ de vitesse en chaque point du corps déformable (Ω) minimise la fonctionnelle introduite par HILL [2]

$$\Psi(V) = \int_\Omega G dx + \int_{\delta\Omega} F ds$$

($dG = \sigma d\bar{\varepsilon}$ et $dF = \tau dVg$) tout en respectant l'incompressibilité et les conditions aux limites de la frontière ($\delta\Omega$). Pour des raisons numériques, il est plus simple de minimiser la fonctionnelle pénalisée :

$$\Phi(V) = \Psi(V) - \tfrac{1}{2} \rho \int_\Omega div^2 V\ dx$$

Le champ de déplacement s'obtient par intégration temporelle du champ de vitesse ; de même le champ des déformations généralisées résulte de l'intégration du champ des vitesses de déformation.

2.4 - Formulation par éléments finis - Discrétisation temporelle

L'élément fini choisi est un quadrilatère isoparamétrique à 4 noeuds. Le champ de vitesse à l'intérieur de l'élément s'obtient en multipliant le vecteur vitesse nodale par la matrice d'interpollation.

Résolution en vitesse

On appelle $\Gamma(V)$ le gradient par rapport aux vitesses nodales de la fonctionnelle Φ discrétisée. La minimisation de Φ sur le champ de vitesses nodales est alors équivalente à la résolution de $\Gamma(V) = 0$. On utilise la méthode itérative de NEWTON RAPHSON en initialisant le champ de vitesse pour une rhéologie Newtonnienne ($p = m = 1$). La solution V^n est obtenue à la nième-itération quand $\Gamma(V^n)$ est suffisamment petit et quand la suite V^n est stationnaire.

Intégration temporelle

On a fait le choix d'un schéma explicite. Les nouvelles coordonnées nodales sont calculées à partir du champ de vitesse :

$$X_{t+\delta t} = X_t + V_t * \delta t$$

et l'écrouissage cumulé par :

$$\bar{\varepsilon}_{t+\delta t} = \bar{\varepsilon}_t + \dot{\bar{\varepsilon}}_t * \delta t$$

2.5 - Prise en compte du contact pièce-matrice

Au cours de la déformation les noeuds du maillage en contact avec la matrice peuvent décoller et ceux initialement libres peuvent venir toucher la matrice ; le contact est unilatéral.

Le décollement est traité en testant, sur chaque champ de vitesse solution, la contrainte normale sur la matrice. Si pour l'ensemble des noeuds, cette contrainte est en appui, les conditions aux limites et le champ solution sont déclarés valides.

Si pour un noeud cette contrainte est en traction (condition irréaliste. un noeud du maillage tirerait sur le côté de la matrice), on modifie les conditions aux limites pour relâcher ce noeud puis on recalcule le champ de vitesse.

Si après déplacement, un point de maillage se trouve à l'intérieur de la matrice, sa position est corrigée par projection orthogonale sur le côté le plus proche. L'erreur commise est du même ordre de grandeur que celle propre à la méthode des éléments finis.

2.6 - Remaillage

Un même maillage peut rarement décrire une opération complète de forgeage. En effet, il n'est pas rare qu'au cours de la déformation, un ou plusieurs éléments dégénèrent en devenant pseudotriangulaires ou même concaves ; il arrive aussi qu'à cause des contacts successifs le maillage initial ne soit pas assez fin pour représenter les nouveaux détails du contour de la matrice.

Il est nécessaire alors de procéder à un remaillage partiel ou complet. Cette opération réalise aussi le transport de l'écrouissage et de toutes les grandeurs incrémentales associées à un point matériel.

Le choix de l'instant le plus tardif du remaillage est dicté par des critères objectifs (perte de volume trop importante due à une mauvaise prise en compte des matrices, incrément local de déformation) calculé par le programme. Cependant, le préparateur de forge peut juger préférable de remailler à partir de n'importe quel instant antérieur.

3 - IDENTIFICATION D'UNE LOI DE FROTTEMENT

3.1 - Formulation d'une loi de frottement

3.1.1 - Critique de la formulation classique de Tresca

En modélisation de forgeage, la représentation classique du frottement est celle de Tresca [3] . Elle fait appel à une notion de seuil de contraintes en-dessous duquel il n'y a pas de glissement.

Si le glissement se produit, alors la contrainte du cisaillement τ est fixée à une fraction de la contrainte d'écoulement σ du matériau forgé : $\bar{m} = \tau/\sigma$ et $0 < \bar{m} < 1$. Cette formulation est particulièrement bien adaptée au cas d'un frottement sec d'un matériau de Von Mises où l'effort résulte de la déformation des pics de rugosité. Elle montré son opérationnalité et ses limites par de multiples corrélations avec l'expérience [4] .

Une telle approche n'est pas adaptée dans le cas d'une formulation fluide. En effet, il n'existe pas de seuil en-dessous duquel l'écoulement n'a pas lieu. Il paraît illogique de corréler la contrainte de cisaillement de frottement en un point de contact à la contrainte d'écoulement qui dépend de la vitesse de déformation dans l'élément de matière juste au-dessus de ce contact. Par exemple, dans le cas d'un glissement sans déformation, le frottement serait obligatoirement nul.

Dans le cas du forgeage isotherme, il est de plus nécessaire de tenir compte de la grande amplitude de vitesse. Entre le début et la fin de l'écrasement, celle-ci peut en effet varier de 4 ordres de grandeur.

Des tests de l'anneau réalisés sur du TA6V en condition isotherme montrent une différence significative entre le coefficient de frottement à 10^{-4} s^{-1} et celui à 10^{-2} s^{-1} (tableau 1). Il est donc nécessaire que la contrainte de frottement dépende de la vitesse .

	10^{-4} s^{-1}	$10^{-3} s^{-1}$	10^{-2} s^{-1}
$\bar{m}$	0,05	0,08	0,10

Tableau 1 : Evolution du coefficient de TRESCA avec la vitesse de déformation initiale
- anneau 6/3/2 matière TA6V
- lubrifiant : émail
- réduction de hauteur : ΔH % = 30%

3.1.2 - Formulation de couche limite

La formulation de couche limite tient compte de la nature de la couche lubrifiante à l'interface matrice/pièce forgée. C'est une couche d'émail pâteux parfois chargé de particules calibrées pour aider au démoulage. Le comportement de ces verres est généralement newtonnien et parfois binghammien (fig. 1). La dépendance de la viscosité avec la pression est généralement faible [5] . Le comportement rhéologique d'un tel matériau peut alors s'écrire : $\tau = \eta \dot{\gamma}^P$ où $\dot{\gamma}$ est la vitesse de cisaillement et η la consistance ou la viscosité dans le cas Newtonnien.

Si on néglige l'écoulement propre de la couche limite due au gradient de pression, la contrainte de cisaillement générée par la couche limite d'épaisseur e d'un tel matériau s'écrit alors :

$$\tau = (\eta/e^p)\, V_g^p$$

Vg désigne la vitesse de glissement. La loi (2.2) dérive de cette expression quand l'épaisseur de revêtement est constante.

3.2 - Détermination des coefficients de la loi de frottement

3.2.1 - Cas du frottement de Tresca

La détermination du coefficient de frottement de Tresca $\bar{m}$ est effectuée de façon courante en forgeant un anneau de géométrie fixée. On mesure la hauteur après forgeage ainsi que le diamètre intérieur, puis on trouve $\bar{m}$ en reportant les variations de ces grandeurs dans des abaques de frottement TVM [4].

L'utilisation de ces abaques repose sur la similitude des écoulements quelle que soit l'échelle de l'anneau forgé. Une analyse dimensionnelle montre en effet que $\bar{m}$ est une des variables adimensionnelles du système.

3.2.2 - Cas du frottement de couche limite

3.2.2.1 - Définition de l'intensite de frottement

Dans le cas d'une rhéologie fluide en loi-puissance, avec un frottement de couche limite, la variable adimensionnelle de frottement est en toute rigueur une variable locale : $f^*(M,P)$ qui compare la puissance dissipée par le frottement en tout point de contour M avec la puissance de déformation en tout point P du volume :

$$f^*(M,P) = 3^{-(m+1)/2} * V_g^p(M) * (\alpha/K) * \dot{\bar{\varepsilon}}^m(P)$$

A partir de cette expression f^* et compte tenu des similitudes géométriques et cinématiques on peut définir l'intensité de frottement d'un écoulement par :

$$f = 3^{-(m+1)/2}\ (\alpha/K)\ L^p\ \dot{\bar{\varepsilon}}^{p-m}$$

où L désigne une dimension caractéristique du frottement et $\dot{\bar{\varepsilon}}$ la vitesse de déformation de référence.

A partir de cette expression, nous allons établir les règles de similitude parfaite puis approchée et en déduire une méthode de dépouillement du test de l'anneau applicable à la détermination des coefficients α et p du frottement de couche limite.

3.2.2.2 - Conditions de similitude parfaite : détermination de p

On considère deux écoulements 1 et 2 dont la loi de comportement vaut:

$$\sigma = 3^{-(m_i+1)/2}\ K_i\ \dot{\bar{\varepsilon}}^{m_i}\ ;\ i = 1,2$$

et la loi de frottement :

$$\tau = \alpha_i * V_g^{p_i}\ ;\ i = 1,2$$

Pour avoir la similitude des champs de vitesse, il est nécessaire d'avoir la similitude des contraintes. Ceci nécessite l'identité entre les exposants de sensibilité à la contrainte rhéologique $m_1 = m_2 = m$ (1) et tribologique $p_1 = p_2 = p$ (2). Le rapport des intensités de frottement s'écrit alors :

$$f_2/f_1 = \frac{\alpha_2/K_2}{\alpha_1/K_1}\ (L_2/L_1)^p\ (\dot{\bar{\varepsilon}}_2/\dot{\bar{\varepsilon}}_1)^{p-m}$$

La similitude du rapport des contraintes de déformation aux contraintes de frottement impose : $f_2/f_1 = 1$ (3). On en déduit que pour garder la similitude entre deux écoulements :

- si $p \neq 0$ le choix d'une échelle spatiale impose celui du rapport α/K. Autrement dit, pour un revêtement ayant une loi de comportement fixée (α, p) l'intensité de frottement dépend de l'échelle spatiale.

  Si $p = 0$ on retrouve un frottement indépendant de l'échelle.

- Si $p \neq m$ le choix d'une échelle temporelle impose celui du rapport α/K. C'est-à-dire que pour un revêtement donné l'intensité du frottement dépend de la vitesse de déformation.

  Si $p = m$, en particulier dans le cas Von Mises $p=m=0$, le frottement est indépendant de la vitesse.

Ces trois conditions assurent l'équilibre mécanique de deux corps déformables cinématiquement semblables. Elles sont donc suffisantes pour assurer la similitude.

Les critères de similitude parfaite compliquent le dépouillement du test de l'anneau. Néanmoins, la connaissance de p, K et m, des échelles spatiale et temporelle et l'application de ces règles permettent de déterminer α à partir d'une abaque (p, m) $\Delta\emptyset_i\% / \Delta H\%$ calculée pour des dimensions d'anneau et une vitesse de forgeage arbitraire.

Pour ce faire, il est nécessaire de connaître p a priori. Ceci n'est généralement pas réalisé. De plus, il semble qu'il faille disposer d'un jeu d'abaques pour tous les couples (m, p) représentatifs d'un matériau et d'un frottement réel. Ces difficultés peuvent être résolues par l'application des règles de similitude approchées.

3.2.2.3 - Conditions de similitude approchée : détermination de p

On considère que deux écoulements pourront être approximativement semblables si m_1 est peu différent de m_2 et p_1 peu différent de p_2. La notion de " peu différent " dépendra de la qualité de la similitude recherchée.

Dans ce cas le rapport des intensités de frottement s'écrit :

$$f_2/f_1 = 3^{(m_2-m_1)/2} \frac{\alpha_2/K_2}{\alpha_1/K_1} (L_2^{p_2}/L_1^{p_1}) \frac{\dot{\varepsilon}_2^{p_2-m_2}}{\dot{\varepsilon}_1^{p_1-m_1}}$$

La condition de similitude approchée impose uniquement $f_2/f_1 = 1$.

La condition de similitude entre un matériau rigide plastique de Von Mises et un matériau du type fluide s'énonce $f = \bar{m}$. Il s'ensuit qu'on peut considérer $\bar{m}$ comme une mesure de l'intensité de frottement.
Le rapport des intensités de frottement pour des anneaux réalisés dans le même matériau et forgés avec le même lubrifiant peut alors s'écrire :

$$f_2/f_1 = \bar{m}_2/\bar{m}_1 = (L_2/L_1)^p \left(\dot{\varepsilon}_2/\dot{\varepsilon}_1\right)^{p-m}$$

Il s'ensuit que p peut se déterminer en comparant les intensités de frottement pour des anneaux de taille différente, et m-p s'obtient à partir du forgeage d'anneaux identiques réalisés à des vitesses différentes.

3.2.2.4 - Application à la détermination des coefficients tribologiques du revêtement mentionné au § 3.1.1

L'anneau est de géométrie 6/3/2 et de hauteur 20 mm. La vitesse de forgeage est constante. La vitesse de déformation indiquée est la vitesse de déformation initiale. La loi de comportement de l'alliage a été déterminée par ailleurs et vaut $\sigma = 105 \times \dot{\varepsilon}^{0,25}$

Les réductions relatives du diamètre intérieur sont reportées sur l'abaque TVM(fig. 2a). Les coefficient de frottement correspondants sont reportés sur un diagramme $m/\dot{\varepsilon}$ (fig. 2b). α est ajusté en reportant les réductions de diamètre sur une abaque (p,m) (fig. 2c).

3.3 - Conclusion

La formulation en couche limite $\tau = \alpha \times V_g^p$ du frottement est compatible avec une formulation fluide du matériau.

Elle représente bien la couche de verre lubrifiant et est particulièrement adaptée à la modélisation d'opérations de forgeage où l'amplitude de variation de vitesse est grande. On a montré dans ce chapitre une méthode d'identification des paramètres α et p. Elle a été appliquée à un émail lubrifiant pour le forgeage isotherme du TA6V.

4 - ETUDE EXPERIMENTALE ET NUMERIQUE DE LA GAMME DE FORGEAGE D'UN DISQUE DE COMPRESSEUR EN TA6V

4.1 - Conduite des forgeages

Le disque forgé est représenté en fig. 3.

4.1.1 - Simulation sur alliage Pb 38 - Sn 62

L'échelle de travail est 1 : 3 des dimensions réelles. Les lopins sont usinés dans une barre extrudée dans un rapport 4 : 1. Avant le forgeage final, les ébauches sont mises à la dimension par un écrasement en bague. Une, élancée, a un rapport hauteur sur diamètre H/Ø = 0,93 (fig. 4a) ; pour l'autre, plus plate, on a H/Ø = 0,40 (fig. 5a). Le forgeage est effectué sur une presse hydraulique. Il est interrompu pour relever la forme de la pièce au conformateur.

4.1.2 - Forgeage numérique

Pour les vitesses de déformation considérées, la loi de comportement de l'alliage Pb 38 Sn 62 est $\sigma = 64 \times \dot{\varepsilon}^{0,15}$. Celle du TA6V vaut $\sigma = 105 \times \dot{\varepsilon}^{0,25}$. L'expérience montre que l'alliage PbSn permet de bien simuler le remplissage de la gravure au cours de forgeage du TA6V. Les simulations numériques ont été effectuées avec la loi de comportement du TA6V. La loi de frottement est celle identifiée au chapître précédent. Trois remaillages ont été nécessaires pour achever le calcul.

4.1.3 - Forgeage isotherme du TA6V

Suite aux simulations effectuées, seule l'ébauche plate a été forgée. Sa mise aux cotes résulte d'un forgeage conventionnel à la presse. Dans ce cas aussi les écrasements ont été interrompus pour un relevé des formes intermédiaires. La lubrification est effectuée avec l'émail caractérisé au chapître précédent.

4.2 - Evolution des écoulements extérieurs : choix des dimensions de l'ébauche

4.2.1 - Simulation Pb-Sn

Dans le cas de l'ébauche élancée, la toile centrale se fait poinçonner ; la surface latérale devient tonnoïde. Pour une réduction de hauteur de 66 %, la jante se referme en contre dépouille sur le noyau central : c'est une amorce de repli (fig. 4b).

La surface latérale de l'ébauche plate touche la paroi extérieure de la matrice dès le début du forgeage. La jante se remplit par un filage simultané vers le haut et vers le bas de la gravure ; cependant l'écoulement vers le haut est favorisé par la dépouille de la matrice (fig.5b). Le remplissage du bossage supérieur et du congé inférieur a lieu en fin d'écrasement et reste imparfait (fig. 5c).

4.2.2 - Forgeage numérique (fig. 6-7)

Pour les deux formes d'ébauches, les écoulements extérieurs calculés sont identiques aux écoulements expérimentaux, l'ébauche plate permet le remplissage correct de la gravure.

4.3 - Morphologie du fibrage : modification du brut de forge

4.3.1 - Fibrage du TA6V et représentation numérique

Pour le TA6V, le fibrage traduit l'anisotropie macroscopique des grains α qui apparaît lors de la conversion du lingot en billette. Lors d'un forgeage tel qu'il est décrit ici, conduit sous le transus β on peut considérer que les grains α se comportent comme des particules dures transportées par la matrice β . Le fibrage calculé résulte aussi du transport des noeuds d'un maillage convectif.

Un fibrage trop sinueux avec des replis conduit à des faiblesses en fatigue oligocyclique.

4.3.2 - Allure du fibrage expérimental (fig. 8)

Il suit assez bien le contour extérieur du disque. Cependant, il est relativement sinueux au débouché de la toile centrale et se replie près de la surface du disque. De plus, il existe trois singularités sur le contour intérieur. Deux replis se sont formés tout autour des noyaux supérieurs et inférieurs à environ 15 mm de la toile. Les forgeages interrompus montrent qu'ils apparaissent lorsque le filage de la jante est arrêtée par le fond et le sommet de la matrice. La troisième singularité se situe au 3/4 de la hauteur du noyau central. Endessous de ce point, le fibrage est ascendant ; au-dessus, il est descendant.

4.3.3 - Allure du fibrage calculé

On a testé deux procédés. Le premier est une description de l'opération réelle : le fibrage initial est celui du lopin après ébauchage final à la presse. Le deuxième aurait consisté en un forgeage direct d'une ébauche usinée dans une barre de grand diamètre : le fibrage initial est cylindrique.

Dans le premier cas (fig. 9), on retrouve un faciès similaire au fibrage réel : en particulier le repli interne qui prolonge l'écoulement, au débouché de la toile et le point singulier au 3/4 du noyau supérieur. Les replis n'apparaissent pas, on peut supposer qu'ils résultent d'une instabilité locale que FORGE 2 ne sait pas détecter.

Dans le deuxième cas (fig. 10c) le fibrage est plus régulier et garde le faciès général de celui de la barre d'origine. On remarque néanmoins la singularité au 3/4 du noyau. L'observation des états intermédiaires montre que celle-ci provient du poinçonnement en début de forgeage (fig. 10a-b). Il apparaît aussi, quoique moins marqué que dans le cas précédent, un début de sinuosité au débouché de la toile.

Ces comparaisons deux deux fibrages montrent bien l'influence des deux opérations de forge sur la macrostructure du produit final. On pourrait être tenté, au vu de ce résultat, de forger une ébauche directement usinée dans la barre mais cette gamme n'assure pas un corroyage suffisant dans le volume du disque (fig. 11).

Une modification du brut qui augmente un peu sa masse réduit les contraintes dans les matrices, consiste à agrandir les congés (R5 → R20) du raccordement toile/noyau ; le fibrage résultant (fig. 12) est tout à fait satisfaisant.

5 - CONCLUSION

FORGE 2 est un outil opérationnel à la forge de la SNECMA pour étudier une gamme de forge de façon rationnelle. Même avec des lois rhéologique et tribologique simples, ce logiciel permet de décider du choix d'un brut de forge et d'une gamme à partir de critères tels que l'évolution du fibrage ou la répartition des déformations.

De l'observation des états intermédiaires entre l'ébauche et la pièce forgée résulte une meilleure compréhension des écoulements et de la formation des défauts. Bien que cet aspect n'est pas été présenté ici, FORGE donne aussi accès aux contraintes sur les matrices.

D'autres développements de ce code, financés par des industriels européens dont la SNECMA et les Services Officiels Français, sont en cours ou en voie d'achèvement au CEMEF (forge 2D avec thermique, 3D avec ou sans thermique, amélioration des temps de calcul). Ils permettront d'accroître le champ d'application de FORGE 2.

REFERENCES

1 GERMAIN Y.; 1985 ; Modélisation par éléments finis d'écoulement viscoplastique avec frottement. Application au forgeage à chaud ; Thèse de docteur-ingénieur - Ecole des Mines de Paris

2 HILL R. ; 1956 ; New horizons in the mechanics of solids ; J. of Mech. and Phys. of solids ; 5 : 60-74

3 BAQUE, P. ; 1973 ; Mise en forme des métaux. Calcul par la plasticité ; DUNOD

4 de PIERRE, V. ; GURNEY, F. ; MALE, A.T. ; 1972 ; Mathematical Calibration of the Ring Test with Bulge Formation ; AFML-TR-72-37

5 SCHEY, J.A. ; 1983 ; Tribology in Metal Working ; ASM

6 SEDOV, L. ; 1972 ; Similitude et dimensions en mécanique ; édition MIR

7 SCHOLZE, H.; 1980 ; Le Verre, nature structure et propriétés ; Institut du verre, Paris.

8 GERMAIN, Y. ; CHENOT J.L. ; MOSSER P.E. ; 1986 ; Finite Element Analysis of Shaped Lead-Tin Disk Forgings ; proceedings of Numiform 86

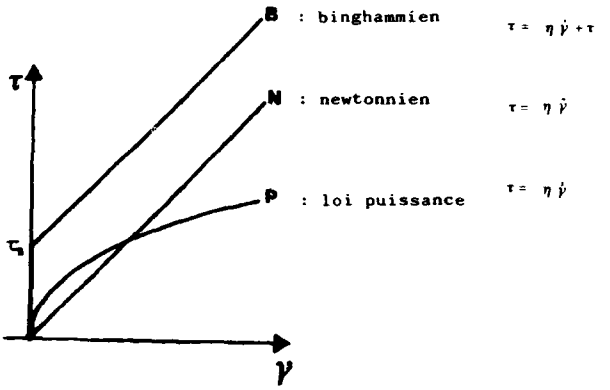

Fig. 1 : Type de comportement rhéologique d'un émail de lubrification de forgeage

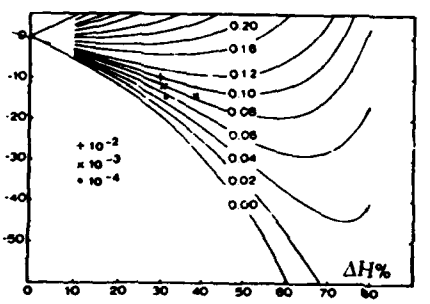

Fig. 2a : *dépouillement* du test de l'anneau suivant une abaque TVM

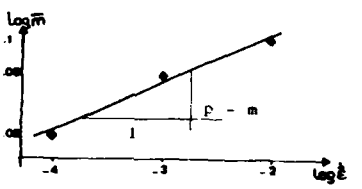

Fig. 2b : identification de p-m

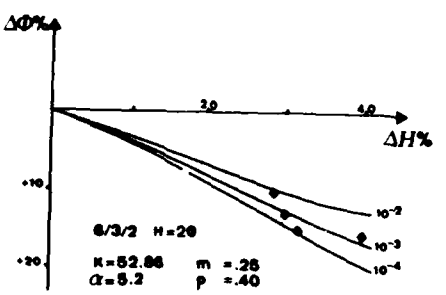

Fig. 2c : ajustement du coefficient α

Fig. 2 : Identification d'une loi de frottement pour une formulation en couche limite - Anneau 6/3/2 - H = 20 mm - matériau TA6V - $\sigma = 105\ \dot{\bar{\varepsilon}}^{0,25}$

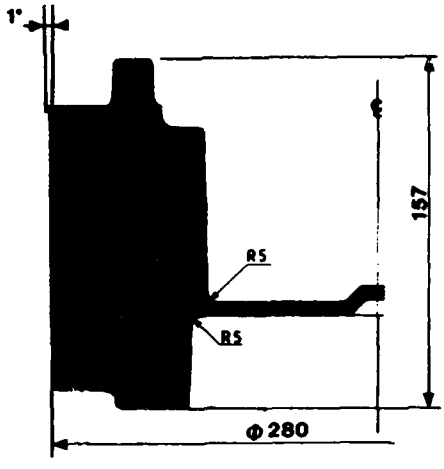

Fig. 3 : Disque de compresseur

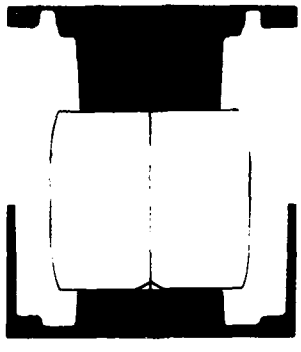

Fig. 4a : ébauche élancée
H/Ø = 0,93

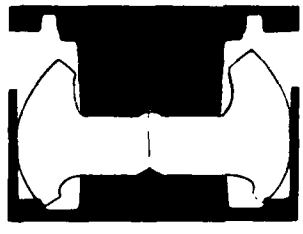

Fig. 4b : formation d'un repli
(cote + 20 ΔH% = - 66%)

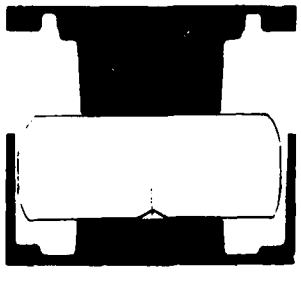

Fig. 5a : ébauche plate
H/Ø = 0,40

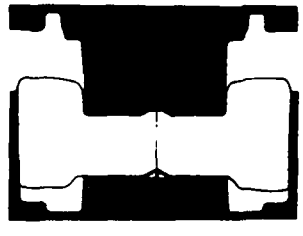

Fig. 5b : filage simultané de la jante (cote + 20 ΔH% = -42%)

Fig. 5c : fin de forgeage l'écoulement est sain

Fig. 4 et 5 : Evolution des contours au cours de la simulation de forgeage avec l'alliage Pb38 Sn62

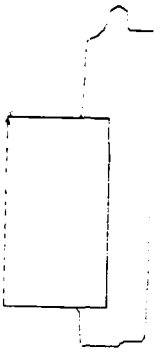

Fig. 6a

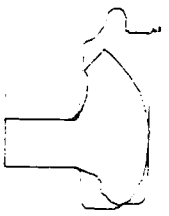

Fig. 6b

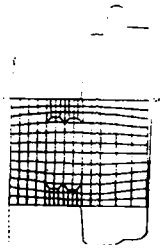

Fig. 7a

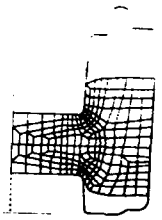

Fig. 7b

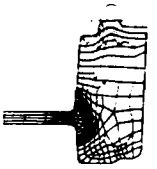

Fig. 7c

début de forgeage

cote finale + 20

cote finale + 2

Fig. 6 et 7 : Evolution des contours au cours de la simulation numérique

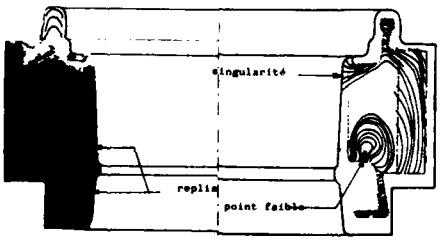

Fig. 8 : Fibrage expérimental sur disque PbSn - Superposition avec le contour de la pièce terminée

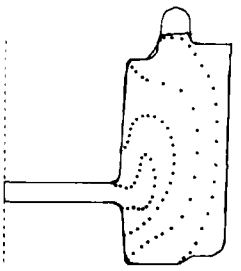

Fig. 9 : Fibrage calculé pour un disque réalisé à partir d'une ébauche forgée conventiellement

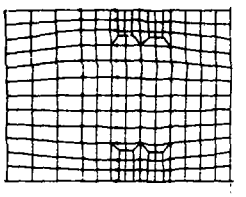

Fig. 10 a ΔH% = 0

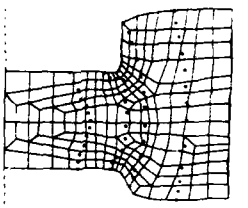

Fig. 10 b ΔH% =-42

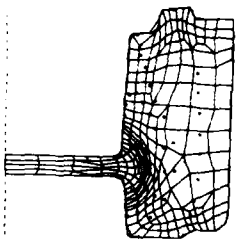

Fig. 10 c ΔH% =-88

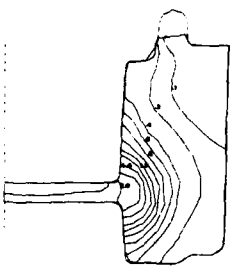

Fig. 11

Fig. 10 : Evolution du fibrage pour un disque forgé à partir d'un lopin

Fig. 11 : Répartition de l'écrouissage

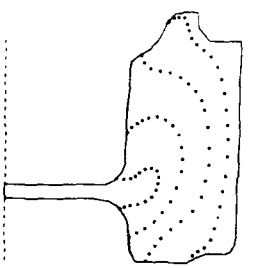

Fig. 12 : Amélioration du fibrage pour un brut de forge modifié

COMPUTER PREDICTION OF INTERNAL STRESSES DURING HEAT TREATMENT*

by

D.Assaker and M.Hogge
LTAS – Thermomécanique
Université de Liège
rue Ernest Solvay 21
B-4000 Liège, Belgium

ABSTRACT: The problem of determining stresses due to thermal and transformation-induced volume changes during the quenching of hot steel bodies is investigated. Since there is no proper experimental way to determine the local stress field during the heat treatment, a finite element model that addresses this problem is developed, which allows for stress history knowledge and prediction of the residual stress field in the finished body.
All thermophysical properties are temperature dependent. In case of steel bodies an additional parameter related to the cooling rate enables to localize microstructure state on a Continuous Cooling Transformation diagram. The efficiency of the model is demonstrated through a detailed computation of stresses in a quenched steel cylinder.

NOTATIONS

t	(Δt)	time (increment)
t_f		cooling time to get from T_0 to T_f when using the exponential law
T	(ΔT)	temperature (increment)
T_0		austenitic temperature
T_f		fixed temperature
τ		theoretical cooling law parameter
δ_{ij}		Kronecker symbol

STRAIN

$\underline{\varepsilon}^e$	$(d\underline{\varepsilon}^e)$	elastic strain (increment)
$\underline{\varepsilon}^p$	$(d\underline{\varepsilon}^p)$	plastic strain (increment)
$\underline{\varepsilon}^{th}$	$(d\underline{\varepsilon}^{th})$	thermal strain (increment)
$\underline{\varepsilon}^m$	$(d\underline{\varepsilon}^m)$	mechanical strain (increment)
$\underline{\varepsilon}^{tot}$	$(d\underline{\varepsilon}^{tot})$	total strain (increment)
k		strain hardening parameter
$\bar{\varepsilon}^p$		equivalent plastic strain
$d\lambda$		plastic strain rate parameter in the flow rule

STRESS

$\underline{\sigma}$	$(d\underline{\sigma})$	stress tensor (increment)
$\bar{\sigma}$		von Mises effective stress
$\underline{t}$		deviatoric stress tensor
F,f		load functions
$\underline{a}$		$\partial f/\partial \underline{\sigma}$
$\underline{g}$		$H*\underline{a}$

MECHANICAL PROPERTIES

E	Young modulus
ν	Poisson's ratio
h	yield stress
h'	strain hardening modulus
$\underline{\underline{H}}$	matrix of elastic compliances

THERMAL PROPERTIES

α_t	linear (tangent) thermal expansion coefficient
α_s	secant thermal expansion coefficient
α_m	mean thermal expansion coefficient

---

* This paper is dedicated to the memory of Professor G. SANDER

0- INTRODUCTION AND LITTERATURE REVIEW

Among general thermo-mechanical loaded structures, the case of bodies subjected to heat processes like quenching is an important one for industrial and economical reasons. Due to the difficulty and cost of the experimental means of investigation, it is very beneficial to preview strain and stress histories during the cooling process and at the end of the quench (residual stresses) by numerical computations such as those issued from Finite Element models. These numerical computations should help practitioners to obtain bodies with known internal strain and stress states and should avoid unfavourable final geometries or cracks.

Macroscopic residual stresses can be divided into two classes:

i) The thermal stresses due to non homogeneous temperature distribution in space and time.

ii) The structural stresses resulting from volume changes during phase transformation in steel bodies.
Both classes may lead to plastic irreversible strains and stresses.

A typical residual stresses distribution for the cross section of a cooled cylinder is represented on fig 1. In case of elastic behavior the stresses are tension stresses at the surface and compression ones at the core (fig 1,curve 1). Surface contraction due to quick cooling is prevented by the core which is still at higher temperatures. No stresses reversal along the radius is observed.
In case of elastic-plastic behavior, the typical stresses distribution is shown on fig 1, curve 2. We observe a stress sign reverse at time t_u. Note that phase transformation may change considerably these stresses profiles in case of steel bodies [see section 3D].

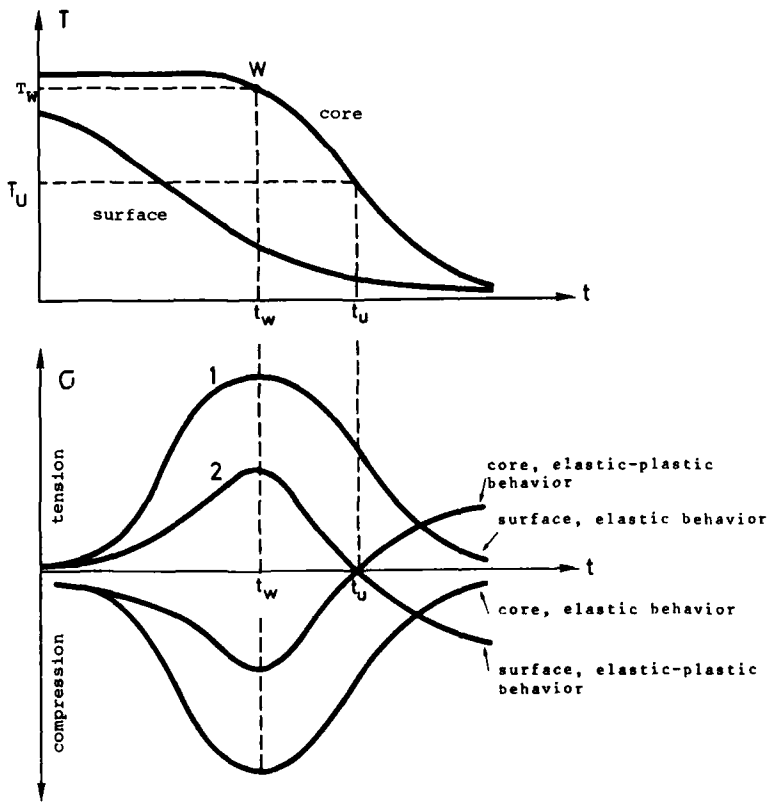

Fig. 1 - Typical temperature and stresses distributions in a quenched cylinder

At first, qualitative explanations of residual stresses distribution were attempted by BUHLER (1930) and ROSE (1950) [S1]. Both of them try to explain the stress state observed at core and surface of quenched cylinders according to steel microstructure.

Quantitative studies were also done on simplified models: elastic or elastic-perfectly plastic materials, constant thermo-physical properties, simplified geometries,...(works by SCOTT (1925), MAURER (1928), MURA (1957), ...)

Recent works are based on nonlinear finite element codes with a thermo-elastic-plastic model using small strain hypothesis and considering (or not) creep effects. The difference between these models is the manner of taking into account phase transformation .

INOUE et al. [I1,I2] studied these deformations by considering that the thermal expansion coefficient α_c is temperature and cooling rate dependent.
SJOSTROM [S1] and HILDENWALL [H1] used an Isothermal transformation cooling diagram [see section 1] and considered phase transformation as carbon content and instantaneous temperature dependent.
DENIS [D1] introduced couplings between phase transformation and stress history.
RAMMERSTORFER [R1] took into account phase transformation by considering sharp variations of α_c with temperature and by reducing the yield stress in the phase transformation temperature intervals.

This brief litterature review is clearly not complete but it outlines the complexities and difficulties in the model:

- All thermo-mechanical properties must be temperature and microstructure dependent.

- Couplings exist between metallurgical properties, temperature history and stress history.

- Determination of the effective thermomechanical properties during cooling for steel bodies: a choice is to be made between an isothermal or a continuous cooling diagram, depending on the heat treatment processes analysed.

This class of problems has long been adressed to by CRM* [M1] and his industrial partners. We have been asked to include all these aspects in the nonlinear finite element code SAMNL of SAMCEF [S2]. Geometries to be studied can be complex and several steel compositions may be present in the same body.

1- STEEL COOLING DIAGRAMS

Steel or steel alloy bodies present during the heat process different phases or microstructures.
We can describe the cooling process with one of the two classical diagrams [C1]:

- Isothermal Transformation diagram (IT diagram)

- Continuous Cooling Transformation diagram (CCT diagram)

When a IT diagram is used in the heat process modelling, we suppose that a sudden cooling (instantaneous) leads the metal from austenitic temperature to a temperature T which is kept constant for the whole transformation history. The metal at T is no longer stable and evolves towards an equilibrium state (perlite, bainite, martensite,...)

In industrial treatments, heat processes cannot be considered as isothermal ones. In fact, the temperature evolves from the austenitic temperature to room temperature in a continuous manner. Using a IT diagram supposes then that the complete cooling curve is divided into several instantaneous temperature increments followed by an isothermal process during a time step. The microstructure of the steel during cooling is then deducted from the IT diagram. This approximation may be severe in case of slow quenching processes.

CRM chooses instead to study thermo-mechanical properties referring to a CCT diagram. This is thinked to be more reliable to give a true image of the effective properties in industrial processes.

*CRM, Centre de Recherches Métallurgiques.
Abbaye du Val Bénoît, 4000 Liège, BELGIUM

This determination is however based on the following approximations:

i) A CCT diagram is valid only for the exact temperature history in the body. Therefore, we should simulate on test machines the effective cooling curves.In fact, for practical and economical reasons, the real CCT diagram is obtained from several imposed exponential cooling laws from austenitic temperature T_0 to T temperature,

$$T(t,\tau) = T_0 \, EXP[-t/\tau] \qquad (1.1)$$

where τ is the cooling law parameter.

This approach has been checked experimentally (hardness measurements) and the real CCT diagram is very similar to the "exponential" one for the quenching processes we are considering here.

ii) The temperature history for each point of the heat treated body is matched (fig 2) by an exponential law of type (1.1), where τ becomes a location dependent cooling law parameter. Its physical meaning is obviously a decay constant. If we define t_f as the cooling time for getting from T_0 to T_f (a given final temperature that insures a stable microstructure), we get

$$\tau = t_f \; / \; \ln [T_0/T_f] \qquad (1.2)$$

i.e. τ is proportional to this local cooling time.

In our model T and τ are hence the parameters that permit to evaluate in each point the thermomecanical properties - especially the coefficient of thermal expansion - used in the stress and strain computational model.
This latter coefficient α_t is the linear (tangent) one which can be very different from the secant one in the phase transformation areas (point 2, fig 3).

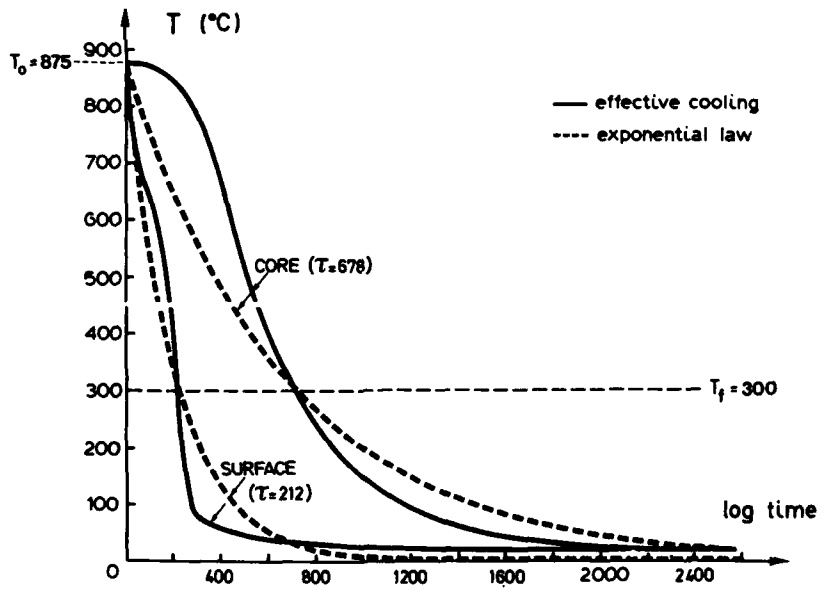

Fig. 2 - Effective and exponential temperature histories

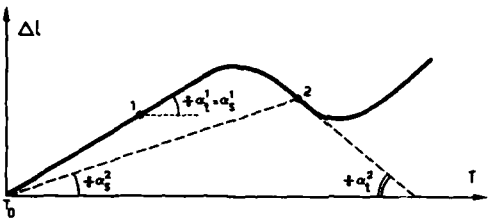

Fig. 3 Linear and secant thermal expansion coefficients

2- PRESENTATION OF THE MECHANICAL AND NUMERICAL MODELS

2.A- THE MECHANICAL MODEL AND THE COUPLINGS BETWEEN PHENOMENA

In thermo-mechanical processes, cross interactions exist between temperature history, stress history and phase transformations as shown on the flow chart below (fig 4).

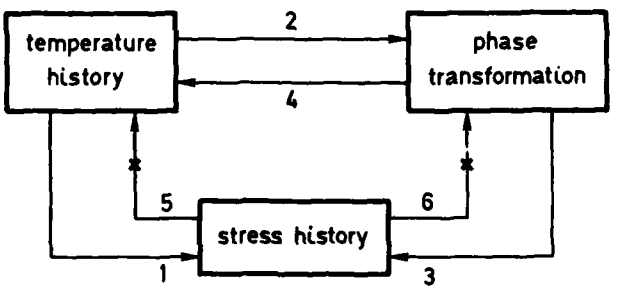

Fig. 4 - Diagram of couplings in the quenching problem

Currently, our mechanical model takes into account the following interactions:

1) Temperature - Stress, through experimental determination of the thermo-mechanical properties and the evaluation of a thermal strain for isotropic materials by

$$\varepsilon_{ij}^{th} = \delta_{ij}\alpha_m^*(T2 - T1) \qquad (2.1)$$

where $$\alpha_m = \frac{1}{T2 - T1}\int_{T1}^{T2} \alpha_t \, dT \qquad (2.2)$$

2) Temperature - Phase transformation,through a Continuous Cooling Transformation (CCT) diagram.

3) Phase transformation - stress,through the phase transformation induced volume changes due to microstructural rearrangements. This is reflected on the variation of the thermomechanical properties and especially on the variation of the linear coefficient of thermal expansion .

4) Phase transformation - Temperature, indirectly through the variation of thermophysical properties with temperature during phase changes.

Our model does not take into account the remaining couplings:

5) Stress - Temperature: the heat generated by the plastic deformation is neglected and does not affect significantly the temperature history.

6) Stress - Phase transformation: we consider here that the CCT diagram is not affected by the stress state.

The mechanical model is therefore a quasi-static one with instantaneous adaptation of the thermomechanical properties to T and τ, both being determined previously by separate numerical or experimental analyses.

2.B- THE INCREMENTAL CONSTITUTIVE RELATIONS FOR THE THERMO-ELASTIC-PLASTIC MODEL

Assuming small strains, the total strain increment is decomposed into 3 components:

$$d\varepsilon^{tot} = d\varepsilon^{e} + d\varepsilon^{p} + d\varepsilon^{th} \qquad (2.3)$$

from which the mechanical strain increment is computed by

$$d\varepsilon^{m} = d\varepsilon^{tot} - d\varepsilon^{th} = d\varepsilon^{e} + d\varepsilon^{p} \qquad (2.4)$$

In equation (2.3) the different components are:

(i) the elastic component $d\varepsilon^{e}$, which is related to the stress state through HOOKE's law

$$\varepsilon^{e} = H^{-1}\,\sigma \quad \text{or} \quad d\varepsilon^{e} = H^{-1}\,d\sigma \qquad (2.5)$$

When E and ν are T and τ dependent, we shall consider the variation of the matrix of elastic compliances

$$d\varepsilon^{e} = H^{-1}\,d\sigma + (dH^{-1})\,\sigma \qquad (2.6)$$

(ii) the plastic component $d\varepsilon^{p}$, which is obtained from the von MISES yield criterion with isotropic hardening. The loading function is therefore

$$F(\sigma,\bar{\varepsilon}^{p},k,T,\tau) = f(\sigma) - h^{2}(\bar{\varepsilon}^{p},T,\tau) = 0 \qquad (2.7)$$

where $$f(\sigma_{ij}) = (3/2)\,t_{ij}t_{ij}$$

h stands for the yield stress, depending on a hardening parameter $k=k(\bar{\varepsilon}^{p})$, temperature T and cooling rate τ.

The variation of h can be obtained through experimental stress-strain relations such as an uniaxial tensile test at different temperatures and cooling rates.

The plastic strain increment is normal to the loading function so that we may write the flow rule

$$d\varepsilon^p = d\lambda(\partial f/\partial\sigma) \ , \qquad d\lambda \geq 0 \qquad (2.8)$$

$$= d\lambda \ a \qquad a = \partial f/\partial\sigma$$

where $d\lambda$ is given by [N1,L2] :

$$d\lambda = \frac{g^T d\varepsilon^m - (h^2 - f)}{a^T g + 4 \bar{\sigma} h h'} \qquad (2.9)$$

In this formula, note that h stands for the yield stress state at the end of the time step, while f is evaluated at the beginning of the time step.

The non-isothermal elastic-plastic incremental relations $d\sigma=f(d\varepsilon^m)$ are obtained by substituting (2.5), (2.8) and (2.9) in (2.4).

(iii) the thermal strain increment $d\varepsilon^{th}$, which is given by the variation of the thermal strain during the time step:

$$d\varepsilon^{th} = \varepsilon^{th}_{T2} - \varepsilon^{th}_{T1} = \int_{T1}^{T2} \alpha_t \, dT = \alpha_m^*(T2 - T1) \qquad (2.10)$$

The preceding constitutive law is introduced by virtue of the principle of virtual work in incremental form into classical displacement type finite elements [N1]. The associate static equilibrium equations are solved by means of a Newton-Raphson solution technique.

3- CALCULATION OF QUENCH STRESSES IN A STEEL CYLINDER

A long cylinder is quenched from the austenitic temperature (875 °C) to room temperature (20 °C).
Our purpose is to study the quench stresses history during the cooling process as a result of volume changes due to phase transformation and temperature gradients.

3.A- Geometry and Finite Element model

A state of generalized plane strain is imposed for a radial strip of material (i.e. the central section of the cylinder), so that the kinematic boundary conditions are (fig 5):

* zero z-displacements at the bottom nodes

* equal z-displacements at the top nodes.

23 axisymetric, rectangular elements with linear displacement field are used in the model (R=114 mm). The mesh is refined near the surface because of the localized steep temperature gradient at the beginning of the quench.

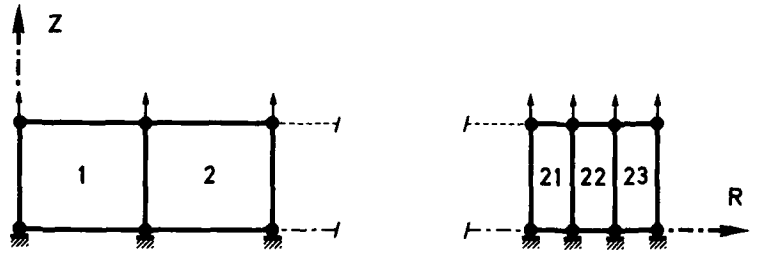

Fig. 5 - Finite element discretization and boundary conditions

3.B- Incremental loading

In the present case, the loading is uniquely due to thermal gradients (no mechanical loading). The temperature history is computed independently of the stress calculation [M2]. We divide the load into 16 increments or time steps (fig 6). The corresponding τ parameter along the cylinder radius is presented in fig 7. It is obtained through the procedure described in section 1.

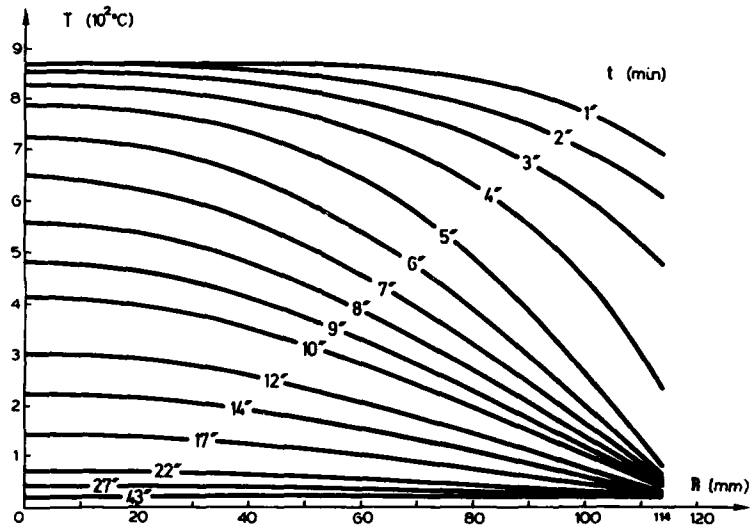

Fig. 6 - Temperature history

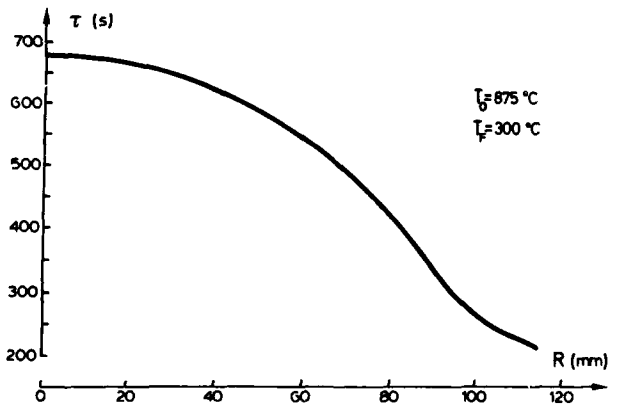

Fig. 7 - Point dependent cooling law parameter

3.C- Thermo-mechanical properties

The yield stress, the hardening parameter and the linear coefficient of thermal expansion are taken as temperature and cooling rate dependent (fig 8, 9).
The effect of the phase transformation on the linear coefficient of thermal expansion is clearly shown in fig 9 (negative values of α_t).
The Young modulus is considered temperature dependent only and Poisson's ratio is constant (ν = 0.33).

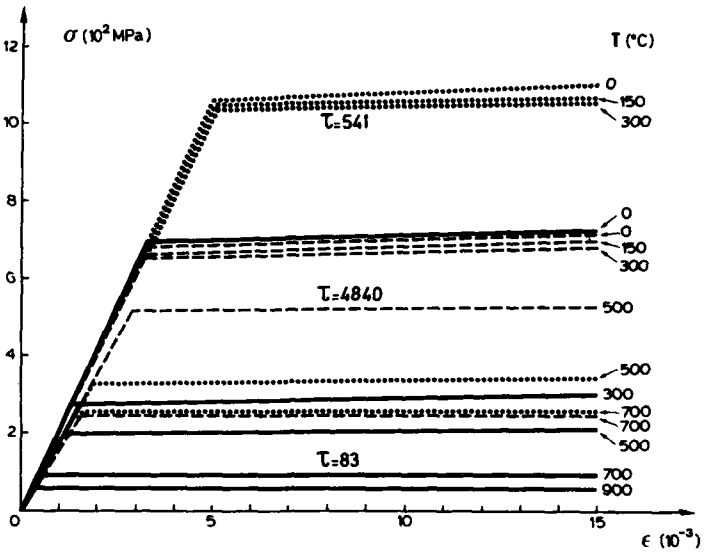

Fig. 8 - Material stress strain relation (T and τ dependent)

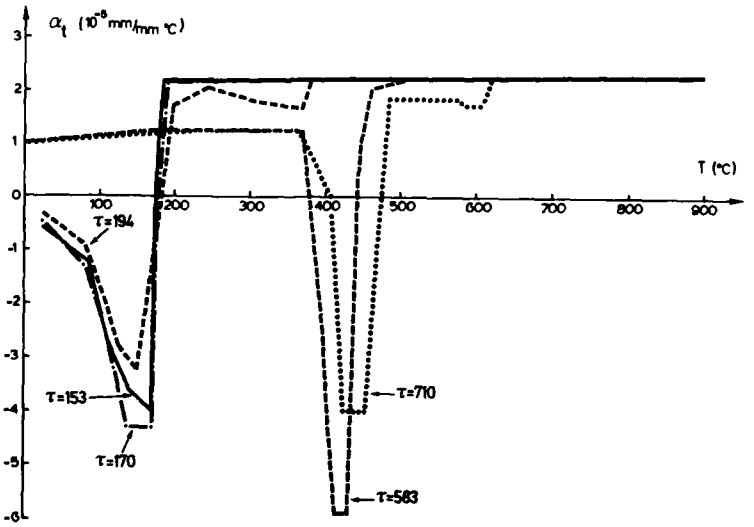

Fig. 9 - Material linear coefficient of thermal expansion (T and τ dependent)

3.D- Numerical results

The element mean stresses variations (σ_r, σ_θ, σ_z) versus radius are presented in fig 10, 11, 12, 13, 14 and 15 for increments 4, 5, 7, 9, 10 and 16, the latter defining the residual stresses.
Another representation taking the variations of the same quantities versus time is given in fig 16 for the near-axis element (element 1) and the near-surface element (element 23).

3.E- Discussion of the results

Since no experimental validation of the present finite element results currently exists, we can only make a number of comments regarding the plausibility of the results (computed results will be compared to measured residual stresses later on) :

1) Obviously σ_r vanishes at the surface at any time and is equal to the σ_θ value at the center of the cylinder.

2) The convergence of the computed results when the mesh or the loading incrementation are refined has been analysed.
In that sake, we show on fig 17 σ_θ and σ_z versus time when the temperature history is applied in 31 increments instead of 16. The same results are shown on fig 18 in case of a refined spatial mesh with 57 elements.
The results are very similar in the 3 computations, therefore we assumed that numerical convergence has been reached.

3) A qualitative examination of stresses shows that we have compression stresses at core and tensile stresses at surface in the beginning of the quench. The reason is that the surface is cooled quickly whereas the core is still at high temperatures. Core will then prevent surface from extending. This distribution will tend to reverse during the quench. The residual stresses are compression stresses at surface and tension stresses at core (Buhler-Rose hypothesis).

4) We have a discontinuity in stress distribution at surface between the 4^{th} time step and the 5^{th} one. We notice a similar discontinuity at core between the 9^{th} and the 10^{th} time step.
Table 1 shows that the reason for that is that surface will exhibit a sharp variation of α_t between increment 4 and 5 (martensitic transformation) while this is the case for the core between increment 9 and 10 (bainitic transformation).

INCREMENT 4		INCREMENT 5		INCREMENT 9		INCREMENT 10	
core	surface	core	surface	core	surface	core	surface
T = 830 τ = 678	T = 240 τ = 212	T = 789 τ = 678	T = 84 τ = 212	T = 484 τ = 678	T = 45 τ = 212	T = 416 τ = 678	T = 41 τ = 212
α_t = 23E-6	α_t = 20E-6	α_t = 23E-6	α_t = -9E-6	α_t = 19E-6	α_t = 4.5E-6	α_t = -29E-6	α_t = -4E-6

4- FUTURE WORK

CRM is now processing experimental validation of the present model on a oil quenched cylinder. Temperature history is measured and thermophysical properties are temperature and cooling rate dependent. Stresses will be evaluated in the median section of the cylinder by Sachs technique.

On the other hand further numerical investigations will be performed on the present model. Different interpolation techniques will be tried and results compared with the current linear interpolation. A kinematic hardening law will be introduced so that cyclic plasticity that can appear in a monotonic quenching process should be correctly handled [R1].

The sensibility of the results to the exponential experiments and to the temperature history matching (τ parameter) will be checked and optimized so as to determine the limit parameter for the different classes of material properties.

Future developments will concern essentially creep effects. Time dependent deformations can affect the stress distribution especially in case of very thick bodies and slow quenching.

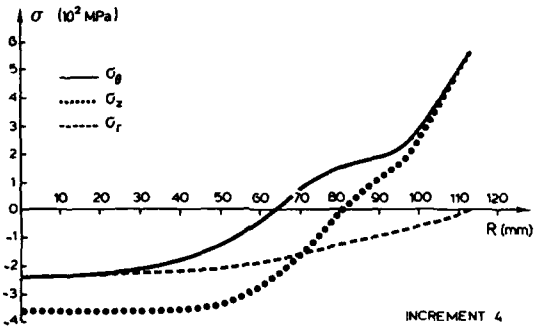

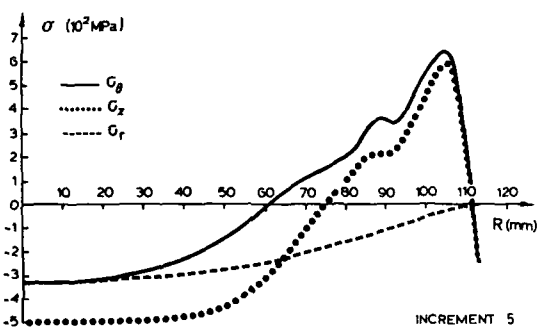

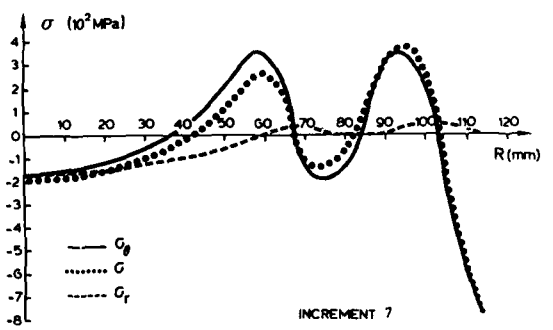

Fig. 10-11-12- Stresses distribution along the radius

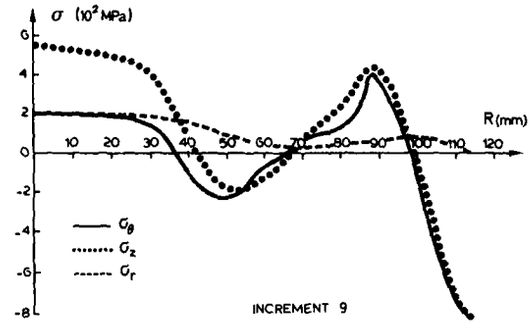

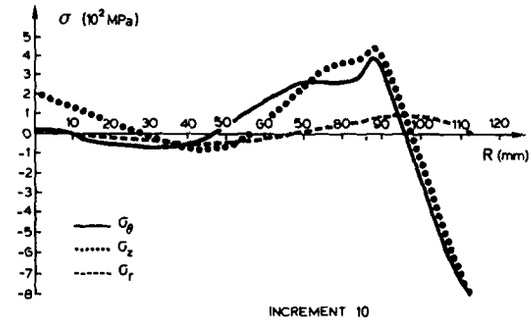

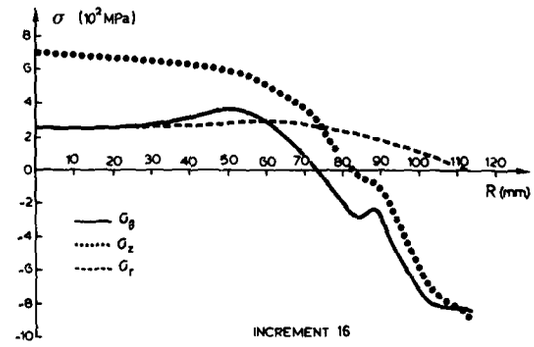

Fig. 13-14-15- Stresses distribution along the radius

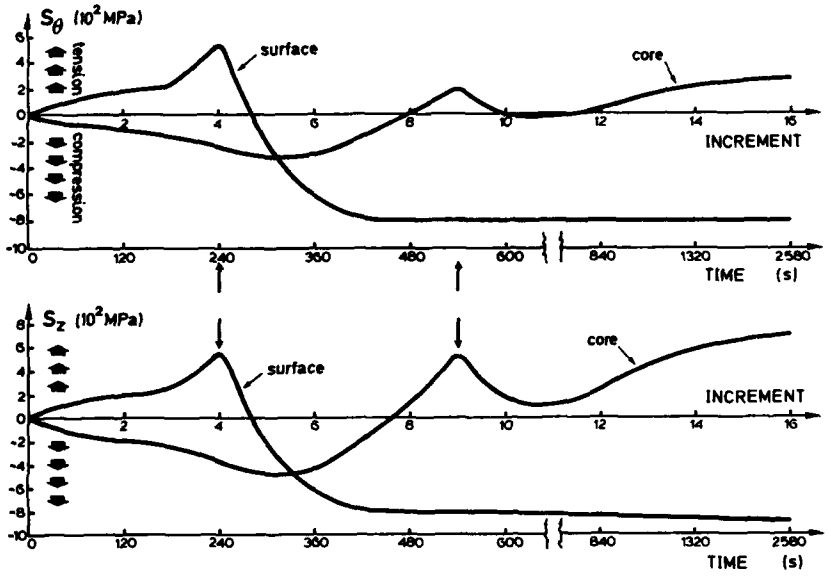

Fig. 16 - Surface and core stress histories (23 elements, 16 temperature increments)

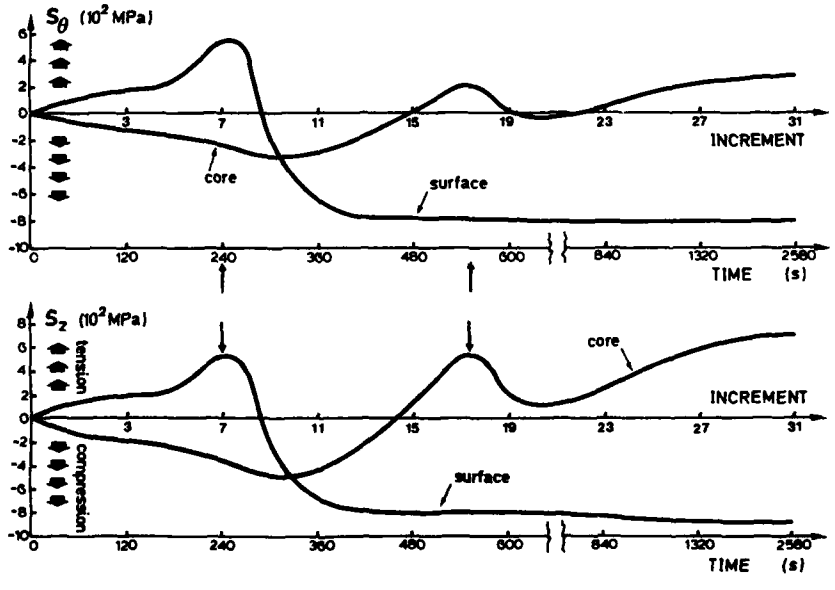

Fig. 17 - Surface and core stress histories (23 elements, 31 temperature increments)

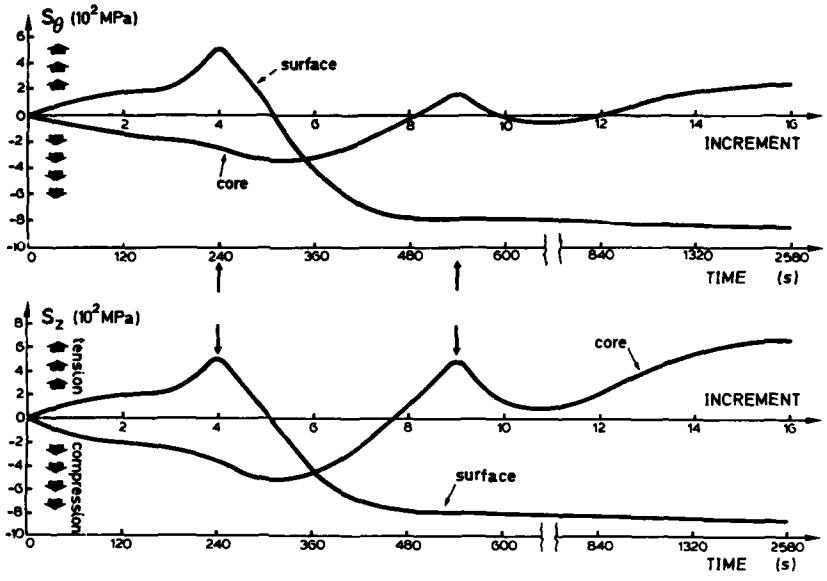

Fig. 18 - Surface and core stress histories (57 elements, 16 temperature increments)

ACKNOWLEDGMENTS

This research has been supported by IRSIA (Institut pour l'Encouragement de la Recherche Scientifique dans l'Industrie et l'Agriculture) and the companies OSB Company and MR (fonderies Marichal Ketin), Belgium. The assistance of CRM in getting the model physical properties is greatly acknowledged. Special thanks are due to MM. A. MAGNEE, M.Sc. Eng, Head of department "New materials and non ferrous", and Eng. M. DUBOIS, for helpful discussions. Special gratitude is due to M. D. COUTSOURADIS, Director, CRM and to Professor G. SANDER († 1987), Belgian Members of the AGARD SMP, for bringing this contribution to the Panel attention.

REFERENCES

C1 J.P COHEUR
Connaissance des matériaux métalliques
Notes de cours, Université de Liège

D1 S. DENIS
Modélisation des interactions contraintes - transformation de phase et calcul par éléments finis de la genèse des contraintes internes au cours de la trempe des aciers.
Thèse de Doctorat- Institut National Polytechnique de Lorraine, 1987

H1 H. HILDENWALL
Prediction of the residual stresses created during quenching.
Linkoping University- Dissertation 39, 1979

I1 INOUE - TANAKA
An elastic-plastic stress analysis of quenching when considering a transformation
Int. j. mech. sc. 1975, vol 17, pp 361-367

I2 INOUE - RANIECKI
Determination of thermal-hardening stress in steels by use of thermoplasticity theory
J. mech. phys. solids vol 26, pp 187-212, 1978

L1 J. LEMAITRE - J.L. CHABOCHE
Mécanique des matériaux solides
Dunod, 1985

L2 G. LASCHET
Etude des contraintes résiduelles de pièces de formes complexes en acier par éléments finis.
Travail de fin d'étude, Université de Liège 1977-1978

M1 A. MAGNEE et al.
Modélisation du refroidissement en four sous vide
Traitement thermique n° 184, juillet 1984, pp 39-48

M2 A. MAGNEE et al.
Contribution of progressive induction to the controled hardening treatment of steels
Advances in surface treatments- Pergamon press, vol 5, déc 1986, pp 59 - 74

N1 C. NYSSEN
Modélisation par éléments finis du comportement non linéaire des structures aérospatiales.
Thèse de doctorat, Université de Liège, 1978-1979

R1 RAMMERSTORFER - FISCHER - MITTER - BATHE - SNYDER
On thermo-elastic-plastic analysis of heat treatment processes including creep and phase changes
Computers and Structures, vol 13, pp 771 - 779, 1981

S1 S. SJOSTROM
The calculation of quench stresses in steel
Dissertation n° 84, 1982, Linkoping University, Sweden

S2 SAMNL
Module de réponse statique non linéaire de SAMCEF
LTAS - Université de Liège

SIMULATION AND DESIGN OF HIGH PRECISION UNIT PROCESSES VIA NUMERICAL METHODS

by

Dr Roger Stafford
Structural Dynamics Research Corporation
2000 Eastman Drive
Milford, Ohio 45150
USA

Abstract

Modern aerospace materials and design practices require ultra-high precision forging, casting, machining and heat treating - often beyond the capabilities of current design practices and production equipment. Manufacturing process engineers need computerised analytical design tools which precisely simulate the process and graphically identify process results such as flow, heat transfer, shrink, void formation, warpage and residual stress. Generic finite element or finite difference codes (e.g. ABACUS, MARC, Q/TRAN) are capable (in principle) of handling process simulations, but the computer power (e.g. CRAY) and special software knowledge requirements make generic codes inaccessible for practical simulations.

SDRC has developed new computer codes specifically tailored for precise and fast simulations of manufacturing processes. Critical aspects of unit processes involve nonlinear transient heat transfer coupled with slow creeping flow. Finite element methods are chosen since CAD and CAE systems support FEM data. Numerical algorithms are adopted which are specifically suited to the problem. Key elements of these simulations will be outlined, such as slidelines, interface conductance elements, automatic remeshing, radiation view factors, conjugate gradient solvers, and special post processing. These result in highly efficient unit process simulations which handle very large problems on medium-sised computers and hence are practical tools for todays manufacturing engineers.

SDRC has integrated unit process simulations with CAD/CAM design systems, MCAE analysis graphics systems, automated inspection, and data base. An example will illustrate data flow, simulation results, and how engineers are using these tools to design new processes for large complex parts.

1 Introduction

Modern jet engines and aerospace structures are increasingly using advanced casting and forging processes. Some of these involve narrow processing windows for temperature, temperature gradient, solidification rate, strain and strain rate. Traditional process design methods involving numerous shop floor trials (castings and forgings) will eventually produce a defect free casting, or a net shape forging.

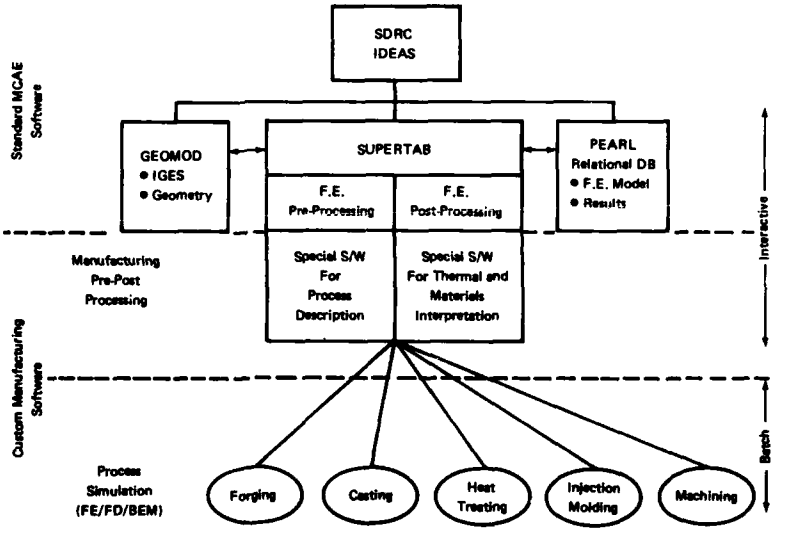

Figure 1: An Integrated Environment For Process Simulation Codes

However, the resultant casting may have a wide mix of dendritic and eutectic structures: the forged turbine disk may contain areas with very little work, and other zones forged at too high a strain rate.

New computer simulation tools for heat transfer and material flow allow engineers to gain more control over the manufacturing process. Casting engineers can control the solidification front gradient and rate to produce a shrink free casting with controlled microstructure. Forging engineers can use these tools to design blocker shapes and press load-stroke curves which will process 100% of a turbine disk within a temperature, strain rate and total strain window. Simulations of furnace heat up and quenching allow one to predict the amount of martensite formation, and the residual stresses.

Over the years, a number of attempts have been made to simulate manufacturing processes with generic software (such as ABAQUS, MARC, COMICS, SINDA and others). The success rate was marginal. SDRC and a few others have taken a different approach by developing a number of special purpose computer codes which just simulate a single unit process. This is possible partly because SDRC has a vast library of graphics and analysis software, plus access to public domain libraries and selected US-DOD software. As a result, SDRC has built several unit process simulation codes which have a level of integration: a common geometry and results data base. Figure 1 shows that while each process simulation is a separate and independent batch program, all use common input/output processing (SUPERTAB) with special features added for each manufacturing process, e.g. forging definition, or quenching martensite prediction.

In the following sections are presented aspects of the numerical methods for flow and heat transfer which allows the unit processes to be successfully simulated. In section 2, inverse heat transfer is used to process thermocouple data so as to precisely model interface effects. Heat treating simulations are discussed in Section 3, and Section 4 discusses casting, both of which use similar technology. Forging involves a different set of issues which are covered in Section 5. Injection molding and die casting are discussed elliptically in Section 6.

2 Inverse Heat Transfer

Most manufacturing process involve significant heat transfer, and most of the heat transfer problems involve difficult nonlinear boundary conditions. Examples are boiling heat transfer during quenching, and metal-mold interface conductance during solidification and gap formation. Many attempts have been made to model interface effects, but the resultant techniques are not quantatively accurate enough (within 10%) for use in process simulation software. Hence, SDRC elected to directly measure the interface effects with special tests and extensive thermocouple data. Inverse heat transfer analysis was used to process the data into a form useful in process simulation codes. In the following we define the inverse heat conduction problem (IHCP), and discuss the techniques developed in CONTA [5] for the nonlinear problems encountered in manufacturing.

2.1 Problem Description

A typical composite plate is shown in Figure 2. It is comprised of three flat plates, each being a different material. The thermal properties of each material are known. The boundary condition on the right is that of perfect insulation, although other boundary conditions including a thermocouple may be used. There are four temperature sensors inside the plate which provide measured temperatures at a series of discrete, nonuniformly spaced times. The objective is to estimate the surface heat flux, q(t), as a function of time. A mathematical description of the problem for nonlinear materials may be defined as:

$$k_i(T)\frac{\partial}{\partial x}\left(\frac{\partial T_i}{\partial x}\right) = \rho C_i(T)\frac{\partial T_i}{\partial t}, \tag{1}$$

$$k_i\frac{\partial T_i}{\partial x}\Big|_{x-} = k_{i+1}\frac{\partial T_{i+1}}{\partial x}\Big|_{x+} \tag{2}$$

$$T_i|_{x-} = T_i|_{x+} \tag{3}$$

$$T(x_j,t_k) = Y_j(t_k), \tag{4}$$

with appropriate initial and boundary conditions, where i refers to the layer number, and Y refers to the thermocouple data. The main objective is to estimate the surface flux history for known material properties. However, closely related techniques can be developed to find material properties. The problem is solved by making the calculated temperatures agree with the measured data via a sequential least squares procedure.

The sensitivity of the solution is given by the first derivative of temperature with respect to the unknown surface flux,

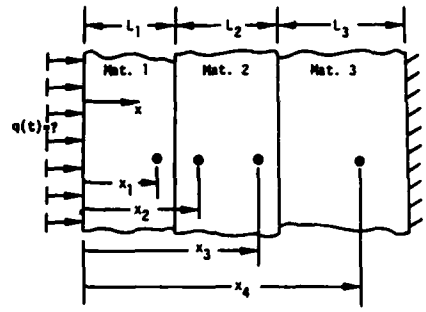

Figure 2: Composite flat plate with four thermocouples

$$X_m(x_j, t_k) = \frac{\partial T(x_j, t_k)}{\partial q_m}, \quad m \leq i$$

The larger the value of X_m, the better the IHCP, or the better the experimental test. If the mathematical model is differentiated with respect to the flux, a similar set of equations is obtained, e.g.

$$k\frac{\partial}{\partial x}\left(\frac{\partial X_m}{\partial x}\right) = \rho C\frac{\partial X_m}{\partial t} \tag{5}$$

Hence, the technique which solves (1) - (4) should also yield the sensitivity data, essential information for practical applications.

2.2 Literature Review

Many numerical methods have been proposed for the solution of the IHCP but most of them can only be used for the linear case. The most widely used method for the nonlinear case is due to Beck [5]. This method is sequential and involves the use of future temperatures for each calculated component of the *surface* heat flux. The procedure permits much smaller time steps (without introducing oscillations in computed heat flux) than making the calculated interior temperatures equal the measured values. *Small* time steps permit extraction of much more information regarding the time variation of the surface heat flux than with large time steps. The most common method of solving the IHCP for composiste bodies and/or bodies with temperature-dependent thermal properties has been the finite difference method which is used in CONTA. The convolution and exact methods are restricted to the linear IHCP.

The IHCP is an ill posed problem because it does not satisfy general conditions of existence, uniqueness and stability. For every realistic surface heat flux history, temperatures can be calculated as a function of time at an interior position. Other temperatures arbitrarily close values to these calculated temperatures can be produced with an infinite number of surface heat fluxes which contain a high frequency sinusoidal component superimposed on the basic heat flux.

In order to obtain a solution it is necessary to restrict the surface flux to having acceptable time variations. Some method to filter out the high frequency components and to stabilise the IHCP is needed. One way is to specify a functional form for the surface heat flux. Another is to add regularizing operators to the least squares term in the form:

$$S = \sum_{j=1}^{m}\sum_{i=1}^{n}(Y_{ji} - T_{ji})^2 + \alpha\sum_{i=1}^{n}q_i^2 \tag{6}$$

where Y_{ji} is a measured temperature, T_{ji} is the corresponding calculated temperature, α is the regularising parameter, and q_i is the ith component of the surface heat flux. Other regularizers which smooth the oscillations involve first or second differences, e.g.

$$\alpha\sum_{i=1}^{n-1}(q_{i+1} - q_i)^2 \text{ or } \alpha\sum_{i=1}^{n-2}(q_{i+2} - 2q_{i+1} + q_i)^2 \tag{7}$$

IHCP codes differ on whether the problem is treated in a sequential or whole domain fashion. By sequential is meant estimating one or some small number of components of heat flux at each time step. In whole domain estimation, the procedure simultaneously extimates all the heat flux components. This is the method the Russians favor, perhaps because it has no stability problems. The advantage of the sequential procedure is that it is much more computational efficient than the whole domain approach, particularly for the nonlinear case.

The question of the relative computational efficiency of the sequential and whole domain estimation procedures is very important. Beck [5] has discussed a case where 100 components of heat flux are to be found. For the nonlinear whole domain estimation procedure, a nonlinear search is needed for these

100 components. For each iteration the complete solution for the temperatures for 100 time steps must be performed more than 100 times. In addition, for each iteration a set of 100 equations having a dense square matrix must be solved; since the number of calculations increases as the cube of the number of equations, this represents much more computation than 100 calculations of two or three simultaneous equations as might be solved in the sequential procedure. Finally for the nonlinear case, many iterations are required for whole domain estimation. In contrast, CONTA uses a sequential procedure and iteration is usually unneccessary. The overall effect is a computational saving of at least two orders of magnitude by using the sequential procedure in CONTA over whole domain estimation.

2.3 The CONTA IHCP

The finite difference equations used in CONTA are based on the Crank Nicolson method. The solution is stabilized with the simplest regularizing operator, (6), and seems to perform well in practice. The use of future temperatures can be controlled by the user, on important feature for nonlinear problems. Sensitively coefficients are efficiently calculated and routinely used in practice. SDRC has modified the code to compute either heat transfer coefficients directly on surface flux; other modifications allow estimation of temperature dependent material properties. Specific applications are discussed in the following sections.

3 Heat Treat Simulation

Heat treatment is one of the most important and widely used manufacturing processes. The mechanical and physical properties of a material can be altered significantly by heat treatment. If performed improperly the material can be degraded or destroyed.

The initial step in the heat treat process is the furnace heatup phase. It is useful to minimize the time in the heatup oven; too long in the furnace means added energy costs and reduced productivity. Modern components are manufactured to near net shape, and it is common to have parts that have thick and bulky sections connected by thin webs. This type of geometry leads to part sag due to creep. Metallurgical deterioration may occur due to excessive time in the oven.

The transit time is the time between the heat up furnace and the quench tank. The hot part can convect and radiate energy to the surroundings. The longer the time of transit the less uniform the temperature distribution becomes in the part. This nonuniformity of temperature distribution prior to quench can lead to reduced mechanical properties and increased part warpage.

Quench media vary significantly in their effectiveness, yielding rates generally from 30° C/s. to 300° C/s. Quenching can be well described by three phases of heat transfer. When the hot metal is first inserted into the quenchant, the liquid adjacent to the hot metal vaporizes and forms a gaseous blanket separating the part from the liquid. Cooling is slow in this vapor-jacket stage because the conductance through the gas layer is low. Soon the bubble blanket begins to collapse and the gas is removed, liquid contacts the metal, vaporizes (removing its heat of vaporization from the metal), and then again forms a bubble. This second stage of quenching provides rapid cooling as a result of large quantities of heat removal associated with less violent bubble formation and much more liquid-metal contact. When the surface of the metal cools to a point where it is below the boiling point of the quenchant, virtually all heat transfer is due to convection across the liquid-solid interface. This third stage of quench has low heat removal rates.

The cooling rate of the part during quench is critical. Martensite formation is totally dependent on quench rate. If the part is cooled too rapidly by quenching, cracks may form in critical areas, or induced residual stresses may be unacceptable. The cooling rate is controlled through the selection of the quenching medium and the surface condition of the part. Quenching media include water, dilute sodium hydroxide solution, sodium chloride brine, oil, oil-water emulsion, and air. The following f .ctors control the characteristics of the quenchant:

1. Temperature
2. Specific heat
3. Thermal conductivity
4. Heat of vaporization
5. Agitation rate

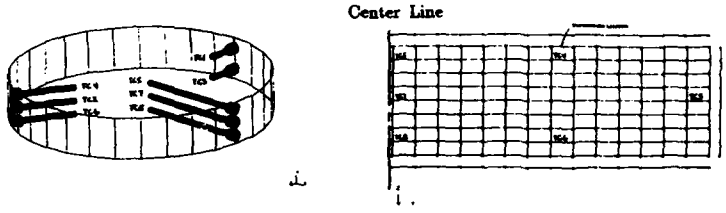

Figure 3: Quenchant Test Specimen and FEM Model

After quench, the part will probably contain residual stresses due to plastic deformation occurring during the time of high temperature gradients which may not fully relax during subsequent tempering. These residual stresses may be critically important when it comes time to machine the part to its final shape. As the part is machined, the removal of material may cause unacceptable deformations to be induced in the part. In addition, the residual stresses may effect fatigue or fracture properties.

3.1 Quench Boundary Conditions

Qualitatively, the cooling mechanism during quench is convection and some general expressions are available to estimate magnitudes in the different regimes of convection heat transfer (pure convection, nucleate boiling, transition boiling, and film boiling). However, for a specific quench media one cannot determine a-priori what its cooling curve will be. Hence we have come to rely on experimental test data from which surface boundary conditions can be derived by solving the IHCP. The standard cylindrical specimens and tests used by heat treaters are useful but not totally adequate. Hence, new test procedures were developed.

An experiment was designed to determine the temperature dependent heat transfer coefficients during quench as a function of part surface temperature. A pancake specimen, 12 inches in diameter and 2 inches thick, was instrumented with eight thermocouples as shown in Figure 3. The pancake was subjected to a typical heat treat cycle, and during quench temperature versus time data was recorded. Figure 4 shows typical surface flux results back calculated by CONTA for a flat surface facing downward. This experiment was repeated several times with the pancake oriented in various positions in order to quantify the effects and repeatability. Once the flux history was known, a finite element model of the pancake was constructed and flux history applied. This test was performed in order to verify the results (flux history) from CONTA. Figure 3 shows the model and the thermocouple locations. If CONTA properly calculated the flux history then good agreement is expected between analysis and test. Figure

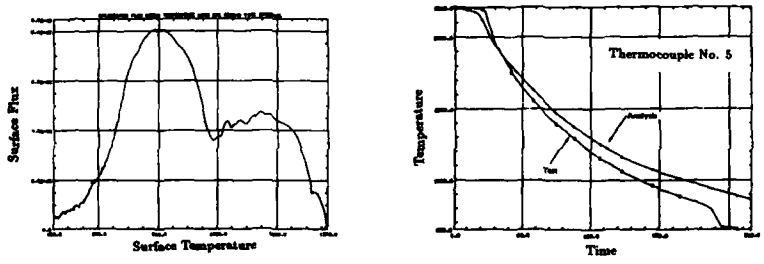

Figure 4: CONTA Flux Results, and Test-Analysis Comparison

4 is a typical thermocouple comparison. The error is typically less than 25° C, vertically, or less than 10 seconds horizontally.

3.2 Thermal/Mechanical Analysis

The energy equation forming the basis of the temperature history calculation with coupled mechanical terms is:

$$\frac{\partial}{\partial x_i}\left(k\frac{\partial T}{\partial x_i}\right) - \rho C_p \frac{\partial T}{\partial t} = \frac{E\alpha T}{1-2\nu}\frac{\partial \epsilon_{mm}}{\partial t} - \sigma_{ij}\frac{\partial \epsilon^p_{ij}}{\partial t} - Q \qquad (8)$$

The first term on the right hand side is the energy change (i.e. temperature drop) due to adiabatic expansion; although this is significant in gases, it is negligible for solids. The second term is the energy

due to plastic flow; this is small in heat treating process (however, it is significant in forging). Hence the energy equation can be solved uncoupled from the equations of motion.

In material (updated, Lagrangian) coordinates the equations of momentum balance are:

$$\frac{\partial}{\partial x_j}(\sigma_{ij}) + b_i = \rho \frac{\partial}{\partial t}\left(\frac{\partial X_i}{\partial t}\right) \tag{9}$$

Inertia forces, the right hand side term, are negligible in heat treating. For a thermo-elastic-plastic-creep model of material behavior, the constitutive law is:

$$\sigma = C(T)\left(\epsilon - \epsilon^t - \epsilon^p - \epsilon^c - \epsilon^m\right)$$

$$\epsilon_{ij} = \epsilon^e_{ij} + \epsilon^t_{ij} + \epsilon^p_{ij} + \epsilon^c_{ij} + \epsilon^m_{ij}$$

That is the total strain is the sum of elastic (e) thermal (t), plastic (p) and creep (c) and martensite formation (m) strains. The stress-strain relations are strongly dependent on temperature, so the equations of motion are strongly coupled to the energy equation, but not visa-versa.

Several finite element programs have the capability of solving nonlinear coupled thermo-mechanical problems, including the commercial systems ABAQUS and MARC. However, speed is very important, hence it is essential to take advantage of the weak coupling. After study of ADINA and public domain software we elected to build a weakly coupled system using TOPAZ (heat conduction), NIKE (nonlinear stress) and FACET (diffuse radiation). All are available at low cost from the National Energy Software Center (Argonne Labs) and are continuously developed and improved by Lawrence Livermore National Labs under DOD and DOE sponsorship.

NIKE	TOPAZ	FACET
• Implicit • Transient • Nonlinear • Bandwidth Minimum • Vectorized • Temperature-Dependent Materials • Thermal Strains • Elasto-Plastic	• Implicit • Transient • Nonlinear • Bandwidth Minimum • Vectorized • Temperature-Dependent Materials • Enclosure Radiation	• View Factors • Shadowing • TOPAZ Interface • Vectorized • Restarts

Table 1: Basic Features Used in Heat Treat Simulation

Table 1 lists the key features of NIKE and TOPAZ. Comparison shows their common origins, e.g. vectorization and bandwidth minimization (Gibbs-Poole-Stockmeyer). NIKE has an excellent material library; the only addition needed was an improved creep capability (primary and secondary). Figure 5 illustrates elliptically how the codes were coupled to simulate heat treat processes. Details of NIKE and TOPAZ are available in publications and manuals and will not be repeated here. The metallurgical predictions are based on a simplified set of the general diffusion equations. The only precipitant not governed by a diffusion equation is martensite. A single diffusion equation is fitted to the isothermal transformation diagram of the particular steel. This effectively lumps together pearlite (Vp) with all other products, hence the volume fraction which converts to martensite is (1.0-Vp). Martensite is diffusionless (time is not a factor in the FCC to BCT transition), so a two term prony series is fitted to the martensite start and finish temperatures,

$$V_m = 0, \; T \geq M_s$$

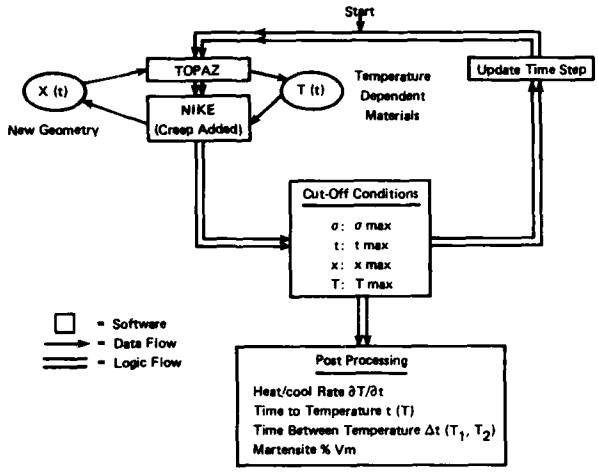

Figure 5: Software Integration and Development

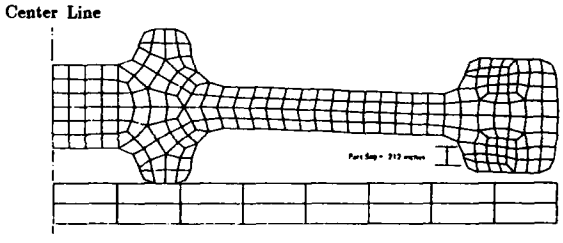

Figure 6: Deformed Geometry at 2,000 Seconds, Furnace Heat Up

$$V_m = a\left(1 - e^{-b\tau}\right), \quad a = 1 - V_p, \quad \tau = \frac{M_s - T}{M_s - M_f}$$

$$V_m = a, \quad T \leq M_f$$

Significant volumetric expansion is associated with martensite formation, so the thermal strain terms in NIKE were modified to become:

$$\epsilon^t = \beta V_m + (\alpha_m V_m + \alpha_p V_p)(T - T_o),$$

β = volumetric expansion from FCC to BCT

Although metallurgists are generally not interested in martensite volume fractions less than 80%, the heat treat software attempts to track martensite formation from 100% down to zero in order to accurately predict stresses during quenching.

The disk shown in Figure 6 illustrates a typical application of heat treat simulation. The material is an aerospace alloy which doesn't form martensite. For furnace heat up, a simple radiation to infinity boundary condition was imposed. The mechanical loading in the furnace was gravity. The properties, both thermal and mechanical, were modeled as temperature dependent. An elastic-creep material model was used. Emissivity was set at a constant 0.85. The initial part temperature was 530° R (70°F) and the furnace temperature was 2160°R (1700°F). It took 2,000 seconds (33 minutes) for the part to heat up to within 10 degrees of the furnace temperature of 2160° R. Figure 7 shows a plot of the maximum Von-Mises stress versus time. The point where the maximum stress occurs changes as the part heats up. Initially, the web region heats faster than the rim and hub. The web tries to expand against the hub and rim as shown in Figure 8. Because of this restrained expansion and the fact that the yield stress is relatively low due to the temperature, the rim actually yields.

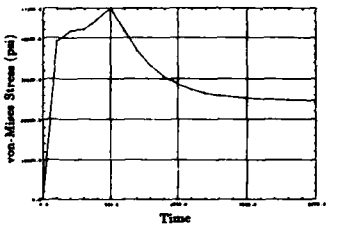

Figure 7: Maximum Von-Mises Stress Versus Time, Furnace Heat Up

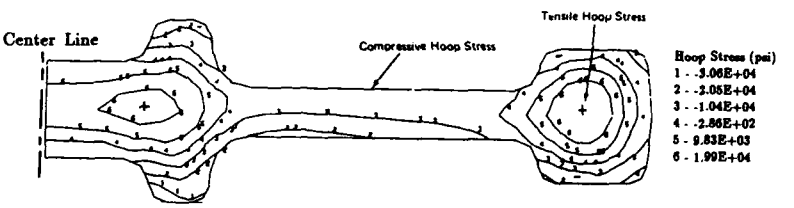

Figure 8: Hoop Stress Versus Time, Furnace Heat Up

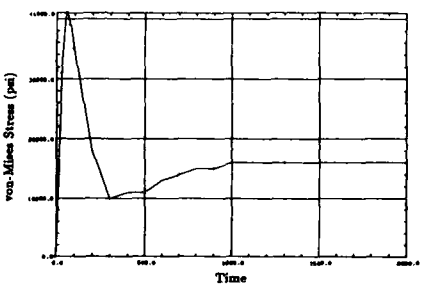

Figure 9: Maximum Von-Mises Stress Versus Time, Quench

The quench simulation was performed using the flux history obtained by CONTA from an instrumented pancake test plus initial temperatures obtained from the end of the furnace heatup. An elastic plastic material model was utilized because of the expected high stresses and period of time as compared with furnace heatup, the creep model is no longer necessary. The maximum Von-Mises stress in the part is plotted as a function of time in Figure 9. The stress peaks early in the cycle at 57 seconds. Two separate phenomena happen during the quench cycle. Initially, the outer skin shrinks rapidly and compresses the material interior to the part. The yield stress of the material is very low as this point due to the high temperature of the interior. In this case, the temperature interior to the part is 2111°R at 57 seconds. The corresponding yield stress is 10,000 psi so yielding occurs.

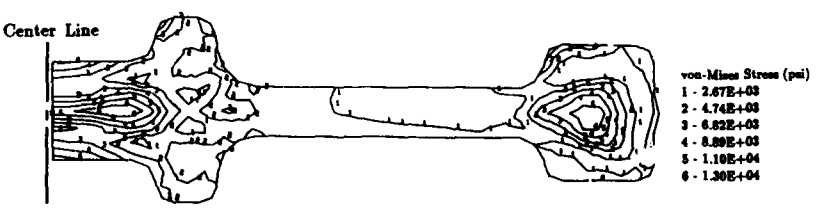

Figure 10: Residual Stress At End of Cycle

As the interior continues to cool, it is restrained from further contraction by the outer skin. When this transition occurs, the outer skin goes into compression and the interior goes into tension. However, at this point in the cycle, the yield stress is above the Von-Mises stress and no further yielding occurs. Any yielding that occurs will result in residual stress. Figure 10 shows the Von-Mises stress state at the end of the cycle (2,000 seconds), and shows a maximum residual stress of 15,100 psi.

4 Solidification Simulation for Castings

The aerospace industry is beginning to use large integral castings in both structure and jet engines. Several processes are being used, including lost foam, sand casting and high precision investment casting. Net shape componenets up to 200 lbs. have been produced with very thin sections. This is achieved by numerous casting trials to develop gate and riser locations and sizes which produce a shrink free part. However, lead times can be two years or more to qualify the production process. Once qualified, the process is effectively frozen as rarely is the money available to requalify a process.

Historically, numerous attempts have been made to develop flow and heat transfer software (finite difference, finite element) which will simulate how castings solidify. A series of recent papers [13] and [19] discusses specific techniques for investment casting. Here we explore some numerical techniques applicable to all casting processes, from grey iron sand processes up to high precision aerospace processes.

A typical finite element simulation of metal solidification requires a nonlinear (radiation, materials properties), transient analysis (200-400 time steps) of a large model. Large parts may consist of 4,000 metal elements (solids) plus up to five times as many for the mold. The objective is to see if the metal will solidify towards the gating, or if liquid metal is trapped by the freeze front. Manufacturing Engineers employ several runs to adjust the gating (and other parameters) so that the first prototype cast is largely free of porosity. No general purpose finite element code and VAX-like computer can handle such problems. Hence, SDRC developed a special purpose finite element code which had to be more accurate and several times faster than any known commercial finite element heat transfer code.

We use TOPAZ [4] as the core capability in heat transfer. TOPAZ was developed by Dr. Arthur B. Shapiro at LLNL and is available through the National Energy Software Center at Argonne National Laboratory. This code was selected largely for two reasons:

1. Handles nonlinearity very well
2. Very fast vectorized FORTRAN 77 code.

Vectorization was done for a CRAY, but this also greatly improves VAX performance. Other TOPAZ capabilities important to us are:

1. Nonlinear material properties
2. Time or temperature dependent boundary conditions:
3. Enclosure (view factor) radiation

The following sections describe the additions and modifications to TOPAZ as well as their motivation. The resulting software has been applied to a number of very large problems; the accuracy and speed are briefly demonstrated.

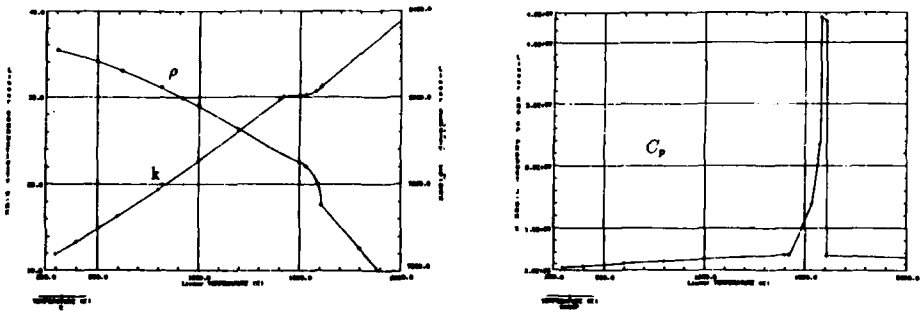

Figure 11: Typical Properties of a Non-Eutectic Alloy

4.1 Material Properties

Casting consists of a sand mold or ceramic shell which contains solidfying metal. The diffusivity ratios exceed eight ($\alpha_m/\alpha_c \geq 8$), and the mold is thermally benign (k and C_p vary slowly—or are constant) except for wet sand. Liquid metal properties are not precisely known, but we have found, for a few alloys that k and ρ are linear and C_p is constant up to about 300° Kelvin of superheat. Solid metal properties are known quite precisely; k and ρ are nearly linear (a small quadratic term), and C_p is linear from solidification down to 500° Kelvin.

Solidification of complex alloys takes place over a fairly wide temperature range. Heat is not released linearly through solidification. Using the atomic weights with the fusion heats of the alloy constituents, one can construct estimates which indicate that the actual heat release rate must be quite nonlinear. Some data for a high strength alloy is illustrated in Figure 11. The capacitance data shows that one of the limiting factors in a simulation is that the maximum temperature change within a time step is limited by the complexity of the material data, typically $\Delta T \leq 10°C$. Since material is soldifying throughout the time interval simulated, this restriction always applies. For typical steel alloys 10° moves the freeze front too far, so time steps are adjusted small enough to obtain at least ten points between T-liquid and T-solid.

When experimental phase transition data is not available (which is usually the case), we recommend the rule of mixtures and a universal curve relating dimensionless liquid fraction to a dimensionless temperature,

$$f_L = e^{-4.005T^*}, \quad T^* = \frac{T_L - T(t)}{T_L - T_S}.$$

Although this approach is really only a best guess, it has been shown to give results within ±4% for a complex high strength alloy, and it does account for variations from one foundary to another, depending on specific chemistry and processing conditions.

$$f_L = e^{-4.005T^*}, \quad T^* = \frac{T_L - T(t)}{T_L - T_S}.$$
$$f_S = 1 - f_L \quad T_S < T(t) < T_L$$
$$k = k_S f_S + k_L f_L \quad k_S = k(T_S)$$
$$\rho = \rho_S f_S + \rho_L f_L \quad k_L = k(T_L), \text{etc.}$$
$$C_p = C_S f_S + C_L f_L + L\frac{df_S}{dT}$$

Table 2: Estimation of Transition Material Properties

Table 2 summarizes the best estimates we know of for transition data. This approach is closely related to atom fraction weighting of specific heats of the constituents. However, the possibility exists that the liquid fraction may vary significantly due to composition changes, as occurs in certain iron alloys.

4.2 Finite Element Formulation For Solidification

The differential equation of heat conduction is:

$$\rho C_p \frac{\partial T}{\partial t} = \nabla^T (k \nabla T) + Q, \tag{10}$$

with initial conditions:

$$T|_{t=o} = T_o(x, y, z),$$

and with boundary conditions

$$n^T(k\nabla T) = q \text{ on } \Gamma_1, \quad T = T(t) \text{ on } \Gamma_2, \tag{11}$$

where $q = q_f - h\Delta T$ handles flux, convection or radiation boundary conditions.

Considerable research has recently been devoted to solidification simulation with finite elements, and attention continues to be focused on the enthalpy formulation (e.g. Crank, in [1], pp 177–200) as a way to avoid the moving boundary tracking required by the Stefan problem;

$$\frac{\partial H}{\partial t} = \frac{dH}{dT}\dot{T} = \nabla^T (k\nabla T) + Q, \quad H = \int_0^T \rho C_p(s)ds. \tag{12}$$

Although (12) looks identical to (10), calculation using dH/dt is quite different. In both cases the objective is to integrate the total heat correctly,

$$\int_o^t \rho C_p \dot{T}\, d_t \doteq L \doteq \int_o^t \frac{dH}{dT}\dot{T}\, d_t \tag{13}$$

When the solidification range $T_l - T_s$ is large and several time steps (e.g. 40) are used to integrate, then either method accurately calculates total heat. Indeed this is the case with most complex alloys, so equation (10) is adopted herein as the code is faster and uses less storage.

In finite element form (10) and (11) become:

$$[\tilde{C}]\ \{\dot{T}\} + [\tilde{K}]\ \{T\} = \{F\}, \tag{14}$$

where:

$$\left.\begin{aligned} C_{ij} &= \iiint N_i^T\,(\rho C_p)\,N_j\,dV, \\ K_{ij} &= \iiint (\nabla N_i)^T\,[\tilde{k}]\,(\nabla N_i)\,dV + \iint N_i^T\,h\,N_j\,dA, \\ F_i &= \iiint N_i^T\,Q\,dV - \iint N_i^T\,q_f\,dA, \end{aligned}\right\}$$

When radiation is the dominant mode of heat loss, it is important to capture its effects accurately and at the same time efficiently. Radiation heat flux at surface i is emitted radiation minus the absorbed portion of the incident radiation,

$$q_i = \epsilon_i\,\sigma\,T_i^4 - \alpha_i\,H_i. \tag{15}$$

All areas exterior to the mold are cold, so H_i is ignored on mold exterior surfaces. Many circular molds have large hollow interiors, and in these cases we calculate the incident radiation as follows. The rate of heat flux leaving a surface is the radiosity, which is the emitted plus the reflected energy,

$$B_j = \epsilon_j\,\sigma\,T_j^4 + \rho_j\,H_j. \tag{16}$$

The incident energy is now calculated by summing the contribution from all surfaces

$$H_i\,A_i = \sum_{j=1}^{n} F_{ji}\,B_j\,A_j,$$

where F_{ji}, the geometric view factor, is the fraction of energy leaving surface i that arrives at surfaces j. Reciprocity reduces this to:

$$H_i = \sum_{j=1}^{n} F_{ij}\,B_j \tag{17}$$

Combining (16) and (17) yields a linear system for the radiosity,

$$\left[\,[\tilde{I}] - [\rho]\cdot[\tilde{F}]\,\right]\{B\} = \left\{\epsilon\,\sigma\,T^4\right\} \tag{18}$$

where $[\rho]$ is a diagonal matrix of reflectivities, and the grey body condition ($\rho = 1 - \epsilon$) is used. After (18) is solved, H is obtained from (16), and (15) computes the surface flux. Note that we could use (16) and (17) to solve for incident energy H directly [9]. However the view factor matrix F would occur in both the matrix and the right-hand-side resulting in much more computational effort for large problems. Hence, the recommended procedure is shown in Table 3.

1. Compute	$\tilde{G}^{-1}$, *where* $\tilde{G} = \tilde{I} - [\rho][\tilde{F}]$
2. Solve (10),	$\{B\} = G^{-1}\cdot\{\epsilon\,\sigma\,T^4\}$
3. Compute H via (8),	$H_i = \dfrac{(B_i - \epsilon_i\,\sigma\,T_i^4)}{(1-\epsilon_i)}$
4. Compute q via (7),	$q_i = \epsilon_i\,\sigma\,T_i^4 - \alpha_i\,H_i$

Table 3: Algorithm for Enclosure Radiation Calculation

Mold emissivity is not usually wave length dependent, hence G-inverse is only computed once.

Radiation is about 10 times more nonlinear than convection: a change of 10° at 1000° causes a 4% change in radiation flux. When solving the finite element equations (14), radiation is best handled if we capture as much of the nonlinear variation as possible via a Taylor series expansion about the current temperature,

$$(\tilde{T}_i + \Delta T_i)^4 = 4\,\tilde{T}_i^3\,\Delta T_i - 3\,\tilde{T}_i^4$$

Hence, the final form for radiation flux is:

$$\left.\begin{aligned} q_i &= h_r\,\Delta T_i + q_r \\ h_r &= 4\,\epsilon_i\left(1 - \frac{\epsilon}{1-\epsilon_i}\right)\tilde{T}_i^3 \\ q_r &= -3\,\epsilon_i\left(1 - \frac{\epsilon_i}{1-\epsilon_i}\right)\tilde{T}_i^4 - \frac{\epsilon_i\,B_i}{1-\epsilon_i} \end{aligned}\right\} \tag{19}$$

where Kirchoffs law ($\alpha = \epsilon$) has been used. The first term, h_r, contributes to the conductivity matrix H, while q_r contributes to the load vector F in (14). We leave h_r constant over a time step, but adjust q_r within the nonlinear iterations.

4.3 Element Formulation

The element set is restricted to a linear brick and its simplifications (wedge, pyramid, tetrahedra). We have concluded that the main advantage of higher order elements (e.g. parabolic elements with midside nodes) is more accurate calculation of heat flux ($q = k\nabla T$). In any case we do not use flux in any quantative way in solidification, but it does provide graphical description of heat flow paths.

A diagonal or lumped capacitance matrix in (14) is highly recommended and we use it exclusively in all solidification problems, even though implicit methods do not require it. Mullen [10] and Liu [11] have shown that a consistent capacitance matrix is only slightly more accurate than lumped capacitance over a wide range of diffusivities. This result can be deduced from a phenomenological view. Thermal wave propagation is very slow (3 inches/min for steel, less for molds) hence transient fluxes can excite only very low heat transfer modes. High frequency modes are heavily damped and require a high amount of energy to excite (See Hogge [1], pp 74–88).

Since the temperature difference across an element is usually small,

$$T_i = T_{avg} \pm 1\%$$

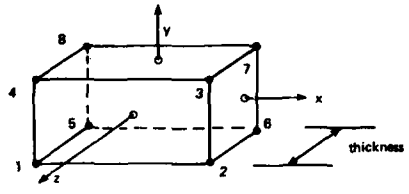

$$\tilde{H} = \iiint \{\nabla T\}^T \cdot [k] \cdot \{\nabla T\}\ dx\ dy\ dz$$

Figure 12: Collapsed Brick as an Interface Element

then the product $[\tilde{C}]\ \{\dot{T}\}$ for each element is well approximated by the row sum of $\tilde{C}$ times $\dot{T}_i$, which is how we diagonalize the capacitance matrix.

Although reduced integration is very attractive for its speed [11], significant errors can be made in the conductance if a 1 pt. rule is used. A 2x2x2 Gauss quadrature is used for both conductance and capacitance; this eliminates hour glass singularities in $\tilde{H}$ and captures the rapid variations in specific heat.

4.4 Interface Conductance Element

Heat transfer across an interface between two dissimilar materials presents a modeling problem. When two thermocouples are placed on both sides of the interface, they will read different temperatures—regardless of how close they are. This is well known for a bolted joint, and it also applies to liquid metal solidifying in a ceramic mold. If there is a temperature drop across the interface, then the interface has a finite conductance. In section [2] we discussed how interface conductance can be determined from experimental measurements, here we derive a finite element to represent interface conductance.

Interface conductance will be represented by a brick element of zero thickness. The element can be derived by collapsing the element in the z-direction. Specifically, let the conductivity $k_x = k_y = 0$, and in the limit as $t \to 0$, let $k_z/t = h$. Henceforth, h is the interface conductance in the integral:

$$\tilde{H} = \iint h(T) \begin{Bmatrix} \partial N_1/\partial\zeta \\ \vdots \\ \partial N_8/\partial\zeta \end{Bmatrix} \left[\frac{\partial N_1}{\partial\zeta} \cdots \frac{\partial N_8}{\partial\zeta} \right] det[J]\, d\xi\, d\eta$$

$$N_1 = \frac{1}{8}(1-\xi)(1-\eta)(1-\zeta)\ , \text{ etc.}$$

As the element collapses, the z-derivative of the 3D shape functions N_1 to N_8 become the 2D shape functions L_1 to L_4. Hence, the integral reduces to:

$$\tilde{H} = \iint h(T) \begin{bmatrix} \tilde{L} \\ -\tilde{L} \end{bmatrix} [\tilde{L}, -\tilde{L}]\, dA, \quad \tilde{L} = (L_1, L_2, L_3, L_4),$$

$$L_1 = \frac{1}{4}(1-\xi)(1-\eta), \text{ etc.,} \tag{20}$$

$$\tilde{H} = \begin{bmatrix} \tilde{M} & -\tilde{M} \\ -\tilde{M} & \tilde{M} \end{bmatrix}, \quad \tilde{M} = \iint h(T)\, L^T \cdot L\, dx\, dy$$

The conductance h is often a strong function of temperature, so h is evaluated at each gauss point using temperatures interpolated from the node points. The interface element has no capacitance. In practical use, the element is located between metal and mold elements; e.g. nodes 1-2-3-4 connect to metal bricks, nodes 5-6-7-8 connect to mold bricks.

4.5 Numerical Integration

Time stepping schemes for (14) have been studied extensively [7; Hogge, ref 1]. The primary advantage of the newer multi-step schemes (see [1], pp 75–90) is that they allow much longer time steps by representing time variation more accurately. In solidification, these methods are not as useful as the time step is limited by material properties or (resolution of the solidification front), not by stability. Hence, we adopt the generalized midpoint scheme, a one step (two level) method which is a generalization of trapezoidal schemes. When this is applied to (14), one obtains after some algebra, the nonlinear equations:

$$[\tilde{C}_{n+\theta} + \theta\, \Delta t\, \tilde{H}_{n+\theta}]\{T_{n+\theta}\} = [\tilde{C}_{n+\theta} - (1-\theta)\, \Delta t\, \tilde{H}_{n+\theta}]\{T_n\} + \Delta t\{F_{n+\theta}\}$$

Subscript $n+\theta$ represents evaluation of the quantity anywhere within the time step interval.[1] The right-hand-side can be simplified if one elects to solve for the temperature increment,

$$[\tilde{C}_{n+\theta}/\Delta t + \theta\, \tilde{H}_{n+\theta}]\{T_{n+1} - T_n\} = \left\{F_{n+\theta} - \tilde{H}_{n+\theta} \cdot T_n\right\} \tag{21}$$

and this is the form we have found most useful in solidification. After solving (21) for the temperature increment, the temperature is updated with

$$T_{n+1} = T_n + \{T_{n+1} - T_n\} \tag{22}$$

We use the Crank Nicolson value ($\theta = 1/2$), which is known to generate spurious oscillations for large time steps where it is only marginally stable. However, we have never observed this in practical problems as the time step must be kept relatively short as discussed in section 4.1.

4.6 Nonlinear Solution

Within each time step we must solve a nonlinear system of equations as explicitly defined in the previous sections. The classic method for solving nonlinear eqns. (21) is the Newton Raphson method, which requires construction of a Jacobian. The only way to construct such derivatives of (21) is numerically; e.g. for n nodes we need n solutions to construct the full $n \times n$ Jacobian. Thus, although the Newton-Raphson scheme gives quadratic convergence, its cost greatly exceeds its benefit over linear convergence schemes.

In our experience direct iteration performs well and costs much less. However, a two step predictor - corrector approach is used as follows. The first iteration includes assembly and decomposition of the coefficient matrix:

$$[C_{n+\theta}/\Delta_t + \theta H_{n+\theta}], \quad \theta = 1/2$$

and $n+\theta$ means that the material properties are evaluated at temperature $T_{n+\theta}$ extrapolated from the previous time step with:

$$T_{n+\theta} = T_n + \theta \cdot \{T_n - T_{n-1}\} \tag{23}$$

The second step and subsequent iterations only involve formulation of the right hand side of (21) with an improved estimate of the Crank-Nicolson temperature,

$$T_{n+\theta} = T_n + \theta \cdot \{T_{n+1} - T_n\}$$

An option is also provided to allow the user to reassemble the coefficient matrix at each iteration, but this is more expensive and rarely used. We have found direct iteration to converge in three to five iterations on typical investment casting solidification problems, since we control MAX $\{T_{n+1} - T_n\} \leq 10°$. Even the high transients during pouring converge in 10–15 iterations. If (21) does not converge, one can always make it converge by reducing the time step—which reduces the nonlinearity by decreasing the temperature change over the time step.

[1] Particular integration schemes are well known: $\theta = 0$ is the forward Euler explicit method; $\theta = 1/2$ is the Crank-Nicholson scheme which has the least error (second order accurate in time step size); $\theta = 2/3$ is the Galerkin scheme which has the best short time (initial transient) behavior, $\theta = 1$ is the backward Euler method. When $\theta > 0$, the schemes are considered implicit.

4.7 Solution Methods

At each time step the finite element system of equations (21) are solved repeatedly to determine the temperature increment over the next time step. This solution process is inherent in nonlinear transient heat transfer analysis and a variety of methods are commonly used. For small models, direct solution methods involving Cholesky factorisation and forward/backward substitution are effective. However, most practical problems require hundreds or thousands of elements, and classical iterative solution methods for linear systems of equations are more competitive for large systems. For example, Wilson [3, pp. 18–29] adopted a Lanczos strategy while the Conjugate Gradient algorithm was studied in Hughes [7] and Chin and Frank [3, pp. 341–352]. Both methods are especially effective for transient thermal problems because they are related, as was shown in [14] and, more importantly, because such problems can be well-conditioned by congruence transformations. For the discussion in this paper we limit attention to the Conjugate Gradient method, although for certain applications the Lanczos method may be equally viable.

Our experience indicates that the computational cost associated with direct solution methods using Cholesky factorisation grows rapidly with problem size, especially in three dimensional models, even to the point of being prohibitive. On the other hand, iterative methods, if quickly convergent, appear considerably more attractive, particularly in view of recent computational hardware advances such as vector processors, extended memory machines and multiprocessing environments. The convergence of Conjugate Gradient methods is predicated upon the minimization [15] of an error functional of the following form:

$$1/2\, x^T A x \; - \; x^T b \tag{24}$$

where A is a symmetric, positive definite Hessian matrix.

The error eliminated at each step in the iteration is proportional to:

$$\frac{\sqrt{\kappa}-1}{\sqrt{\kappa}+1} \tag{25}$$

where $\kappa(A)$ is the spectral condition number of A. The apparent conditioning of the Hessian matrix in (24) can be improved by an appropriate congruence transformation so that for $y = B\,x$ the conditioned error functional is

$$1/2\, y^T\, B^T A B y \; - \; y^T\, B^T b \tag{26}$$

for B nonsingular. The convergence of the Pre-conditioned Conjugate Gradients (PCG) is thus governed by $\kappa(B^T A B)$ and clearly, from Equation (25) , the ultimate objective of pre-conditioning is to make the conditioning number approach unity, which occurs if B is an easily obtainable approximation of the inverse Cholesky factor of A. Methods of conditioning by approximate factorizations were discussed in [16] and, more recently, in [17,18].

Several qualitative characteristics of PCG are noteworthy and have been borne out in our numerical experimentation. As suggested in (25), the convergence of PCG is not dependent on the number of elements in the model. Further, convergence to a given accuracy is achieved in the same number of iterations for a given condition number of the PCG problem because this condition number, in turn, is largely independent of problem size. Hence, incremental computer resource for an increase in problem size is required only to process additional elements, and this cost grows linearly with problem size. Another beneficial characteristic of PCG is the fact that the solution at the previous time step, e.g. (23) with $\theta = 1$ can be used as the initial estimate in the iteration. This is in contrast to the inability of direct methods to take advantage of a known approximation to the solution.

Finally, but equally important, PCG for nonlinear Finite Element applications is amenable to vectorised and multi-processor machines because assembly of global matrices is not required in the numerical evaluation in the Conjugate Gradient algorithm, as well as in the application of the preconditioners. Our work in the area of approximate factorization methods in pre-conditioning continues. Improvements in conditioning are manifested in the somewhat remarkable computer resource reductions indicated in the next section for the simplest of pre-conditioners, namely that of diagonal scaling.

4.8 PCG

Standard TOPAZ uses a Cholesky skyline solver preceeded by a Gibbs-Poole-Stockmeger bandwidth minimisation. The CPU time of this solver is proportional to $N * BW^2$, where N is the matrix size and BW is the half bandwidth. With complex 3D problems the bandwidth becomes very large and solution times can become enormous - even for a fast code like TOPAZ.

To generate a relatively unbiased comparison, a cube with nonlinear material properties (including latent heat of fusion effects) was generated. Linear type (non varying film coefficient) convective boundary conditions were applied to all exterior surfaces. The models were of consistent geometry but varying numbers of elements (varying from 2x2x2 up to 10x10x10). Standard TOPAZ is compared to a widely available general purpose finite element code in Figure 7. The two programs took approximately the same number of iterations to converge and about the same number of time steps. The PCG solver was implemented so that precise comparison could be made with standard TOPAZ, and these results are included in Figure 7. Convergence of the PCG solver was set to six digits (.01 degrees), and three to five

iterations (sweeps through the element list) were required - regardless of problem size. Hence, CPU time for PCG increased linearly with the number of elements as expected. For actual solidification problems with about 5,000 DOF (and about 5,000 elements), PCG was about ten times faster than Cholesky for linear problems.

The nonlinear equations of each time step (21) are best solved by direct iteration. Certain features of the PCG method make it well suited to solving mildly nonlinear systems via the direct iteration method. Our direct iteration solution of (24) is a predictor corrector scheme of the general form

$$\left\{X_{n+1/2}\right\} = 1/2\ \left\{X^{*}_{n+1}\right\} + 1/2\ \left\{X_n\right\}, \tag{27}$$

$$\left\{X^{*}_{n+1}\right\} = \left[A(X_{n+1/2})\right]^{-1} \cdot \left\{b(X_{n+1/2})\right\}.$$

Which converges rapidly if $[A]$ and $\{b\}$ are nearly linear functions of $\{X\}$; typically (24) converges in 2 to 4 iterations. When the Cholesky solver is used for (27), each iteration is exact (to machine accuracy), when all that is needed is a better estimate of $\left\{X_{n+1/2}\right\}$ for improved evaluation of $[A]$ and $\{b\}$. In Figure 14, we show how the PCG method converges the temperature at a typical node point where large changes are occuring. This asymptotic convergence is ideal for the direct iteration solution (27). After two conjugate gradient steps, we update the matrices as in (27) and continue with more conjugate gradient steps before updating again. Usually only two to four updates of the equations are required to converge the nonlinear system as temperature change is restricted to ten or twenty degrees.

The result is that the PCG solver converges (21) in about the same number of steps, regardless of whether the problem is linear or nonlinear. This provides a further speed improvement of two to four over the Cholesky solver.

4.9 Conclusion

The previous sections have laid out a series of techniques used to improve the performance of a finite element heat transfer code. These enable one to solve, on VAX-like hardware, problems which would stretch a CRAY, e.g. 10,000 to 30,000 DOF, 400–800 enclosure radiation surfaces, 100–300 time steps. These new features were added to TOPAZ, and the resulting finite element analysis system, combined

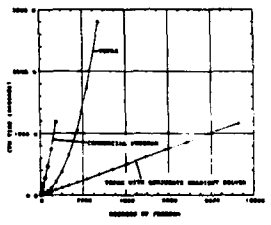

Fig. 13: CPU Time Comparison

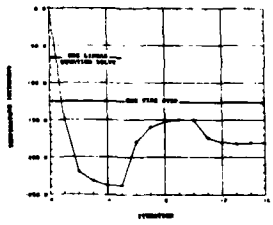

Fig. 14: Typical PCG Convergence

with the graphics pre- and post-processing software, provides a powerful capability for designing improved gating systems for very complex parts. Foundry engineers can modify the gating, rerun the analysis and view the results in a matter of hours. The simulation system allows the casting engineer to explore new techniques and processes impossible to develop on the foundry floor with trial and error methods. The next software development will be to add postprocessing for metallurgy predictions.

5 Forging

Forging is a process in which a metal billet is preheated and deformed plastically by a sequence of shaped dies under high pressure. The forging die designer seeks to control the process so that the material is deformed within a window of temperature, strain and strain rate. This processing window depends upon, among other things, preform design, workpiece temperature, die lubrication, and die velocity. The die designer also seeks to minimise cost by minimising the number of processing steps. A computer program that simulates the forging process enables the designer to evaluate a given process and numerically redesign the process to optimise quality and minimise cost.

In the early 1970's the theoretical basis for such a simulation program was established by Lee and Kobayashi [1] at the University of California, Berkeley. They introduced a rigid-viscoplastic finite element method which ignores elastic strains, assumes the workpiece remains incompressible and treats the plastic deformation as a flow problem. An outgrowth of this work was a two-dimensional, finite element computer program, ALPID (Analysis of Large Plastic Incremental Deformation) [6,8], which was designed specifically to simulate the forging of metals. The workpiece is decretised by linear, quadratic or cubic quadrilateral elements, and the dies are modeled as rigid moving bodies which impose

dynamically defined friction boundary conditions on the workpiece as it deforms. ALPID has been generalised to handle arbitrarily shaped dies [12] and to simultaneously solve the heat transfer equations [20].

The flow formulation in ALPID involves several approximations which warrant discussion. The "flow" formulation in ALPID is generally applicable if the plastic strains are very large compared to elastic strains (which are ignored). Residual stresses and stresses in so-called 'dead zones', which are present in most extrusions and forgings, cannot be easily calculated. Dead zones cause ALPID to have convergence problems, residual stresses are important in the prediction of workpiece crack initiation.

5.1 Rigid Viscoplastic Versus Elasto-plastic

An alternative to the ALPID rigid viscoplastic formulation which addresses these issues is an elastic-plastic formulation. Through the 1960's and early 1970's applications of elasto-plastic codes were restricted to relative small strains, and various attempts at very large strains were unsuccessful. Recently Nagtegaal [25] has proposed a fundamentally different approach: an integral form of the constitutive rate equations. This allows Lagrangian and Eulerian codes to achieve equal accuracy. This approach was implemented in the MARC program by its developers, along with appropriate capabilities for describing die boundaries.

Recently MARC and ALPID have been compared on identical problems [22] so as to obtain a true comparison of both approaches for forging. The model was an aluminum ring specimen squashed to a 30% height reduction, no remeshing was required. The authors concluded [22] that both ALPID and MARC can be expected to produce results in good agreement with each other. However, the ALPID code is several times (about 5 to 8) more efficient than MARC. The advantage is due to ALPID's simplified rigid-viscoplastic formulation and the fact that the code is specifically designed for metal forming. Real forging problems require hundreds of elements and several hours of computer time for ALPID, hence MARC is rarely used in practice.

5.2 Automatic Remeshing for ALPID

Accurate simulations of complex, multi-step forging processes have been difficult or impossible to obtain using ALPID, primarily due to the requirement for frequent redefinition of the finite element mesh. Most realistic forgings reduce the original height of the workpiece by 60-70 percent total, about 1% per time step. Without remeshing the accuracy of the simulation is compromised by severe distortion of the finite elements. More peculiar to ALPID, however, is the need to ensure that the boundary nodes in contact with the dies remain closely spaced so that the boundary element edges conform to the complex die contours as illustrated in Figure 15. Frequent remeshing not only is time consuming for the user, it also denies him easy access to a continuous history of field variables at material points defined by nodes. EALPID, an enhanced version of ALPID, developed by Structural Dynamics Research Corporation (SDRC), offers capabilities which address these problems. The user has access to special tracking options which provide a time history (uninterrupted by remeshing) of stress, strain and thermal quantities at specified material points. Also, during the batch process, EALPID automatically redefines the finite element mesh and adapts the mesh definition to minimise the overlap of the workpiece boundary elements and the dies. Other types of adaptive meshing have sought to intensify the density of nodes where the field variables exhibit steep gradients. Hageman and co-worker [23] have developed an adaptive remeshing procedure that ensures conformity of a finite element mesh to a moving rigid boundary of arbitrary shape, the primary requirement in forging.

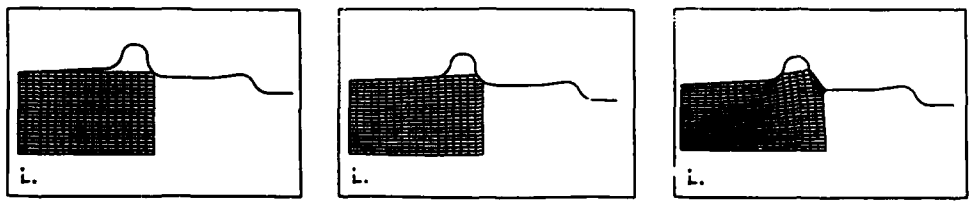

Figure 15: An ALPID Simulation Without Remeshing

5.3 Adaptive Remeshing Strategies

An obvious advantage to automatic, adaptive remeshing for simulations that require 20-30 remeshes is the enormous savings in the users time and effort. Perhaps a more important advantage, however, is greater reliability of the numerical results. Remesh criterion are precisely defined and uniformly applied; it does not depend upon a mesh that 'looks bad', nor does it wait for the extreme conditions signaled by a negative Jacobian.

There are two forms of remeshing implemented in EALPID. The first, called nodal adjustment, improves the shape of the finite elements but does not change the element topology. The second, called Free Mesh Generation [124], or FMG, redefines the element topology according to localized commands; FMG also ensures well formed elements. Both EALPID remeshing procedures conserve the volume and the current shape of each material region.

5.4 Nodal Adjustment

In EALPID's nodal adjustment procedure the position of each free node is defined to be an average of all other nodes connected by a single element edge. Nodes on free surfaces are restrained, those on an axis of symmetry are partially restrained (they can move along that axis), and the remaining nodes are free. The nodes are processed in numerical order and the entire procedure is repeated a sufficient number of times to ensure convergence. The iterative procedure can be represented by the equations:

$$X_i^{n+1} = \text{Average}\left(\sum X_j^n\right) \qquad (28)$$
$$Y_i^{n+1} = \text{Average}\left(\sum Y_j^n\right)$$

where i ranges over all nodes, j ranges over the nodes connected to the ith node, and n is the iteration counter. Figure 16 illustrates the effects of this nodal adjustment procedure.

5.5 Remeshing with FMG

An FMG (free mesh generation) remesh is triggered when any one of three criteria is satisfied:

- Die overlap (or void) exceeds some fraction of total workpiece cross section area, e.g. 0.1%
- An interior node is too close to a die boundary, expressed as a fraction of element edge length

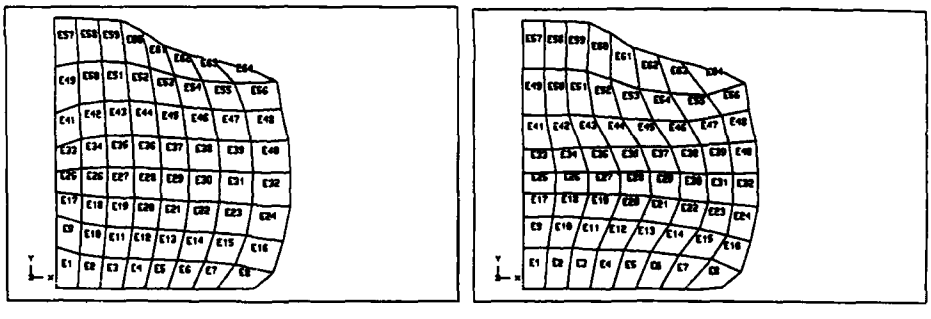

Figure 16: An Example EALPID Mesh Before and After Nodal Adjustment

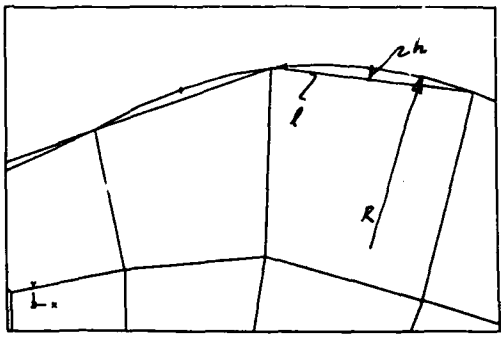

Figure 17: Part-Die Overlap/Void

- An element becomes severely distorted relative to its initial shape

the remesh is initiated, mesh point grading values are assigned so as to concentrate nodes where die overlap areas are largest. Details of the algorithms and derivations are available in [15]; only the concepts are presented here. Along the part surfaces which contact the die, grading values are assigned which contact the die, grading values are assigned which reduce part-die overlap (or void) to an acceptable value (user defined). If we assume the die boundary is a circular arc, as shown in Figure 17, then the arc radius and overlap area are:

$$R = \frac{l^2}{8h}, \quad A = \frac{l^3}{16R} \tag{29}$$

Hence, element side length is nearly proportionally to the cube root of overlap area. Since many element sides must be defined, an iteration scheme of the form;

$$l_i = f\left(A_{min}^{1/3}, \; A_{max}^{1/3}\right) \tag{30}$$

is used to redefine mesh grading values. Then total overlap area is recomputed and compared to an allowable error,

$$A^n = \sum \left(l_i^3/16R_i\right) < \epsilon A_w \tag{31}$$

where A_w is total workpiece area and ϵ is user defined. If the total overlap is still too large, *Amin* is reduced and (30) is re-applied. A typical FMG remesh is shown in Figure 18, and illustrates how the automatic adaptive remeshing procedure enables EALPID to have its mesh dynamically conform to complex die shapes. User intervention is minimised and the results are accurate and reproducible.

5.6 Interpolation

After each remesh EALPID interpolates the time integrated quantities of the analysis (stress, strain, and temperature) by employing a local, spline fitting procedure developed by Franke [21]. Briefly, the cross

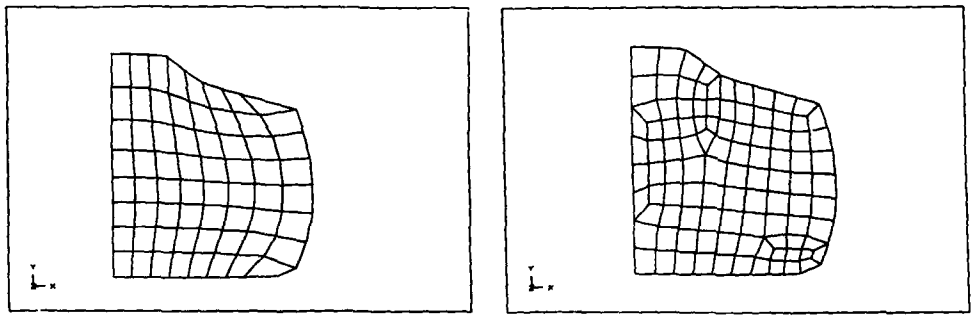

Figure 18: An EALPID Mesh Before and After an FMG Remesh

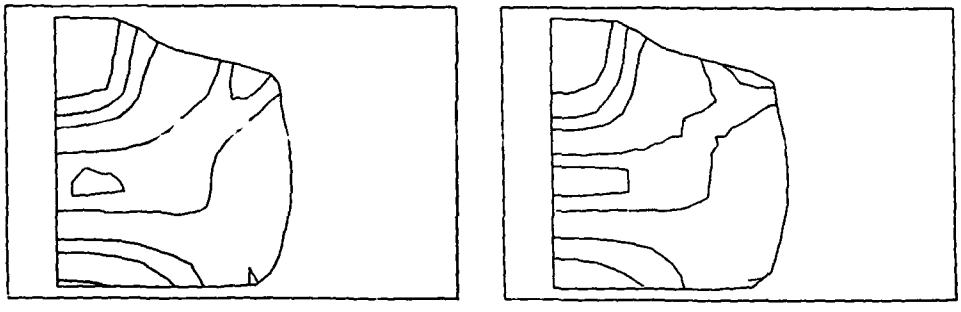

Figure 19: Effective Strain Before and After Remeshing and Interpolation

section of the workpiece is subdivided into a number of overlapping rectangular regions. In each region a thin plate spline is fit to the data at the computational points (nodes or integration points) of the old mesh. Then the data at the computational points of the new mesh are obtained from a weighted sum of the splines, the weighting functions being products of normalised piecewise cubics. This interpolation procedure was chosen first because it was found to be more accurate than the 'lumped mass' least squares procedure, especially at new points that are outside the domain of the old. Secondly, when there are a large number of points to interpolate, this procedure is more efficient than a least squares interpolation. Figure 19 shows contours of effective strain before and after remeshing and interpolation.

5.7 Other Capabilities

Besides the essential adaptive remeshing, practical usage is enhanced by a number of other features. One of these is point tracking, which allows the nodes of the initial mesh to be followed through the numerous remeshes to the final part. Stress, strain and temperature can be plotted at tracking points; connectivity graphically displays total material movement. Simultaneous heat transfer was added and coupled to EALPID to simulate warm and cold die forging. Specifically, the viscoplastic work was added to heat transfer, and temperature dependence was added EALPID material laws. Die velocity controls were added to simulate various forging machines such as hammers, scotch-yoke mechanisms, and feedback control systems, or to keep the material within critical processing windows. User defined velocity functions can be used to simulate the performance of specific machines. Users may also change dies to simulate the shift from blocker to finisher, and maintain the shape and strain history of the part. Automatic bandwidth minimisation after each remesh keeps EALPID running at top speed.

5.8 Conclusions

The rigid viscoplastic finite element approach of ALPID is the most cost effective approach to forging simulation; it is almost an order of magnitude cheaper than MARC. The automatic remeshing and interpolation of EALPID are essential ingredients for practical industrial use in forging die design. Numerous other additions have extended EALPID to a wide range of practical process simulations.

6 Cyclic Processes

The previous sections have concentrated on the technology for simulating processes commonly used for very high performance aerospace components. However, die casting and thermoplastic injection molding continue to increase in popularity decades after their introduction. During the 1970's software development emphasized the filling process, but it soon became evident that cooling plays a key role in quality and cost. Typically more than half of a die casting cycle is cooling. This section will review briefly the key concepts for numerical simulation of cooling. For a detailed discussion of cooling and filling see [26,27].

The two most important issues in the cooling analysis are to reduce cycle time and improve the quality. This is achieved by cooling the part as fast as possible, but uniformly across its span and equally across the thickness. The design of both the part and the cooling system are important to both cycle time and quality. Poorly cooled areas (hot spots), due to poor cooling line placement or excessive part thickness, can result in warpage, residual stresses, surfaces blemishes and cracks. A numerical heat transfer simulation of the production cycle can help estimate cooling time, set appropriate process conditions, and predict part solidification in sufficient detail to guide the design of the part and the mold cooling system.

6.1 Cycle Averaged Methods

Early software relied on the concept of cycle-averaged heat transfer. This converts a cyclic problem into a steady state problem where the results are average values over the cycle. Hence, heat transfer analysis and solidification prediction in the part (plastic, aluminum, zinc) is not possible mathematically. The user must supply material injection temperature, part ejection temperature and cycle timing and/or mold temperatures. Then the heat transfer software can compute mold temperature and heat transfer paths to the water lines, subject to various assumptions or modifications. One early package used shape factors for die heat transfer, resulting in a very fast analysis. Recent packages have replaced the shape factors with 2D or 3D linear finite element analysis, or a linear boundary element analysis.

The cycle averaged approach has a number of short falls, key points being:

- Variations over the cycle are blurred; local die hot spots seriously underestimated
- It cannot predict cycle time, and time to reach ejection temperature
- It cannot predict die surface temperature versus time nor material temperature at ejection time without input the user would rather not provide (e.g. die surface temperature)

Hence, the main use of cycle averaged analysis is to balance the cooling load between core and cavity and across the die.

6.2 Efficient Transient Analysis

Recently SDRC has introduced a cyclic process cooling analysis code which addresses most of the objections to the cycle averaged codes [26]. Heat transfer within the part is fully coupled with a three dimensional representation of the mold and a network flow analysis of the coolant. The simulation is an iterative procedure based on a transient model of the part, a time periodic model (Fourier transform) of the mold and a steady state model of the coolant. The part is analyzed by a nonlinear finite difference model. The mold is analyzed in the frequency domain using a procedure based on the boundary element method, and the inverse Fourier transform allows coupling to the part analysis. The zero Fourier mode is the cycle average.

The simulation can predict cycle time and time dependent temperatures and fluxes in the part, dies, and coolant without requiring any initial guesses of mold temperature and cycle time. Contour plots over the parts surface include:

- Time to reach ejection temperature
- Material temperature at ejection time
- Mold surface temperatures throughout the cycle
- Cooling network flows
- Thermal power per cycle in each component

For plastic injection molding, several comparisons with test data indicate that the package predicts temperatures with $\pm 3°C$ when the process is modeled in sufficient detail.

6.3 Conclusions

The cyclic processes of die casting and injection molding can be analysed to the same high levels of accuracy demonstrated for forging, heat treating and casting. The advantages of true cyclic cooling simulation over cycle averaged analysis are becoming widely recognized. The SDRC software is accurate enough to help process designers make quantitative decisions on part dimensions, cooling line placement and flow rates. The major source of error is that sometimes important features like inserts are not modeled.

7 Summary

A series of numerical methods have been briefly outline which address specific issues in the numerical simulation of casting, forging and heat treating processes. These numerical techniques have been added to EALPID, TOPAZ, and NIKE and integrated into the I-DEAS MCAE environment. This gives manufacturing engineers access to the same geometry and finite element models used by design engineers. Hence, the manufacturing engineer and design engineer can work in parallel to jointly design the part and process to obtain the most cost efficient part in the least time.

The specific numerical methods outlined herein should finally be discussed in a different context. While they indeed have made process simulations possible, the user must have a high level of training, experience and judgement. No computer program is bullet proof, but nonlinear process simulation codes are full of traps for the unwary. New numerical methods will continue to improve our ability to simulate manufacturing processes and make them more stable. The techniques and progress shown herein should be viewed as the beginning of a quiet revolution taking place in manufacturing.

8 Acknowledgements

The development of software at SDRC is partly funded by *ad hoc* industry associations. Many SDRC staff have contributed to the developments discussed herein. Anthony Rice and David Pinella developed the inverse heat transfer and heat treat simulations; Dr. Laura Hageman and Nadine Mack invented the strategies for adaptive automatic remeshing; Dr. Thomas Burton conceived the methods for simulating cyclic processes. General Electric Company deserves special mention, particularly the Plastics Application Center and Aircraft Engines and especially Dr. Sulekh Jain and Mr. Leo Buchakjain for their insight into forging and casting.

9 References

1. Lewis, R., Morgan, K., Schrefler, B. editors, "Numerical Methods in Heat Transfer, Vol. II," Proc. of 2nd Intl. Conf., Venice, July 1981, J. Wiley, 1983.

2. C.H. Lee and Shiro Kabayashi. "New solutions to rigid-plastic deformation problems using a matrix method," Trans. ASME, J. Engineering for Industry, 95:865-873, 1973.

3. Lewis, R., Morgan, K. editors, "Numerical Methods in Thermal Problems, Vol. IV," Proc. of 4th Intl. Conf., Swansea, 1985, Pineridge Press, 1985.

4. Shapiro, A.B., "TOPAZ—A Finite Element Heat Conduction Code for Analysing 2-D Solids," Lawrence Livermore National Laboratory, March 1984.

5. Beck, J., Blackwell, B., St. Clair, C., Inverse Heat Conduction, Wiley-Interscience, 1985.

6. Shiro Kobayashi. "Rigid-Plastic Finite-Element Analysis of Plastic Deformation in Metal-Forming Processes," Technical Report, Air Force Materials Laboratory, 1979.

7. Hughes, T., "Unconditionally Stable Algorithms for Nonlinear Heat Conduction," Comp. Meth. in Appl. Mech. and Engng, Vol. 10, 1977, pp. 135–139.

8. S.I. Oh, G.D. Lahoti, and T. Altan. "ALPID - A general purpose FEM program for metal forming," In Proceedings of NAMRC-IX, 1981.

9. Huebner, K., Thornton, E., The Finite Element Method for Engineers, Wiley, 1982, pp. 605–611.

10. Mullen, R., Belytschko, T., "Dispersion Analysis of Finite Element Semidiscretizations of the Two Dimensional Wave Equation," Int. J. Num. Meth. Engng, Vol. 18, 1982, pp. 11–29.

11. Liu, W., Belytschko, T., "Efficient Linear and Nonlinear Heat Conduction with a Quadrilateral Element," Int. J. Num. Meth. Engng., Vol. 20, 1984, pp. 931–948.

12. S.I. Oh. "Finite element analysis of metal forming problems with arbitrarily shaped dies," Int. J. of Mechanical Science, 17, 1982

13. Rice, A.B. Puckett, S.J. and Buchakjian, L., "Investment Casting Process Design, Part I: Software For Process Design/Redesign," ASME Intl. Computers in Engng. Conf., New York, Aug. 9-13, 1987, Vol. 2.

14. Page, C.C., Saunders, M.A., "Solution of Sparse Indefinite Systems of Linear Equations," SIAM J. Numer. Anal, Volume 12, No. 4, September, 1975.

15. Hestenes, M.R., Stiefel, E., "Methods of Conjugate Gradients for Solving Linear Systems," Journal of Research of National Bureau of Standards, Vol. 49, No. 6, pp. 409–436, December, 1952.

16. Hageman, L.A., Young, D.M., Applied Iterative Methods, Academic Press, New York, 1981.

17. Hughes, Thomas J.R., Levit, Itshak and Winget, James, "An Element-by-Element Solution Algorithm for Problems of Structural and Solid Mechanics," Computer Methods in Applied Mechanics and Engineering, Vol. 36, No. 2, pp. 241–254, 1983.

18. Hughes, Thomas J.R., Winget, James, Levit, Itshak, and Tezduyar, Tayfun, "New Alternating Direction Procedures in Finite Element Analysis Based Upon EBE Approximate Factorizations," Proc. of Symposium on Recent Developments in Computer Methods for Nonlinear Solid and Structural Mechanics eds. S. Atluri and N. Perrone, ASME meeting, University of Houston, Houston, Texas, pp. 75–109, June 20–22, 1983

19. Stafford, R.O., Rice, A.B., Pinella, D.F., "Investment Casting Process Design Part 2: Solidification Simulation," ASME Intl. Computers in Eng. Conf., New York, Aug 9-13, 1987 Vol. 2

20. Nuno M.R.S. Rebelo. "Finite Element Modeling of Metalworking Processes for Thermo-Viscoplastic Analysis," PhD thesis, University of California, Berkeley, 1980

21. Richard Franke. "Smooth Interpolation of Scattered Data by Local Thin Plate Splines" Comp. and Maths. with Appls., 8:273-281, 1982.

22. Jay, A., Lionberger, S. R. and Fine, A.D., "Finite Element Metal-Forming Analysis: Two Approaches," Proc. ASME Joint Pres. Vessels and Piping, and Computers in Engng. Conf., Chicago, July 1986

23. Hageman, L.J., "Automatic Adaptive Remeshing in EALPID, an Advanced Forging Simulation Program", ASME Intl. Computers in Engng. Conf., Vol. 2, New York, Aug. 9-13, 1987

24. "I-DEAS Level 3, Supertab©Engineering Analysis, Pre- and Post-Processing, User Guide, Reference Manual, and Menu Flow Chart" Structural Dynamics Research Corporation, 1986.

A mixed Eulerian- Lagrangian finite element method for Simulation of thermo-mechanical forming processes

J. Huetink and J. van der Lugt
University of Twente, dep. Mechanical Engineering
P.O Box 217, 7500 AE Enschede
Netherlands

Abstract

A mixed Eulerian- Lagrangian finite element method is developed by which nodal point locations can be adapted independently from the actual material displacements. Numerical difficulties due to large element distortions, as may occur when the updated Lagrange method is applied, can be avoided by this method. Movement of (free) surfaces can be taken into account by adapting nodal surface points in a way that they remain on the surface. Hardening and other deformation path dependent properties are determined by incremental treatment of convective terms.A local and a weighed global smoothing procedure is introduced in order to avoid numerical instabilities.
The method has been applied to simulations of an upsetting process, a wire drawing process and a cold rolling process. In the simulation of the rolling process, both workpiece and roll are simultaneously analysed in order to predict the flattening of the roll. Special contact-slip elements are developed for the the tool- workpiece interface.

1. INTRODUCTION

Simulation of metal forming processes by the finite element method using the updated Lagrange method is restricted with respect to the deformation range because the element mesh may be completely distorted after a number of steps. Besides boundary conditions must generally be adapted after each step or after a number of steps because of the changing contact between tool and nodal material points. A simultaneous simulation of workpiece and tool cannot be carried out if slip occurs. A simultaneous simulation of workpiece and tool is of particular interest in problems with considerable heat conduction and heat production, as well as in problems where deformations of the tool cannot be neglected (rolling of tin plate). Therefore a procedure has been developed in which nodal point locations can be (incrementally) adapted independent of the material displacement increments. Conditions for free or forced surface movements can be satisfied. An updated Lagrange approach as well as an Eulerian approach can be regarded as special cases of the procedure. Therefore it is called the mixed Eulerian- Lagrangian formulation.
The procedure was first presented by one of the authors in 1982 [1]. An extensive description is given in [2].

2.MATHEMATICAL MODELING

The mathematical model is based on general principles of continuum mechanics: equilibrium, compatibility and constitutive relations. In this paper we will present a brief description restricted to quasi-static isothermal conditions and time independent material properties. (A description including thermal effect and time dependent material properties is given in [2,3]).

2.1 Constitutive equations

The constitutive equation for elastic-plastic material can be written as [2,5,7,8,10,11]:

$$\overset{\nabla}{\underline{\sigma}} = \underline{D}:\underline{d} \qquad (1)$$

where $\overset{\nabla}{\underline{\sigma}}$ is the Jaumann rate of the Cauchy stress tensor:

$$\overset{\nabla}{\underline{\sigma}} = \dot{\underline{\sigma}} - \underline{\omega}\cdot\underline{\sigma} + \underline{\sigma}\cdot\underline{\omega} \; . \qquad (2)$$

$\underline{D}$ is the elastic plastic "tangent modulus" tensor, depending on the material properties, the stress and the deformation history. The tensor $\underline{d}$ is the rate of deformation tensor defined as the symmetric part of the gradient of velocity $\underline{v}$,

$$\underline{d} = \tfrac{1}{2}\,(\underline{v}\cdot\underline{\nabla} + \underline{\nabla}\cdot\underline{v}) \qquad (3)$$

and ω is the spin tensor defined as the anti-symmetric part of the gradient of velocity $\underline{v}$,

$$\underline{\omega} = \tfrac{1}{2}\,(\underline{v}\cdot\underline{\nabla} - \underline{\nabla}\cdot\underline{v}) \qquad (4)$$

The equilibrium condition yields:

$$\underline{\sigma}.\underline{\nabla} + \underline{f} = 0 \qquad (5)$$

Note: vectors are denoted by subscript wiggles, and tensors by subscript bars.

2.2 Contact and friction

The analysis of forming processes cannot be restricted to product deformations only. One has to include into the analysis the product-tool contact region, friction at the product-tool interface and sometimes even the tool itself. This calls for a finite element approach to model the contact conditions, especially in the multi-body case. A finite element formulation for simulation of this contact has been presented by the authors in [9].The contact description is inspired on the assumption of a friction layer with a small but finite thickness . Stick-slip constitutive behaviour is introduced as non-associated elasto-plasticity (elastic properties in thickness direction and elastic-plastic deformation in shear).

Consider two bodies A and B and a (candidate) contact region C [4]. Define a reference surface S between the bodies, having equal normal or directional distances to either body:

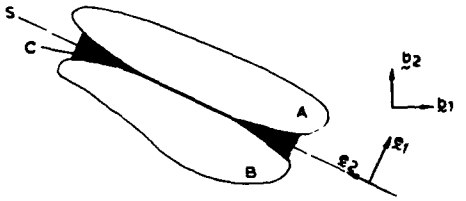

Fig. 1 Contacting bodies A and B with (candidate) contact region C and reference surface S.

Referring to Fig. 1, two coordinate systems are defined: a global, fixed, coordinate system ($\underset{\sim}{b}_1, \underset{\sim}{b}_2$) and a local, corotating, coordinate system ($\underset{\sim}{e}_1, \underset{\sim}{e}_2$):

$$\underset{\sim}{e}_i = Q_{i\alpha}\underset{\sim}{b}_\alpha \tag{6}$$

The time derivative can be expressed as:

$$\dot{\underset{\sim}{e}}_i = \dot{Q}_{i\alpha}\underset{\sim}{b}_\alpha \;\Rightarrow\; \dot{\underset{\sim}{e}}_i = -\Omega_{ik}Q_{k\alpha}\underset{\sim}{b}_\alpha = -\Omega_{ik}\underset{\sim}{e}_k \tag{7}$$

where Ω_{ik} denotes rate of rotation of the local basis, which in this paper is defined to equal the rate of rotation of reference surface S.

2.2.1 Stress and shear deformation in the contact region

Since contact stresses are considered to be tractions applying to only one surface (interface) S, it can be denoted as a first order tensor $\underset{\sim}{\tau}$:

$$\underset{\sim}{\tau} = \tau_i\underset{\sim}{e}_i \tag{8}$$

Taking time derivatives:

$$\dot{\underset{\sim}{\tau}} = \dot{\tau}_i\underset{\sim}{e}_i + \tau_i\dot{\underset{\sim}{e}}_i \;\Leftrightarrow\; \dot{\underset{\sim}{\tau}} = \dot{\tau}_i\underset{\sim}{e}_i + \Omega_{ij}\tau_j\underset{\sim}{e}_i \tag{9}$$

Alternatively $\dot{\underset{\sim}{\tau}}$ can be split up into a corotational derivative $\overset{\nabla}{\underset{\sim}{\tau}}$ and a rotational change $\underset{\sim}{\Omega}\cdot\underset{\sim}{\tau}$:

$$\dot{\underset{\sim}{\tau}} = \overset{\nabla}{\underset{\sim}{\tau}} + \underset{\sim}{\Omega}\cdot\underset{\sim}{\tau} \tag{10}$$

Hence, tensor components for $\overset{\nabla}{\underset{\sim}{\tau}}$ must satisfy:

$$\overset{\nabla}{\underset{\sim}{\tau}} = \dot{\tau}_i\underset{\sim}{e}_i \tag{11}$$

The momentaneous situation in the contact region is shown in Fig. 2:

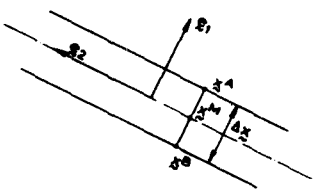

$$\underset{\sim}{x}^A = \underset{\sim}{x}^M + \tfrac{1}{2}\Delta\underset{\sim}{x}$$
$$\underset{\sim}{x}^B = \underset{\sim}{x}^M - \tfrac{1}{2}\Delta\underset{\sim}{x}$$

Fig. 2 Position of related points.

The rate of deformation is defined by:

$$d_i = \dot{x}_i^A - \dot{x}_i^B = \Delta\dot{x}_i \tag{12}$$

Thus tensor $\underset{\sim}{d}$ denotes relative surface velocity, corrected for rotation of the reference surface

$$\underset{\sim}{d} = \Delta\underset{\sim}{v} - \underset{\sim}{\Omega}\cdot\Delta\underset{\sim}{x} \tag{13}$$

Constitutive behaviour is taken analogous to elasto- plasticity. The rate of

deformation is assumed to consist of a reversible (elastic) part and a non-reversible (plastic, c.q. slip) part. A linear relation is assumed between corotational stress derivative and the elastic part of rate of deformation, hence:

$$\overset{\nabla}{\underset{\sim}{\tau}} = \underline{\underline{E}}\cdot(\underline{\underline{d}} - \underline{\underline{d}}^{el}) \qquad \text{with} \quad \underline{\underline{E}} = \begin{bmatrix} E_{11} & 0 \\ 0 & E_{22} \end{bmatrix} \tag{14}$$

It is assumed that normal relative displacement is strictly elastic. The non-elastic rate of deformation is assumed to have the direction of the tangential stress. The slip criterion is defined for Coulomb friction:

$$-\mu\tau_1 + |\tau_2| = 0 \tag{15}$$

From (14) and (15):

$$\overset{\nabla}{\underset{\sim}{\tau}} = \underline{\underline{E}}\cdot\underline{\underline{d}} - \underline{\underline{Y}}\cdot\underline{\underline{d}}\ , \quad \text{where} \quad \underline{\underline{Y}} = \begin{bmatrix} 0 & 0 \\ \mu\,\mathrm{sgn}(\tau_2)E_{11} & E_{22} \end{bmatrix} \tag{16}$$

The above relation is valid in case of slip (plastic) deformation. For the elastic situation: $\underline{\underline{Y}} = \underline{\underline{0}}$, for the open situation: $\underline{\underline{Y}} = \underline{\underline{E}} = \underline{\underline{0}}$. $\underline{\underline{E}}$ and $\underline{\underline{Y}}$ are generally combined into a deformation stiffness tensor $\underline{\underline{\mathcal{D}}}$ by stating $\underline{\underline{\mathcal{D}}} = \underline{\underline{E}} - \underline{\underline{Y}}$, and contact behaviour becomes:

$$\overset{\nabla}{\underset{\sim}{\tau}} = \underline{\underline{\mathcal{D}}}\cdot\underline{\underline{d}} \qquad \text{alternatively:} \quad \dot{\tau}_i = \mathcal{D}_{ij}d_j \tag{17}$$

3. VIRTUAL POWER AND FINITE ELEMENT FORMULATION

For the two bodies A, B (Fig. 1) the virtual power yields:

$$\int_{V_B+V_A}\delta d_{ij}\sigma_{ij}dV + \int_{S_{contact}}(\delta v_i^A - \delta v_i^B)\tau_i dS + \int_{S_{free}}\delta v_i T_i dS = 0 \qquad \forall\delta v_i \tag{18}$$

Finite elements are derived in the usual way, the real velocity distribution is approximated by interpolation of nodal point velocities v_i^N:

$$v_i = \Psi^N v_i^N \tag{19}$$

The finite element formulation for the body interior is derived by substitution of eq.(19) and eq.(1) into the rate of change of the first integral of eq.(18). Thisformulation is straight forward and can be found in many books and papers considering finite elements [6,7,8] as far as the linearized (incremental) solution of the nodal velocities is concerned.

The description of the contact element is derived from the rate of change of the contact surface integral in (18). The rate of deformation (slip) and spin in the contact region are approximated using (19) by respectively

$$d_i = B_{ik}^N v_k^N \quad \text{and} \quad \Omega_{ik} = \overset{*}{B}{}_{ikl}^N v_l^M \tag{20}$$

Substitution of (19) and (20) into the rate of change of the contact surface integral results into a stiffness matrix equation for the contact-slip element with components:

$$K_{lm}^{NM} = \int_{S_{contact}}\Big(B_{il}^N\mathcal{D}_{ij}B_{jm}^M + \overset{*}{B}{}_{kil}^N\Delta x_k\mathcal{D}_{ij}B_{jm}^M + B_{kl}^N\tau_i\overset{*}{B}{}_{kim}^M + \overset{*}{B}{}_{kjl}^N\Delta x_j\tau_i\overset{*}{B}{}_{kim}^M\Big)dS \tag{21}$$

4. INCREMENTAL STRESS FORMULATION

Nonlinearity and path-dependence necessitate an incremental solving procedure. After solving incremental displacements, the stresses are calculated in integration points. The bulk elements used are 4-noded linear isoparametric elements with constant dilatation [6,7,8]. For a 4-noded contact element two integration points are defined each of which is chosen at a point x^M (Fig. 2) halfway the corresponding nodal points. This position enables a more accurate determination of the open-close condition in the nodal points.

In the mixed Eulerian Lagrangian formulation material displacement and nodal (grid) point displacement are uncoupled. Uncoupling of material and grid point displacement implies that in addition to the incremental calculation as in the Updated method, convection must be taken into account in order to be able to update the state at the grid points. The stress increment is given by [1,2]:

$$\Delta\underline{\underline{\sigma}} = \hat{\underline{\underline{\sigma}}}\Delta t + (\Delta\underline{x} - \Delta\underline{u})\cdot\vec{\nabla}\underline{\underline{\sigma}} \tag{22}$$

$$\underline{\underline{\sigma}} = \underline{\underline{\sigma}}^{\circ} + \Delta\underline{\underline{\sigma}} \tag{23}$$

where $\Delta\underline{u}$ is the material displacement increment derived from the solved nodal

point velocities and $\Delta\underset{\sim}{x}$ the nodal displacement increment.

$$\Delta\underset{\sim}{u} = \underset{\sim}{v}\,\Delta t = \psi^N \underset{\sim}{v}^N \Delta t \qquad (24)$$

The first term on the righ thand side of (22) equals the stress increment as in the Updated method, the second term represents the convective stress increment.

The determination of the convective stress increment complicates the solution procedure considerably because the stress gradient is needed and this cannot be calculated directly at element level. The convective terms are calculated from the differences between the values in adjacent elements of each material-associated quantity respectively. Firstly at element level nodal point stresses are calculated using local least square smoothing [12]. Thereafter mean nodal stresses σ^N are calculated from all adjacent elements resulting in a continuous stress field.

$$\underset{\sim}{\sigma}^e = \psi^N \underset{\sim}{\sigma}^N \qquad (25)$$

The stress gradient at element level is now determined from $\underset{\sim}{\sigma}^e$. A more smoothed stress field is obtained if prior to the next increment the integration point stresses are replaced by values determined from eq.(25) using the appropriate local coordinates in the interpolation function ψ^N. However, this field will generally not satisfy nodal point equilibrium. Therefore The integration point values are not completely replaced by the smoothed values obtained from eq. (25), but are calculated as a weighed sum of eq.(23) and eq.(25). The weight factor depends on the relative displacement $\Delta\underset{\sim}{u} - \Delta\underset{\sim}{x}$ and the element size. Nodal point equilibrium can be achieved using an iteration method related to the Hu-Washizu principle [6].

The stress components in the contact elements are related to a coordinate system defined by the orientation of the contact element. These stress components are not necessarily continuous. Consequently it is not possible to calculate nodal stresses as mean values of all adjacent elements. Besides, the smoothing procedure would give incorrect stress predictions. Therefore a procedure has been used by which the calculation of mean nodal stresses is restricted to elements of the same type.

5. SURFACE MOVEMENT

Movement of (contact) surface points can be taken into account by adapting nodal surface point locations in such a way that they remain on the moving surface. The procedure is illustrated in Fig. 3 . It is observed that the new position of nodal surface points is not exactly on the surface found by the element boundaries if the material displacement increments are followed. However, if the new position of the nodal points would have been chosen on these element boundaries, material is lost at every increment. When using a spline, the amount of lost material is more or less in equilibrium with the added material.

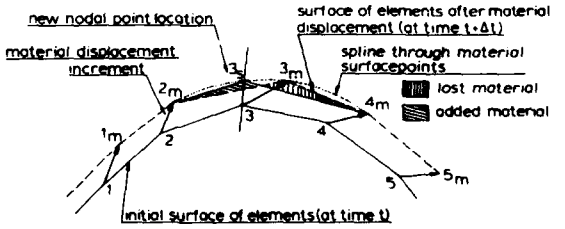

Fig. 3 Adaptation of nodal surface point location.

6. SIMULATIONS OF FORMING PROCESSES

The first process which has been simulated is the upsetting process, a process which can be regarded as a benchmark problem for metal forming. The upsetting process is defined as the axial compression of an axi- symmetrical body between two undeformable plates. The plates are assumed to be sufficiently rough to suppress slip at the interfaces. The finite element dicretization consists of 48 isoparametric elements with four nodes and constant dilatation according to Nagtegaal et.al. [7]. The material properties used are those of low carbon steel with code CK15. The undeformed mesh is shown by Fig 4. Only a quater of the cross section is modeled because of symmetry. The analysis was carried out using the mixed Eulerian- Lagrangian method. The element location is adapted in a way that too much distortion of the elements is avoided, whereas the expansion of the contact surface is continuously taken into account by adapting nodal surface point location according the procedure discussed in section 5. The deformed mesh is shown by Fig. 5.

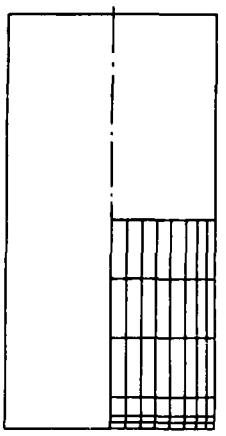

Fig. 4. Initial finite element mesh for simulation of the upsetting process.

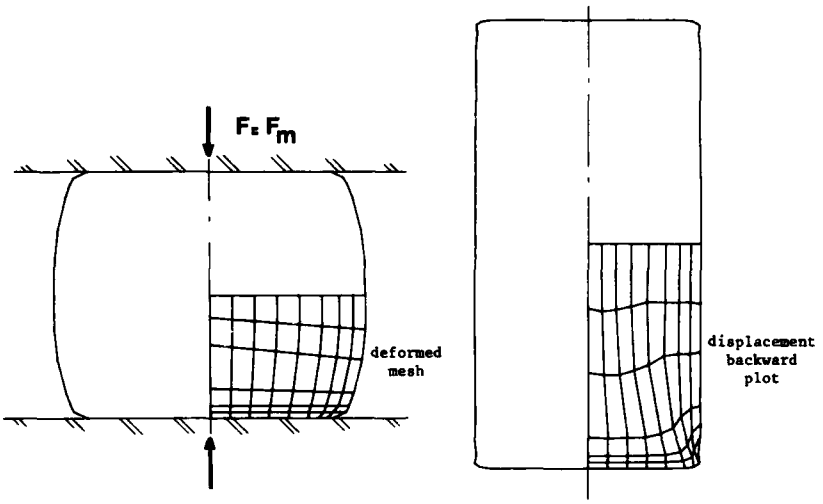

Fig. 5 Deformed mesh after upsetting, and displacement backward plot

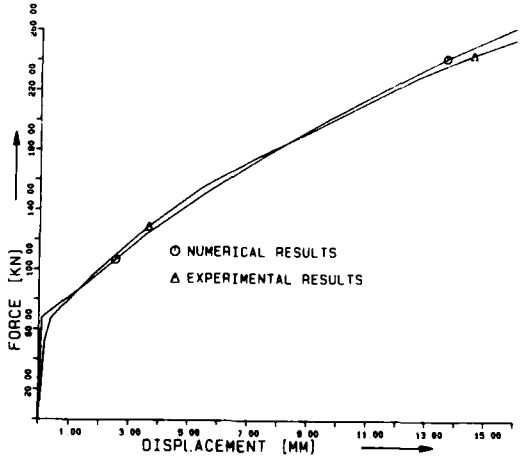

Fig. 6 Load-displacement curve of the upsetting process.

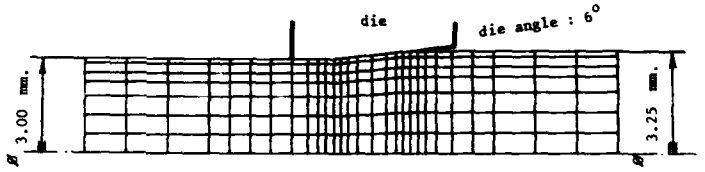

Fig. 7 Finite element mesh for simulation of the wire drawing process

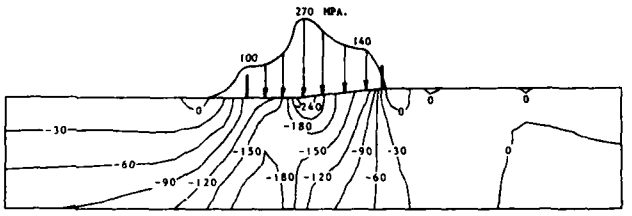

a) radial stress and normal stress at the die interface.

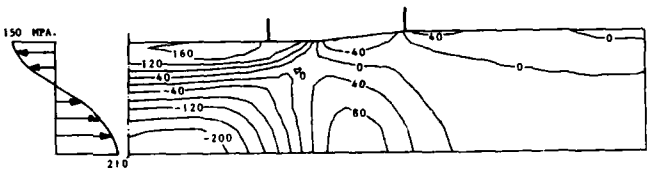

b) axial stress

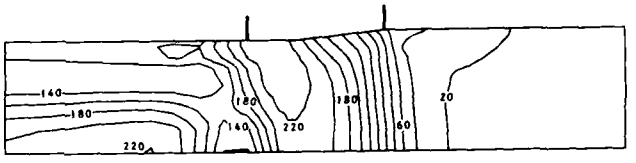

c) equivalent (Von Mises) stress

Fig. 8 Predicted stress distribution of the wire drawing process after a stationary state is reached

Fig. 5 also shows the 'displacement backward plot', obtained by subtracting the total material displacements of the particles that finally coincide with the nodal points, from the final location of the nodes. The discrepancy between the shape of the billet in the backward plot and the initial shape is a measure for the accuracy of the simulation. It can be observed that in the intersection between the cylindrical free outer surface and the contact surface a small piece of material is lost due to the incremental expansion of the contact surface.

The simulation has experimentally been verified by an upsetting test on a cylindrical billet of low carbon steel with code CK15. The measured and the predicted load- displacement curve is shown by Fig. 6. It can be observed that there is a rather good agreement between experiment and prediction.

The second process that is simulated is a wire drawing process. the finite element mesh is shown by Fig. 7. The material used is soft copper. Fig. 8 shows the predicted stress distribution. A highly inhomogeneous axial stress distribution appeared in the wire after reduction. This stress distribution will remain in the wire after unloading (the neutral point is shifted after unloading). similar residual stress distribution have been measured by means of Röntgen diffraction.

An other simulation was carried out for stand 3 in a 5-stand cold rolling mill at HOOGOVENS IJmuiden BV., The Netherlands. The geometry and finite element mesh are shown in Fig. 9 and Fig. 10 respectively. Only half of the problem is modeled because of symmetry.

The rolled material is low carbon steel, the roll is taken into account as an elastic structure in order to predict roll deformation. The contact elements are located between roll and rolled material, the coefficient of friction is 0.07.

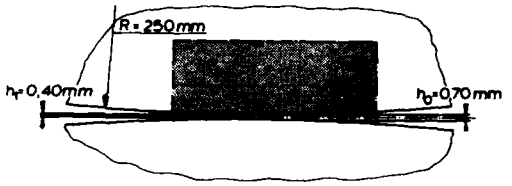

Fig. 9 Geometry of the cold rolling process.

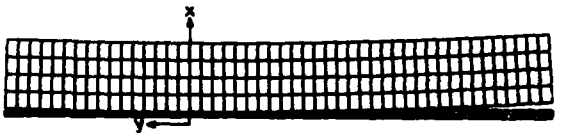

Fig. 10 Element mesh of the cold rolling simulation.

The simulation has been performed in 425 steps. In the first 15 steps an entry and exit tension of 110 N/mm^2 was applied to the rolled material. In each following step a displacement increment of the roll of 0.0001R was prescribed until a steady state was achieved.

The resulting normal and shear stress distribution on the interface roll and rolled material is given in Fig. 11. The point where the shear stress reverses is called the neutral point ; roll velocity equals rolled material velocity. From entry towards neutral point the roll is moving faster than the rolled material, from neutral point towards exit the roll is moving more slowly than the rolled material. This is characteristic for cold rolling processes.

Fig. 12 shows the undeformed and the deformed roll shape. The deformed roll deviates from a circular shape and the roll deformation has a relatively strong effect on the total reduction. In this simulation only a small part of the roll was modelled, if a greater part of the roll is modeled the effect of roll deformation will be stronger. This is a point of investigation in the future.

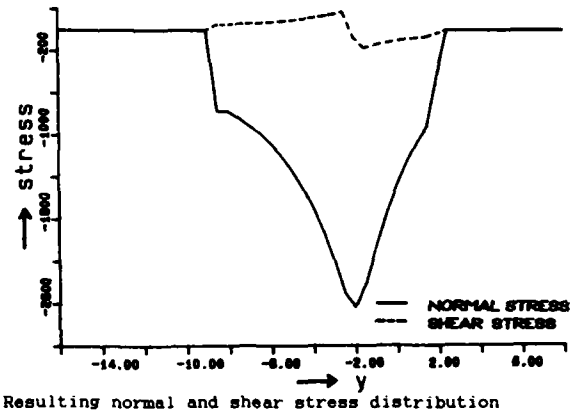

Fig. 11 Resulting normal and shear stress distribution

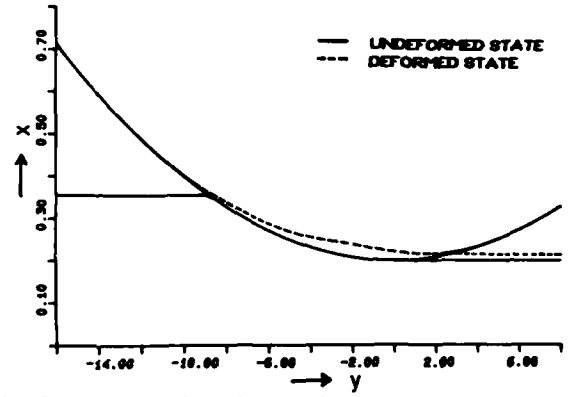

Fig. 12 Undeformed and deformed roll shape.

REFERENCES

1. Huetink, J., 'Analysis of metal forming processes based on a combined Eulerian-Lagrangian finite element formulation', Proc. Int. Conf. Num. Meth. Industr. Forming Processes, 501-509, 1982.
2. Huetink, J., 'On the simulation of thermo- mechanical forming processes',Thesis, University of Twente, The Netherlands, 1986.
3. Lugt, J. van der and Huetink, J.,'Thermal- mechanically coupled finite element analysis in metal forming processes', Comp. Meth. Appl. Mech. Eng., 54 (1986), 145-160.
4. Baaijens, F.P.T., Veldpaus, F.E. and Brekelmans, W.A.M., 'On the simulation of contact problems in forming processes', Proc. 2nd Int. Conf. Num. Meth. Industr. Forming Processes, 85-90, 1986.
5. Prager, W.-Introduction to Mechanics of Continua, Ginn, New York, 1961.
6. Zienkiewicz, O.C. -The Finite Element Method, McGraw-Hill, New York, 1983
7. Nagtegaal, J.C., Parks, D.M. and Rice, J.C., 'On numerically accurate finite element solutions in the fully plastic range', Comp. Meth. Appl. Mech. Eng., 4 (1974), 153-177.
8. Nagtegaal, J.C. and Jong, J.E. de, 'Some computational aspects of elastic plastic large strain analysis', Int. J. Num. Meth. Eng., 17, (1981), 15-41.
9. Huetink, J.,Lugt, J. van der, Miedema, J.R. 'A mixed Eulerian- Lagrangian contact element to describe boundary and interface behaviour in forming processes', Proc. Int. Conf. Num. Meth. Eng. (NUMETA), vol 1 paper D17, Martinus Nijhof publ., Dordrecht, Neth.(1987).
10. Besseling, J.F., A thermodynamic approach to rheology, Proc. IUTAM symp.on irreversible aspects of continuum mechanics, Springer-Verlag, Wien (1968) 16-53.
11. Besseling J.F., Models of metal plasticity; Theory and experiment, Plasticity today, edited by A. Sawczuk and G. Bianchi, Elsevier (1985), 97- 113
12. Hinton, E., and Gampbell, J.S., Local and global smoothing of discontinuous finite element functions using least square method, Int. J. Num. Meth. Eng., 8 (1974), 461-480

FINITE-ELEMENT-SIMULATION OF METAL-FORMING PROCESSES

by

Dr.-Ing. A.E. Tekkaya
Asst. Professor
Mechanical Engineering Department
Middle East Technical University
06531 Ankara
TURKEY

SUMMARY

For the metal forming industry, numerical simulation procedures, through which the tremendous costs for process development and experimental tools can be reduced, are gaining an increasing significance.

In this paper, a finite element code, based on the well-known elastic-plastic formulation by McMeeking and Rice will be given and some interesting industrial metal forming aplications will be discussed. The finite element approach is of updated Lagrangian type utilizing a generalized Prandtl-Reuss flow rule together with the v.Mises yield criterion. Nonlinearities resulted by the material response and the complex kinematics of the problem are handled numerically through the self-correcting and the midpoint stiffness methods.

Examples of application cover the analysis of residual stresses in extrusion, the simulation of the Sachs boring-out method, as well as the simulation of instabilities and deep-drawing.

1 INTRODUCTION

The current trend in metal-forming is to produce geometrically complex workpieces which are almost net-shaped. This leads necessarily to more costly tools and pressing machines, so that the profit basically depends on the process development time and the costs of the experimental trial-and-error analysis. Under these circumstances, numerical simulation procedures, through which the tremendous costs for experimental tools can be reduced, gain industrial *significance*.

Among various numerical analysis techniques, the most effective ones are the finite element procedures. Although, first finite element formulations for the analysis of linear elastic problems have been given in the early 1960's the development of formulations for the analysis of problems involving nonlinearities has started some decades later and is still going on. Especially, the analysis (or equivalenty: the "simulation") of metal forming problems exhibits a complex mathematical and physical nature, involving all possible nonlinearities:

i) Geometric nonlinearities: If the initial and final configurations of a-not necessarily deforming-body differ by a finite amount, so-called "geometric" nonlinearities arise due to the no-more-linear kinematics of the motion of the body.

ii) Material (or physical) nonlinearities: The nonlinear dependence of stresses onto strains in a deforming body is named as "material (or physical)" nonlinearity.

iii) Nonlinear boundary conditions: If the natural boundary conditions change with time as a function of deformation, they are called "nonlinear".

The first known formulation for the finite element analysis of metal forming problems is the so-called initial stress approach by Zienkiewicz et al. [1].Based on an elastic-plastic material description, this formulation ignores completely geometric nonlinearities as well as nonlinear boundary conditions. Hence, the application of this method to practical forming processes is very limited.

The rigid-plastic formulation developed by Lung [2] and independently by Lee and Kobayashi [3] as the viscous-plastic formulation by Zienkiewicz and Godbole [4] prove themselves as very efficient for the analysis of metal-forming processes. Justified through the fact that elastic strains are smaller than the plastic ones for three orders of magnitude during practical forming problems, material behaviour is modeled by neglecting the elastic response completely. By this simplification the kinematic nonlinearities can be by-passed legally in the solution, leading to reduced computational times. An excellent application of this formulation is given in [5] with a special emphasis on the handling of nonlinear boundary conditions. Yet, this type of formulations fail in two principal cases of application:

a) if the simulation involves the analysis of spring-back, residual stresses and similar memory-based elastic phenomena, and

b) if friction between dies and the elastic portion of the workpiece is of interest.

In such cases a so-called "complete" analysis of the problem is required. That is, the material response have to be modeled by an elastic-plastic constitutive relationship. The first sound formulation using an elastic- plastic material law has been given by McMeeking and Rice [6]. Here, a hypoelastic constitutive equation has been used, whereas the formulation has been based on a variational principle by Hill [7]. An alternative formulation founded on Lee's idea [8] of an unloaded, intermediate configuration has been given by Argyris and Doltsinis [9]. Their constitutive equation is of hyperelastic type.

The purpose of this paper is to demonstrate the advanced level reached in the field of finite element simulations of metal-forming processes. For this purpose, firstly a finite element procedure based on a hypoelastic material law will be briefly described and then some examples of industrial applications will be given.

2 ELASTO-PLASTIC FORMULATION

The outline of the finite element formulation will be given in three steps: variational statement, material law and numerical solution. These steps are covered sequentially in the following sections. All thermal effects are neglected.

2.1 Variational Statement

Consider a body with the current volume V and the current surface area A. If this body is deforming under the action of the surface traction $\underline{t}$, the equilibrium equations are given by the principle of virtual displacements (by neglecting body-forces):

$$\int_V \underline{T}: \delta(\underline{u}\underline{\nabla})\, dV = \int_A \underline{t}.\delta\underline{u}\, dA\ . \tag{1}$$

Here, $\underline{T}$ is the Cauchy stress tensor, $\underline{u}$ the displacement vector and $\underline{\nabla}$ the gradient operator. Since the elasto-plastic constitutive equations are in rate form, eq.(1) has to be in rate form too. Following the procedure in [10] yields

$$\int_V [\hat{\underline{T}}: \delta\underline{L} + \underline{T}: (\delta\underline{L}^T.\underline{L})]\, dV = \int_{A^0} \underline{t}^0.\delta\underline{v}\, dA^0 \tag{2}$$

as the correct rate form of eq.(1). Here,

$$\hat{\underline{T}} = \dot{\underline{T}} + \underline{T}(\underline{I}:\underline{L}) + \underline{T}.\underline{W} - \underline{W}.\underline{T} - \underline{D}.\underline{T} - \underline{T}.\underline{D} \tag{3}$$

is the so-called Truesdell rate of Cauchy stress, $\underline{L}$ the velocity gradient, $\underline{W}$ and $\underline{D}$ the antisymmetric and symmetric parts of $\underline{L}$, respectively. Notice that the surface integral in eq.(2) is referred to the initial, load-free configuration. Yet, the use of the Truesdell rate of Cauchy stress in a constitutive equation leads to unsymmetric stiffness equations during the finite element discretization. This problem can be overcome through the updated Lagrangian approach by assuming that the current configuration coincides instantaneously with the reference configuration. This assumption leads to the variational statement of the problem [6]:

$$\int_V [\overset{*}{\underline{G}}: \delta\underline{D} - 2(\underline{D}.\underline{T}): \delta\underline{D} + \underline{T}: (\delta\underline{L}^T.\underline{L})]\, dV = \int_A \underline{t}^0.\delta\underline{v}\, dA\ . \tag{4}$$

Herein, $\overset{*}{\underline{G}}$ denotes the Jaumann rate of Kirchhoff stress. Now, expressing the stress rate through a constitutive relation like

$$\overset{*}{\underline{G}} = \underline{\underline{\mathcal{C}}} : \underline{D} \tag{5}$$

will complete the mathematical frame of the formulation. Before defining the elasto-plastic material tensor $\underline{\underline{\mathcal{C}}}$, the difference between the variational statement given by eq.(4) and the one for the so-called "small-strain" case-see e.g.[1]-should be noticed. For this purpose, eq.(4) can be rewritten as

$$\int_V (\dot{\underline{T}}: \delta\underline{D} + \delta R + \delta C)\, dV = \int_A \underline{t}^0.\delta\underline{v}\, dA \tag{6}$$

with the rotational term

$$\delta R = (\underline{\underline{T}}.\underline{\underline{W}} - \underline{\underline{W}}.\underline{\underline{T}}):\delta\underline{\underline{D}} \tag{7}$$

and the convective term

$$\delta C = [\underline{\underline{T}}(\underline{\underline{I}}:\underline{\underline{D}})-\underline{\underline{D}}.\underline{\underline{T}}-\underline{\underline{T}}.\underline{\underline{D}}]:\delta\underline{\underline{D}} + \underline{\underline{T}}:(\delta\underline{\underline{L}}^{T}.\underline{\underline{L}}). \tag{8}$$

However, the "small strain" principle reads [1],

$$\int_V \overset{\circ}{\underline{\underline{T}}}:\delta\dot{\underline{\underline{\varepsilon}}}\, dV = \int_A \overset{\circ}{\underline{t}}.\delta\underline{v}\, dA\ . \tag{9}$$

Comparing eqs.(9) with (6), it gets apparent that the terms δR and δC are absent and that the infinitesimal strain tensor $\underline{\underline{\varepsilon}}$ is used instead of the rate of deformation tensor $\underline{\underline{D}}$ as well as the current rate of traction $\overset{\circ}{\underline{t}}$ instead of $\overset{\circ}{\underline{t}}^{\circ}$.

2.2 Elasto-Plastic Material Tensor

The elastic-plastic material law applied is the linear combination of the generalized Hooke's law for elastic deformations and the Prandtl-Reuss relationships for plastic deformations. The bases for this combination are the rates of deformation, such that

$$\underline{\underline{D}} = \underline{\underline{D}}^{el} + \underline{\underline{D}}^{pl} \tag{10}$$

with $\underline{\underline{D}}^{el}$ and $\underline{\underline{D}}^{pl}$ the elastic and plastic parts of the total rate of deformation tensor, respectively. Eq.(10) leads to the elasto-plastic material tensor as follows [10]:

$$\underline{\underline{\mathcal{E}}} = 2G\left\{\underline{\underline{I}} + \frac{\nu}{1-2\nu}\underline{I}\underline{I} - \beta\,\frac{\underline{\underline{I}}'\underline{\underline{I}}'}{\frac{2}{3}k_f^2\left[1+\frac{\bar{T}}{3G}k_f'(\varphi)\right]}\right\} \tag{11}$$

and

$$\beta = \begin{cases} 0 & \text{for } \bar{T}(\underline{\underline{I}}) \quad k_f(\varphi) \quad \text{and} \quad \dot{\bar{T}}(\underline{\underline{I}}) < 0 \\ & \text{or, } \bar{T}(\underline{\underline{I}}) < k_f(\varphi) \\ 1 & \text{for } \bar{T}(\underline{\underline{I}}) \quad k_f(\varphi) \quad \text{and} \quad \dot{\bar{T}}(\underline{\underline{I}}) > 0\ . \end{cases} \tag{12}$$

Here, G denotes the elastic shear modules, ν the Poisson's ratio, k_f the flow stress, φ the equivalent plastic strain, $\bar{T}$ the v.Mises equivalent stress and $\underline{\underline{I}}'$ the deviatoric Cauchy stress tensor. Eqs.(11) and (12) preassume isotropic materials, isotropic work-hardening and plastic volume constancy.

It must be emphasized that the use of $\underline{\underline{\mathcal{E}}}$ as the operator, mapping $\underline{\underline{D}}$ onto $\overset{*}{\underline{\underline{G}}}$ is justified through the fact, that the elastic strains during industrial metal forming processes are nearly infinitesimal for almost all of the metals used. Hence, there is practically no difference in mapping the rate of deformation onto the Kirchhoff stress or Cauchy stress. The only obligation which must be fulfilled is that the mapping must be done onto an objective stress measure [11]. Because of the same reason, i.e. the almost infinitesimal amounts of elastic strains during metal forming, the question, which kind of objective stress rate is the appropriate measure turns out to be immaterial. Therefore, the results obtained by using Truesdell, Jaumann or some other objective stress rate differ only for an insignificant amount for practical metal forming processes.

3 NUMERICAL SOLUTION

The usual discretization procedure of eq.(4) results in a global stiffness equation of the form

$$[K_T]\{a\} = \{\overset{\circ}{F}^{\circ}\} \tag{13}$$

with $[K_T]$ the global tangent stiffness matrix, $\{a\}$ the nodal velocities and $\{\overset{\circ}{F}^{\circ}\}$ the nodal

force rates. Eqs.(13) are linear in the nodal velocities. However, applied within a finite time interval Δt, eq.(13) gets

$$[K_T^*]\{\Delta b\} = \int_{\Delta t}[K_T]\{a\}\,dt = \{\Delta f^\circ\} \tag{14}$$

which is nonlinear in the nodal displacement increments $\{\Delta b\}$. Depending on the kind of sources of this nonlinear dependency, different numerical solution techniques are applied:

3.1 Numerical Treatment of the Physical Nonlinearity

The physical nonlinearity is handled by the midpoint stiffness method (see e.g.[12]). Fig.1 depicts the iterative character of this method. In the first iteration, a displacement increment $\{\Delta b_1\}$ is obtained from eq.(14), replacing $[K_T^*]$ by $[K_T]$ for a given load increment $\{\Delta f^\circ\}$. Using $\{\Delta b_1\}$, stress increments ΔT and Δk_f are found integrating eq.(5) over Δt. Computing the midpoint stress values from

$$\left.\begin{aligned}\{T\} &= \{T_1\} + 0.5\{\Delta T\}\\ \{k_f\} &= \{k_{f_1}\} + 0.5\{\Delta k_f\}\end{aligned}\right\} \tag{15}$$

a new stiffness matrix $[K_m]$ can be found. The solution of

$$[K_m]\{\Delta b\} = \{\Delta f^\circ\} \tag{16}$$

delivers a new displacement increment vector $\{\Delta b_2\}$. Now, again for this last solution, the repetition of the above procedure leads to a new midpoint stiffness and hence to a new solution. As a convergence criterion, the iteration limit has been used. In an extensive survey [13] this limit has been found as 3-4 for typical metal forming processes.

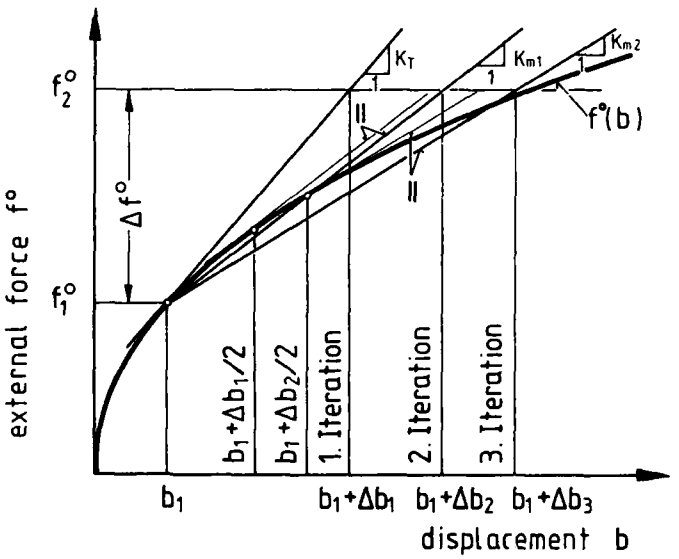

Fig.1: One-dimensional sketch of the midpoint stiffness method.

The critical problem of integrating the constitutive equations (eq.(5)) has been solved by the elastic-predictor-secant-corrector method by Mallett [14]. Fig.2 explains this approach considering a nine-dimensional deviatoric stress space in (T'). If the stress state at the beginning of the increment is denoted by point A (see Fig.2), firstly a hypothetical stress state at point C is found assuming purely elastic response ("elastic-predictor step"). Then, by a plastic-corrector step, the final stress state, denoted by point E, can be found. The unknown factor e is solved from

$$k_f = \sqrt{3/2}\ |\{T'\}^A + 2eG\{D'\}\Delta t| \tag{17}$$

and the plastic strain rate $\{D^{pl}\}$ is given by

$$\underline{D}^{pl} = \frac{\underline{T}' : \underline{D}'}{\frac{2}{3}k_f^2\left(1+\frac{1}{3G}k_f'\right)}\ \underline{I}' \ . \tag{18}$$

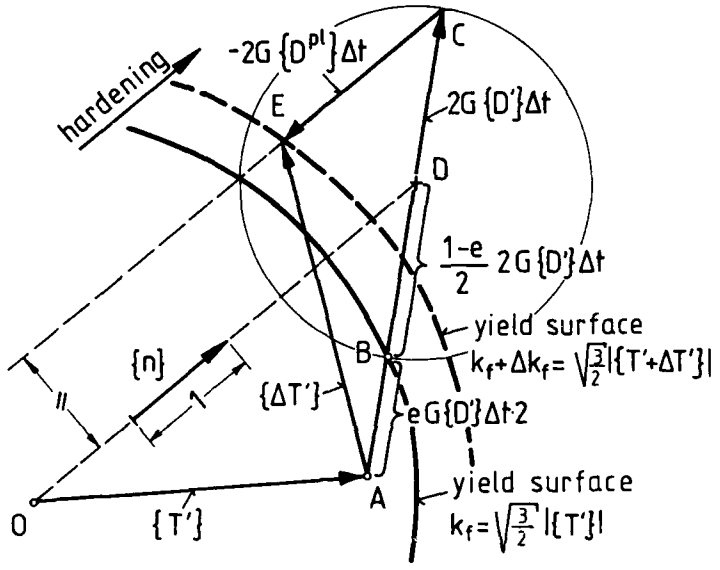

Fig.2 : The elastic-predictor-secant-corrector method for the integration of the material law,[14].

3.2 Numerical Treatment of the Geometric Nonlinearity

The rate-character of the physical nature of metal forming processes as well as the nonlinear boundary conditions require small time steps in the numerical solution of the problem. This obligation can be used in the handling of geometric nonlinearities. The employed solution method is the so-called self-correcting approach [15] and is shown schematically in Fig.3. With the converged solution $\{\Delta b\}$ of eq.(16) the new geometry of the body can be found as $\{b_2\} = \{b_1\} + \{\Delta b\}$. For this configuration the out-of-balance forces are given by

$$\{\Delta F\} = \{f_s^a\} - \int_V [B]^T \{T\}\ dV \tag{19}$$

where [B] is the form matrix of the interpolation functions. Now, for the next load increment eq.(16) is corrected as

$$[K_m]\{\Delta b\} = \{\Delta f_s^a\} + \{\Delta F\} \ . \tag{20}$$

In this way, the drifting of the numerical solution from the exact one is prevented and the inherent error δb (see Figure) is kept small thanks the small increment size.

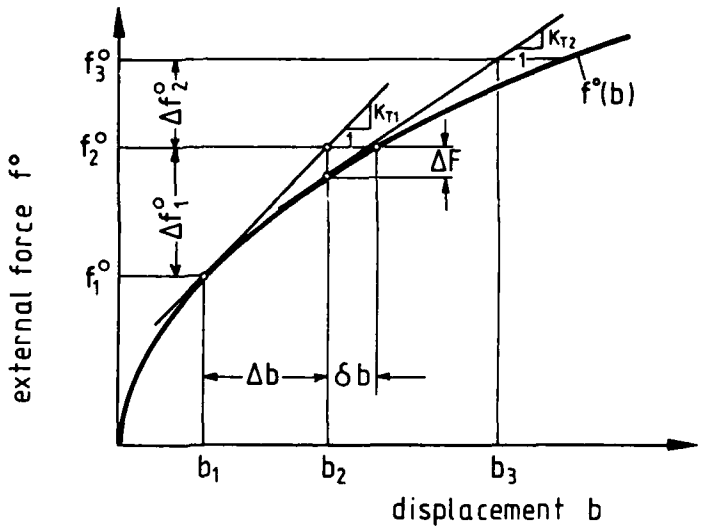

Fig.3: One-dimensional sketch of the self-correcting Euler method.

3.3 Numerical Treatment of Nonlinear Boundary Conditions

Metal forming tools mostly own a complicated geometry. The consequence of this fact for the mathematical model is, that boundary conditions are encountered, which change from point and from time to time. The exact treatment of this problem would require infinitely small time steps. Since this is not possible, a feasible approximation of the boundary conditions must be done.

Fig.4 shows the iterative procedure adopted to handle nonlinear contact problems. Consider a material point P of the workpiece sliding along a tool surface (not necessarily developable). For the first iteration, the degrees of freedom of point P are constraint such that sliding is allowed only in a plane tangent to the tool surface in point A. This condition delivers a radial increment of Δr_1. For the next iteration, the sliding plane is given by PP_2 (for the general three-dimensional case the additional displacement increment has to be considered also). The convergence of this procedure is excellent. Except for the very first increment, convergence can be accelerated by using the converged Δr-value in the first iteration of the following increment.

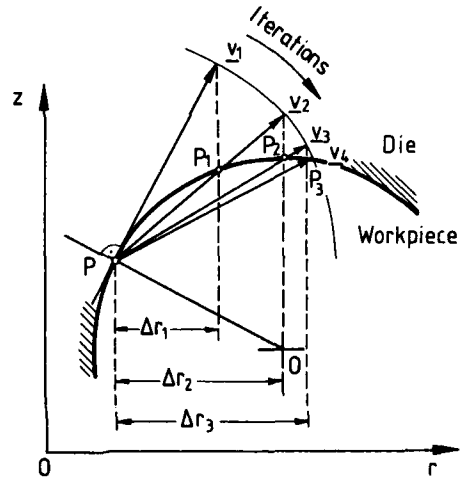

Fig.4: Iterative treatment of nonlinear boundary conditions.

4 APPLICATIONS

The theoretical and numerical fundamentals given in the preceeding sections have been implemented in the program-system EPDAN (acronym for: Elastic Plastic Deformation ANalysis), [10]. In this section some selected industrial applications of EPDAN in the field of metal forming are presented in a compact form.

4.1 Determination of Residual Stresses in Extruded Workpieces

Cold extrusion is one of the most important metal forming processes. A basic concern in judging the quality of the products, is the level of the residual stresses in the extrudates. These stresses may assume values much larger than the yield strength of the material. Depending on the utilization of the products in service, residual stresses may effect the performance of these considerably [16]. Therefore, there exists a prime interest to know the distribution of inherent stresses in extruded products.

Fig.5 shows the scheme for computing the residual stresses in industrial extrusion. Since very slight plastic deformations change the residual stresses drastically, a complete consisting analysis of the production process is absolutely necessary. Following Fig.5 it is noticed, that in the first step the pressing process is simulated by EPDAN. Here, the die is assumed as rigid. The second step consists of computing the spring-back of the die after pressing ceases. Here, the die is analysed by the ASKA finite element code, [17]. Using the output of ASKA, EPDAN unloades the system in step 3 and simulates the ejection of the workpiece in step 4. Although, the main deformation occures during pressing, very slight plastic deformations are encountered in the ejection stage due to the elastic spring-back of the die in the unloading stage. How the residual stresses are effected by the ejection is demonstrated impressively in Fig.6.

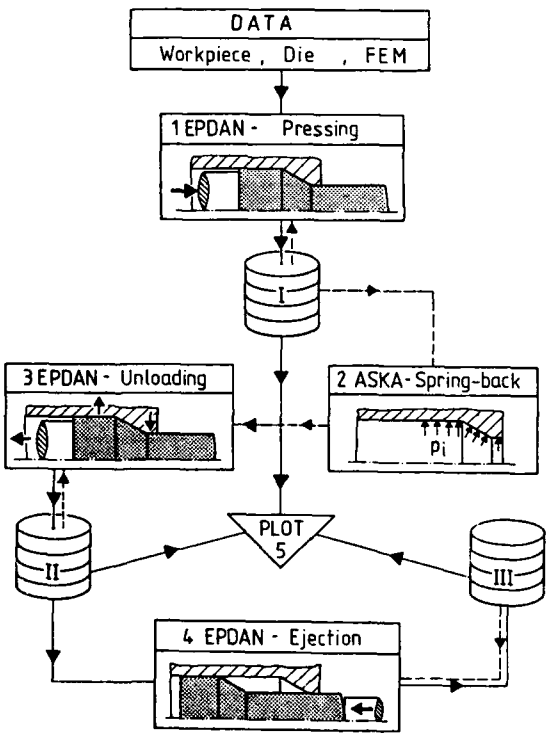

Fig.5: Computation of residual stresses in extruded workpieces: a system analysis.

Fig.6a displays the computed axial stress distribution in a specimen during the pressing stage. The area reduction is 50% and the material used is the typical cold-extrusion steel Ck 15. The analysis was conducted using 259 iscparametric quadrilateral elements. It is noticed that tensile residual stresses exist in the surface layers of the extrudate and compressive ones in the core. The high magnitudes of the tensile stresses are dangerous

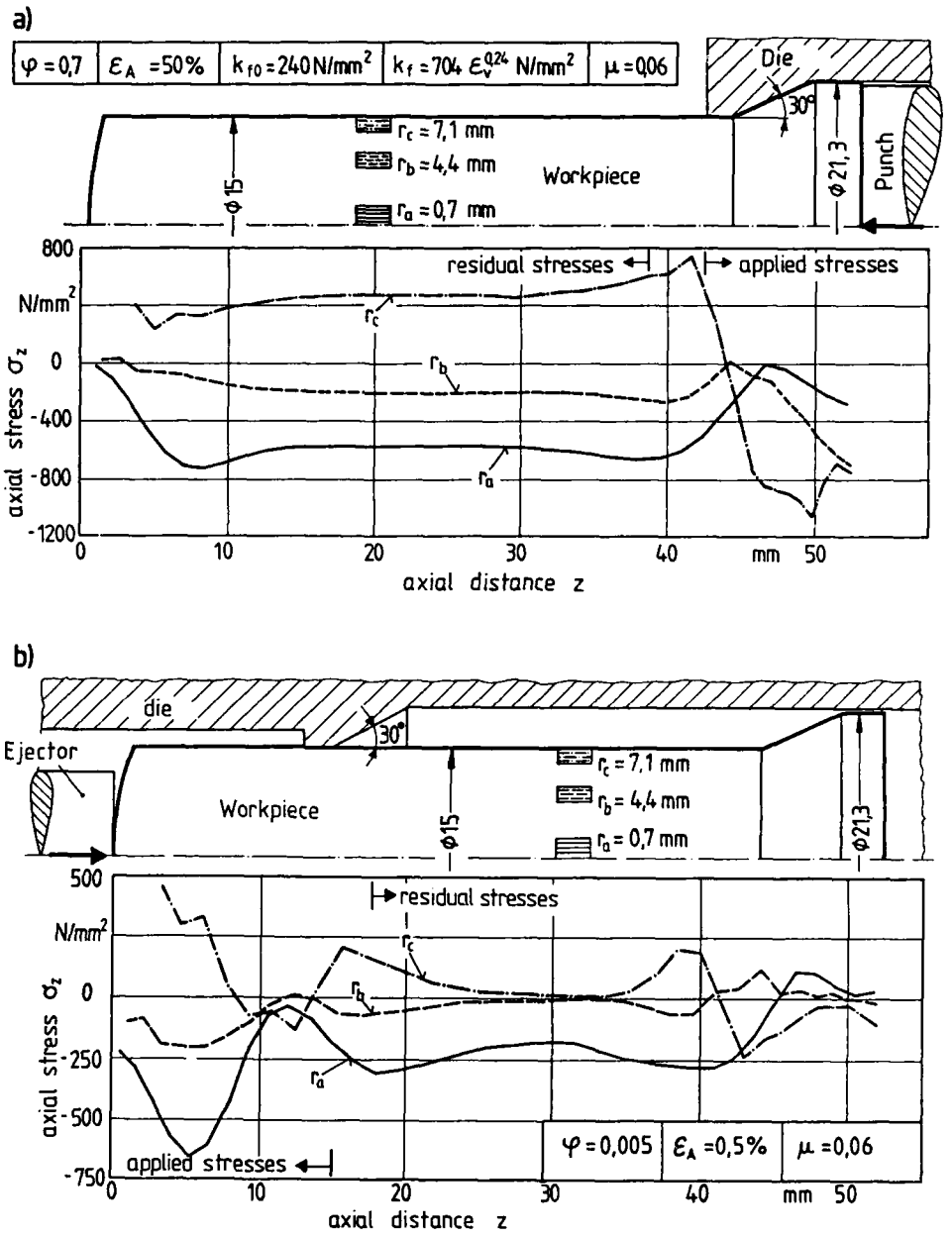

Fig.6 : a) Axial stresses in a workpiece during extrusion.
b) Axial stresses in an extruded workpiece during ejection.

from the fatique and corrosive point of view for the service performance of the workpiece. However, after the punch is drawn back at the shown geometry of the workpiece in Fig.6a, the die spring-backs and slightly compresses the extrudate in the land region. Using the internal pressure onto the die as computed by EPDAN, the radial spring-back is found by ASKA as 0.02 mm for a die with an outer diameter of 160 mm and a height of 102 mm. This radial spring back corresponds to an area reduction of only 0.5% during the ejection stage. Fig.6b shows how this small amount of deformation effects the residual stress distribution. Residual stresses reduce heavily and change even their sign in the surface layer of the

extrudate.

As an industrial utilization of the above stated analysis, different ways of controlling residual stresses during extrusion have been derived, allowing to produce workpieces with predetermined stress levels, [18].

4.2 Numerical Simulation of the Sachs Boring-Out Method

A powerful experimental method to measure axially homogeneous residual stresses in cylindrical workpieces is the Sachs boring-out method [19]. The basic idea of the method is to compute the residual stresses from the measured surface strains which are produced by boring-out layers of material from the cylindrical specimen. For the sake of checking the mathematical procedure mapping the measured strains into the residual stresses, the Sachs boring-out method as applied to extruded specimens is simulated by EPDAN (see Fig.7). Firstly, a workpiece has been extruded numerically. Then, the extruded shaft ("extrudate") has been cut off numerically from the remaining billet in order to obtain a cylindrical specimen with inherent stresses. Now, in the third step, again numerically, layers of material have been bored-out successively by "measuring" simultaneously the surface strains. The boring-simulation has been modelled simply by reducing the internal nodal forces along the respective cutting line to zero; hence no fracture criterion has been applied. After some definite number of holes are cut, the residual stresses in the original specimen are computed using the recorded surface strain by the algorithm given in [19].

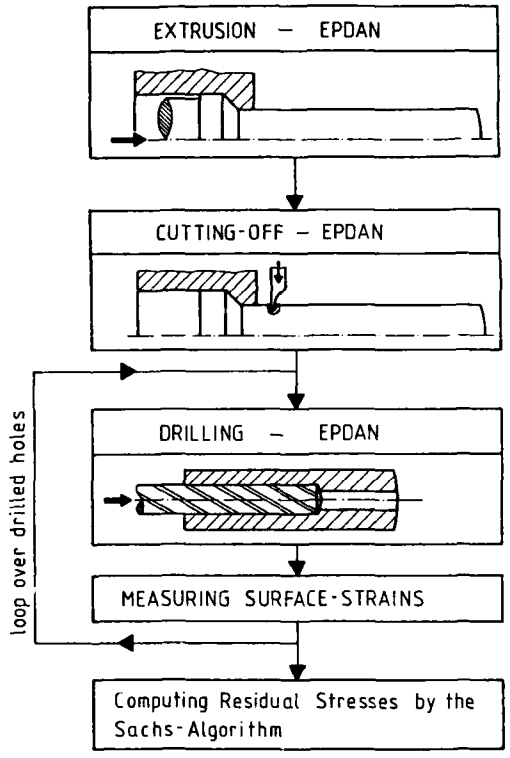

Fig.7 : Numerical simulation procedure of the Sachs boring-out method.

As an example, Fig.8 gives the results of an comparison between the axial residual stresses in the workpiece as computed by EPDAN directly, and as computed by the Sachs scheme based on the strain results of the numerical simulation of the experimental procedure. In the given case, extrusion has been performed for a relative area reduction of 0.8%. The residual stress distribution as found by EPDAN immediately after the extrusion stage is given in Fig.8 through a solid line, and is treated here as the reference solution. Thenafter, six holes have been cut into the extrudate yielding six pairs of axial and circumferential surface strains. Using these surface strains and applying the Sachs

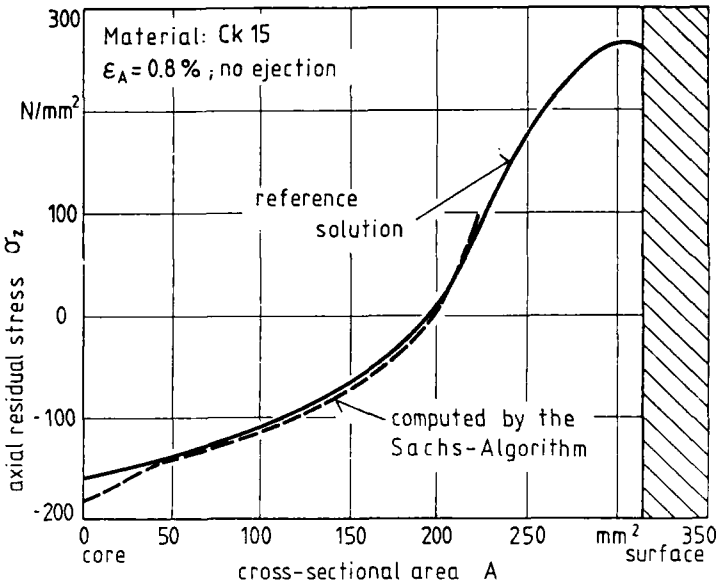

Fig.8 : Comparison between the true residual stress distribution and the "measured" one by the Sachs boring-out method.

equations resulted the "experimentally" found residual stress distribution denoted by a dashed line in Fig.8. At a first glance, the agreement between the reference (or true) stress distribution and the "measured" one seems to be satisfactorily. However, it must be noticed that besides a 15% error in the core of the specimen, the "experimental" solution trends to diverge from the exact one to the surface of the specimen.

4.3 Numerical Simulation of Instabilities

The knowledge of application limits for metal forming are of prime importance for the production planing department. In the case of wire or rod drawing, this limit is given by the necking (followed by the fracture) of the workpiece between the drawing clamp and the drawing die. In order to determine the critical relative area reduction for which the above stated instability occurs an extensive analysis of the drawing process has been conducted in [20]. For an included die-cone angle of 25^0, an friction coefficient of 0.04 and a workpiece material of Ck 15, the analysis delivers the critical area reduction as 50%. For this critical area reduction Fig.9 displays the evolution of the neck for some selected clamp displacements. 585 isoparametric quadrilateral ringelements have been used and the computations have been performed on a CRAY 1/M array-computer.

4.4 Numerical Simulation of Deep-Drawing

Recently, EPDAN has been extended to simulate also sheet metal forming processes,[21]. The extentions consist basically of a modified contact algorithm. This has been necessitated through the increased number of contact zones in the problem. Fig.10 gives an example for the simulation of deep-drawing of axisymmetric cups with flange. In the analysis, the drawing-ratio has been taken as β = 2.0 and the flat punch diameter as d_{St} = 60 mm. The drawing clearance is u_z = 2.0 mm and corresponds to the initial sheet thickness. The material modeled is a typical drawing steel of the quality RRSt 14. The analysis has been conducted using 160 isoparametric quadrilateral ring elements. The use of solid elements instead of membrane or shell elements has the advantage, that it is possible to simulate also the common ironing of the sheet between the punch and the die. Furthermore, the use of solid elements allows to get the complete solution of the problem including the bending moments, shear forces etc. in any cross-section of the sheet. Therefore, solid elements have been preferred in the analysis, despite the higher computational times and storage requirements as compared with membrane or shell elements.

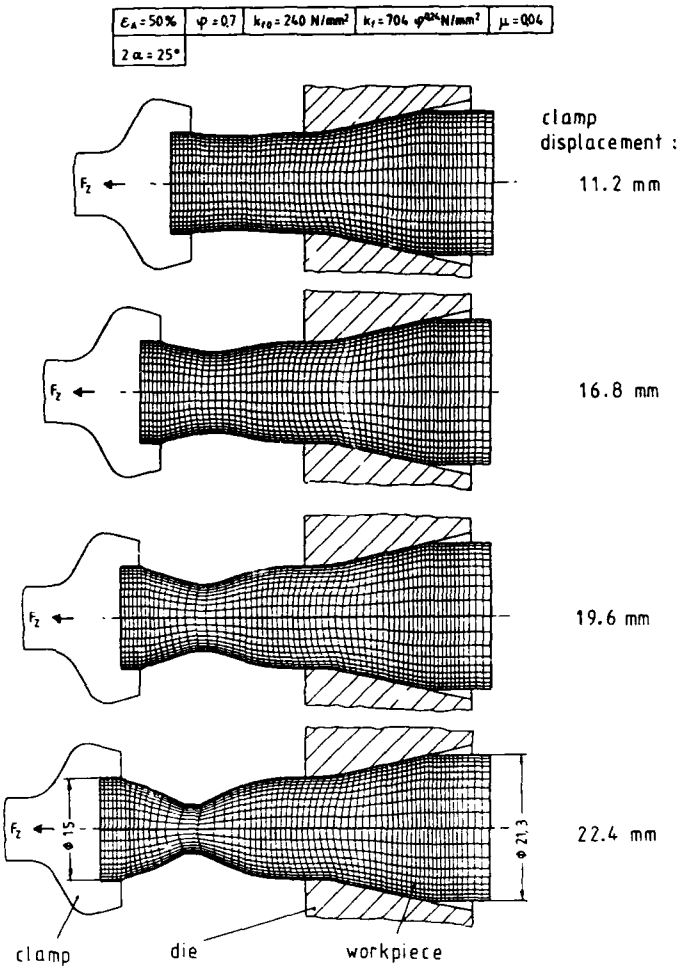

Fig.9 : Determination of the critical area reduction for drawing processes through a finite element simulation by EPDAN,[20].

The computed evolution of the plastic zones in Fig.10 agree excellently with experimental observations. Firstly, up to a punch travel of 0.08 mm, the sheet gets plastic at the punch and die radii due to bending (plastic states are specified by a dark symbol at every integration point of an element in Fig.10). Then, the free part of the sheet between the die and the punch is stretched plastically. Due to work-hardening, the transmitted force through this sheet portion into the flange increases, so that, after a punch travel of 3.2 mm the flange starts to deform plastically. The sheet material beneath the flat punch head gets plastic at a punch travel of 4.0 mm and behaves after 12.5 mm elastically due to the hardening of the material.

5 SUMMARY AND CONCLUSIONS

In this paper, the theoretical and numerical fundamentals of the finite element code EPDAN have been reviewed. The examples of application have demonstrated the efficiency of EPDAN in simulating bulk-metal as well as sheet-metal forming processes. Although, the given examples have been all of an axisymmetric type, the extension to general three-dimensional problems is possible and rather straightforward. Especially, after the introduction of the high-speed computer generation (e.g. the CRAY2) three-dimensional simulations will gain popularity, even in the industry.

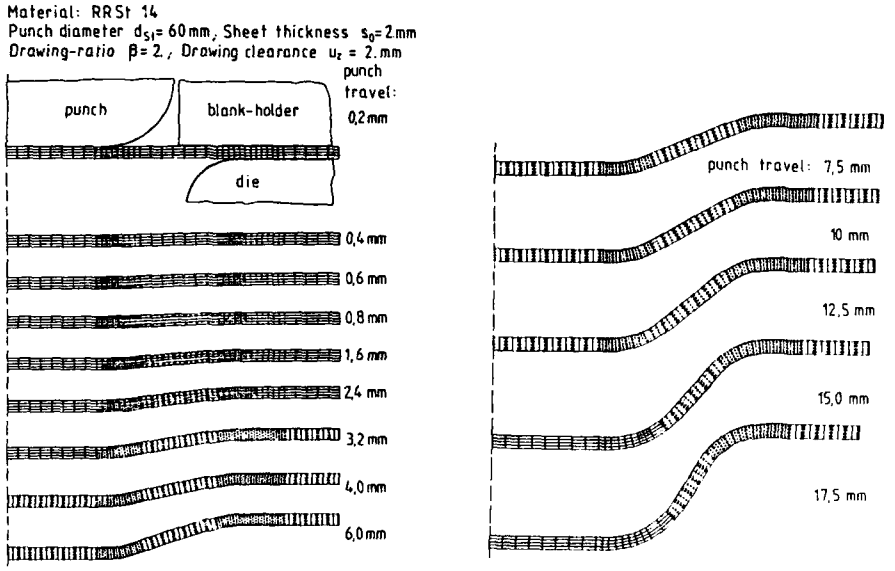

Fig.10 : Evolution of the plastic zone in deep-drawing as computed by EPDAN, [21].

References

1. Zienkiewicz, O.C.; Valliappan, S.; King, P.: Elasto-Plastic Solutions of Engineering Problems. "Initial Stress" Finite Element Approach, Int.J.Num.Meth.Engg., 1(1969), pp.75-100.

2. Lung, M.: Ein Verfahren zur Berechnung des Geschwindigkeits-und Spannungsfeldes bei instationären starr-plastischen Formänderungen mit finiten Elementen, Dr.-Ing.Dissertation, Technische Universität Hannover, 1971.

3. Lee, C.H.; Kobayashi, S.: New Solution to Rigid-Plastic Deformation Problems Using a Matrix Method, J.Engg.Ind., Trans.ASME, 95(1973), pp.865-873.

4. Zienkiewicz, O.C.; Godbole, P.N.: Flow of Plastic and Viscoplastic Solids with Special Reference to Extrusion and Forming Processes. Int. J.Num.Meth.Engg., 8(1974), pp.3-16.

5. Roll, K.: Einsatz numerischer Naeherungsverfahren bei der Berechnung von Verfahren der Kaltmassivumformung. Berlin/Heidelberg/New York: Springer, 1982.

6. McMeeking, R.M.; Rice, J.R.: Finite-Element Formulations for Problems of Large Elastic-Plastic Deformation. Int.J.Solids Structures, 11(1975), pp.601-616.

7. Hill, R.: Some Basic Principles in the Mechanics of Solids without a Natural Time. J.Mech.Phys.Solids, 7(1959), pp.209-225.

8. Lee, E.H.: Elastic-Plastic Deformation at Finite Strains. J.Applied Mechanics, Trans. ASME, 36(1969), pp.1-6.

9. Argyris, J.H.; Doltsinis, J.St.: On the Large Strain Inelastic Analysis in Natural Formulation, Part I: Quasi-Static Problems. Comp.Meth.Appl.Mech.Eng., 20(1979),pp.213-251.

10. Tekkaya,A.E.: Ermittlung von Eigenspannungen in der Kaltmassivumformung, Berlin/ Heidelberg/New York/Tokyo: Springer-Verlag, 1986.

11. Eringen, A.C.: Mechanics of Continua. New York: John Wiley & Sons, Inc., 1967.

12. Ramm, E.: Geometrisch nichtlineare Elasto-Statik und Finite-Elemente. Habilitationsschrift, Universitaet Stuttgart, 1976.

13. Du, G.: Untersuchung über die numerische Genauigkeit der Berechnungen von Problemen der Kaltmassivumformung mit Hilfe der Methode der Finiten Elemente. Diplomarbeit (unpublished), Institut für Umformtechnik, Universitaet Stuttgart, 1985.

14. Mallett, R.L.: Private Communications.

15. Yamada, Y.; Wifi, A.S.; Hirakawa, T.: Analysis of Large Deformation and Stress in Metal Forming Processes by the Finite Element Method. In: Metal Forming Plasticity, Berlin/Heidelberg/New York: Springer-Verlag, 1979, pp.158-176.

16. Tekkaya, A.E.: Beitrag zur Berechnung von Umformeigenspannungen in Fliesspressteilen. In: Proceedings of the Seminar "Neuere Entwicklungen in der Massivumformung", Stuttgart, 7.-8. June 1986, pp.4/1-4/32.

17. Argyris, J.H. et al.: ASKA User's Reference Manual. ISD-Report, Nr.73, Stuttgart, 1971.

18. Tekkaya, A.E.; Lange, K.: Determination of Residual Stresses in Industrial Extrusion. In: Proceedings of the XII. NAMRC, Houghton/Michigan, May/June 1984, pp.103-110.

19. Sachs, G.: Der Nachweis innerer Spannungen in Stangen und Rohren, Z.Metallkunde, 19(1927), pp.352-357.

20. Gerhardt, J.; Tekkaya, A.E.: Simulation of Drawing-Processes by the Finite Element Method. In: Proceedings of the 2nd ICTP, Stuttgart, 1987, to be published.

21. Herrmann, M.: Finite-Element-Simulation des Tiefziehens rotationssymmetrischer Näpfe mit Flansch. In: Seminarband "Neuere Entwicklungen in der Blechumformung", Stuttgart, 10.-11.June 1986, pp.3/1-3/24.

Acknowledgement

Grants for the support of this work from the "Stiftung Volkswagenwerk" Hannover/FRG are gratefully acknowledged.

GENERIC CASTING MODELING

William T. Sha
Argonne National Laboratory
9700 South Cass Avenue
Argonne, Illinois 60439
USA

SUMMARY

Casting is one of the most direct methods of producing industrial parts, or components, in a desired shape. It permits economical fabrication of streamlined, intricate, integral parts. Because casting provides design flexibility, metallurgical versatility, and economic benefits, it is a fundamental and vital technology for any industrial nation.

Although the casting process has been used for hundreds of years, it involves a host of complex phenomena that are still not thoroughly understood. To date, casting remains a highly empirical technology, and production of new castings requires an expensive, time-consuming, trial-and-error approach. The dominant phenomena are fluid motion and heat transfer, which control the quality of the final product--grain size and shape, porosity, and segregation of alloying elements. In recent years, mathematical modeling of casting has received increasing attention; however, a majority of the modeling work has been in the areas of heat transfer, solidification, metallurgical phenomena, and stress/deformation analyses. Very little work has been done in modeling fluid flow of the liquid melt. This paper presents a detailed model of fluid flow coupled with heat transfer of a liquid melt for casting processes. The model to be described in this paper is an extension of the COMMIX code and is capable of handling castings of any shape, size, and material. While much of the emphasis in this paper is placed on fluid flow and heat transfer, a brief mention of R&D needs in modeling of metalurgical aspects, as well as stress/deformation is also outlined. A feature of this model is the ability to track the liquid/gas interface and liquid/solid interface. It can also calculate alloy element distributions providing that constitutive relations such as interfacial drag between alloy elements are available. The flow of liquid melt through the sprues, runners, and gates into the mold cavity is calculated, along with three-dimensional temperature and velocity distributions of the liquid melt throughout the casting process.

1. INTRODUCTION

Casting is one of the most direct methods of producing industrial parts, or components, in a desired shape. It permits economical fabrication of streamlined, intricate, integral parts. Because casting provides design flexibility, metallurgical versatility, and economic benefits, each year many thousands of cast shapes are produced, ranging in size and weight from a fraction of an inch to many feet and from a few ounces to over 250 tons.

Although the casting process has been used for hundreds of years, it involves a host of complex phenomena that are still not thoroughly understood. The dominant phenomena are fluid motion and heat transfer, which control the quality of the final product--grain size and shape, porosity, and segregation of alloying elements. Often the desired casting shape is highly irregular. Consequently, the flow region in a casting mold is geometrically complicated, involving sprues, runners, gates, branching channels, etc. arranged in various combinations. Furthermore, flows into the mold are moving, and change from liquid melt to solid. Air and other gases may be trapped within the molten material, forming a multicomponent flow mixture. Nonuniform heat transfer, coupled with large temperature gradients and buoyancy forces, can produce natural-convection currents in molten regions. Under certain conditions, the flow may be turbulent. All these factors rule out any hope of a purely analytical analysis of the process. It is only now, with the development of advanced computer technology and sophisticated numerical methods that we are able to characterize detailed flow fields and temperature distribution along with motions of mold filling and solidification in a mold with complex shape.

While much work has been done in the past on heat transfer and solidification modelings, advanced fluid-flow modeling of casting has received attention only in recent years (1-4). The benefits resulting from the study of fluid flow in the casting process are: (a) to provide a consistent and correct set of initial conditions for solidification analysis after mold filling; (b) to give the needed information for optimizing the placement of gates, dimensioning of passages, designation of casting speeds and quantification of filling times; (c) to control and possibly eliminate cold shut, erosion of mold, and porosity problem associated with entrainment of air or other types of gases in the mold and surface; and (d) to provide a better understanding of microstructure of a casting as a result of the fluid flow pattern and heat transfer during solidification. Among the casting areas where fluid flow coupled with heat transfer modeling plays an important role may include (a) free surface, liquid-melt filling of cavity molds of

complex shapes, (b) natural convective flow in liquid melt, (c) convective flow in liquid melt induced by external forces (e.g., electromagnetic stirring), (d) eddy currents/magnetic pressure encountered in electromagnetic (EM) levitation casting, and (e) ultrasonic treatment of solidification (cavitation induced shock wave).

Although this paper is primarily concerned with the fluid flow and heat transfer modeling for castings, a brief mention of R&D needs in modeling of metallurgical phenomena and stress/deformation is also presented. A computer program, COMMIX (COMponent MIXing) (5-7), is the basic tool used for generating the results in this paper. COMMIX is a fully three-dimensional, steady-state/transient, single-/multi-species, and single-/multiphase code for thermal hydraulic analysis of single- and multi-component systems. The COMMIX code was originally developed for nuclear reactor applications and it has been extensively used for many other industries. Among the unique features of COMMIX, the new porous-medium formulation (8-10) is perhaps the most significant. With this formulation and its associated parameters of volume porosity, directional surface porosity, distributed resistance and distributed heat source or sink, COMMIX can, for the first time and in a unified and consistent manner, model anisotropic flow and temperature fields with stationary structures, as well as simulate multidimensional thermal hydraulic environment of either a single component (e.g., nuclear reactor, fuel rod bundle, heat exchanger, piping system, casting mold, etc.), or a multicomponent system (e.g., heat exchanger with piping system, casting mold with sprues, runners, and gates, etc.) that is a combination of these components. Another unique feature of the COMMIX code is the single/multi-species capability which can track alloy element distribution in an alloy casting product.

In the subsequent sections of this paper, the mathematical model, e.g., governing equations and solution techniques used in the COMMIX code will be presented. The unique features of COMMIX will be described to acquaint readers with the code. Free surface flow capability has been implemented into the COMMIX code and a brief description of free surface flow is presented. Preliminary results from the initial case studies are presented to demonstrate the COMMIX capabilities. Finally, a brief outline of R&D needs in modeling of metallurgical phenomena and stress/deformation is given at the end that also covers our planned future approaches and activities.

Mathematical Modeling in Fluid Flow and Heat Transfer

A system of conservation equations of mass, momentum, and energy is derived via local volume averaging, and solved numerically by the COMMIX code as a boundary value problem in space and an initial value problem in time. A two-equation k-ε turbulent model is provided as user's option where k is a turbulence kinetic energy and ε is the dissipation rate of k. All these equations are described separately as follows:

Conservation of Mass

$$\gamma_V \frac{\partial \rho}{\partial t} + \nabla \cdot \gamma_A \rho \underline{u} = 0 \tag{1}$$

where ρ = density,

$\underline{u}$ = velocity vector,

t = time,

γ_V = volume porosity which is the ratio of the volume occupied by fluid in a control volume to the total control volume,

γ_A = directional surface porosity is the ratio of the flow area in a control surface at a given direction to the total control surface in that direction,

$$\nabla = \frac{\partial}{\partial x}\underline{i} + \frac{\partial}{\partial y}\underline{j} + \frac{\partial}{\partial z}\underline{k}$$

x,y,z = principal directions in Cartesian coordinates, and

$\underline{i},\underline{j},\underline{k}$ = unit vector in the x, y, and z direction, respectively.

Conservation of Momentum

$$\gamma_V \frac{\partial \rho \underline{u}}{\partial t} + \nabla \cdot \gamma_A \rho \underline{u}\underline{u} = -\gamma_V \nabla P + \nabla \cdot \gamma_A \underline{\underline{\tau}} + \gamma_V(\rho \underline{g} - \underline{R}) \tag{2}$$

where P = pressure,

$\underline{\underline{\tau}}$ = viscous stress tensor,

$\underline{g}$ = gravitational acceleration, and

$\underline{R}$ = distributed flow resistance.

Conservation of Energy in Terms of Enthalpy

$$\gamma_V \frac{\partial \rho h}{\partial t} + \nabla \cdot \gamma_A \rho h \underline{u} = \gamma_V \frac{dP}{dt} - \nabla \cdot \gamma_A \kappa \nabla T + \gamma_V (J_E + \phi + Q_w) \tag{3}$$

where κ = conductivity

T = temperature

J_E = heat source

ϕ = dissipation rate per unit volume, and

Q_w = heat transfer rate at wall.

Turbulent Transport Equations

Transport Equation for k (Turbulent Kinetic Energy)

$$\gamma_V \frac{\partial \rho k}{\partial t} + \nabla \cdot \gamma_A \rho \underline{u} k = \gamma_A P_k + \gamma_A G_k - \gamma_V \rho \varepsilon + \nabla \cdot \gamma_A \left(\frac{\mu_{tur} + \mu_{lam}}{\sigma_k} \right) \nabla k \tag{4}$$

where $P_k = \mu_{tur} \left[\frac{\partial u_i}{\partial x_j} \left(\frac{\partial u_i}{\partial x_j} + \frac{\partial u_j}{\partial x_i} \right) \right]$

$$G_k = - \frac{\mu_{tur}}{\rho \sigma_k} \frac{\partial \rho}{\partial T} \left(\frac{\partial T}{\partial x_j} g_j \right)$$

μ_{tur} = turbulent viscosity = $\frac{C_D \rho k^2}{\varepsilon}$

μ_{lam} = molecular or laminar viscosity,

σ_k = turbulent Prandtl number for k

C_D = empirical coefficient (recommended value is 0.09).

Transport Equation for ε (Dissipation rate of k)

$$\gamma_V \frac{\partial \rho \varepsilon}{\partial t} + \nabla \cdot \gamma_A \rho \underline{u} \varepsilon = C_1 \gamma_A \frac{\varepsilon}{k} (P_k + G_k) - C_2 \gamma_V \frac{\rho \varepsilon^2}{k} + \nabla \cdot \gamma_A \left(\frac{\mu_{tur} + \mu_{lam}}{\sigma_\varepsilon} \right) \nabla \varepsilon \tag{5}$$

where σ_ε = turbulent Prandtl number for ε

C_1, C_2 = empirical coefficients (recommended values are 1.44 and 1.92 respectively)

Equations 1 through 5 are solved with a set of appropriate initial and boundary conditions which are detailed in Refs. 6 and 7. Two solution procedures (6,7), semi-implicit method, i.e., modified ICE (11), and fully implicit method, i.e., modified SIMPLER (12), are provided as user's options. It is to be noted that the modified ICE is suitable for fast transient such as mold filling problems and the modified SIMPLER is suitable for steady state calculation or slow transients such as solidification applications.

The solution techniques used in the COMMIX code (6,7) may best be illustrated by using simplified flow diagrams. Figure 1 presents an overall flow diagram (outer loop). A simplified flow diagram of the solution technique (inner loop) is shown in Fig. 2. Figures 3 and 4 are simplified flow diagrams for the mass-momentum loop and the energy loop respectively.

Unique Features of the COMMIX Code

The following are unique features of the COMMIX code (7).

- **New Porous-Medium Formulation:** COMMIX uses a new porous-medium formulation with the parameters volume porosity, directional surface porosity, distributed resistance, and distributed heat source or sink. With this formulation, the COMMIX code has the capability to model anisotropic flow and temperature fields with stationary structures. The porous-medium formulation with the additional parameter of directional surface porosity represents a unified approach to thermal-hydraulic analysis. Because of this feature, it is now possible to perform a multidimensional thermal-hydraulic simulation of either a single component, such as a casting mold, etc., or a multicomponent system such as a mold with sprues, runners, gates, etc. This new porous medium formulation is particularly useful in simulating irregular geometries.

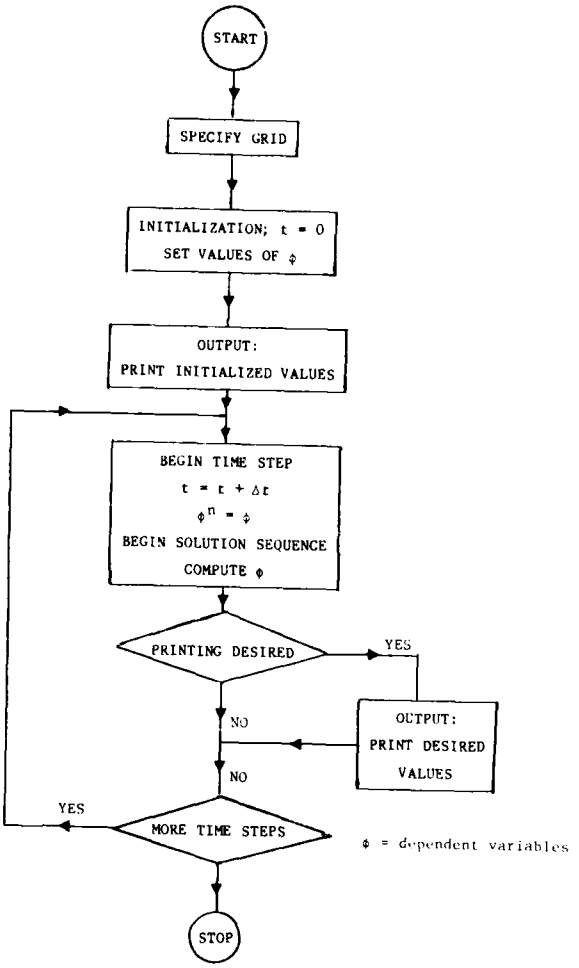

Fig. 1. Overall Flow Diagram

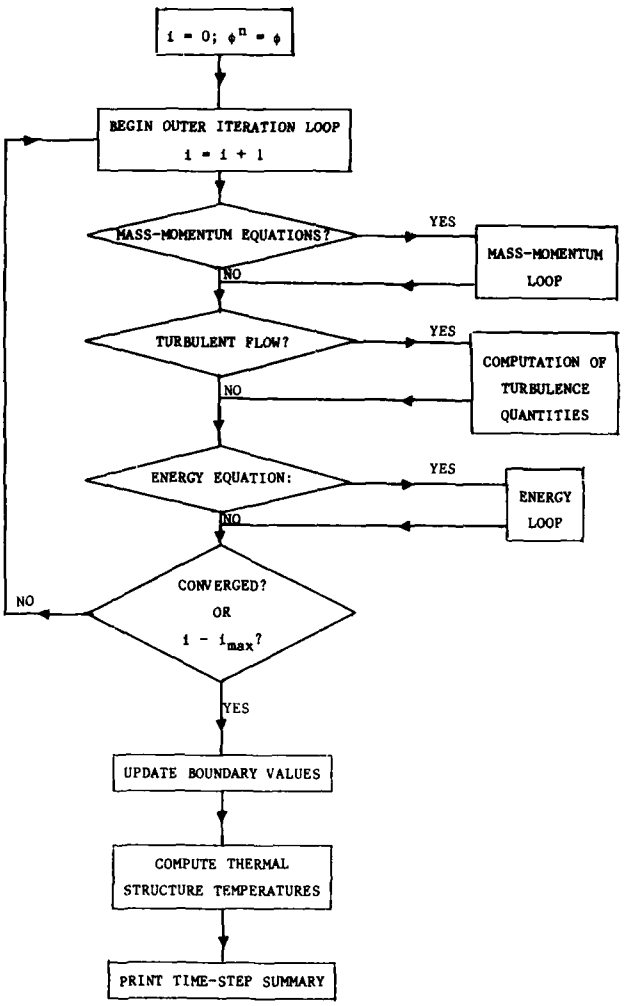

Fig. 2. Simplified Flow Diagram of Solution Technique

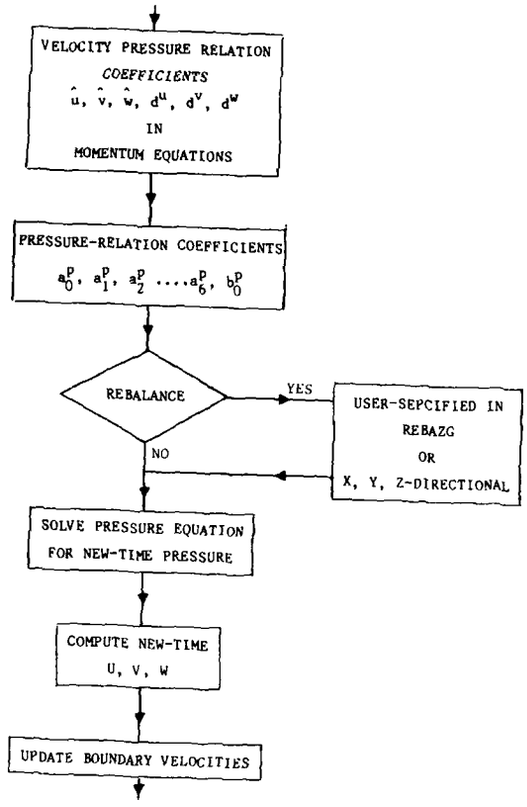

Fig. 3. Simplified Flow Diagram of Mass-Momentum Loop

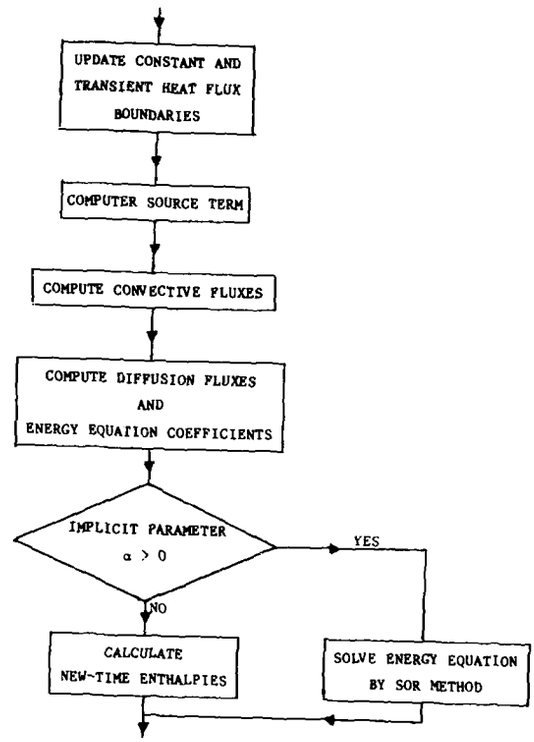

Fig. 4. Simplified Flow Diagram of Energy Loop

- **Two Solution Procedures:** In COMMIX, two solution procedures, semi-implicit and fully implicit, are available as a user's option. The semi-implicit procedure, a modification of the ICE technique, is designed for fast transient analysis, where the interest is to examine flow phenomenon in the time period of the order of Courant time step size. The fully implicit procedure, named SIMPLEST-ANL and similar to the SIMPLE/SIMPLER algorithms, is designed for normal and slow transients, where the interest is to examine phenomena at times that are larger than Courant time step size.
- **Geometrical Package:** A special geometrical package has been developed and implemented that permits modeling of any complex geometry in the most storage-efficient way.

- **Skew-Upwind Difference Scheme:** A new volume-weighted skew-upwind difference scheme has been developed and implemented that reduces numerical diffusion observed in simulations of flow inclined to grid lines. The scheme also eliminates temperature over/undershoots that are found to occur when simulations are performed with normal skew-upwind differencing schemes.

- **Turbulence Modeling:** The following four turbulence model options are provided to give COMMIX-1B (a derivative of COMMIX) a wide range of applications:

  - Constant turbulent diffusivity model
  - Zero-equation mixing length model
  - One-equation (k) model
  - Two-equation ($k-\varepsilon$) model

- **Generalized Resistance and Thermal Structure Model:** The COMMIX code also contains: (a) a generalized resistance model to permit specification of resistance due to internal structures, and (b) a generalized thermal structure formulation to model thermal interaction between structures (casting mold wall) and surrounding fluid.

- **Modular Structure:** The code is modular in structure, which expedites rapid implementation of the latest available drag models, heat-transfer models, etc. It also permits solution of 1D, 2D, or 3D calculations.

Free Surface Flow

To use the COMMIX code to model the filling of a mold, an additional capability for free surface flow must be added for a given mold configuration which is subdivided into a number of computational cells. These Eulerian cells remain fixed in space and have a temperature, pressure, velocity, etc. associated with each of them. In addition to the standard variables, a variable F (fractional volume of fluid) (13) is introduced for each cell to keep track of fluid, interface, and empty regions within the configurations, where F = 1 indicates a cell full of fluid, F = 0 indicates an empty cell. At any given time, the variable F can be scanned over the configuration and each cell classified as being

1. Full - cells containing fluid and bounded only by other full and surface cells.
2. Empty - cells with no fluid and bounded only by other empty and surface cells.
3. Surface - interface cell, bounded by other surface, full, and at least one empty cell.

The governing equation for F (fractional volume of fluid) (13) is

$$\frac{\partial F}{\partial t} + \underline{U} \cdot \nabla F = 0 \ , \tag{6}$$

which implies that F is a quantity that moves with the fluid. In discretizing the above equation, several physical and numerical constraints must be observed:

1. The value of F must be between 0 and 1 inclusive. A cell cannot be less than empty or more than full.
2. Fluid cannot be transported through more than one cell during a time step. This gives rise to the Courant time step limitation that

$$\Delta t \sim < \left| \frac{\Delta x}{\underline{U}} \right|_{min} \tag{7}$$

3. A full cell stays full if only surrounded by other full cells. Since a full cell is next to only other full cells and surface cells, the only way F can change is if a void is convected in from an adjacent surface cell which has just emptied.

4. An empty cell remains empty if surrounded only by other empty cells. Since an empty cell is adjacent to only other empty and surface cells, the only way F can change is if fluid is convected in from an adjacent surface cell which has just filled.

5. A cell containing an interface can be either filling or emptying. However, if a surface cell becomes full during a time step, any fluid excess will convect to adjacent empty cells. Conversely, if a surface cell empties, any additional void will convect into adjacent full cells.

The velocity field is determined in the standard way between cells containing some fluid (surface and full cells). Interface boundary conditions are used to set the velocity between surface and empty cells. No velocity calculation is needed between empty cells. In consideration of rules 1 through 5 above, it is seen that no calculation of F is needed in empty cells surrounded by other empties or fulls surrounded by other fulls. Indeed, no fractional volume of fluid calculation need be done except in cells containing an interface. Adjustments to adjacent full or empty cells are made only when considering surface cells which have either been filled or emptied respectively.

Isolating the F calculation to cells containing an interface and bypassing the calculation for full and empty cells substantially reduces the number of calculations required for tracking the interface and represents a departure from the standard VOF method (14). This reduction is particularly important in 3-D analyses for which the vast majority of cells are away from the interface.

The above method provides a very effective and economical technique for tracking the fluid interface. Work is continuing to couple all the features of the COMMIX code to the interface tracking technique. When completed, a code with synergistic features is expected which can give new insights into the casting process.

Numerical Results from the COMMIX Code

Typical results obtained from the COMMIX code for mold filling are shown in Figs. 5 through 13. Figure 5 presents the dimensions of the mold and the COMMIX computational mesh set-up. Figures 6 through 13 show the time sequence of liquid melt filling the mold cavity. In this particular numerical simulation, the liquid melt was assumed isothermal with selfreplenishment to maintain constant elevation at A-A as shown in Fig. 5. A diaphragm is located at elevation B-B which was breached at t = 0 and the liquid melt rushes into the cavity where t stands for time. Figures 14 through 17 present the sequence of solidification configurations of the liquid melt as a function of time. In this calculation, it was assumed that (a) the fluid is water/ice, (b) a single value enthalpy determines state, (c) the initial water temperature is 10°C, and (d) at time = 0, all walls drop to -40°C. Similar work on mold filling was presented in Ref. 3; however, it was limited to two-dimensional analyses.

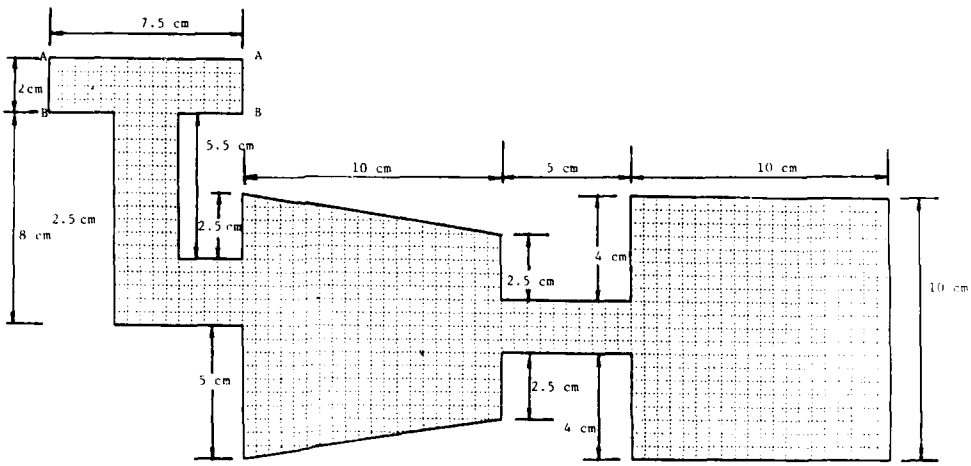

Figure 5. Computational Mesh Set-up and Dimensions

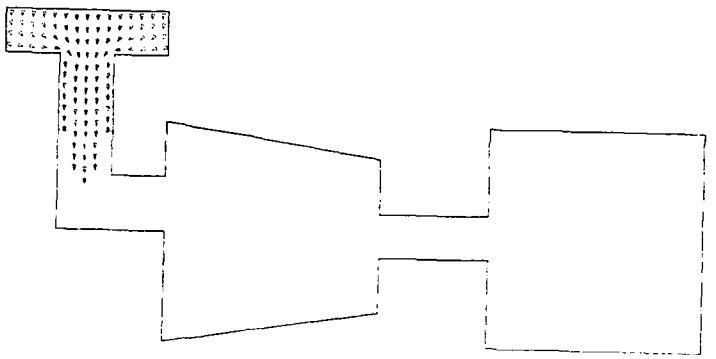

K = 1
- 5.00 M/S

Figure 6. Mold Filling at time = 0.10 s

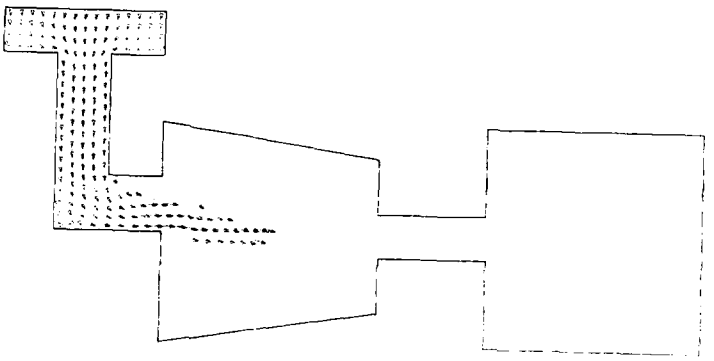

K = 1
- 5.00 M/S

Figure 7. Mold Filling at time = 0.20 s

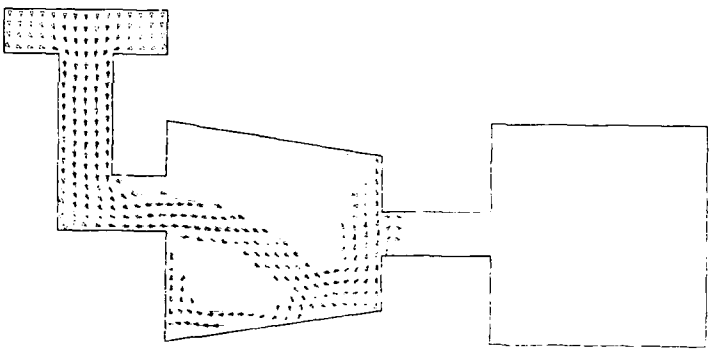

K = 1
- 5.00 M/S

Figure 8. Mold Filling at time = 0.40 s

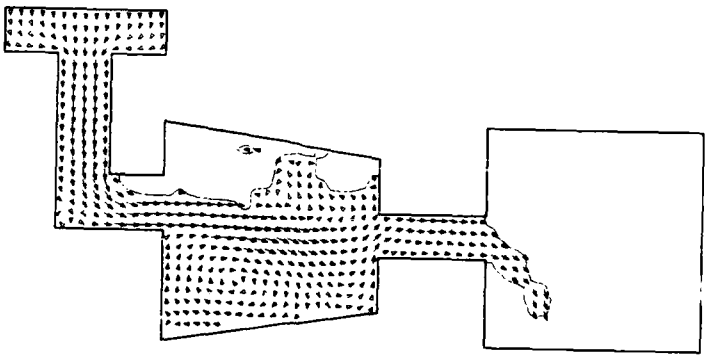

K = 1 ⟶ 5.00 M/S

Figure 9. Mold Filling at time = 0.60 s

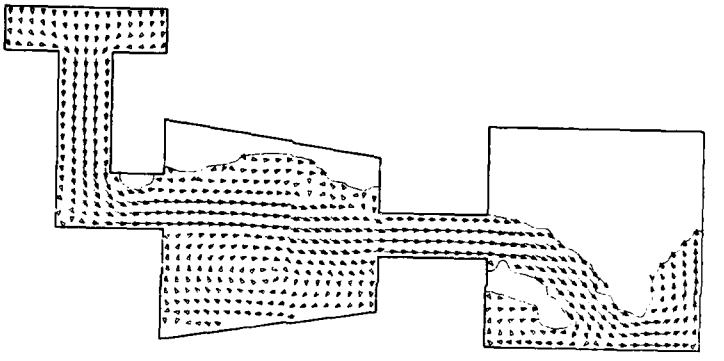

K = 1 ⟶ 5.00 M/S

Figure 10. Mold Filling at time = 0.80 s

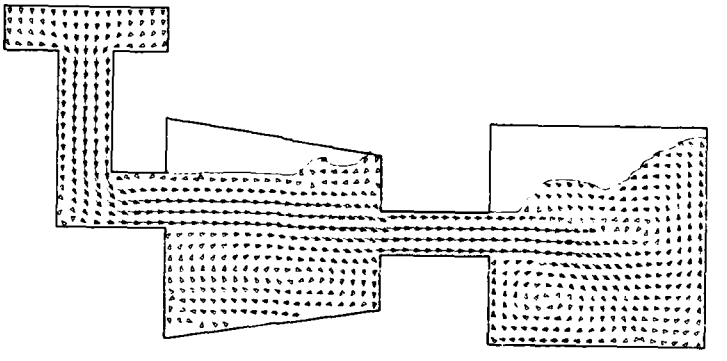

K = 1 ⟶ 5.00 M/S

Figure 11. Mold Filling at time = 1.00 s

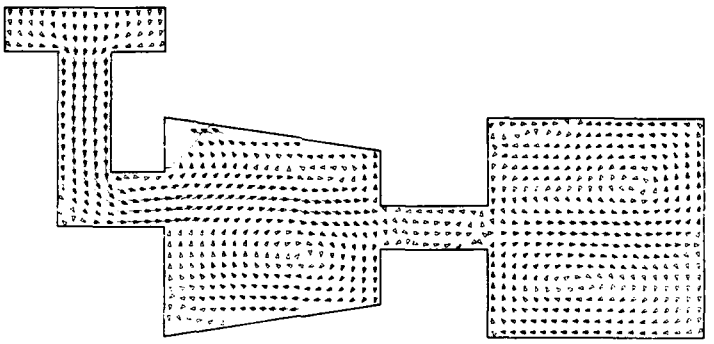

K = 1 → 5.00 M/S

Figure 12. Mold Filling at time = 1.20 s

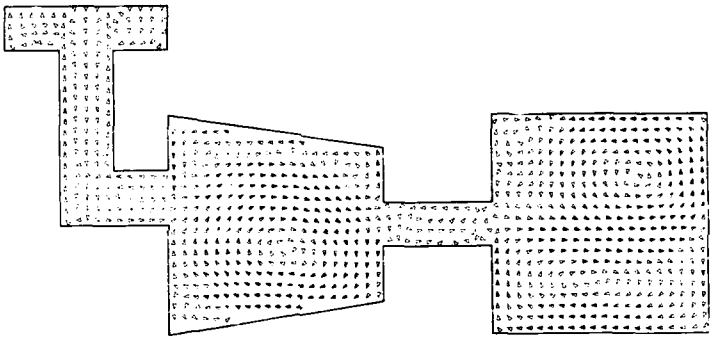

K = 1 → 5.00 M/S

Figure 13. Mold Filling at time = 1.30 s

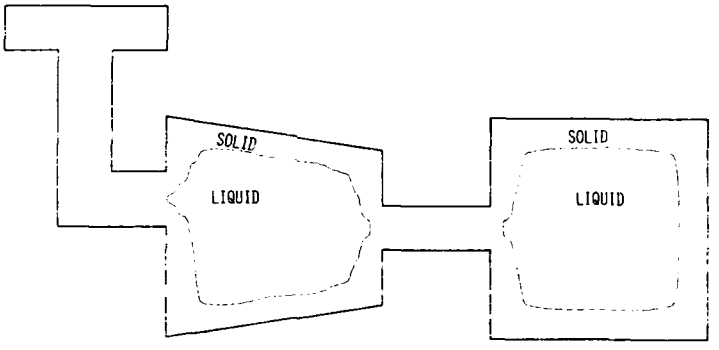

K = 1

Figure 14. Solidification at time = 1660.0 s

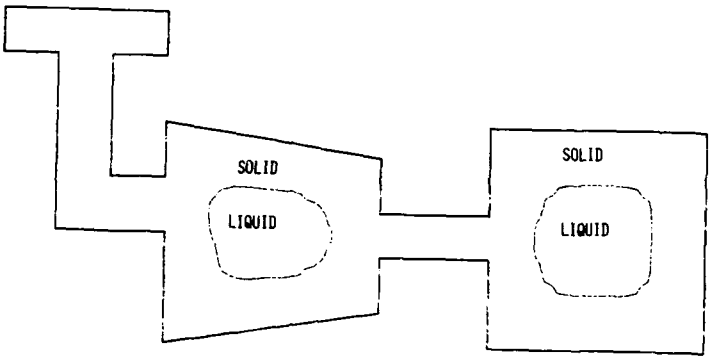

K = 1

Figure 15. Solidification at time = 5040.0 s

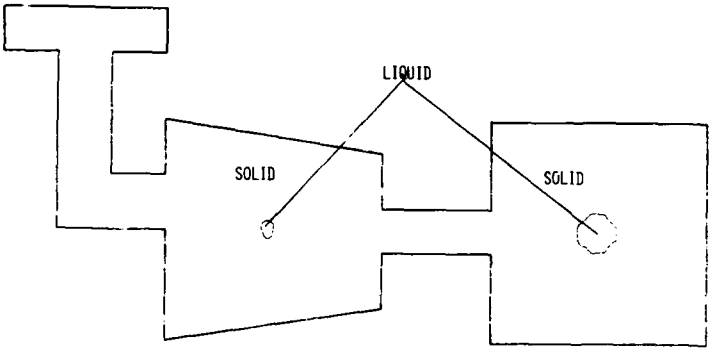

K = 1

Figure 16. Solidification at 10580.0 s

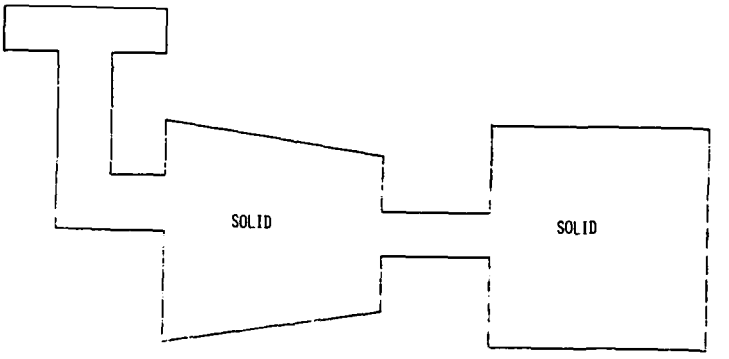

K = 1

Figure 17. Solidification at 12300.0 s

Discussions and Conclusions

Although water/ice has been used to demonstrate COMMIX capabilities, it should be noted that the governing equations and solution techniques in COMMIX are entirely general and applicable to other materials (e.g., metals, plastics, composities, etc.) used in several major casting techniques (i.e., investment casting, die casting, injection molding, etc).

The new porous-medium formulation can be viewed as an approximation of irregular geometries which are often encountered in casting molds. This formulation is particularly suitable for the marshy zone where dendrites may be modeled using the concept of volume porosity and directional surface porosity in fluid flow calculations. It appears that the new porous-medium formulation presented here is very advantageous for casting modeling and has been proven to be numerically very efficient. It is intended, however, that if the exact treatment of irregular geometries is found to be necessary, the boundary fitted coordinate transformation (15-18) should be used. The boundary fitted coordinate transformation option will be provided as a user's option in a future version of the COMMIX code.

The method described in this paper represents a state-of-the-art of fluid flow and heat transfer modeling of the casting process. Although a great deal of additional modeling work is needed however, the work presented here should serve as a foundation for future generic casting modeling. It should be mentioned that both natural convection of liquid melt and air/gas entrainment are encountered in almost all casting processes. Very little work has been done in these areas. The COMMIX code can readily attack these problems which have significant impact on the quality of castings.

A number of metallurgical phenomena in casting processes should be investigated and implemented in the COMMIX code. These models are phase transformation, interface stability, mechanisms of formation of dendrite, nucleation, volume shrinkage during solidification, and micro- and macro-segregations, etc. Another area that needs attention and effort is the development of a consistent set of thermal physical properties of various materials often encountered in casting industries.

Both micro- and macro segregation problems are of great concern to the casting industry. In order to resolve these problems once and for all, one must start from fluid mechanics. This is because the segregation is caused mainly by convection of alloy elements in a liquid melt.

It is generally agreed in the community of computational fluid dynamics that the finite difference (FD) or finite volume (FV) approach is ahead of the finite element (FE) method at the present time. This is certainly not true in the field of computational structure dynamics. It should be pointed out that many recent advances in the FE method are benefited directly from the knowledge and experience gained from the FD or FV approach. For example: skew elements to evaluate convective term in FE is comparable to use upwind difference in FD or FV; one point quadrature to evaluate integrals in FE is comparable to simple averaging used in FD or FV; etc. It is our intention to channel our effort to develop the necessary interfacing software between fluid flow and heat transfer calculations using FD or FV and structure analysis using FE. Also, our generic casting modeling work will be implemented in futuristic medium size computer systems with parallel procesors. A simplified flow diagram for integrated analysis of the entire casting process is shown in Fig. 18.

We recommmend that all phenomenological models or constitutive relations must be validated with appropriate and carefully designed separate experiments, and COMMIX results must be validated with integral experiments under a variety of operating conditions.

Finally, the generic casting modeling as proposed in this paper based on the first principle is possible. It requires well-planned coordination and long term developmental efforts and support. The benefit derived from the generic casting modeling is enormous since most of the materials used in the industry are formed by casting (ingot).

References

1. M. C. Flemings, "Process Modeling," Proc. Modeling of Casting and Welding Processes, ed. Brody and Apelian, New Hampshire, Aug. 3-8, 1980 (The Metallurgical Society, 1981) P. 533.

2. Proc. Modeling of Casting and Welding Processes II, Henniker, New Hampshire, July 31-Aug. 5, 1983 (The Metallurgical Society, 1984).

3. R. A. Stoehr et al., "Modeling of Filling of Complex Foundry Molds," this Symposium.

4. H. M. Domanus, Y. Y. Liu, and W. T. Sha, "Fluid Flow and Heat Transfer Modeling for Casting," Proc. of Third Conference on Modeling of Casting and Welding Processes, Santa Barbara, California (January 12-17, 1986).

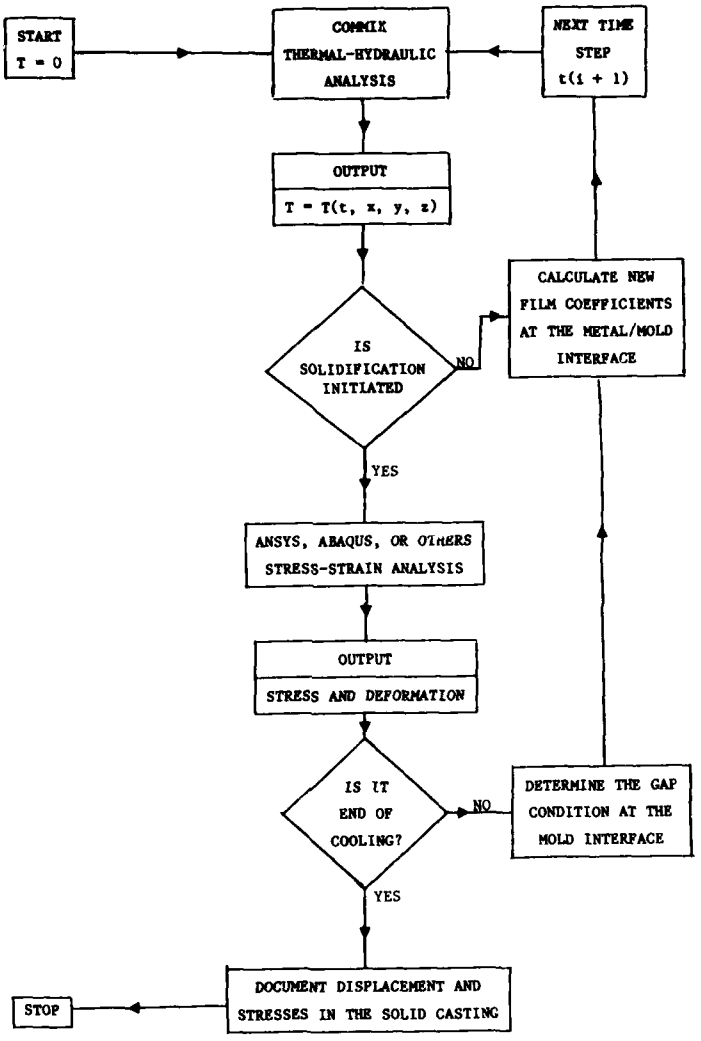

Fig. 18. Flow Diagram for Integrated Analysis

5. W. T. Sha et al., Argonne National Laboratory, "COMMIX-1: A Three-Dimensional Transient Single-Phase Component Computer Program for Thermal Hydraulic Analysis," 1978, NUREG/CR-0785, ANL-77-96.

6. H. M. Domanus et al., Argonne National Laboratory, "COMMIX-1A: A Three-Dimensional Transient Single-Phase Computer Program for Thermal Hydraulic Analysis of Single and Multicomponent Systems," Vols. I and II, 1983, NUREG/CR-2896, ANL-82-25.

7. W. T. Sha et al., Argonne National Laboratory, "COMMIX-1B: A Three-Dimensional Transient Single-Phase Computer Program for Thermal Hydraulic Analysis of Single and Multicomponent Systems," 1985,NUREG/CR-4348, ANL-85-42.

8. W. T. Sha, "A New Porous Media Approach to Thermal Hydraulic Analysis," Trans. Am. Nuc. Soc., Vol. 39, 1981, pp. 510-512.

9. W. T. Sha, B. T. Chao, and S. L. Soo, Argonne National Laboratory, "Local Volume-Averaged Transport Equations for Multiphase Flow in Regions Containing Distributed Solid Structures," 1981, NUREG/CR-2354, ANL-81-69.

10. W. T. Sha, B. T. Chao, and S. L. Soo, "Porous Media Formulation for Multiphase Flow with Heat Transfer," Nuclear Engineering and Design, Vol. 82, 1984, pp. 95-106.

11. F. H. Harlow and A. A. Amsden, "Numerical Calculations of Multiphase Fluid Flow," J. Computational Physics, Vol. 17, 1975, pp.19-52.

12. S. V. Patankar, Numerical Heat Transfer and Fluid Flow, Hemisphere Publishing Company, 1980.

13. C. W. Hirt and B. D. Nichols, "Volume of Fluid (VOF) Method for the Dynamics of Free Boundaries," J. of Computational Physics, Vol. 39, 1981, pp. 201-205.

14. B. D. Nichols, C. W. Hirt, and R. S. Hotchkiss, Los Alamos National Laboratory, "SOLA-VOF: A Solution Algorithm for Transient Fluid Flow with Multiple Free Boundaries," 1980, LA-8355.

15. W. T. Sha and J. F. Thompson, Argonne National Laboratory, "Rod Bundle Thermal-Hydraulic Analysis Using Boundary Fitted Coordinate System," 1979, ANL-78-1, NUREG/CR-0001.

16. Brian C-J. Chen, William T. Sha, M. L. Doria, R. C. Schmitt, and J. F. Thompson, Argonne National Laboratory, "BODYFIT-1FE: A Computer Code for Three-Dimensional Steady-State/Transient Single-Phase Rod-Bundle Thermal-Hydraulic Analysis," 1980, ANL-80-127, NUREG/CR-1874.

17. W. T. Sha, Argonne National Laboratory, "Boundary Fitted Coordinate Transformation for Thermohydraulic Analysis in Arbitrary Three-Dimensional Geometries," 1981, ANL-81-54, NUREG/CR-2313.

18. K. Miki and T. Takati, "A Domain Decomposition and Overlapping Method for the Generation of Three-Dimensional Boundary Fitted Coordinate System," J. of Comp. Phys., Vol. 53, No. 2, 1984, pp. 319-330.

Acknowledgement

The author wants to acknowledge his coworker Dr. H. M. Domanus for his significant contribution to the work presented here.

A NUMERICAL MODEL OF DIRECTIONAL SOLIDIFICATION OF CAST TURBINE BLADES

by

Ghislaine Lamanthe
SNECMA Gennevilliers
291 Avenue d'Argenteuil
F92230 Gennevilliers, France

and

L.Vermot des Roches
LSG2M
Ecole des Mines
F54402 Nancy, France

SNECMA and LSG2M have developed a finite element model of the thermokinetics of the directional solidification of cast turbine blades. The main difficulty to be solved to obtain an appropriate modelling of the phenomenon lies in the high amount of radiative heat transfers, in a case where geometry is complex, thermal gradients high and boundary conditions variable with time. The model treats these transfers by meshing the radiant surfaces and applying shape factors. The other requirements of such an approach are : an appropriate knowledge of the boundary conditions of the furnace, and the thermal properties of materials (ceramic shells, etc ...).

Experiments have shown a fair consistency between the thermal fields predicted by the model and temperature data recorded during the solidification of a cluster of complex bars representative of turbine blades.

1 - INTRODUCTION

The manufacturing of complex advanced gas turbine blades using directional solidification requires tightly controlled heat transfers, especially when single crystal growth is involved : defects such as local misorientations or micropores are closely related to the thermal history of the parts during solidification. The geometry of the clusters and the process parameters must be accurately determined to produce metallurgically and mechanically acceptable parts.

To avoid a purely experimental development for every new part, which would be costly and time consuming, SNECMA has undertaken with Ecole des Mines de NANCY the development of a computer program combined with experimental verification. The initial stage of this work was performed with comparison between predicted and measured data for the solidification of parts with of simple geometry, such as cylindrical bars (ref. 1).

In the subsequent steps we considered the modelling of parts and clusters of increasing complexity (ref. 2 and 3) to build the simulation of the unidirectional solidification of a turbine blade. This paper summarizes the studies concerning clusters of rather complex bars which can very well represent the thermal behaviour during blade solidification.

2 - HEAT TRANSFER ANALYSIS

The experiments were performed in a laboratory furnace shown schematically in figure 1. The mold made by the lost wax process is heated in a chamber under secondary vacuum. When the metal is poured in the shell the solidification initiates on the water cooled chill plate.

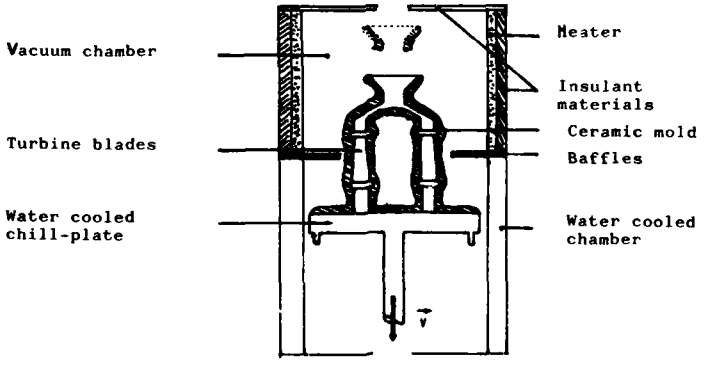

Fig. I : DS furnace scheme

Then the mold is withdrawn at a suitable rate into the cold chamber. The heat transfers can be described as follows :

- radiation received by the mold from the heater
- radiation emitted by the mold to the cooler
- radiation between two parts of the outer surface of the mold
- conduction in the mold
- heat transfert between the mold and the chill-plate
- latent heat release in the solidifying alloy.

Natural convection in the molten alloy can be neglected due to the stabilizing effect of thermal gradient in the liquid phase.

Freezing occurs near the baffle ; the size and the shape of the mushy zone which mainly determines the crystal growth can be controlled by controlling the thermal gradient (G) and the solidification rate (R). G and R can be checked, afterwards, by metallurgical investigations.

3 - NUMERICAL APPROACH

A general purpose Finite Element (F.E.) program for heat transfer analysis (MODULEF) which has been improved to solve our particular problem is used. The geometry of the bars, and obviously of the cluster, can only be described by a 3D-mesh. The main difficulty to be solved, for a satisfactory modelling of the phenomenon, lies in the calculation of all net radiation energy flux lost at the mold surface, which changes continuously, since the mold is withdrawn out of the furnace.

Assuming that the DS furnace is a cylindrical box containing the casting, an analysis of the radiation exchange inside such an enclosure can be formulated, in a convenient manner, by using the " net radiation method " described in ref. 4. Let us divide the entire inner surface of this enclosure into areas so that, over each of them, the temperature and the reflected and emitted scattering energy are uniform ; if the emissivities of bodies can always be considered to be equal to absorptivities, then a heat balance on a surface area S_k belonging to the mold ($\varepsilon_k \neq 1$) gives :

$$\psi = \frac{\varepsilon_k}{\varepsilon} \cdot (\sigma \cdot T_k^4 - B_k) \qquad (1)$$

$$(\sigma = 5{,}675.10^{-8}\ W/m^2\ K^4)$$

where T_k is the current temperature of S_k

ε_k its emissivity,

B_k its radiosity (see ref. 4) calculated by solving the following linear system $[X] \cdot [B] = [R]$

X is a square matrix depending on the radiative properties of the mold (ε) and on the geometrical shape of the mold through a set of view factors f_{ij}. R is a vector depending on all surface temperatures T_k, in the enclosure, on radiative properties of the mold and surroundings and on view factors between mold and furnace.

As far as view factors are concerned, a FORTRAN program has been developed based on FE calculation. We just emphasize that all view factors, previously calculated outside the FE resolution, must be corrected during simulation due to time-dependent baffle locations. (1) is implemented in the FE program after the following linearisation :

$$\psi_k = h_k \cdot (T_k - T_k^*) \qquad (2)$$

$$h_k = (\sigma \cdot \varepsilon_k / 1 - \varepsilon_k) \cdot (T_k^2 + T^{*2}_k) \cdot (T_k + T^*_k)$$

$$T^*_k = \sqrt[4]{(B_k / \sigma)}$$

The main difference with simpler previous models (ref. 1) lies in the way of computing h_k and T^*_k. Usually, T^*_k is an average value of the temperature of the hot or cold zone depending on the time-dependent location of the mold in the furnace.

The determination of the physical characteristics of the materials is very important, and their variation with time must be considered especially at high temperature.

4 - RESULTS

Computed results and test data were compared for bars with rather complex geometry, shown on figures 2 and 3. These bars were used to make the calculation shorter and the experiments easier owing to their symmetrical shape which allows a lower number of experimental points and decreases the complexity of the mesh and then the duration of the calculation.

Clusters of such bars were cast, and temperatures were measured during the solidification, in the alloy as well as in the ceramic mold. The measured temperature distributions in the furnace were used as thermal limit conditions for the calculation. They are variable with time and must be evaluated at every step.

The experiment and the simulation shown below are an illustration of our work. The bars were cast with Ni-based superalloy in a refractory ceramic shell and withdrawn at a constant rate of 390 mm/h during 1500 s (ref. 5).

Fig. 2

Geometry of the bar with the position of some thermocouples

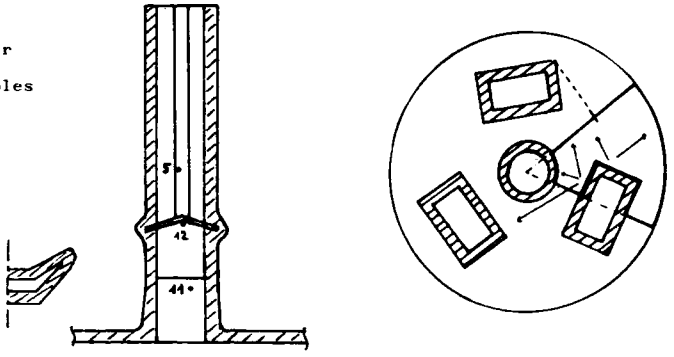

Figure 4 presents the variation of temperature with the time for points located in the massive area (thermocouple n° 11) and in the airfoil, in the alloy. The solid lines are the computerized results and the dotted lines the experimental results.

Fig. 4

calculated (——) and experimental (- -) variation of temperature with time in the alloy

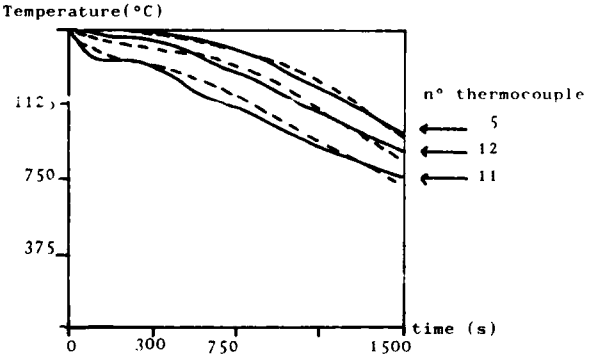

The figure shows a good agreement, except just after pouring when the effect of the chill-plate is the most important. After a few minutes the solidification is slower and the mushy zone advances at a constante rate. The bar portion representative of the blade solidifies after this moment. Data recorded after this stage are really significant for the casting engineer, who can analyse the cooling rate. It appears that the cooling rate in the mushing zone increases as the solidification front progresses along the airfoil span

In fact it is unreallistic to look for an absolute consistency because of the respective limitations of experiment and calculation : for example measurements with an accuracy of a few degrees, on the other hand the calculation depends on the value of thermophysical properties which are not exactly known.

Figure 5 gives the position of the solidus and liquidus isotherms in the alloy as a function of the withdrawal time during the solidification of the cluster.

Agreement between measured and calculated curves is excellent. This figure allows to determine the solidification time t_1, the size of the mushy zone H and the rate of isotherm advancing rate R. In this case R is equal to the withdrawal rate as long as a thick zone is solidifying ; after an initial short time, the length of which depends on the thermal distribution, the rate R increases for liquidus isotherm. When the solidus enters the same area its rate increases too, then it reaches a value which remains constant up to the end of the process. The mushy zone is located on both sides of the baffles.

Fig. 5

Liquidus and solidus position as a function of the withdrawal time

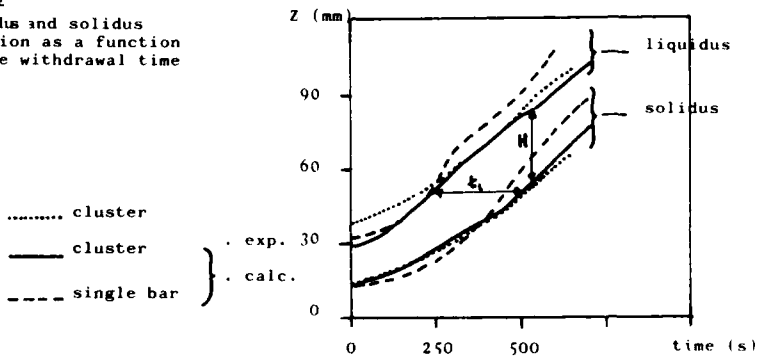

Figure 5 compares also the evolution of liquidus and solidus positions in a bar, which is part of a cluster, with the evolution in a bar cast alone, that is without taking into account the environnement of the cluster (ref. 2). The rate of solidification is higher in the second case and the size of the mushy zone increases too.

A typical calculated isotherm distribution, as presented in figure 6, illustrates the evolution of the isotherms. There is always a hotter zone in the inner part of the cluster and the isotherm are not looped. When the part is cast alone, only the airfoil modifies the isotherms (figure 7). In this case we find no particular problem of solidification and we can explain some metallurgical difference between these the cluster and the separate bar.

Fig. 6 a)

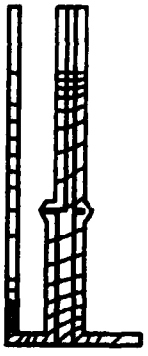

Fig. 6 b)

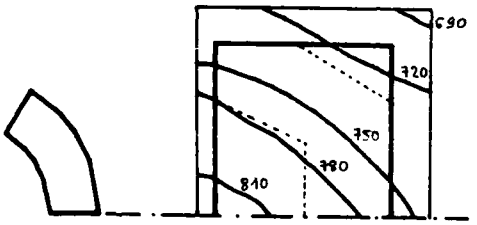

Fig. 6 : solidus position as a function of time in the part cast in a cluster
a) in a vertical section
b) in the platform

Fig. 7 a)

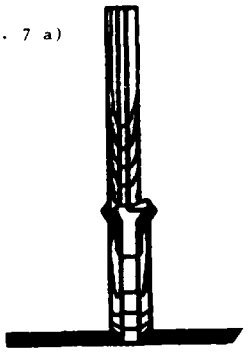

Fig. 7 b)

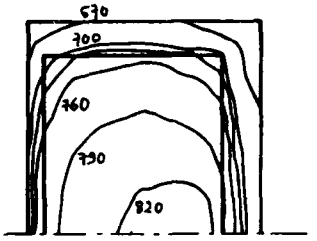

Fig. 7 : solidus position as function of time in the part cast alone
a) in a vertical section
b) in a platform

Such a distribution is useful to evaluate theoretically the possibility of occurence of metallurgical defects, such as grain faulting or shrinkage defects ; the evolution of the defects with the experimental parameters (temperature, withdrawal rate, thermal gradient) as well as with the geometrical and thermal characteristics of the cluster can be evaluated to optimize the process.

5 - CONCLUSION

The results presented above show that it is possible to simulate the directional solidification of rather complex clusters of parts. We improved a 3D-FEM computer program by taking the radiation heat transfer into account. So, we evaluated the view factors with a suitable calculation and realized a 3D mesh.

By calculating the thermal gradient G and the solidification rate R we can follow the solidification of the part. For example, we compared the casting of a single bar with that of cluster and saw that in the second case R is reduced (-25%) and G is increased (+ 50%).

With this program we are able to describe the solidification of blades and to predict some aspects of their metallurgical structure. The SNECMA GENNEVILLIERS foundry plant has now all the elements of a complete CAO system : materials thermal parameters, furnace modelisation, process procedure, 3D mesh coupled with thermal modelling. With such a system the foundry engineers will be able to optimize the directional solidification of complex blades.

REFERENCES

1 L. VERMOT DES ROCHES - Oral communication
Conf. of European Materials Research Society - STRASBOURG - June 1986

2 L. VERMOT DES ROCHES - Conf. " Transferts Thermiques aux Températures élevées "
Ecole Centrale.CHATENAY MALABRY - 5-7 May 1987

3 L. VERMOT DES ROCHES - Paper submitted to Conf. of Solidification Processing -
SHEFFIELD - 21-24 september 1987

4 R. SIEGEL - J.R. HOWEL - " Thermal Radiation Heat Transfer "
Mc GRAW HILL - 1981

5 L. VERMOT DES ROCHES - Thesis - NANCY - 1987

USE OF VENDOR CONSORTIUMS FOR IMPLEMENTATION OF PROCESS SIMULATION TECHNOLOGY

BY

SULEKH C. JAIN, Manager, CAE Projects and Forging Technology, GE-Aircraft Engines, 1 Neumann Way, Cincinnati, Ohio 45215, U.S.A.

KENNETH C. MADDUX, Manager, Advance Manufacturing Engineering, SDRC, 2000 Eastman Dr., Milford, Ohio 45150, U.S.A.

ABSTRACT

The aerospace Vendor Supplier Industry in the United States is now moving from the 'Trial and Error' approach to the 'Plan, Predict and Produce' philosophy. This new discipline offers reduced development time, near net shapes, improved part quality, reduced inspection, and hence reduced overall cost. The emphasis now is to make it right the first time in the shortest time and at least cost.

During the last decade there has been a tremendous amount of progress in the development of fundamental Computer Aided Engineering (CAE) tools for unit manufacturing process simulation. Much of this effort in the United States has been sponsored and funded by the United States Air Force and other government agencies. The tools have been correlated and validated to actual problems in laboratories and shop floors and a reasonable level of confidence and vendor acceptance has been achieved. These tools include simulation for:

- Forging
- Extrusion
- Heat Treatment
- Investment Casting
- Ring Rolling
- Chip Removal

The challenge now is to implement these tools at vendor sites and to utilize these technologies on an ongoing basis to assist in preventing real world problems.

In today's business environment, Original Equipment Manufacturers (OEM) such as GE must work closely with its key vendors to supply and implement this technology. GE has made extensive use of vendor consortiums in this effort to apply the latest process simulation technology.

This paper describes the success and the status of implementation of this technology at major United States aerospace forging vendors.

INTRODUCTION

TODAY'S BUSINESS AND TECHNICAL ENVIRONMENT

Business pressures today are forcing major changes in every step of the product development cycle from design conception through production. These pressures include an emphasis on making the product 'right' the first time, to reduce the occurrence of poor quality, to reduce costs and to take advantage of just-in-time production techniques. There is a strong tendency towards smaller volume batch production with less opportunity to recover up-front design and manufacturing engineering and tooling costs. As a result of lower volumes, higher quality and increased product performance requirements, the non-touch or indirect labor contribution as a percentage of product cost has risen significantly. Finally shorter product life cycles requiring more frequent product introductions have resulted in a shortage of truly skilled and experienced design and manufacturing workforce especially in the metal working industry. Each of these business pressures have placed more emphasis on developing lower cost, higher quality products in smaller volumes and in less time.[1]

The world today is one global market with various wage structures and work ethics, but nearly identical engineering and production capabilities available to nearly every country and company. Superior product differentiation or attributes will result from how well a company is able to assemble the right tools, manage the new product development cycle and capture the experience of its best employees.

Manufacturers who do not constantly strive to improve their manufacturing processes are rare. In fact, most are extinct or soon will be. Manufacturing survives on change because markets and competition change and new processes and methods have an impact on cost and quality.

The jet engine has won a unique place in metal working manufacturing because it is one product that has been in continuous production for many years. Throughout this period, the design of jet engines has seen a constant change and so has its manufacturing. The constant search for new designs, materials and production processes has helped to lower costs and improve quality.

GE AND ITS VENDORS

GE - Aircraft Engines (GE-AE) is a leading manufacturer of jet engines for both commercial and military aircraft. GE-AE has a strong partnership with its suppliers. Today roughly 50 percent of the aggregate cost of GE-AE's engines represents the costs of components purchased from outside suppliers.[2] That is a $3 billion share of a $6 billion level of sales. See Figure 1.

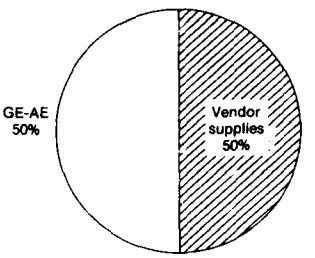

Figure 1
Typical Jet Engine Component Breakdown GE vs. Vendor Supplied Components

Moving into 1987 and the decade beyond, GE and its suppliers face a whole new set of demands. Higher quality engines will need to be manufactured on time at the lowest possible cost. To compete in a world market, yesterdays good will not be good enough. GE-AE and its suppliers must be the best to compete in the world market.

What will it take to remain a GE supplier? To remain a world class leader in jet engine business, GE-AE expects five things from its suppliers:

(1) absolute product integrity
(2) highest quality product
(3) on-time delivery
(4) lowest product cost
(5) most importantly leadership in new technology innovations and its implementation

Manufacturing of engineered materials has entered the computer age for improved productivity and cost efficiency. Development of computer integrated manufacturing (CIM) along with flexible manufacturing systems. CAD / CAM, process design and simulation and automatic process control and inspection etc. reflect an entirely new method of manufacturing. Growing industrial computing power and software, artificial intelligence, better communications and networking offer high leverage for making strategic change now.

PRODUCT COST

The current cost breakdown of producing a product or component is an important guide to reducing costs in the future. As shown in Table 1, the cost breakdown for various industries is very similar.

TABLE 1 - Product Cost Breakdown

	Aerospace Defense	Automotive	Electronic
Direct / Touch Labor	8%	13%	5%
Indirect - Labor & Overhead / Non Touch	27%	27%	25%
Materials—(Raw and Procured Parts)	65%	60%	70%

It can be seen from this information that the cost of material is the largest single cost component with indirect costs second. However, when one reviews where industry has made capital investments to improve productivity, one finds that industry has invested heavily in robotics and factory automation to reduce touch labor costs. Operation management has received considerable attention for reduced inventories and increased equipment use. While these are important areas, industry has largely neglected the materials and indirect aspects of product cost.

Raw material costs can be reduced through improved product design using alternative materials and optimal designs. Manufacturing can lower material costs through reduced inventories (using just-in-time delivery scheduling) and more importantly producing more nearly net shaped parts. As OEMs such as GE-AE move towards a strategy of more components being supplied by vendors it becomes difficult to maintain control over the degree of near net shape achieved.

Computer Aided Engineering (CAE) for the manufacturing engineer, and specifically process simulation addresses reducing the non-touch and materials aspects of product cost. Concurrent engineering (between OEM and vendors) is facilitated by CAE process and material simulations, this leads to improved productivity of the manufacturing engineer's activity as shown in Figure 2.

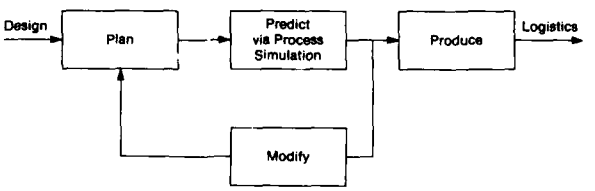

Figure 2
The Role of Process Simulation in Manufacturing Engineering

VENDOR PROFILE

A typical profile common to many United States parts suppliers and vendors is:

- Small company
- Relatively old facilities
- Low profit margin
- Limited resources to invest in new manufacturing technology
- Up & down sales cycle
- Not priced competitively with offshore vendors

Hence, concurrent engineering between the OEM and the vendor is difficult to implement.

In response to this situation, progressive OEMs are working closely with their vendors to develop manufacturing process simulation technololgies under vendor consortiums and assisting in implementing these technologies at these vendors. These progressive OEMs and vendors realize that they have a co-destiny relationship to survival and growth. The benefits of this relationship include:

- More flexibility to design changes
- Better quality through process optimization
- More innovative solutions by the vendor
- Lower cost
- Processes that fit the vendor's production capabilities
- Shorter delivery times, "first time right"
- Retaining of local suppliers for better communication

TAGUCHI APPROACH FOR PRODUCT AND PROCESS DESIGN

The work of Taguchi in the area of designing for quality has received considerable attention in the engineering field and suggests more 'up-front' engineering effort.[3] His contribution is to push the quality issue upstream in the design and manufacturing engineering activity, well ahead of actual manufacturing. At the center of his framework is the interpretation of quality as measured by total loss due to functional variation in the performance of a product caused by manufacturing variations as shown in Figure 3.

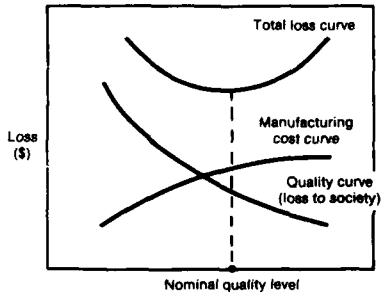

Figure 3
Loss Curve for Product

Taguchi advocates a three-stage product or process development cycle:

- System Design - Application of experience and technology to define the process alternatives.
- Parametric Design - Parametric study of the product and process to determine the optimal nominal values of parameters.
- Tolerance Design - Use of the loss function to develop economic trade-offs which give rise to the setting of production tolerances for the factors identified in the Parameter Design.

The concept in this approach is to avoid random looping in the System Design stage and never getting to the Parameter and Tolerance Design Stages. Only by continuing onto the Parametric Design stage can one truly understand the proposed process and from this understanding gain knowledge that will lead to defining the best possible product and process. The Parameter Design stage consists of:

- The use of unit process simulation to optimize the process
- The use of design of experiments methods to search and evaluate for the best performance
- The concept of robust process design wherein levels of control parameters which minimize the variation in the process from external sources for a maximum margin of safety are sought

A fundamental tool in the Taguchi method calls for the use of manufacturing process simulations to evaluate alternative processes.

PROCESS MODELING / SIMULATION

Interest in numerical solutions to all classes of deformation and fluid flow processes has grown significantly in the last two decades. This interest is now being utilized in manufacturing.

Increasing competition in industry and the emerging frontiers in science and technology lead to ever increasing additional demands for more accurate analyses of industrial processes. The shift in solution methodologies has been from analog to digital, analytical to integral method solutions and integral method solutions to discretization methods i.e. finite difference, finite volume and finite element methods. The most popular method today for modeling bulk deformation processes is the finite element method because of the ease in implementing boundary conditions and obtaining accurate solutions.

The technological revolution occurring throughout the industrial world has advanced computer-aided design and manufacturing engineering (CAD / CAM / CAE) technology significantly. This technology makes a higher quality product possible. Today forging, casting and several other industries are taking advantage of CAD / CAM / CAE to meet customer demands for higher quality, lower cost products.

For example in the forging industry computers can be applied in three basic areas as illustrated in Figure 4.

- Analyzing and simulating the forging process (predicting material flow, stresses, temperatures, forces and energy).
- Preparing part, die and fixture drawings (drafting) and generating numerical controlled (NC) cutter paths to produce NC machined models (for copy machining), electrodes for electric discharge machining (EDM) or to produce a die directly from a die block.
- Using a coordinate measuring machine (CMM) to control part, die, model or electrode dimensions.

Development of reasonably accurate and inexpensive computer software to simulate metal flow during the forging process allows the ultimate advantage of computer applications in forging. This allows running forging experiments on the computer such as simulating the finish forging of a blocker design. Experiments (on the computer) can be repeated until satisfactory results are obtained, which would reduce the number of necessary and expensive die tryouts.

This computerization of the manufacturing processes via CAD / CAM / CAE leads us to what is called today SIMULTANEOUS / CONCURRENT / LIFE CYCLE Engineering.

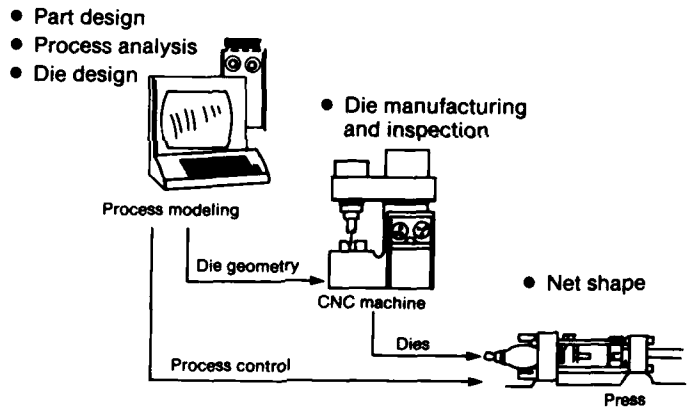

Figure 4
The Role of Computers in CAD and CAM

SIMULTANEOUS / CONCURRENT / LIFE CYCLE ENGINEERING

Ransom Olds, Henry Ford, Karl Benz and Adam Opel did not design an automobile and then turn it over to a manufacturing engineer who decided how to produce it. Those pioneers of the automobile industry were both product and process engineers. They designed the cars and the factories that built them.

Long before it was fashionable, they were practicing simultaneous / concurrent engineering (See Figure 5). Unfortunately, as the industrial activities grew, the trend was away from that idea. Product engineers would design a product, and then turn it over to the manufacturing engineer, who had to work out how to make it. Now with the advent of the computer, we can go back to the original approach. Simultaneous engineering brings back these groups (that historically have had friction between them) together. This approach brings together early-on or 'up-front' personnel to address both the design of the product and the design of the manufacturing process. Thus, the combination of design, materials and manufacturing

methods can be more readily optimized. Traditionally these critical decisions have been made by both the design, materials and manufacturing engineers in a process shown in Figure 6.

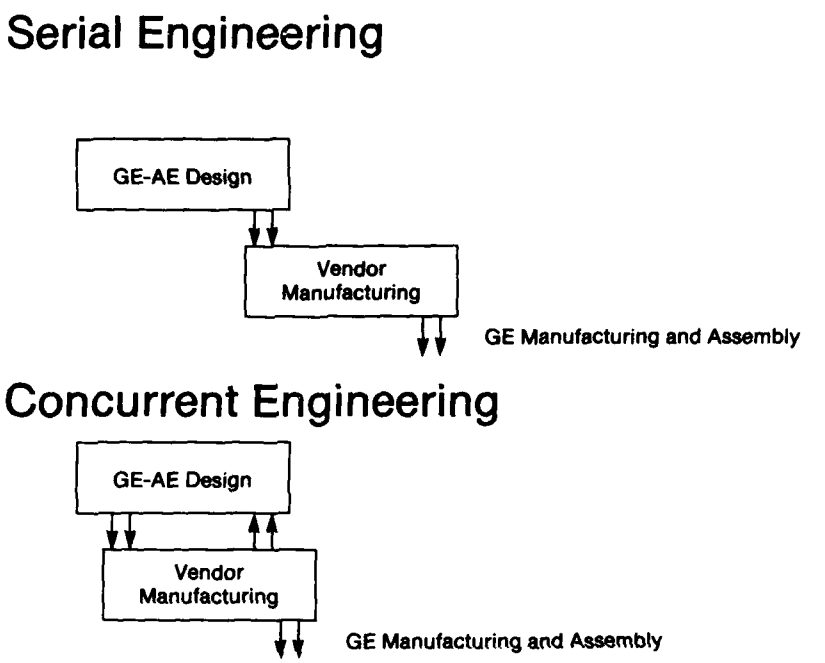

Figure 5
Serial vs. Concurrent Engineering

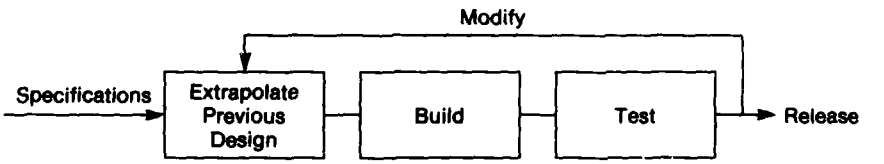

Figure 6
Traditional Engineering Process

Studies have shown that many of the early critical decisions are made when only a small percentage of development funds have been spent in the development process. This results in early 'locking in' the performance of the product. These tough early decisions when there is little information and time available, largely determine the ultimate success (or failure) of a product.

This process worked well for small improvements. Today, the situation is quite different. The development team is forced with totally new products and materials to design, produce and introduce in much shorter time with less help from their experience.

Computer Aided Engineering (CAE) tools available today allow the designer to evaluate alternative designs, select the most promising, and optimize the design (determine 'best' parameters) before prototype build and test.

To accomplish a similar goal for manufacturing, the manufacturing engineer must participate in the same type of revolution that the designer has gone through. That is, the manufacturing engineer will need to utilize tools such as 3-D solid modeling

to design, visualize and document the manufacturing process and then evaluate alternative processes using finite element analysis tools in an approach similar to that used by the design engineer as shown in Figure 7.

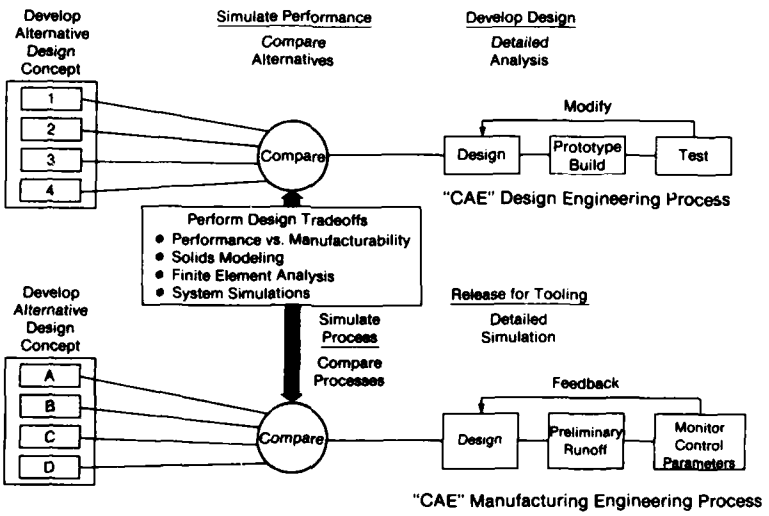

Figure 7
CAE Tools for Concurrent Engineering

With the appropriate shared CAE tools, concurrent engineering will be easier to implement. With the right CAE tools, the manufacturing engineer will be able to make critical 'early' process design decisions with more knowledge and understanding for better products, processes and fewer surprises on the shop floor. Furthermore, concurrent engineering can help to avoid design configurations which might be difficult or expensive to produce.

One can utilize many existing tools to create a CAE system for the manufacturing engineer. A major feature or need of CAE systems that designers have learned is to have all the major elements integrated into a system. One integration approach used by I-DEAS (Integrated Design and Analysis System) CAE system is shown graphically in Figure 8.

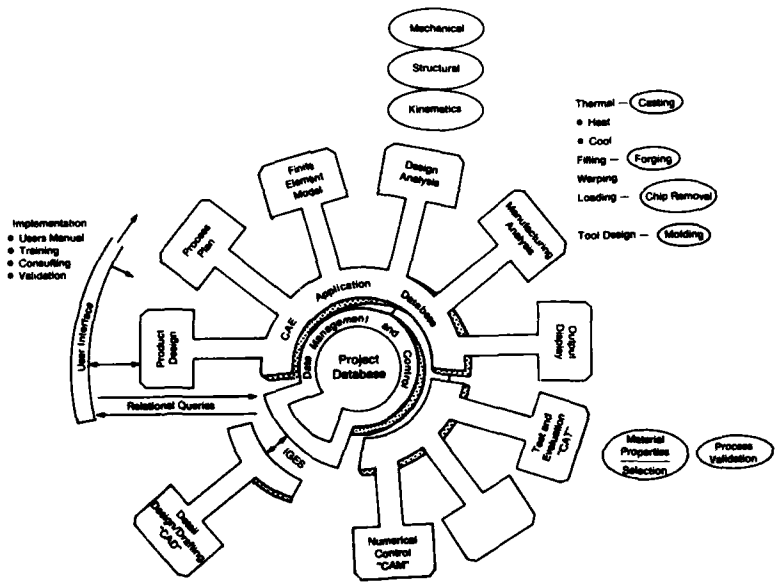

Figure 8
Integrated CAE Software System Design for Manufacturability

ELEMENTS OF AN INTEGRATED CAE SYSTEM

The major tools or elements of a CAE system required by the manufacturing engineer are listed and described below. Many of the tools are being used by design engineers.

- Graphic systems, such as 3-D Solid Modelers or CAD system for the design, visualization and documentation of a proposed manufacturing process.
- Electronic data transfer procedures between various graphics systems.
- Pre-Processors for generation of finite element models from the stored graphic description of the part.
- Manufacturing process simulation analysis tools for each manufacturing process of concern.
- Post processing or graphic output display of results tailored to the specific manufacturing process of concern.
- Database organization to handle the large amount of graphics, material properties and pre / post output that is generated for the transient analysis of the manufacturing process.
- Data management control system to control, update, notify and for approval of design changes during the product and process development process.
- Training of personnel in new technology and methods.
- Maintenance and support of software. This is especially important in the area of complex manufacturing process simulation. Hot line support for the user is required when problems arise.

As one reads through the list of tools the manufacturing engineers need for an effective CAE system, the similarity to those currently available to designers become apparent, except for the individual manufacturing unit process simulations. Hence, one should be able to utilize many existing tools to create a CAE system for the manufacturing engineer. An example of one fully integrated CAE system is shown in Figure 9.

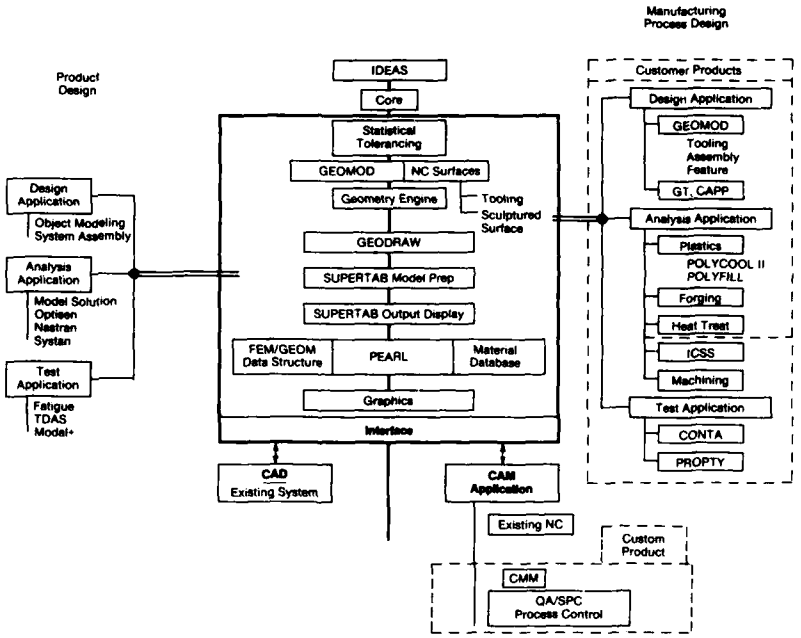

Figure 9
Integrated CAE System

In this system, 3-D solid models are developed in GEOMOD™. This geometry is used to create finite element meshes in SUPERTAB™ which are then interfaced to a variety of design and manufacturing analysis tools. Finally, the results are displayed by OUTPUT DISPLAY™. Each module of the system is integrated to an application database with PEARL™ serving as the relational database for storage of the module results. The user-friendliness feature of the integrated systems is a major attribute that the manufacturing engineer needs.

Thus, a similar framework with many of the major modules in place already exists for the manufacturing engineer. The availability of effective manufacturing process simulations for a variety of processes, such as forging, die casting, injection molding, sand and investment casting, chip removal, metal forming, heat treating, etc., is the major missing piece of technology; such simulations are being developed today.

The primary ingredients for process simulation are the mathematical formulation of the mechanics of the process, database (material and equipment), geometric and numeric data base (of the component) and the process design (manufacturing sequence, design of starting and intermediate shapes, quality assurance and inspection requirements, equipment capability and other constraints).

While most of the material database can be represented and input into the simulation model as a constitutive equation, the design of the process is often based on prior art, history, knowledge, experience and extrapolation. This art and experience can be expressed in the form of knowledge based expert system and be utilized in the design of the manufacturing process. Thus, expert systems are an adjunct to the process simulation tools and not a stand-alone tool for determining the sensitivity of the process and its optimization.

The major elements that are required to develop a successful manufacturing engineering system are shown in Figure 10. In addition to the process simulation analysis programs, a parallel effort in experimental testing for parameter determination, model validation and database creation is required.

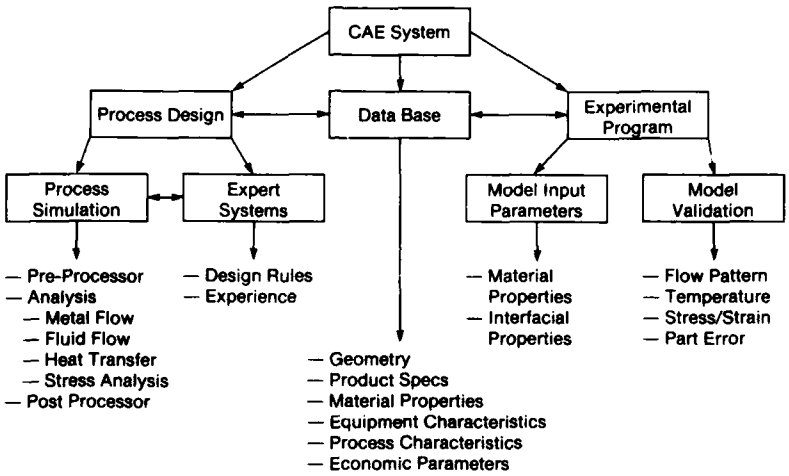

Figure 10
Generic Technical Approach for Manufacturing Process Simulations

MANUFACTURING PROCESS SIMULATION PHILOSOPHY

In order to develop simulations for a large number of manufacturing processes required for jet engine components, the use of core software 'modules' for each fundamental mechanism in the process, such as transient heat transfer, fluid flow etc. are utilized for several manufacturing processes. These modules are coupled together to simulate the desired manufacturing process.

In general, the software process simulation modules are public domain codes that allow access to the source code for tailoring to specific processes. This tailoring is important not only to allow specific capabilities to be implemented, but also to reduce the run time to acceptable values. The most effective approach is to utilize and modify existing software wherever possible.

The total phases for implementation of a CAE Project such as a Process Simulation for a unit manufacturing process simulation is shown in Figure 11 and includes implementation at the vendor.

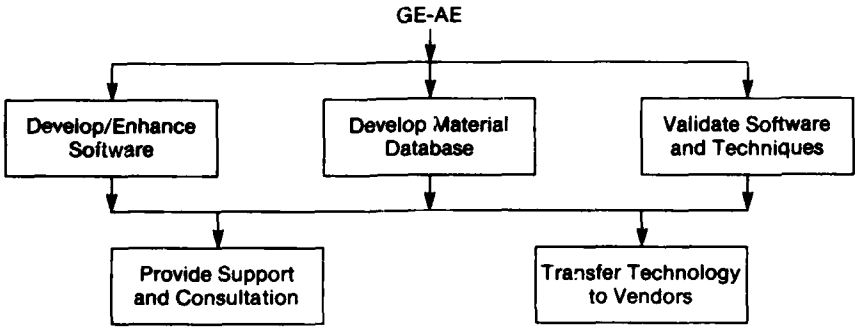

Figure 11
Typical CAE Project Phases

STRATEGY FOR TECHNOLOGY TRANSFER & IMPLEMENTATION AT GE-AE FORGING VENDORS

It has been shown earlier that GE-AE buys 50% of the goods and services from its suppliers. Out of these, forgings and related products constitute major single items that GE-AE buys. It must be pointed out that these forgings are used in many critical applications such as disks, seals, shafts, casings, and airfoils. GE-AE buys all of its forged, extruded and ring rolled components (except small airfoils) from its suppliers. It is thus apparent that GE-AE has a codestiny with its forging vendors. In order to meet the demands of higher quality, lowest cost, on time delivery, global competition, constantly changing technologies in jet engine design, materials and manufacturing, GE-AE's survival depends on the strength, superiority, technical and economical competence of its forging vendors. Thus GE-AE has a vested interest that its forging vendors remain world class producer of forgings by utilizing and implementing the latest state-of-the-art technologies.

With the advent of computers in manufacturing, the pace of change in manufacturing is extremely fast. Apart from our few major forging suppliers, one often finds that many suppliers are small and may not have the necessary in-house skills or resources to implement new innovations and technologies.

Forging industry itself in the United States has been facing hard times for the past 6-7 years. Many of the traditional markets such as heavy machinery, mining, and petroleum industries are in recession. The share of forgings in automotive is coming down due to inroads from other materials and technologies. As a consequence even well established major forging companies find it difficult to constantly invest in new technologies. Yet this is what GE-AE requires from its suppliers.

Realizing this predicament GE-AE has been a catalyst and facilitator in transferring and implementing many of these CAE related technologies at its vendor forge shops as shown in Figure 12. Listed below are some of the ways technology is being generated, transferred and implemented.

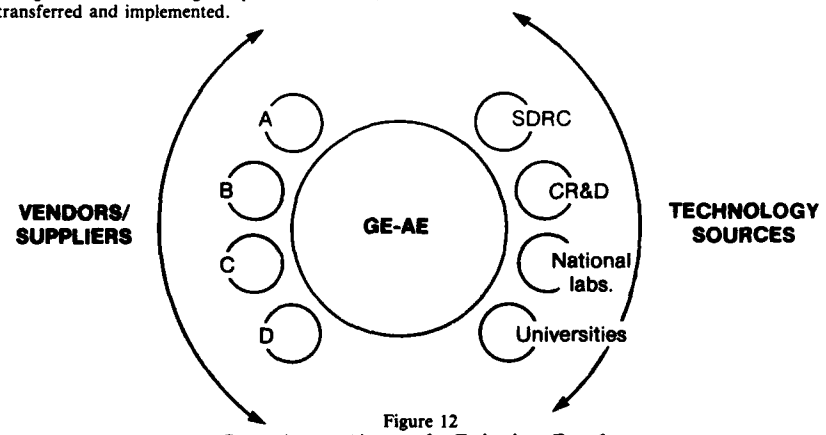

Figure 12
Consortium Architecture for Technology Transfer

1. **ROLE OF USAF AND DoD**

The United States Air Force, Navy, Army, DARPA and many other government agencies generate, fund and transfer technologies. This is shown in Figure 13. Through its Processing Science and Manufacturing Science Programs (MAN SCI), USAF has been instrumental and responsible for developing the basic tools, concepts, methodologies and software for CAE in forging and bulk plastic deformation type unit processes. These include material workability maps, dynamic

material maps and finite element programs like ALPID (Analysis of Large Plastic Incremental Deformation). Manufacturing technology (MAN TECH) type programs have provided an environment and vehicle in testing some of these technologies in actual production conditions. One such program is the MAN TECH IBR program which has created an environment in taking concepts from 'Lab to Shop' or Art-to-Part. Similarly, Technology Modernization Programs (TECH MOD) have been responsible in developing and implementing CAE techniques in manufacturing proceses. One recent example is investment casting.

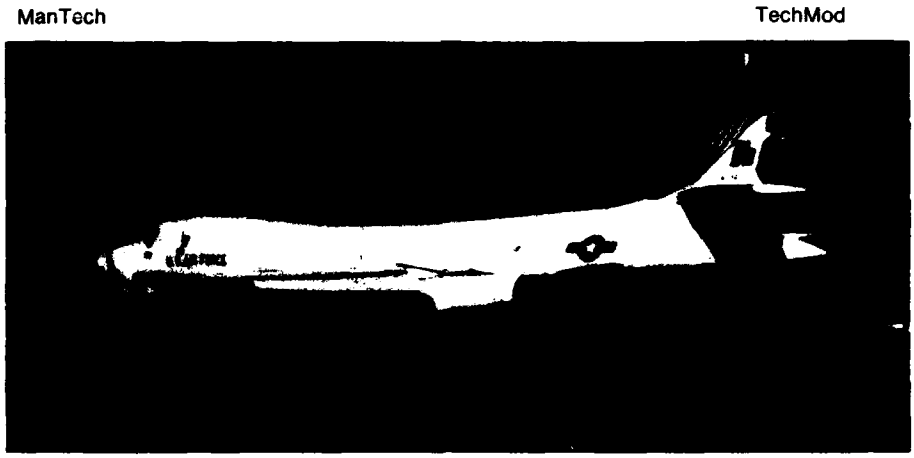

Figure 13
Air Force / DoD Programs in Technology Development and Implementation

2. ROLE OF GE-AE, ITS FORGING VENDOR CONSORTIUM AND TECHNOLOGY SOURCES

The role of GE-AE, Forging Vendors and Technology Sources in transferring and implementing core CAE technologies from Air Force / DoD, etc. is shown in Figures 14, 15, and 16.

The concept of technology transfer via use of consortiums is not new. Over the past years there have been many consortiums and literature is full of many examples. Throughout the United States, new consortiums are forming at a rate of about two a month[4]. GE-AE and its forging vendors' consortium is beneficial from the following standpoints.

- Financial leverage by vendor participation
- Software more practical and usable
- Implementation at vendors, easier and faster

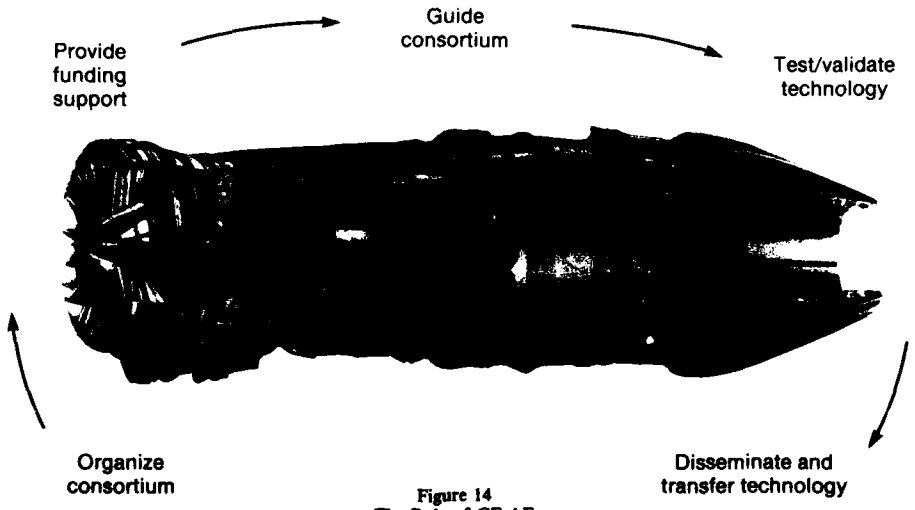

Figure 14
The Role of GE-AE

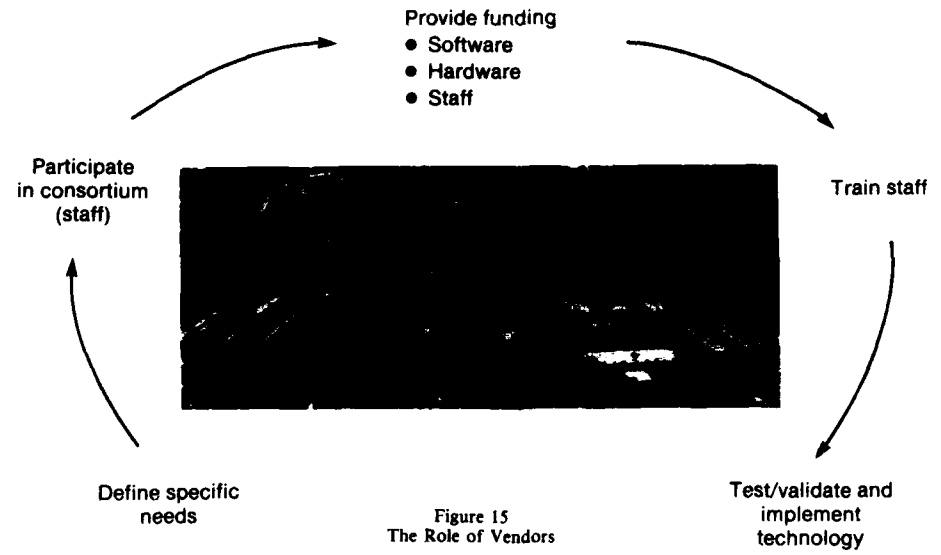

Figure 15
The Role of Vendors

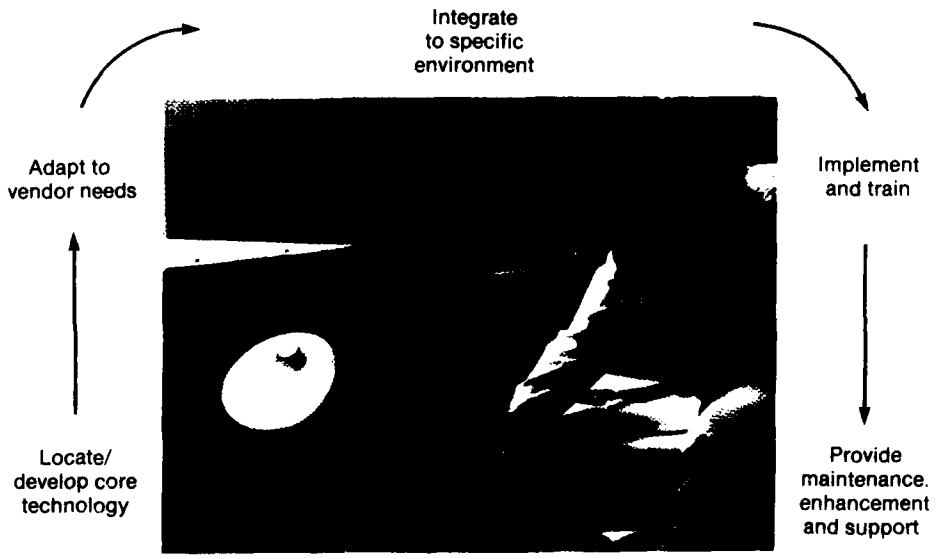

Figure 16
The Role of Technology Sources

IMPLEMENTING CONSORTIUM DEVELOPMENT PROGRAMS

The major steps involved in carrying out a complete consortium based development program are described below:

- MANAGEMENT COMMITMENT

  Management must be behind any major development program. Funding must be allocated, staff must be dedicated to the program and other resources set aside for the project. In addition, management must help define the strategic role of the new technology with the business objectives of the enterprise. That is, if the technology results of the program are not integrated into the business properly their effect will fall short of potential.

- PROBLEM DEFINITION

  The overall scope of the program should be well defined. Often, expectations can exceed what is capable of being developed and implemented. Staff personnel who are responsible for making decisions based on the results of the simulations should be involved so as to define their specific requirements.

- CONSORTIUM ORGANIZATION

The organization of the consortium is the next step. The authors have found that vendor companies that compete head-on can work together jointly in these technology development programs. However, it often requires a third party to bring the right people together. The consortium must have a central organizer to manage the financial and technical program aspects. This central organizer should develop master task lists from consortium input, conduct voting to prioritize development effort and then manage the development. In general, each consortium member has specific tasks such as testing, QA, etc. Frequent communication among consortium members is a requirement for success.

- TECHNICAL PLAN

The creation of an effective plan forms the framework of subsequent technical development. In general, manufacturing processes are extremely complex and simplifying assumptions must be made in order to simulate a process in reasonable time. The technical plan defines the major phases and sub tasks that are used to track and control the program. Key elements of any effective plan should include:

- Use of existing commercial or public domain software
- User friendly, consistent user interface
- Adaption and enhancement of existing software
- Parallel development of software, testing and database
- Computer hardware issues can be a problem. In general, the authors have found that most consortium members have or can easily obtain VAX computers. This common, readily available CPU makes software upgrading easy and allows for easy use of a wide variety of available software. This would not be the case for special computers.

- TASK ASSIGNMENT

As mentioned before, each member of the consortium should have well defined tasks. In this manner the members feel like they have ownership of the results.

- TECHNOLOGY DEVELOPMENT

The actual development and enhancement of the software and testing is now carried out. Monthly meetings and status reports are held to review progress and monitor / guide this development.

- DATABASE GENERATION

The building of databases is an ongoing process. The materials database is required to run the simulations. Tabular data can be entered, curve fitted and plotted. A wide variety of other options are available. Other data bases can include 3-D part geometry solids models and part features, finite element models and others.

- QUALITY ASSURANCE / VALIDATION

QA involves both software bug QA as well as accuracy validation of the software as compared to measured test results. Software QA involves running a wide variety of sample problems that exercise all the features of the program. Program accuracy validation involves comparing test results to actual test parts run on the shop floor. This validation work provides information on how much the software can be trusted. In the forging area in one case experienced forging engineers predicted that the hub area would fill first, then the rim area. Both ALPID and test results indicated the opposite. After this validation, the experienced forgers trusted the simulation.

- DOCUMENTATION / TRAINING

Documentation should include both monthly / periodic progress reports as well as final project report describing all the technical details of the program as well as problems completely worked so a new user can follow through a problem. Training classes specifically for the new software should be held for two to three days with on-site follow-up visits as required.

- HOTLINE SUPPORT

Support personnel must be available to assist users in the application of new tools especially during the first applications.

- CONTINUING ENHANCEMENTS

Once the initial software is completed and users begin to apply the software to real world problems, additional enhancement will be identified. The authors have found that the consortium normally continues to enhance technology. System improvements requests are a means to communicate problems and questions for resolution.

- USERS GROUP / WORKSHOPS

User groups have been found to be an excellent way of communicating technical approaches and for defining new enhancements required in the software.

Other requisites for successful implementation are

- Ongoing management involvement in the project
- A partnership relationship between users, and consortium members at several levels of responsibility
- Real time computing skills

Technology transfer requirements range from training, user group support and implementation support. The objective is to bridge the gap between research and development and the manufacturing community's acceptance and support.

EXAMPLES OF MANUFACTURING PROCESS SIMULATIONS & TECHNOLOGY IMPLEMENTATION

To illustrate the state-of-the-art in manufacturing process simulations, the following examples in forging and heat treatment are described in detail. Figure 17 illustrates some of the areas that process simulations have been developed for or are being considered. The approach in developing and implementing this technology has been shown earlier in Figure 11.

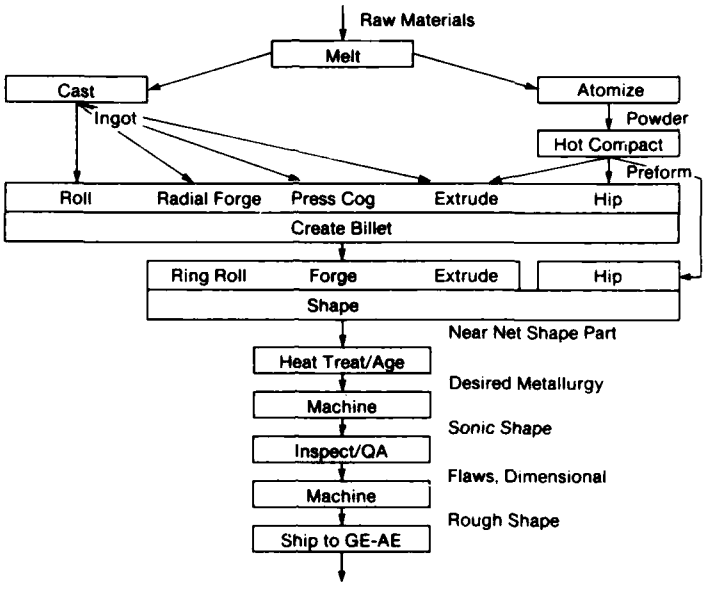

Figure 17
Unit Manufacturing Processes at Vendor Sites

FORGING PROCESS SIMULATION

The key to improving the forging design process - and hence to meeting the business challenges of lower cost and higher productivity - is in understanding exactly what happens in a given process. Computer models provide the necessary information.

The actual trial work of modifying forging die and preform geometry can be significantly reduced. ALPID, (Analysis of Large Plastic Incremental Deformation) a finite element software program developed by the United States Air Force[5] provides an efficient and economical simulation of the forming process. Currently available, the ALPID program examines two-dimensional geometries of visco-plastic materials and the analysis provides vital data on load displacement relationships, metal flow and local process variables such as strain, strain rate, stress and temperature distributions. One can then determine a) whether a part can be formed without internal and external defects and b) the distribution of local material properties and microstructure at different regions in the formed part. ALPID also makes it possible to evaluate die stresses and deflections using standard elastic or elastic-plastic stress analysis programs.

ALPID characterizes the intrinsic workability of the workpiece material so that deformation rates and temperatures are readily identified. Under these specific conditions, called a 'processing window', materials can be fabricated to obtain the fewest defects and best material characteristics possible for the material. The analysis produces material maps which can be used to define the process control algorithm.

Enhancements of the ALPID program have been underway since 1984 at Structural Dynamics Research Corporation (SDRC), under the sponsorship of GE and its forging vendors. These enhancements have improved the program's user-friendliness. They have introduced automatic remeshing, defect tracing throughout the forging process thermal capability for non-isothermal forging process and a relational data base for storing descriptions of material properties.

A second program, for heat treatment simulation called NIKE-C, predicts transient temperatures and resulting thermal stresses, and distortions. It also predicts sag of the workpiece in the heat treating furnace and the potential for cracking of workpieces during furnace heat-up and subsequent quenching. The ability to predict such events is needed to address the increasing difficulties encountered in heat treating nearnet shapes in new materials, such as titanium aluminide and some varieties of Rene 95, which are prone to quench-cracking. NIKE-C is based on the public domain programs NIKE and TOPAZ developed by Lawrence Livermore Laboratories. Like ALPID, NIKE & TOPAZ have been further developed by SDRC under the sponsorship of GE and its forging vendors.

Since simulation reduces costly shop floor experimentation, this leads to reduced manufacturing costs, shorter lead times, improved process controls and better prediction of properties. Role and scope of process simulation in forging process design and its control is shown in Figures 18 and 19.

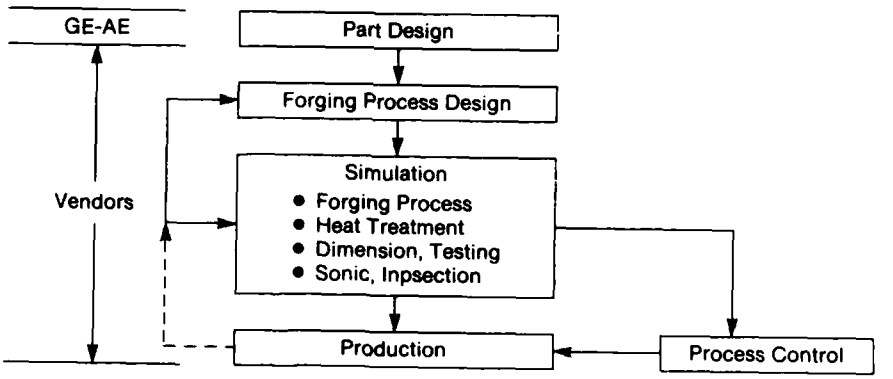

Figure 18
Forging Process Sequence

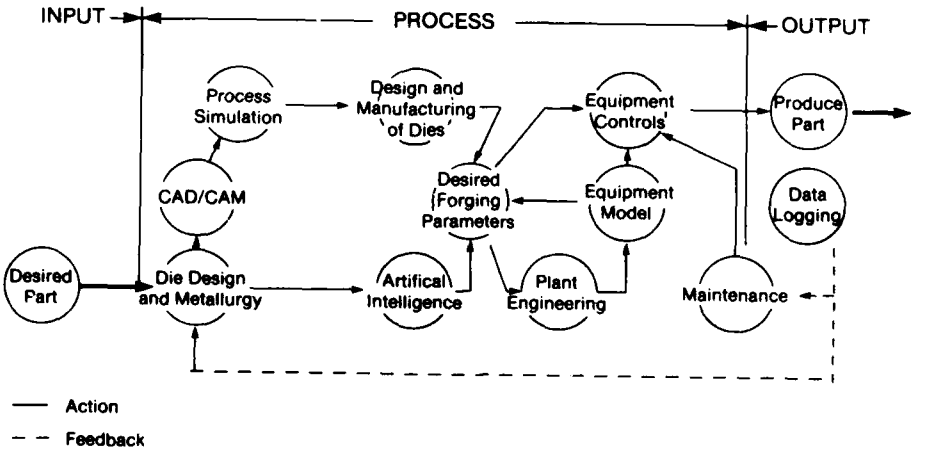

Figure 19
CAE Approach to Forged Component Development and Production

ALPID AND NIKE-C AT WORK

Many GE-Aircraft engine parts have now been modeled to predict metal flow and die filling patterns, the influence of different preform shapes, the strain (or total work) distributions in the finished forging, and die loads for die stress analysis. The simulations have shown areas of potential defects or forging problems, and the flow patterns have revealed the design of better preform shapes.

The application of ALPID to a compressor disk forging is illustrated in this example. The work was done at GE-AE and one of its forging vendors[6].

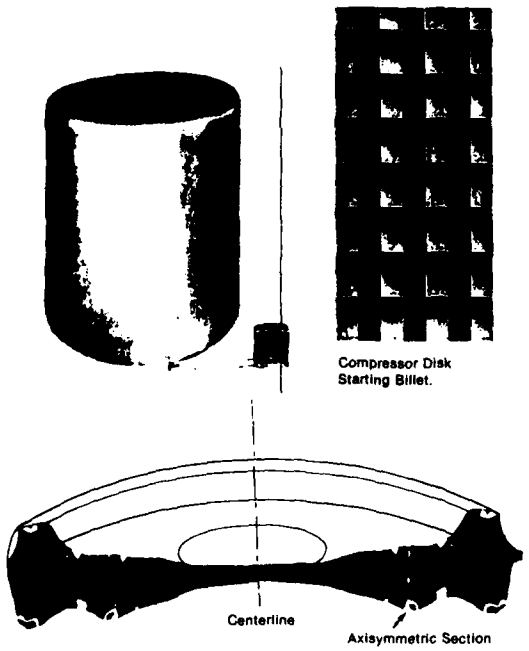

Figure 20
Figure Showing the Starting Billet Shape and the Forged Compressor Disk

Similarly many other critical rotating parts have been simulated at GE-AE and forging vendors to design the process at the front end, solve shop problems and improve product quality.

The results of modeling the disk provide a good example of the ways modeling can improve the forging process.

Figure 20 shows the mesh of alternating colors representing the original billet. Since the billet is symmetrical, only one half *is shown here. The final machined part is shown in Figure 21. The deformation of the orginal mesh to the final forged* shape is shown in Figure 22. The arrows in Figure 23 depict the predicted direction of metal flow. The flow lines provide information for optimizing the ultrasonic inspection plan for the finished part.

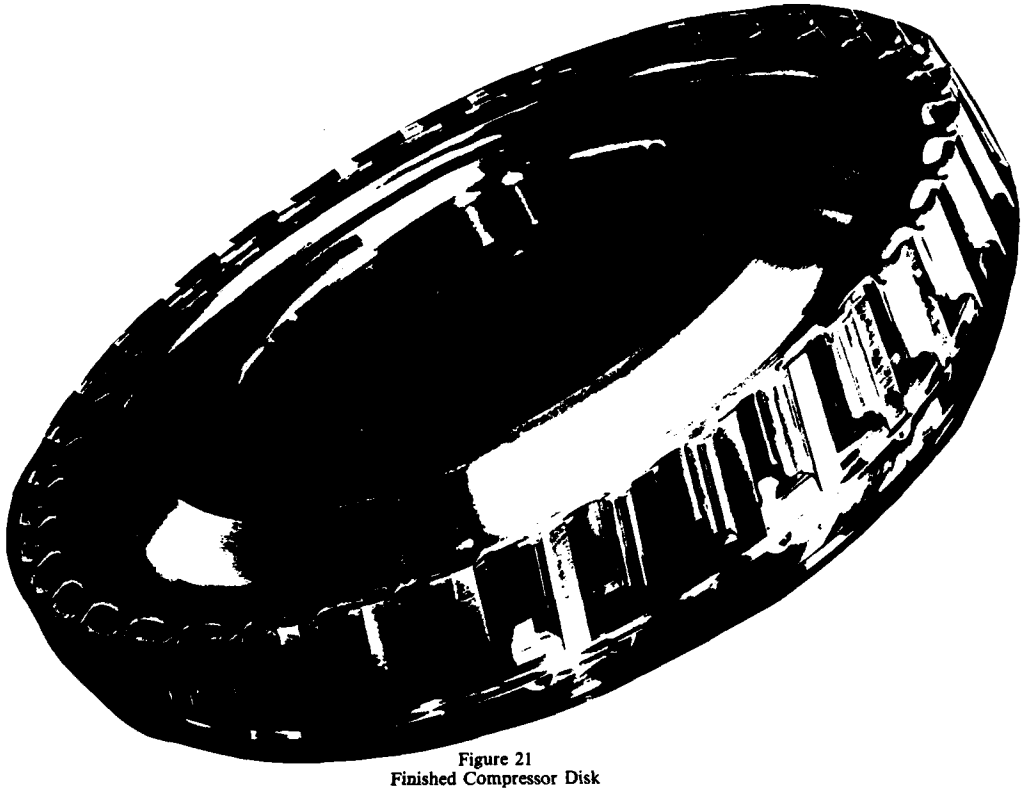

Figure 21
Finished Compressor Disk

In addition to flow pattern and defect movement, the finite element model provided complete information on the distributions of other quantities of interest such as distribution of hydrostatic pressure, total effective strain, the effective stress, and the maximum shear stress in the finished forging. It is desirable to have a compressive hydrostatic pressure to prevent cracking, and the model showed the needed pressure everywhere except at the flash area, which is discarded in any event. The strain distribution indicates the amount of working the different regions of the forging undergo, and in this model strain is within specifications for the compressor disk.

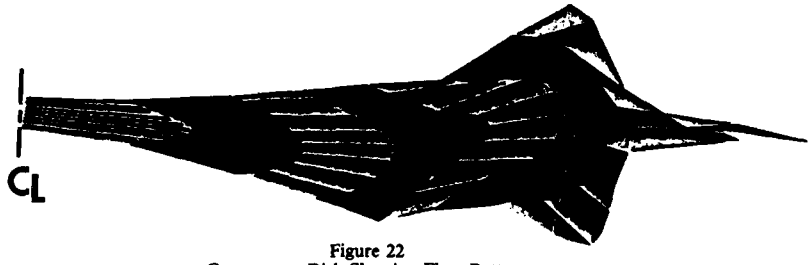

Figure 22
Compressor Disk Showing Flow Pattern

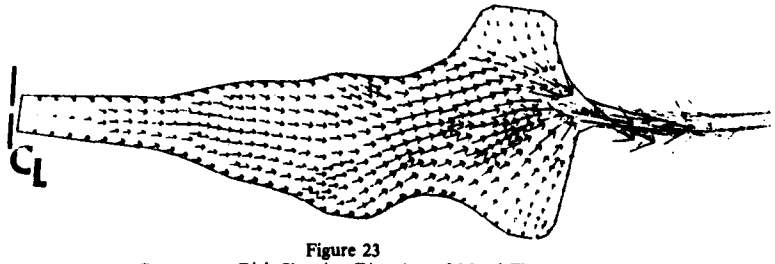

Figure 23
Compressor Disk Showing Direction of Metal Flow

PROCESSING WINDOW & DYNAMIC MATERIAL MAPS

From the ALPID output display, the forging engineer can determine if the die has filled without defects, if the forge press is sized correctly for the process and if the proper processing window (temperature and strain rate) has been reached to achieve the desired quality levels. 'Processing windows' have been defined for selected materials that result in the desired material microstructure as illustrated in Figure 24 for Ti-6242 [7]. If the workpiece temperatures and strain rates are held within the specified limits as predicted by ALPID, the desired material microstructure will result. Changes in blocker shape and process parameters can be evaluated with the ALPID simulation until an acceptable process is developed. Such processing maps have been developed by GE-AE and its forging vendors for several of the alloys used in the jet engines.

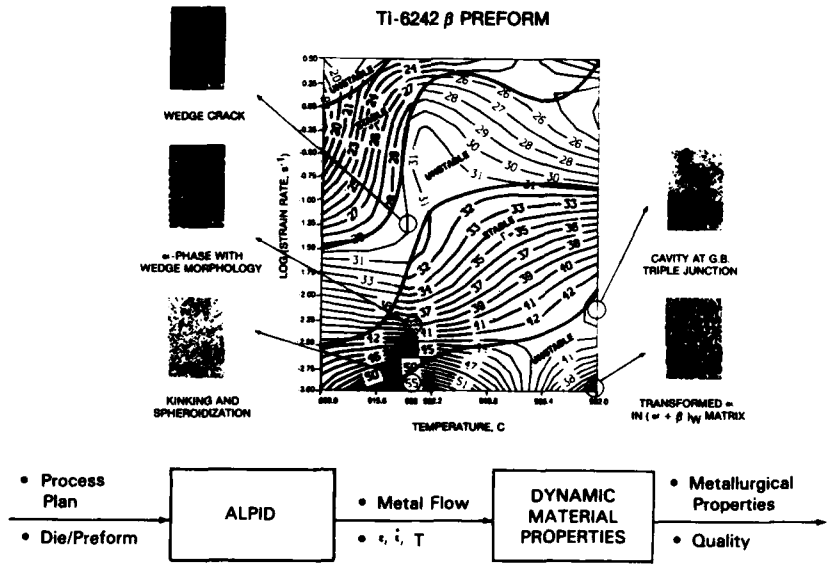

Figure 24
Typical Material Map

DIE STRESS ANALYSIS

Working from the ALPID generated forging forces, the forging engineer next designs the die and evaluates stresses and deflection to insure the die will withstand the forging loads. From a stored solid model library of die blanks, the die geometry can quickly be designed by Boolean operations in the 3-D solid modeler which allows a user to subtract the part geometry from a standard die block. This geometry can then be used to create the NC commands to machine the die. An analysis of the die is then carried out with resulting stresses and deflections presented to the user as illustrated in Figure 25. For an elastic-plastic die analysis, ANSYS or NIKE [8] programs can be used.

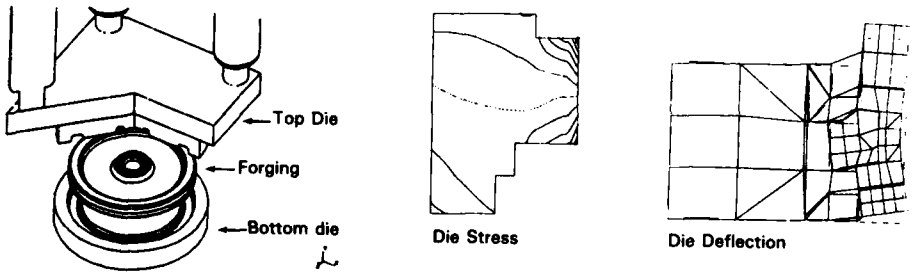

Figure 25
Die Analysis Results

HEATUP AND QUENCHING SIMULATIONS

The manufacturing engineer next specifies the heat treating process for the forged part. Often, near net shaped parts, such as turbine disks, fail during the heat treat because of high thermal stresses developed during quenching or through sagging during furnace heatup. As shown in Figure 26, thin and thick areas in a part cool at different rates which can produce very high stresses. If problems are predicted, the part shape or process can be altered to avoid scraped parts.

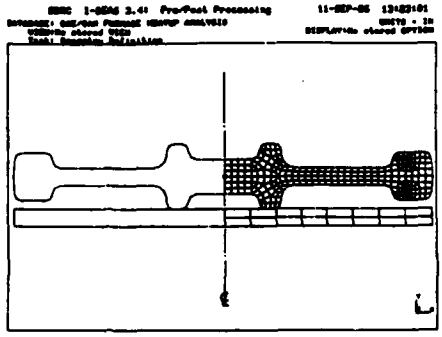

Figure 26
Typical Near Net Shapes

For this simulation, the TOPAZ heat transfer program (used in forging) was coupled with the NIKE structural analysis programs to simulate the furnace heatup and quenching process. During workpiece quenching, a steam or gas blanket develops around the part that controls heat transfer to the quench media. As the part temperature drops the steam or gas blanket thickness changes, and the surface film coefficients change. These temperature dependent film coefficients can be determined experimentally by quenching an instrumented simple cylinder and computing the surface film coefficients with an inverse heat transfer code. These surface film coefficients are then input to the coupled heat transfer / mechanical simulation program. Both stress and distortion due to creep in the furnace during part heatup and during quenching are predicted and displayed to the user as graphical output as shown in Figure 27.

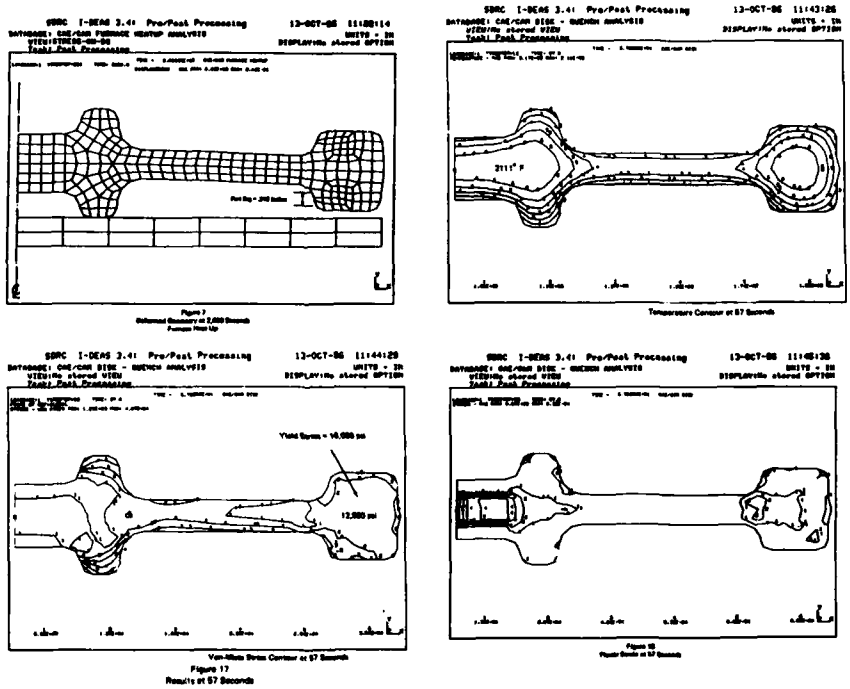

Figure 27
Heat Treat Simulation Results

This simulation is being used by a number of different forging vendors as shown in Figure 28. Real world parts are now being analyzed with the Heat Treat Simulation Program.

Figure 28
An Engineer at a Forging Vendor Using a Computer Terminal, Simulating Heat Treatment

LESSON LEARNED FROM CONSORTIUM

After participating in a number of development consortiums, several significant lessons have been learned. These include:

(1) Set realistic goals
Unrealistically high goals can sometimes be set that result in incomplete programs. It is better to start with a series of smaller programs that are incrementally developed and implemented.

(2) Make management support evident
Everyone on the team must be aware that management stands behind the project and will provide the resources necessary to make it a success. Ongoing management involvement is required.

(3) Put a Champion in Charge
There should be a person in the company who understands and promotes the technology and is able to impart his / her enthusiasm to other members of the implementation team. A champion will see the project through, against all obstacles.

(4) Get the Affected Departments on the Team
The implementation team should have participation from R&D, manufacturing, industrial engineering, quality, metallurgy, tooling, management information system, design engineering etc. Also include system users on the team.

(5) Financial Commitment
Development, training and implementation of a new technology like manufacturing process simulation cannot be done on a shoestring budget. Taking current staff out of day-to-day problem solving is required to effectively train them. Hardware investments in computers and terminals will be required. Initially, it will seem that traditional methods are more effective, but as each new manufacturing problem is solved using process simulations, the pay off will increase until the old traditional methods are discarded.

(6) Not Invented Here (NIH) Syndrome
Consortiums don't work well with individuals that always want to develop technology in-house. Consortiums are best suited, when technology from various sources are brought together, interfaced and enhanced to create new technology. On a general technical basis, the consortium members must work together. Naturally, proprietary information and company specific data should not be disclosed or distributed to the consortium.

(7) Use Best Existing Technology
Consortium members expect results. The authors have found that spending time researching the best available technology and putting together 'modules' of technology is important. DoD programs, National Labs and Universities are all sources of basic technology.

(8) Validation: Use Well Defined Examples
Use simple problems or examples for simulation validation demonstrations. This will help in making believers out of non believers. Also work with people slowly to create confidence and change philosophy away from "we have always done this way" or "this is the only way to do things".

CAE IN MANUFACTURING: STATUS OF IMPLEMENTATION

While the full implementation of CAE for Manufacturing engineering is a major undertaking, there is a phased implementation approach that allows for orderly building and transition of new methods into an organization. The key is to not wait but to start. The recommended approach of getting started and implementing available technology and development where appropriate will significantly improve productivity and advance a company over the one that waits for the entire system to be developed. In fact, the CAE system will never be fully developed but rather will evolve and be enhanced over time.

A suggested phased implementation is shown graphically in Figure 29. This approach has the feature that benefits results after each phase of implementation so that a return on the investment is realized.

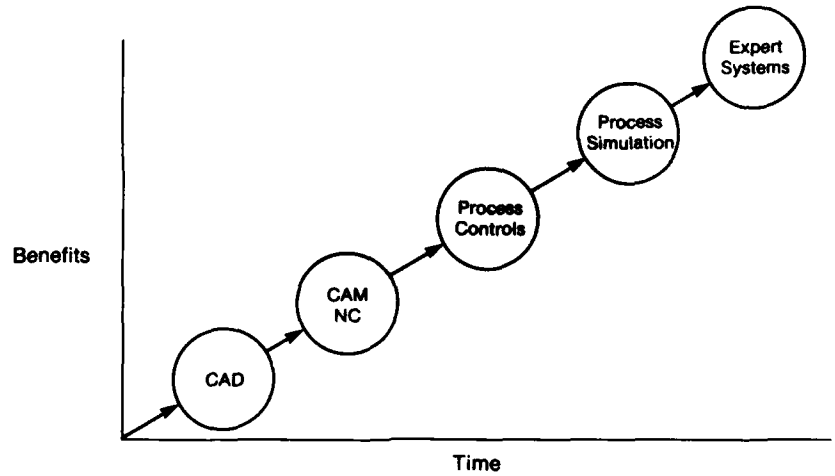

Figure 29
Typical Time Phased Implementation of CAE

CAD, CAM and Process Control tools are commercially available today. Manufacturing process simulations are an emerging technology that will work today closely with controls to permit intelligent, real time response to changes on the shop. In addition, process simulation will interface with Expert System which initially recommend a processing scheme that is evaluated by the simulation with results presented to a diagnostic Expert System for process optimization.

The application of CAD / CAM / CAE is becoming more widespread in forging and casting industries. Computer simulation of forging, die fill, die stress analysis and workpiece heat treating (that predicts the transient, non linear temperature and stresses in the workpiece during furnace heat-up and subsequent quenching) will become a way of life. Aircraft jet engine manufacturers including GE-AE have now started requiring process simulation for selected critical forged rotating parts (such as engine disks) from the forge companies that are bidding on these parts. The simulation information must cover such processes as forging and heat treating.

As a result of the consortium activities at GE-AE, many of its suppliers / vendors have been able to implement these new process simulation tools. Implementation includes; tool development, validation, training, generation of database to execute these tools. As a result, real problems are now being solved.

Process simulation tools are increasingly being utilized, and planned upfront for alloy development, process development, inspection, process control and quality assurance. Many major forgers have started significant activities in process simulation and integrating these with process design, equipment and process control. The trend is that technology starts at one end and propagates down through the entire industry.

In addition to the investment in hardware and software tools, companies must also make an investment in their manpower skills. This investment in people must also be planned, budgeted and managed as completely as the investment in CAE tools. Formal training sessions with user and technical manuals are required to train staff in the use of the new CAE tools.

Even the most skilled people and the most advanced tools must be applied correctly to the right problems to achieve effective results. In practice, this means that companies must focus their investments on strategically important problems. This focus must come from the combined thinking of design and manufacturing engineering, research and market planning people. Real gains can be accomplished through a well balanced mix of new CAE tools and management techniques integrated into a modern manufacturing management system. Achieving concurrent or simultaneous engineering means altering traditional organizational approaches to design and manufacturing. One approach is to create project oriented teams with shared data rather than maintaining traditional functional lines of responsibility.

An important management consideration in implementing the CAE system for manufacturing is that the current organization will need to change.[9] CAE is not the process of automating the current engineering tasks which are often in a different time sequence, and interface with different groups within an organization. A key feature of the new approach is to spend more time and money up-front to make the right decisions in the process design and analysis stage. Managers need to resist the urge to rush to prototype production that often freezes production methods. Design and manufacturing engineers will have to work more closely together, share information, and more importantly, share mistakes with each other. From mistakes knowledge can be gained at the privacy of the computer terminal rather than under the bright lights of the shop floor.

The payoffs or benefits of a CAE system for engineering include:

- Reduced
  - Lead and delivery time
  - Response time to product changes
  - Trial-and-error
  - *Overall costs*
- Improved
  - Productivity
  - Surge capability
  - Material and equipment utilization
  - Process and product characteristics
  - Consistency and quality
  - Inspection procedures
- Higher standardization of design through the creation of a computerized central data base
- Process knowledge rapidly gained through the use of computer simulations

Based on the experience of the authors, the constant dollar cost of manufacturing a component normally drops with time as improvements are made and experience is gained as shown in Figure 30. With the use of CAE, manufacturing costs fall much faster since experience is gained sooner through computer simulations.

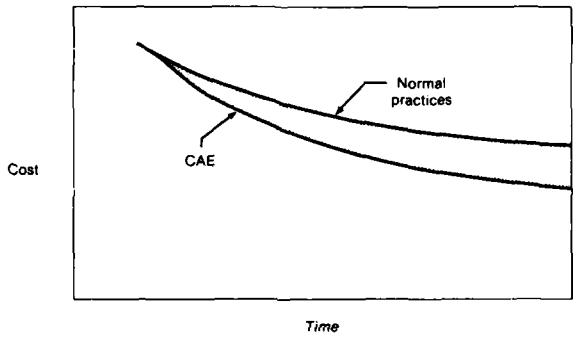

Figure 30
Cost to Develop a Component Process With and Without CAE

The process development time savings potential is even more impressive as shown in Figure 31. The processes of the future can be run, evaluated and changed through process simulations today.

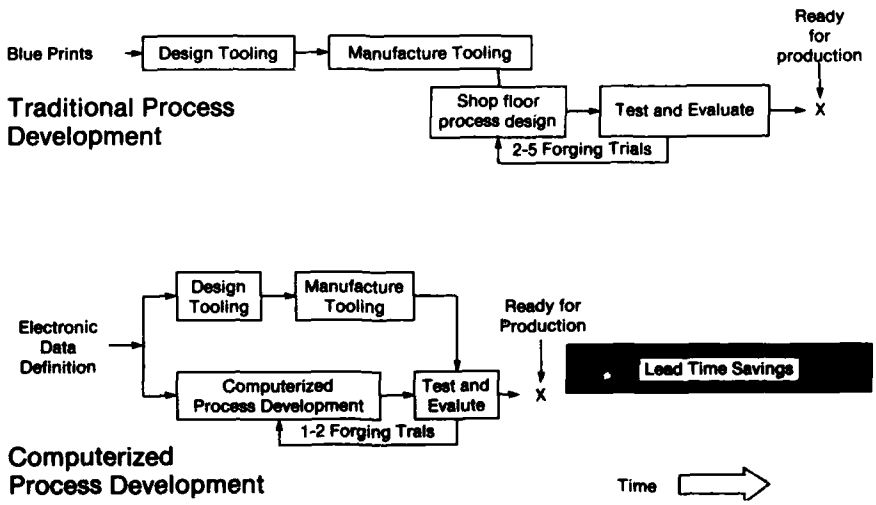

Figure 31
Time to Develop A Component Process With and Without CAE

REFERENCES

(1) Skinner, W., 'Manufacturing; The Formidable Competitive Weapon, John Wiley & Sons, 1985

(2) MACH3, March / April 1987 - GE-AE Publication pp 2-4.

(3) DeVor, R.E., Kapoor, R., Hayashida and Subramani, G., Proc. of the 14th North American Manufacturing Research Conference, 1986 pp 535-542).

(4) Manufacturing Week, July 20, 1987, Page 17

(5) Altan, T., Oh, S., and Gegel, H., 'Metal forming. Fundamentals and Applications', American Society for Metals, Metals Park, Ohio 1980 pp 220-223.

(6) Srivatsa, S., The Leading Edge, a GE-AE Publication, Winter 1986 / 87, pp 4-9.

(7) Prasad, Y., Gegel, H., et. al. 'Modeling of Dynamic Material Behavior Hot Deformation: Forging Ti-6242', Metallurgical Transactions A, Vol. 15A October 1984

(8) Hallquist, J.O., 'NIKE 2-D a vectorized, Implicit Finite Deformation, Finite Element Code for Analyzing the Static and Dynamic Response of 2-D Solids', Lawrence Livermore National Laboratory, February 1983.

(9) Marks, P., 'Managing Computer-Aided Engineering Technology', AMA Managment Briefing, 1983.

INTRODUCTION INDUSTRIELLE DE LA MODELISATION DE SIMULATION DE PROCEDES EN FORGE ET FONDERIE AERONAUTIQUE

par

Eric Bachelet et Yves Honnorat
SNECMA — Direction Technique
BP 81
91003 Evry Cedex
France

1. INTRODUCTION

La SNECMA a entrepris, depuis environ dix ans, le développement de programmes de modélisation de la solidification équiaxe des aubes de turbine en superalliages moulés sous vide, obtenues par le procédé de fonderie en cire perdue. Ce développement faisait partie d'une approche globale du procédé visant à en réduire le caractère empirique qui se manifestait par des taux de rebuts de pièces pour raisons métallurgiques - taille de grains, microporosité ... - fluctuants ; les causes de ces rebuts n'apparaissaient pas toujours clairement et étaient assignées tantôt à la matière de base des pièces et donc au choix des alliages ou à leur élaboration défectueuse, tantôt à une mise au point des gammes de fabrication incorrecte ou trop "sensible", tantôt à une mauvaise application de ces gammes en atelier par suite de dérives des équipements ou des pratiques opératoires.

Il était espéré qu'une approche combinant :

- une meilleure connaissance des phénomènes physico-chimiques, alors mal connus, notamment des réactions de phase se produisant dans l'intervalle de solidification, par des études de base engagées par ailleurs,

- la modélisation de l'évolution thermique et du déroulement de la solidification dans les pièces,

permettraient de cerner les causes des fluctuations de la qualité et d'y apporter remède.

Cette approche s'étant révélée féconde, SNECMA l'a étendue à la modélisation de la solidification dirigée, puis à la modélisation du forgeage et du traitement thermique des pièces forgées en se donnant un objectif supplémentaire : celui d'économiser sur les coûts et les délais de mise au point de pièces en tirant parti de la possibilité de simuler rapidement l'influence de différents paramètres de fabrication. Concrètement ces objectifs impliquaient le développement de modèles capables non seulement du calcul des grandeurs physiques, telles que température, déformations, remplissage des moules et matrices etc..., mais également de la prédiction des microstructures (taille de grain, ségrégations, ...) et des paramètres et défauts métallurgiques (écrouissage, porosités, ...) associés.

L'exposé qui suit ne vise pas à présenter des logiciels ou des résultats particuliers, mais à analyser certaines des difficultés rencontrées pour disposer d'un outil industriel opérationnel, à examiner comment la modélisation peut s'insérer dans un processus industriel de mise au point de pièces et d'une manière générale à illustrer l'intérêt de ces méthodes en forge et fonderie de pièces aéronautiques elle s'adresse tant à des spécialistes travaillant au développement de codes de calculs.le plus souvent en milieu universitaire,qu' à des responsables industriels confrontés à des problèmes de développement et de fabrication.

2. L'OBTENTION DE DONNEES MATERIAUX

Une exploitation réaliste des modèles de simulation en fonderie et en forge de pièces aéronautiques requiert la connaissance de données thermiques, ainsi que du comportement mécanique, physico-chimique et métallurgique des pièces à créer mais aussi des moules, des matrices et de leurs interfaces. Les tableaux I et II illustrent les principales données nécessaires à une modélisation étendue. Cet aspect de la modélisation souvent considéré a priori comme trivial, pose des problèmes de divers ordres :

- une partie des données à obtenir - la plus petite - concerne des grandeurs bien définies mesurées par des méthodes classiques pour lesquelles les seules difficultés rencontrées trouvent leur source dans les températures en général élevées en cause : chaleurs massiques, coefficients de dilation etc..., de matériaux solides homogènes tels que les alliages à couler ou à forger, les matériaux de matrices ou de moules ...Ces températures atteignent couramment 1500°C en fonderie de superalliages et environ 1150°C en forge.

  Même dans ces cas simples, la performance des modèles est directement liée à une réflexion dans la préparation des mesures, qui doit s'appuyer sur une bonne connaissance du procédé.

Ce point peut être illustré en fonderie de précision par le cas de caractéristiques thermiques des matériaux réfractaires constituant les moules carapaces et leur emballage ; ces carapaces sont réalisées à partir d'un empilement de couches de grains de céramiques obtenu par des opérations successives de trempé en barbotines et de saupoudrage qui font ensuite l'objet d'un frittage ; la structure résultante est de type composite (cf figure 1) : les deux premières couches internes du moule plus réfractaires et de structure plus fine que les couches de renfort constituent une zone de faible épaisseur (≈ 1 mm) par rapport à l'épaisseur des couches de renfort (≈ 4 mm) et dans un premier temps, on peut être tenté de négliger cette hétérogénéité par souci de simplification des mesures (et du modèle). Or, il est connu des praticiens que la nature des premières couches peut considérablement influer sur le remplissage des moules et sur les structures métallurgiques finales des pièces coulées. De fait, des mesures effectuées à la SNECMA visant à caractériser thermiquement différents types de couches, montrent qu'on peut avoir des variations dans un rapport 1 à 4 entre les conductivités thermiques des différents types de premières couches et d'1 à 2 entre leurs diffusivités. Il y a bien lieu de considérer les carapaces comme des matériaux composites et de les caractériser en conséquence au prix de difficultés expérimentales. L'intérêt de la démarche de modélisation est dans ce cas de susciter une analyse quantitative du rôle de paramètres appréhendés jusqu'alors empiriquement. Cette analyse quantitative peut servir ensuite de guide à une évolution ultérieure du procédé.

- Une mention doit être faite des données de fonderie concernant le métal liquide, caractéristiques thermiques, viscosité ..., qui compte-tenu des températures en cause posent de grandes difficultés pratiques de mesure. La principale d'entre elles, la chaleur latente de solidification peut être obtenue en exploitant des résultats d'analyse thermique différentielle. Les autres nécessitent des instrumentations de moule très délicates et onéreuses (cf figure 2), voire des montages spécialisés d'expériences nécessitant un matériel, des éprouvettes et une technique expérimentale dont les délais d'acquisition se chiffrent en années.

  - pour certaines données essentielles, les mesures effectuées intègrent des phénomènes complexes de nature hétérogène : leur significativité pose alors problème. Cet obstacle est rencontré par exemple dans la prise en compte du frottement en forgeage à chaud ; les ébauches sont revêtues d'un revêtement protecteur et lubrifiant qui se déforme en cours de forgeage. Des coefficients de frottement peuvent être mesurés par le "test de l'anneau" à partir d'un écrasement qui permet de suivre l'évolution de la forme d'un anneau réalisé dans le métal à forger et revêtu de manière représentative. Une analyse mécanique de cet essai montre que le champ de vitesses de glissement et de contraintes à l'interface anneau-matrice est fortement hétérogène ; l'examen d'anneaux après forgeage indique que la distribution de lubrifiant est elle même fortement hétérogène : un film d'épaisseur intiale uniforme peut conduire à des zones de contact sec voisines de zones avec accumulation de lubrifiant (cf figure 3). La mesure du coefficient de frottement ne donne accès qu'à une expression moyenne de ce comportement. On peut penser que l'incidence de cette approximation sur des grandeurs telles que l'effort de forgeage sera faible, mais qu'en revanche la précision des écoulements et des contraintes locales dans certains zones de singularité de forme souvent associées à la formation de défauts pourra être biaisée. Il est clair qu'il n'existe pas de solution simple satisfaisant à ce problème ; une réflexion sur la représentativité des données matériaux doit dans ce cas éclairer sur les limites du modèle.

  - les données relatives à la prédiction des structures et des défauts métallurgiques qui constitue un des objectifs important des modèles en forge et en fonderie, sont les plus difficiles à établir. En fonderie d'aubes de turbine, les structures métallurgiques dépendent des paramètres thermiques locaux en cours de solidification, gradient et vitesse de solidification, auxquels il faut ajouter en fonderie équiaxe l'efficacité des germinants. En forge, elles sont déterminées par les structures métallurgiques initiales et le chemin thermo-mécanique local jusqu'au refroidissement après forgeage ; dans ce dernier cas, la microstructure "instantanée" peut régir le comportement mécanique du matériau de manière suffisament sensible pour qu'il soit utile de considérer le couplage entre ces deux facteurs. En cas de couplage fort cette prise en compte devient indispensable. Même dans le cas d'une microstructure peu évolutive on conçoit que dans ce cas les données matériaux doivent être constituées d'ensembles complexes incorporant de nombreuses informations de caractère semi-empirique et de lois physiques. S'il n'y a pas de couplage entre la microstructure et les phénomènes simulés dans le modèle de base, on a intérêt à dissocier ces aspects de prédiction de microstructures et des défauts qui demeurent aujourd'hui souvent rudimentaires, dans des annexes ou des sous-programmes du modèle de base.

On retiendra de cet examen des données matériaux nécessaires à la modélisation que les études visant à leur obtention constituent une tâche essentielle dont le coût sera au moins égal à celui de la création des programmes de calcul à la base du modèle. La réflexion sur ces programmes doit être menée par des ingénieurs ayant une bonne connaissance des procédés modélisés. Cette réflexion quand elle est bien menée, permet de cerner certaines limites des modèles : une des premières applications de ceux-ci consiste d'ailleurs à réaliser des tests de sensibilité aux données matériaux afin de déterminer où doivent porter les efforts de caractérisation.

3. VARIABILITE ET COMPLEXITE DU PROCEDE

Les concepteurs de modèles visent en général à la prise en compte la plus étendue possible des phénomènes physiques intervenant dans le processus simulé dans un souci d'exactitude et de précision des prévisions : il convient toutefois de bien réaliser qu'une modélisation est une approximation issue de choix qui ne sont pas toujours satisfaisants, valable dans des conditions qui peuvent être étroites.

L'ingénieur d'études de procédés soucieux d'effectuer une modélisation réaliste rencontre souvent des difficultés dans le choix des conditions initiales et aux limites et dans l'évolution de ces dernières dans le temps ; ces difficultés peuvent provenir de deux sources :

- l'une réside dans la variabilité des conditions réelles dans lesquelles sont effectuées certaines opérations, cette variabilité étant généralement estimée admissible voire inévitable par les praticiens en l'état de l'art du procédé.

- l'autre provient de la complexité de certaines phases du processus qui peut rendre leur modélisation peu praticable ou non fiable et donc inciter à une simplification abusive du modèle.

Ces deux points peuvent être illustrés par une discussion sur le choix de l'origine des temps et des conditions initiales en solidification équiaxe d'aubes de turbine. Dans ce procédé, les moules sont pré-chauffés dans un four à l'air à une température généralement comprise entre 900°C et 1100°C, puis transférés au travers d'un sas dans une enceinte sous vide où la coulée a lieu. Le temps s'écoulant entre la sortie du moule du four de préchauffe et le déclenchement de la coulée proprement dite est de l'ordre d'une minute mais peut varier de plusieurs dizaines de secondes :

- certaines opérations élémentaires du transfert sont assurées manuellement par un opérateur et donc sujettes à variabilité.

- le déclenchement de la coulée n'est effectué qu'après atteinte d'un certain nombre de conditions :

  . niveau de vide dans l'enceinte de coulée,
  . niveau de température du métal liquide ...

  elles mêmes sujettes à des variations pour de multiples causes.

La température effective du moule au moment de la coulée dépend des aléas mentionnés ci-dessus. La coulée proprement dite est, elle, un processus automatique étroitement contrôlé en durée (de l'ordre de quelques dixièmes de secondes), et en débit instantané, les fondeurs sachant que la moindre variabilité à ce stade peut se traduire par des défauts inacceptables de remplissage du moule.

Les conditions pratiques de la coulée étant celles que nous venons de passer en revue, il faut s'interroger sur la façon de les intégrer dans un modèle de solidification. Le moment de la sortie du moule du four de préchauffe est celui où le moule étant à une température uniforme spécifiée, les conditions initiales sont les mieux définies. Démarrer la simulation à ce stade requiert toutefois de simuler un processus de refroidissement du moule dans l'air puis sous vide, donc d'en spécifier la durée, puis à partir du champ de températures hétérogènes obtenue, de simuler le remplissage du moule par le métal liquide.

Or ce processus est très complexe : la géométrie des canaux dans lesquels s'écoule le métal est compliquée, leur section peut être faible, et les écoulements ont lieu en parallèle compte tenu de la multiplicité des amenées de métal qu'il est en général nécessaire de ménager sur une même pièce. D'autre part les échanges thermiques au cours du remplissage peuvent être déterminants pour l'écoulement proprement dit : la différence de températures entre moule et métal liquide est de plusieurs centaines de degrés, ces températures respectives se situant de part et d'autre de l'intervalle de solidification ; les flux extraits à la paroi du moule sont donc relativement importants ; compte tenu des vitesses d'écoulement du métal liquide et de la faiblesse des sections des canaux, l'extraction de chaleur en paroi influe très notablement sur l'évolution de température du métal et sur sa viscosité.

Dans ces conditions, un calcul avec couplage hydrodynamique et thermique s'avère très délicat (ce qui n'est pas le cas pour des pièces de plus grandes dimensions ou de géométries moins complexes). Ces considérations conduisent à prendre, pour origine du temps de la simulation, la fin du remplissage du moule. Un champ complexe de températures initiales doit alors être spécifié ; il peut bien sûr être obtenu par instrumentation de moules en fonderie, mais ceci est contradictoire avec l'objectif d'économies sur la durée et le coût de la mise au point et ne peut être réalisé que dans quelques expériences dont les résultats doivent être transposés à d'autres configurations.

Que peut donc apporter la modélisation dans un tel cas ?

- tout d'abord, un effort d'analyse des conditions réelles d'opération en atelier (et non celles des gammes spécifiées) afin de déterminer les séquences du processus qui seront modélisées et de leur spécifier des conditions initiales et aux limites.

- la possibilité d'effectuer des simulations de l'influence des conditions initiales et aux limites qui permettent d'analyser les mécanismes de variations dans les performances du procédé ; dans l'exemple précédent on pense aux champs de températures initiales que des mesures en atelier permettent de mesurer en fonction du temps de transfert entre four de préchauffe et début de la coulée,

- enfin, une incitation puissante à une meilleure définition des conditions opératoires en atelier, réalisée au mieux par l'implantation d'outils automatisés dont les paramètres de fonctionnement soient surveillés. Les résultats de simulation constituent des arguments particulièrement convaincants dans la mesure où ils offrent la possibilité d'isoler l'influence de causes particulières.

4. INDUSTRIALISATION DES MODELES

Un examen de l'intérêt à transformer un modèle en outil opérationnel dans un contexte de production passe par un bref rappel du processus de préparation et de mise au point des gammes de fabrication, des difficultés opérationnelles rencontrées et des conditions imposées, difficultés et conditions spécifiques du cas pratique qui se pose et que nous illustrerons par des exemples tirés de la forge et de la fonderie de précision de pièces de moteurs aéronautiques.

- Processus de mise au point des gammes

Le metteur au point a un objectif général - définir des conditions de fabrication économiques de pièces répondant aux spécifications du client qui doit conduire à deux résultats : le dessin d'outillages (moules de noyaux et d'injection, de cires, matrices de forge ...) et la définition du processus opératoire et des paramètres de fabrication associés.

Les spécifications concernent la géométrie des pièces à obtenir ainsi que leur qualité métallurgique : selon le type de pièce à produire l'accent peut être remis sur l'un ou l'autre de ces aspects :

. En fonderie d'aubes de turbine, la veine des aubes et leurs cavités internes le cas échéant, sont obtenues directement en fonderie avec de grandes exigences de précision (tolérances d'environ ± 0,15 mm pour l'enveloppe de la pièce) ; les exigences de qualité métallurgique sont également sévères au moins pour les aubes mobiles très sollicitées : elles concernent la structure cristalline, la taille des grains en fonderie équiaxe, la distribution de microporosité, éventuellement la distance entre branches de dendrites secondaires, l'absence de microfissures de retrait à chaud ... et dans ces conditions, l'intervalle admissible de conditions de coulée est souvent étroit.

. En forge de précision, les défauts sont plutôt associés à la géométrie des pièces et à la reproductibilité des tolérances dimensionnelles spécifiées par les aérodynamiciens : La maitrise de la forme dépend entièrement du forgeron tandis que la qualité métallurgique des pièces résulte largement de celles des demi-produits approvisionnés par la forge.

. En forge de grosses pièces (disques ...) les exigences sont essentiellement d'ordre métallurgique, conséquence de l'étroite relation entre les caractéristiques mécaniques acceptables et la structure métallurgique de ces pièces : on cherche à optimiser des structures métallurgiques garantes de durées de vies et dépendant étroitement des conditions de forgeage. Ces pièces sont toujours entièrement usinées et l'obtention géométrique des bruts pose en général peu de problèmes.

Il faut noter que la géométrie des pièces autrefois représentée sur des plans de papier, est maintenant de plus en plus systématiquement-au moins pour les pièces de formes complexes comme les aubes - fournie aux Méthodes de Fabrication sous forme mathématique obtenue directement dans le cadre d'un processus de conception et de dessin assisté par ordinateur (système CATIA ...) : sections définies par points et surfaces décrites par des fonctions d'interpolation entre sections, dans un référentiel convenu. Les Méthodes de Fabrication vont elles-mêmes concevoir et dessiner les outillages pour ces pièces à partir du même type de méthodes assistées par ordinateur.

Aux objectifs concernant les pièces elles-mêmes, s'ajoute celui de production économique : il conduit à prendre en compte entre autres le coût de la matière mise en oeuvre, le nombre et la nature des opérations d'atelier, leur productivité (nombre de pièces dans un moule ...), le coût des outillages. Ce dernier point peut être déterminant pour l'économie du procédé : c'est le cas en forgeage isotherme de disques de superalliages avec l'utilisation de matrices en alliages à base de molybdène dont le coût d'achat actuel est d'environ 7.000 francs le dm^3 ; dans un tel cas, le metteur au point doit alors impérativement définir une gamme conduisant à des sollicitations admissibles sur les outillages.

En toute hypothèse, la mise au point va être un processus itératif complexe dans lequel la modélisation peut être source de réduction de coût et de délais en permettant d'éviter la création d'outillages inadaptés et de limiter les essais en atelier.

A quelles exigences concernant les modèles cela conduit-il ?

- Commodité d'emploi des programmes

Les techniciens responsables de la mise au point des pièces n'ont pas, sauf exception, reçu de formation poussée en informatique ni en sciences des matériaux. Les modèles développés dans les organismes de recherche doivent souvent être révisés pour rendre leur exploitation simple voire "conviviale". Ces caractères impliquent :

. Une bonne structuration des programmes isolant par modules distincts les entrées et sorties selon leurs fonctions et articulant clairement les logiciels d'exploitation : données matériaux, géométrie, conditions initiales et aux limites ; les choix concernant les données brutes à stocker doivent apparaître simplement : variables, fréquence des pas de temps ...

. des procédures de dialogue guidant l'utilisateur

. des modules de post-traitement permettant une bonne visualisation des résultats : traceurs de courbes, coupes de pièces avec ligne d'iso-valeurs, perspectives...

- Existence d'interfaces simples pour générer des maillages volumiques

La plupart des programmes de modélisation résolvent les équations complexes qui régissent les phénomènes pris en compte par des méthodes numériques de type éléments finis ou différences finies. Ceci passe par la création d'un maillage de la pièce à modéliser. La modélisation ne requiert pas en général une précision dans la définition des surfaces extérieures aussi grande que celle demandée par le client, et les surfaces extérieures peuvent sans dommage être assimilées à des succession de facettes planes. Dans le cas de modèles bi-dimensionnels (forgeage de pièces axisymétriques par exemple) la création de maillage ne pose aucune difficulté. En revanche, la création de maillages de pièces tridimensionnelles complexes telles que des aubes dont les géométries sont décrites mathématiquement est, en l'absence de mailleurs automatiques, une opération extrêmement lourde. Ce point est d'autant plus important que les itérations de mise au point peuvent conduire à reprendre partiellement les maillages : c'est le cas en modélisation de la solidification d'aubes ou on est par exemple amené à modifier le nombre et la position des attaques de coulée, la géométrie des pièces, l'emballage local .... La modélisation ne peut etre considérée comme opérationnelle que si elle permet de réaliser rapidement des itérations, ce qui exige de disposer de systèmes de maillage interfacés avec les programmes de conception assistés par ordinateur d'outillages.

- Optimisation des algorithmes de résolution

Les phénomènes modélisés en forge et en fonderie sont instationnaires et les systèmes d'équations qui les régissent non linéaires : ceci conduit a des temps de calcul et des coûts de modélisation élevés ; c'est particulièrement le cas pour les modèles tridimensionnels compte tenu des géométries complexes des systèmes étudiés. Les efforts entrepris pour optimiser les algorithmes de résolution sont donc à poursuivre vigoureusement.

5. CONCLUSION

La revue des problèmes rencontrés dans l'industrialisation de programmes de modélisation en forge et en fonderie aéronautique indique clairement qu'ils sont encore loin de constituer des outils banalisés de mise au point de gammes de pièce. Il apparait d'une manière générale que la fécondité des modèles est en proportion directe de la richesse de la base de données et des analyses physico-chimiques qui les supportent. Les difficultés mises en évidence trouvent leur source pour une part dans la complexité des procédés à simuler et pour le reste dans celle des géométries traitées. Ce dernier obstacle devrait être levé avec le développement de mailleurs tri-dimensionnels performants.

Les bénéfices de la modélisation justifient néanmoins déjà largement les investissements qu'elle représente et la SNECMA qui travaille dans ce domaine depuis une décennie tire largement profit en production des aspects suivants :

- incitation à une analyse fine des procédés

- possibilité de réaliser des études de sensibilité à certains des paramètres de fabrication,

- possibilité de dimensionner ou d'optimiser des équipements (capacité des presses de forgeage, configuration thermique des fours de solidification dirigée),

- moyen efficace pour resserrer et automatiser les conditions de fabrications.

C'est dans le domaine de la grosse forge de pièces axysimétriques que l'intégration de la modélisation est la plus avancée. Les retombées qu'elle permet d'obtenir dans le dimensionnement des matrices la rendent indispensable dans le cas du forgeage isotherme.

TABLEAU 1

DONNEES NECESSAIRES POUR LES MODELES DE SOLIDIFICATION

1.	PREVISION DE L'EVOLUTION DES TEMPERATURES DE LA FRACTION SOLIDE	
	. DONNEES THERMIQUES (MODELES THERMOCINETIQUES SIMPLES)	
	ALLIAGE	- CONDUCTIVITÉ THERMIQUE - CHALEUR MASSIQUE - DÉGAGEMENT DE CHALEUR LATENTE DANS L'INTERVALLE DE SOLIDIFICATION
	MOULE CERAMIQUE	- CONDUCTIVITÉ - CHALEUR SPÉCIFIQUE - EMISSIVITÉ
	MATERIAU D'EMBALLAGE	- CONDUCTIVITÉ (INTÉGRANT LA SEMI-TRANSPARENCE EN RAYONNEMENT) - EMISSIVITÉ - EVENTUELLEMENT COEFFICIENT DE TRANSFERT
	NOYAU	- CONDUCTIVITÉ THERMIQUE - CHALEUR MASSIQUE
	INTERFACES	- COEFFICIENT DE TRANSFERT MÉTAL-SOLE ET MOULE-SOLE EN SOLIDIFICATION DIRIGÉE
	. DONNEES PHYSICO-CHIMIQUES	- SOLIDIFICATION
	ALLIAGE	- EVOLUTION DE LA FRACTION SOLIDE EN FONCTION DE LA TEMPÉRATURE
2.	DONNEES RHEOLOGIQUES (CAS DE MODELISATION THERMOCINETIQUE ET HYDRODYNAMIQUE COUPLEE)	
	ALLIAGE	- VISCOSITÉ
3.	PREVISION DE LA QUALITE ET DES STRUCTURES METALLURGIQUES	
	. TAILLE DE GRAINS EN FONDERIE EQUIAXE	: MODÉLISATION DIFFICILE. L'EFFICACITÉ DES GERMINANTS DÉPEND DES CONDITIONS THERMIQUES, HYDRODYNAMIQUES ; SEULE APPROCHE PRATIQUE : DES CRITÈRES SEMI-EMPIRIQUES.
	. TAILLE DE LA STRUCTURE DENDRITIQUE	: RELATIONS EMPIRIQUES λ_P (VS, GS) EN SOLIDIFICATION DIRIGÉE ; λ_S (V_R, MATURATION EN SOLIDIFICATION ÉQUIAXE)
	. MICROPOROSITE EN FONDERIE EQUIAXE	: MODÉLISATION INTÉGRALE DIFFICILE, PERMÉABILITÉ DU RÉSEAU DENDRITIQUE EN COURS DE SOLIDIFICATION, RETRAITS DE SOLIDIFICATION DÉPENDANCE DES OLIGO-ÉLÉMENTS - RELATIONS EMPIRIQUES PLUS FACILES.
	. MICROPOROSITE EN SOLIDIFICATION DIRIGÉE	: - MICROPOROSITÉ RÉPARTIE : DIMENSION RELIÉE PAR UNE RELATION EMPIRIQUE À LA TAILLE DE LA STRUCTURE DENDRITIQUE PRIMAIRE - MICRORETASSURE : CRITÈRES EMPIRIQUES
	. FORMATION DE FISSURES A CHAUD	: - COEFFICIENT DE DILATION - MODULE D'ÉLASTICITÉ - CRITÈRES DE RUPTURE

TABLEAU II

DONNEES NECESSAIRES POUR LES MODELES DE FORGEAGE

1. PREVISION DES ECOULEMENTS		
• **DONNÉES THERMIQUES**		
ALLIAGE FORGE (BASE Ti OU Ni)	- CONDUCTIVITÉ THERMIQUE	
	- CHALEUR MASSIQUE	
	- EMISSIVITÉ TOTALE OU COEFFICIENT DE TRANSFERT THERMIQUE AVEC LE MILIEU EXTÉRIEUR.	
MATERIAUX POUR MATRICES (ACIER, BASE Ni OU Mo)	- IDEM	
• **DONNÉES MÉCANIQUES**		
ALLIAGE FORGE	- LOI DE COMPORTEMENT RHÉOLOGIQUE LE PLUS SOUVENT VISCO-PLASTIQUE NON COUPLÉE AVEC LA MICROSTRUCTURE	
INTERFACE PIECE MATRICES	- LOI DE FROTTEMENT	
2. PREVISION DE LA QUALITE METALLURGIQUE DES PIECES FORGEES		
- LOI D'EVOLUTION DE LA MICROSTRUCTURE	- EXEMPLE : SEUIL DE RECRISTALLISATION ε ($\dot{\theta}$) ET ÉVOLUTION DE LA TAILLE DE GRAIN AVEC LA MICROSTRUCTURE. UN COUPLAGE RHÉOLOGIE MICROSTRUCTURE PEUT ÊTRE ACQUIS.	
- CRITERES D'ENDOMMAGEMENT	- FISSURATION - CAVITATION	RELATION ENTRE L'APPARITION DE CES PHÉNOMÈNES ET DES GRANDEURS MÉCANIQUES
3. PREVISION DE LA DUREE DE VIE DES OUTILLAGES		
MATERIAUX POUR OUTILLAGES	- COEFFICIENT DE DILATATION - MODULE D'ÉLASTICITÉ - CRITÈRES DE RUPTURE FRAGILE - COURBES DE FATIGUE THERMIQUE	

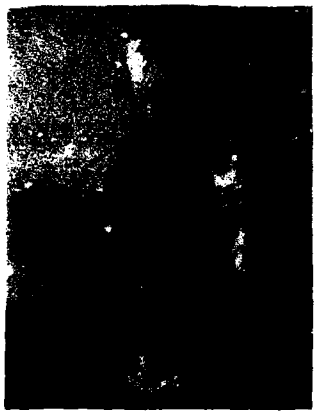

Figure I - Grappe de coulée en cire perdue instrumentée pour la mesure des évolutions de température en cours de coulée et solidification.

Figure II - Coupe micrographique d'une carapace céramique pour fonderie de précision

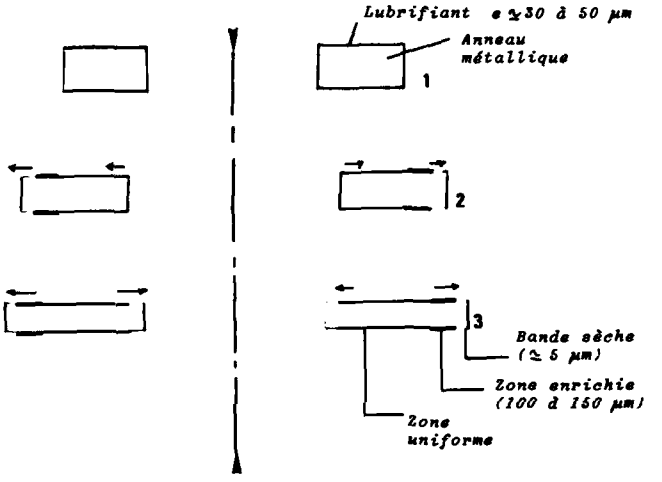

Figure III - Evolution d'un anneau et des couches de lubrification au cours d'un essai d'écrasement en conditions isothermes

AN APPLICATION OF COMPUTER MODELLING TO ISOTHERMAL FORGING

by
P.S. Bate
Inco Engineered Products Ltd.
Wiggin Street,
Birmingham. B16 0AJ
England.

Summary

In isothermal forging the workpiece is maintained at a reasonably constant temperature throughout the deformation. This involves having the forging dies at the workpiece temperature, and removes a major constraint on the forging process by allowing slow deformation. This permits the forming of materials considered difficult, or even impossible, to forge conventionally, to shapes which minimise the amount of material to be removed in subsequent operations and with controlled microstructural development during the deformation.

Because the dies must withstand high temperatures and the process times are long, the method is restricted to the production of high values components. This makes the process inherently expensive and so a reliable simulation is useful for process design. Within certain constraints, mainly those concerned with adequate representations of material behaviour, finite element methods can provide such a simulation. The method used to model disc and blade-section forging within IEPL is described; this is a two-dimensional finite element analysis using a finite incremental/iterative technique for elasto-viscoplastic materials. The mesh is defined by material points, and can be readily redefined during the simulation. Graphical display of the material deformation allows likely problems, such as poor die filling and folding, to be identified.

The results of the modelling can only be as good as the constitutive relationship assumed for the material. Experiments using simple stress state testing have revealed that commonly used relationships are inadequate for predicting the flow stress of important materials. The type used in the modelling described here attempts an improved relationship, involving a structure related state variable. The evolution of this variable in the model can, together with experimental simulations, give a reasonable indication of the development of microstructure during forging.

Other results of the simulations include the predictions of stresses within the dies, using the surface loading data and elastic finite element analysis, and the forging load required. The results can also be used with ductile fracture criteria to identify possible cracking problems in the workpiece.

The finite element technique used is capable of simulating thermomechanical deformations so that the effect of deviations from true isothermal conditions can be analysed, and "hot die" forging simulated.

Introduction

Conventional forging, using either hammer or press, is a fairly rapid operation. This is often an advantage of the process in terms of cost, and also allows tooling to be used which, because it does not have to experience the same temperature as the workpiece, is fairly inexpensive.

The constraint of short die to workpiece contact times limits the use of conventional forging to certain alloys. This is often because of limited ductility at high strain rates, or because the flow stress within an acceptable temperature range would be too great at such rates.

Removing the short contact time constraint leads to process variants where the dies are at the same, or somewhat lower, temperature than the workpiece. These are referred to as, respectively, isothermal and hot die forging. As well as the points mentioned above, both of these processes, particularly isothermal forging, give significantly greater freedom in the amount of deformation achievable during a single forging operation. The longer process times and the need for the dies to withstand loading at high temperatures means that the processes are significantly more expensive than conventional forging, and because of this their application is restricted to critical parts, where the additional process cost is justified by the increased performance of the final part.

With these processes, with their high costs and critical product applications, there is a great incentive to model or simulate the material deformation. All models are, of course, approximations, whether they be physical, using some analogue material such as wax or lead-tin alloy, or numerical. Numerical models tend to be preferred for many reasons, and with currently available digital computers the finite element

method is in a dominant position. This is potentially an accurate and flexible technique for many applications. The material large-deformation problem is however highly complex and the numerical solution significantly more difficult than, say, elastic small deformation problems. Despite the difficulties, there has been some success in applying finite element techniques to the forging process.

There have been several developments of the basic methods of finite element analysis in the metal forming field. Some developments of note are those due to Kobayashi and co-workers[1,2] and Zienkiewicz and co-workers[3,4]. These have used formulations based on rigid-plastic or rigid-viscoplastic material models with incompressibility enforced by techniques such as Lagrangian multipliers or penalty functions. An alternative involves treating the material as an elasto-plastic or elasto-viscoplastic solid, significant advances with this approach are those due to McMeeking and Rice[5], who get the updated-Lagrangian formulation on a firm basis, and Nagtegaal and Veldpaus[6], whose extension of that formulation to larger deformation steps allowed the elastoplastic based models to compete with the rigid-plastic based ones, with some advantage in fundamental assumptions (if none of great significance in its results!).

Although not required for an ideal isothermal process, the inclusion of a thermal solution linked to the mechanical one is an advantage. Deviations from true isothermal conditions may occur and it is useful to have the capability to simulate any such occurrence. The provision of thermomechanical modelling is necessary for hot die simulations, of course. Thermomechanical formulations have been reported, for example by Zienkiewicz, Onate and Heinrich[7] with rigid-plastic material models, and by Wertheimer[8] for the elasto-plastic case.

It is, in principle, possible to achieve any degree of accuracy required using these techniques, particularly the elasto-plastic based methods. However, this is not the case because of two factors. These are the material constitutive relationship and the boundary condition modelling. Both the material and the die contact behaviours are likely to be complex, and the degree to which the idealisations used in the modelling reflect the real case have a great effect on how useful a numerical simulation can be. The derivation of reasonably representative descriptions of material and of contact surface behaviour is quite difficult, and some of the approximations used in modelling fall short of being adequate.

Finite element modelling has been adopted within the INCO Engineered Products Ltd. group for the simulation of isothermal forging. The techniques used are described below and some examples are given.

Computer Modelling

The modelling is performed using a group of programs, these carry out the actual finite element analysis and pre- and post-processing functions. The finite element analysis is two dimensional, and capable of both plane strain and axisymmetric simulations. The method used is based on that proposed by Nagtegaal and Veldpaus[6], being incremental-iterative with an elasto-viscoplastic material model. The finite strain and rotation measures are not calculated as in (6) but approximately using truncated series. Solution within each finite deformation increment is found by a damped full Newton-Raphson method. Solution of the linear equations is by Choleski LDL decomposition, with skyline storage of the array. Four element types can be used, these are 3- and 6-node triangles and 4- and 8-node quadrilaterals. Apart from the linear triangle, these elements are isoparametric with reduced integration. The 6-node triangle is now used exclusively. This element with reduced (3 point) integration gives good results for near-incompressible analysis and, if triangular elements are adopted then simple mesh generation techniques can be used. The mesh generation forms the core of the pre-processing operation. In the method used, only the boundary nodes (triangle vertices) need be defined or altered, the internal nodes are then distributed, depending on the boundary node density, within the boundary and DeLaunay triangulation used to form the primitive elements[9]. Mid-side nodes are then added, nodal positions are refined and the nodes are renumbered to minimise the size of the profile of the linear equations. A modified reverse Cuthill-McKee algorithm is used for this renumbering. If the preprocessing is a remeshing operation then several quantities must be transferred to the new mesh. Simple linear 3-point interpolation is used, as is common practice.

Other preprocessing operations involve defining the dies as polygons, from given design data, creating the incremental control data and forming the arrays used for subsequent evaluation of die stresses. At present these arrays, which relate die point tractions to surface stresses, are formed using elastic finite element analysis, a possible future development would be the use of boundary element techniques for this linear problem.

Postprocessing operations involve the generation of graphical output and the actual calculation of die stresses together with certain "damage accumulation" quantities in the workpiece. These latter values are intended to be an indication of the likelihood of fracture in the actual forging, but this aspect has received relatively little attention by us so far.

When non-isothermal conditions are modelled, the thermal and mechanical solutions

are weakly coupled and both parts recalculated at each iteration. Dies are treated very approximately as linear heat sinks and free surface loss is taken to be by radiation. Any heat due to deformation is included, of course, and the properties of the material, including the thermal values, are defined as functions of temperature. The viscoplastic description of the material has some new features. The material is assumed, as usual, to be isotropic with isotropic hardening and associated J2 flow. The current effective flow stress was originally defined by power functions of total effective strain and strain rate, but this proved inadequate for any of the materials tested so far. Total effective strain was removed from the description, and a variable used which is intended to follow more closely the microstructural changes which occur in hot deformation. The use of this variable and its evolution are based, to some extent, on the work of Immarigeon[10], but the structure state variable has been made a more abstract quantity with the emphasis on flow stress prediction rather than any real microstructural parameter. Types of behaviour which can be simulated using this approach are shown in Figure 1. The ability of this material model to follow the rate change behaviour of Udimet 720 nickel alloy is shown in Figure 2. This model is fairly flexible, and works adequately for titanium alloys and aluminium alloys.

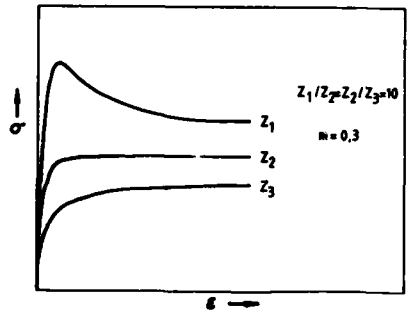

FIGURE 1 Some example monotonic stress-strain behaviours that can be produced by the material model used in the finite element analysis

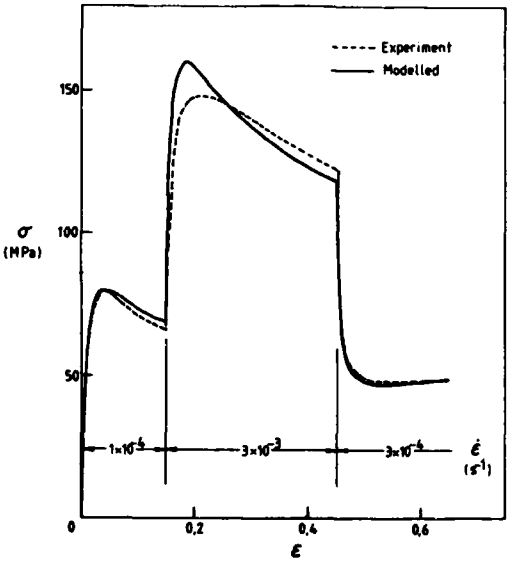

FIGURE 2 A comparison of experimental (compression) and model material behaviours; a rate change test on Udimet 720

The friction model used reflects a certain ignorance of the real case. Either simple Coulomb friction, a constant thickness viscous layer, or any combination of these two can be used. For most of the lubricants used, the viscous layer model seems to work quite well. The frictional properties are set up as functions of temperature.

The programmes are currently run using a DEC microVAX II computer. Typically, 100-200 steps are taken with convergence to a fractional displacement norm of 0.001 occurring in an average of 5-6 iterations, though usually less and occasionally rather more, as is usual. Despite the fact that an elastoplastic type method is used, the time penalty is probably not significant, as the linear equation solution accounts for about 60% of the CPU time on an average size problem, the total time being about 6 hrs.

Some typical examples showing results of the modelling are given below.

Examples

Three examples of axisymmetric forging simulations are given here. While these are fairly representative of typical practice, none of these correspond to actual forgings produced within IEPL.

(1) The first example is typical of the type of simulation carried out for isothermal disc forgings. A schematic sectional view of the start and finish configurations of the process is shown in Figure 3. This shape is somewhat similar to some compressor disc forgings, and the material model used was that for IMI titanium alloy 834. The predicted monotonic stress-strain behaviour of this alloy is shown in Figure 4. There is some flow softening in this material, particularly at the higher values of Z (the Zener-Holloman temperature corrected strain rate).

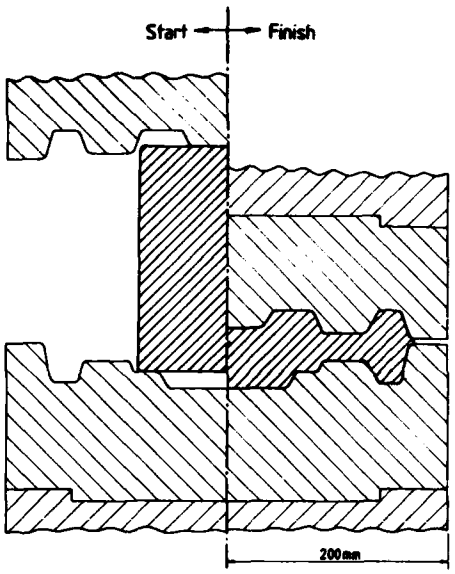

FIGURE 3 Schematic diagram of the initial and final configurations for the forging of example disc EXA1

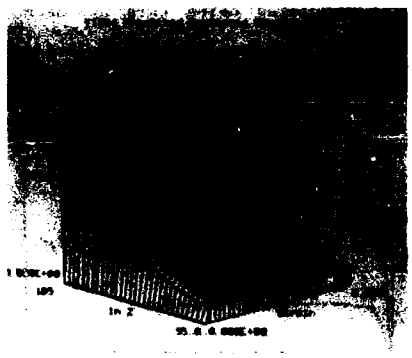

FIGURE 4

In this example the temperature was 980°C throughout, and the top die was moved down at a decreasing velocity. The total process time was 2000s. Figure 5 shows the initial mesh and die profiles, this mesh consisted of 164 elements and had 365 nodes. An intermediate stage is demonstrated in the next series of diagrams. The process automatically halted at 1180s due to poor mesh-die fitting, the proportion of workpiece not contained had exceeded a pre-set tolerance. The deformed mesh at this stage is shown in Figure 6, this being the third mesh as two remeshing operations had already been performed. The process may halt for other reasons, but die/mesh mismatch is the most common. The displacement increments at nodes is shown in Figure 7, this type of plot is useful for indicating incipient folding in the model. The total strain is shown in Figure 8, the hydrostatic stress in Figure 9 and the effective strain increment in Figure 10. The strain rate can be readily related to this latter quantity because the time step, in this case 10s, is known.

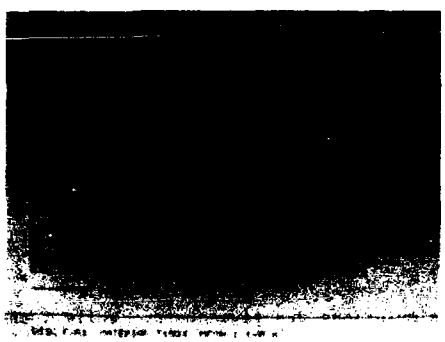

FIGURE 5

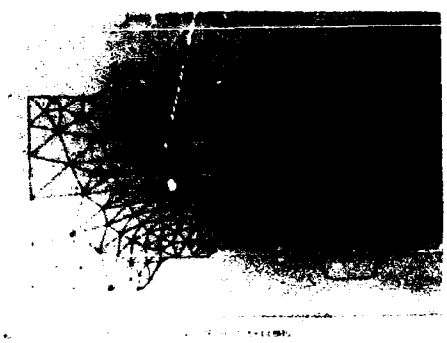

FIGURE 6

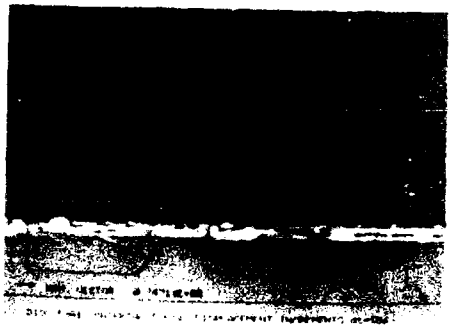

FIGURE 7

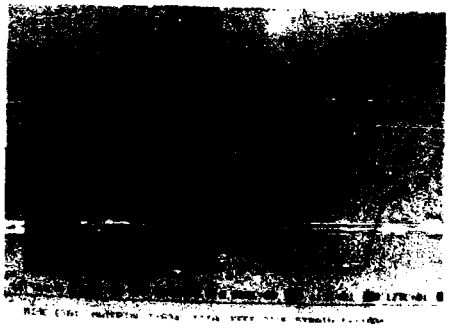

FIGURE 8

FIGURE 9

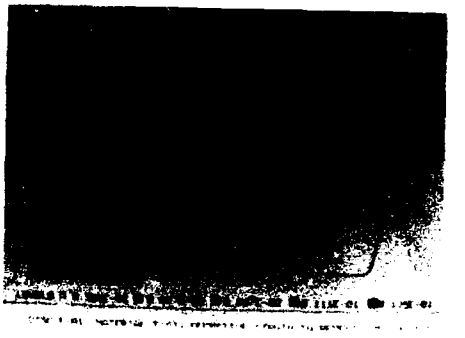

FIGURE 10

A further five remeshing operations were required before the simulation was complete. In the latter stages smaller deformation and time increments were used as material began to form forging flash. The process halts when either rotation or deformation gradient increments exceed certain preset values. The final deformed mesh is shown in Figure 11, and the total strain in Figure 12. Figure 13 shows the final values of the "structure-related" variable. In this example there is little difference between the variation of this and that of total strain, and in this alloy at 980°C the extent of structural refinement possible is limited because of the high volume fraction of the softer, beta, phase.

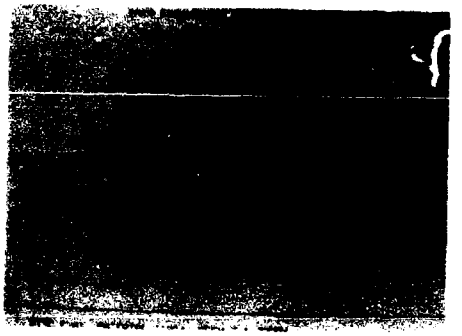

FIGURE 11

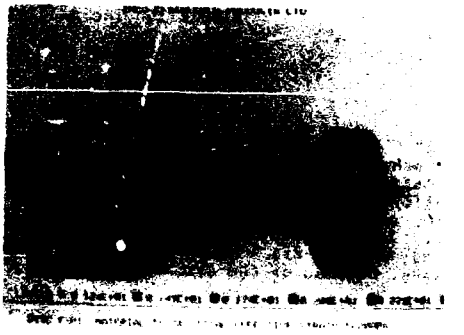

FIGURE 12

FIGURE 13

The total loads and maximum stresses on the dies are important to the forging design. For this example the forging load and the maximum tensile stress in the bottom die are shown in Figure 14; this stress occurring close to the innermost internal radius on that die. Such loads and stresses would be acceptable in practice. Several other stress-derived quantities are evaluated for the dies apart from the maximum principal value.

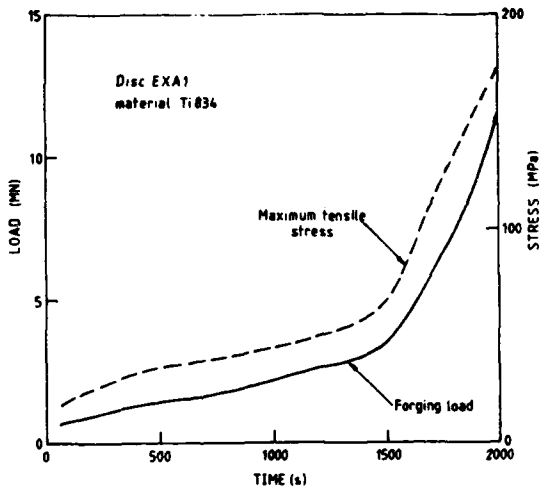

FIGURE 14 The predicted forging load, and maximum tensile stress in the bottom die, for example disc forging EXA1

(2) In the second and third examples a simple disc shape is simulated with both isothermal and hot die conditions. A schematic of the start and finish forging configurations is shown in Figure 15. The material model used is for the nickel alloy Udimet 720, the predicted monotonic stress-strain behaviour is shown in Figure 16, and as with the titanium alloy there is flow softening, more pronounced at higher Z. In both of the following examples, the initial material temperature was 1100°C and the top die was moved down at a decelerating rate with a total process time of 170s. Because of the symmetry here, only one quarter section need be modelled.

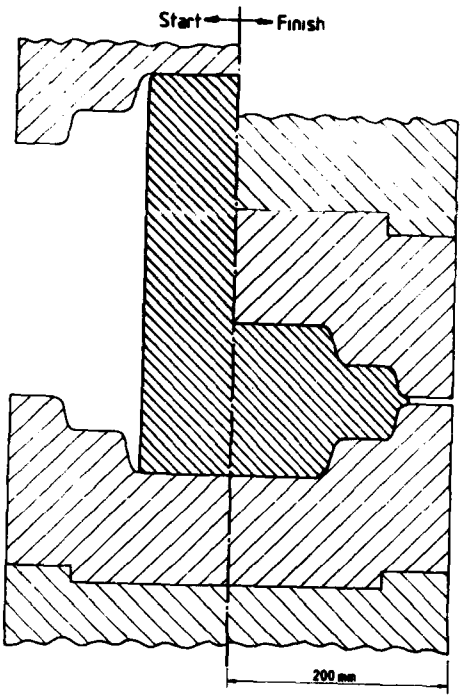

FIGURE 15 Schematic diagram of the initial and final configurations for the forging of example disc EXA2

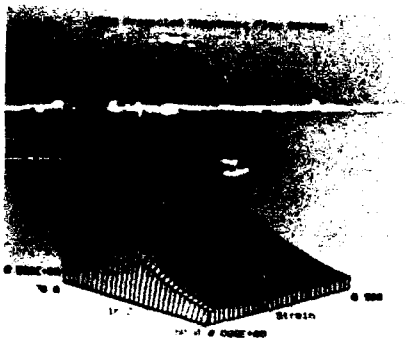

FIGURE 16

(a) In this case the dies were at 1100°C also, so isothermal conditions were assumed. In fact, with this rather rapid operation, there would be a likelihood of some deformational heating but this is ignored here. An intermediate stage, at 70s, is illustrated, the deformed mesh in Figure 17 and the strain increments (in this case equivalent to strain rate) in Figure 18. The end of the process at 170s is shown in Figures 19,20 and 21, with the deformed mesh, the total strain and the structure-like variable. The cavity has very nearly filled just as flash is about to form.

FIGURE 17

FIGURE 18

FIGURE 19

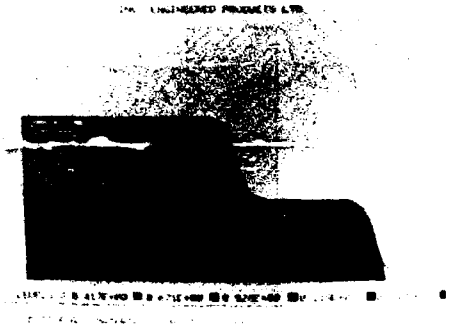

FIGURE 20

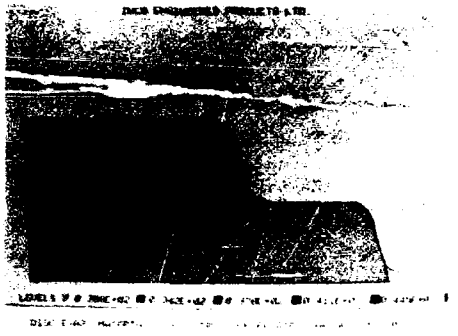

FIGURE 21

(b) Here the dies were set at 960°C. Differences in the deformation compared with the isothermal case are quite apparent, an intermediate stage, at 100s, produces the deformed mesh shown in Figure 22, with strain rates shown in Figure 23. The effect of the temperature distribution, Figure 24, upon the material is fairly clear. As noted above, there is some influence of deformation heating at these higher rates. Differences can also be seen at the assumed end of the process, Figure 25 showing the deformed mesh. Here die filling is not complete even after some flash extrusion and a higher billet volume would be required. Surprisingly, the forging load for the hot die forging was only about 50% higher than for the isothermal case at 170s, with similar differences in maximum die stresses, although these occurred close to the region where the hot die simulation had not finished filling. There are marked differences in the structural refinement between hot die and isothermal cases, however, Figures 26 and 27 show the total strain and structure-related variable distribution for the hot die case, and clearly show the increased variation of refinement predicted, due to the temperature variation, the final extent of which is given in Figure 28. If the structure cannot readily be adjusted by heat treatment, then hot die forging would be at a disadvantage in this respect even though, with simpler shapes, it has advantages in allowing the use of cheaper die materials.

FIGURE 22

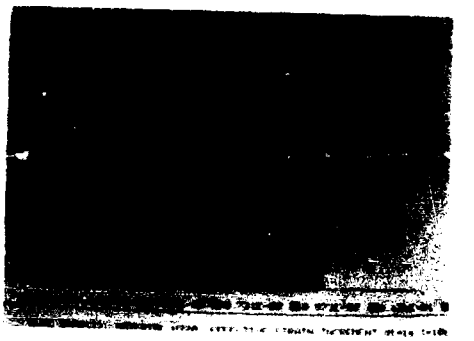

FIGURE 23

FIGURE 24

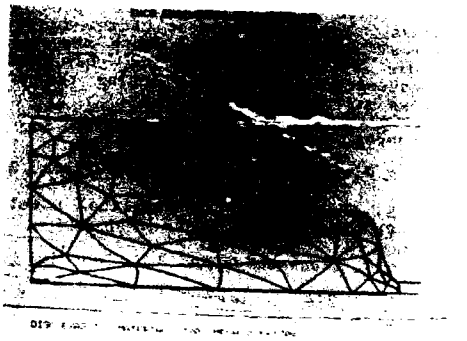

FIGURE 25

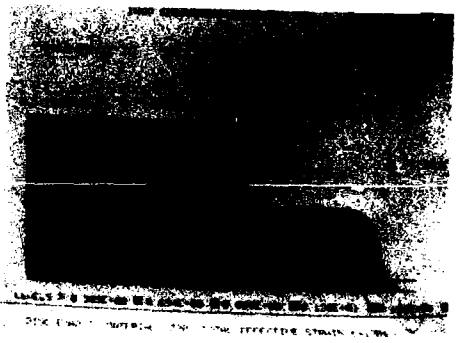

FIGURE 26

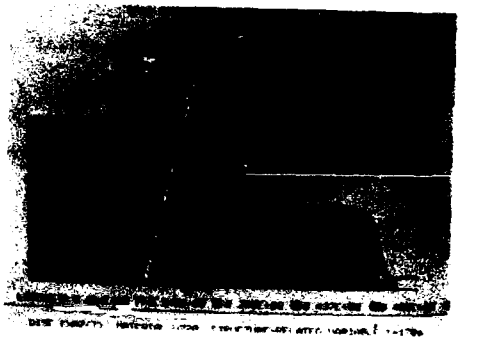

FIGURE 27

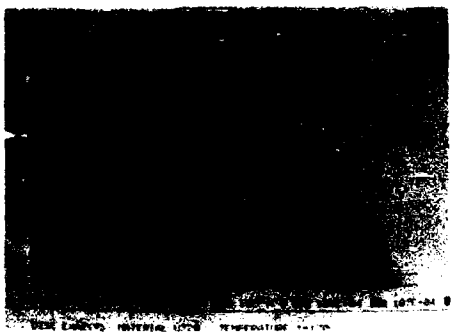

FIGURE 28

Conclusions

Finite element methods can provide a useful means of simulating the forging process. They can be most useful in the case of isothermal and hot-die forging of critical aerospace parts, where they not only assist with aspects of design such as die filling and loading, but also with understanding the development of microstructure and damage during the processing, and evaluation of the effect of process variables.

References

(1) C.H. Lee and S. Kobayashi: Trans. ASME J.Eng.Ind.,95, 1973, p865

(2) S. Kobayashi: in "Numerical modelling of manufacturing processes", ASME PVB-PB-025, 1977, p49

(3) O.C. Zienkiewicz and P.N. Godbole: Int.J. Num. Meth.Eng., 8, 1974, p3

(4) O.C. Zienkiewicz, P.C. Jain and E. Onate: Int. J. Solids Struct., 14, 1978, p15

(5) R.M. McMeeking and J.R. Rice: Int. J. Solids Struct., 11, 1975, p601

(6) J.C. Nagtegaal and F.E. Veldpaus: in "Numerical methods in industrial forming processes", Pineridge, 1982, p1

(7) O.C. Zienkiewicz, E. Onate and J.C. Heinrich: Int. J. Num. Meth. Eng., 17, 1981, p1497

(8) T.B. Wertheimer: in "Numerical methods in industrial forming processes", Pineridge, 1982, p425

(9) J.C. Cavendish, D.A. Field and W.H. Frey: "The mathematics of finite elements and applications", Academic, 1985, p83

(10) J-P, Immarigeon: in AGARD LS-137 1984, paper 4

THE APPLICATION OF PROCESS MODELLING TO HEAT TREATMENT OF SUPERALLOYS

By
R. A. Wallis, N. M. Bhathena, P. R. Bhowal and E. L. Raymond
Cameron Forge Company, P. O. Box 1212,
Houston, Texas 77251-1212 U.S.A.

SUMMARY

Quenching experiments have been carried out with a flat disk having thermocouples embedded in it. Cooling curves from such tests have provided input data for an inverse heat conduction model which has been used to determine the relationship between the heat transfer coefficient and the part surface temperature for different quenching media. The coefficients obtained have been used in finite element models to predict the temperature and stress distribution within components during heat treatment. The quenching models were validated by trials carried out with instrumented subscale and full size turbine disk forgings.

The models have been used to determine the quenching media required to give the cooling rates necessary to meet the property specifications for superalloy components. They have also been used, qualitatively, to reduce the residual stresses developed during quenching with a subsequent reduction in distortion problems during machining. A further application has been the elimination of cracking during the quenching of crack sensitive alloys.

1. INTRODUCTION

Over the past few years the heat treatment of superalloy forgings for aircraft components has become considerably more difficult. The designers of components in new engines are pushing the alloys closer to their maximum attainable strength limits and, in an effort to reduce costs, the forgings are becoming closer to net shape. Increasing the strength of many alloys, however, is possible only by rapidly quenching a forging during heat treatment. This can result in distortion and cracking problems. It is, therefore, becoming vital to have an understanding of what is happening to the parts during heat treatment.

Over the past two years, Cameron has worked intensely on developing process models to predict the temperature and stress distribution in parts during quenching. The work is aimed at being able to heat treat parts correctly (i.e. meeting property requirements and not distorting or cracking) the first time, eliminating the costly and time consuming trial and error method.

The first step in the development of such process models is to obtain an understanding of the heat extraction rates of the quenchants used.

2. THE DETERMINATION OF THE HEAT TRANSFER COEFFICIENTS IN QUENCH TANKS

A disk of alloy 718 (267 mm diameter by 70 mm thick) was fitted with thermocouples at various depths from the surface. The disk was then quenched in different media and cooling curves such as those shown in Figure 1 obtained. These data were used as input into a finite difference inverse heat conduction computer program "CONTA"[1], originally developed at Michigan State University, which calculates the transient surface temperature of the disk together with the corresponding surface heat flux/heat transfer coefficient.

Heat transfer data for one type of oil is shown in Figure 2, and follows the typical trend for boiling heat transfer[2,3]. At high temperatures (above about 850°C) film boiling occurs and the vapour blanket formed on the surface of the disk limits heat transfer. As the surface temperature falls, transitional boiling heat transfer occurs and the vapour film becomes unstable. The heat extraction rate in this region is significantly higher. Nucleate boiling, characterised by the rapid formation of bubbles, appears to take place between about 480 and 400°C. The rate of bubble generation decreases with a decrease in surface temperature, and hence the heat extraction rate over this temperature range decreases rapidly. At lower temperatures (below about 400°C) heat transfer is by convection only.

Figure 2 also shows that over the transition and nucleate boiling regions, the heat transfer coefficient for the bottom surface of the disk was less than half that for the top surface. The disk was heat treated on a flat cast alloy tray 38 mm deep and comprising 10 mm wide material for support and 115 mm square openings. The support tray impedes the escape of the vapour formed beneath the disk and hence heat transfer from the bottom surface is reduced. This phenomenon is important since the cooling rate in the bottom part of a forging will be different from that in the top part. When heat treating alloys which are cooling rate sensitive, this will translate into different property levels being obtained in the top and bottom parts of a component.

Similar heat transfer data have been obtained for other quenching media, and for forced air cooling.

3. VALIDATION OF FINITE ELEMENT PROCESS MODELS

As mentioned previously, the aim of the programme was to develop process models to simulate the temperature and stress distribution within components during heat treatment. The two finite element programs used to model the process were TOPAZ2D[4] (for calculation of temperatures) and NIKE2D[5] (for calculation of stresses), both developed at Lawrence Livermore National Laboratory. In order to validate the modelling techniques, a series of tests were carried out with instrumented forgings.

In the first series of experiments, a small contour forging (294 mm diameter by 88 mm thick) of alloy 718 was fitted with thermocouples and quenched in different media. Figure 3 shows the comparison between the temperatures predicted by the finite element model and the experimental data. The test was carried out from the arbitrarily high temperature of 1177°C in an attempt to check the accuracy of the model over the full temperature range for which heat transfer coefficient data were available. During the time that the piece is in transit from the furnace to the oil tank (the first 1.3 minutes) heat is transferred predominantly by radiation, and the temperatures fall relatively slowly. Shortly after the forging is immersed in the oil tank, however, the temperatures fall very quickly, particularly near the surface and at the corners (e.g. point C). It may be seen that there is good agreement between the model and the experimental results.

Following the success with the small contour forging, a series of tests were carried out with an instrumented full size turbine disk forging (approximately 630 mm diameter by 115 mm thick) made of alloy 901. The comparison between the model and experimental results are given in Figure 4. The case shown is where the forging was heated to 1177°C, transferred from the furnace to a set of fans in 0.83 minute, forced air cooled for 2 minutes, transferred from the fans to an oil tank in 1 minute, and finally oil quenched. Even during multiple step cooling, agreement between the model and experimental results is good.

4. HEAT TREATMENT PROCESS MODELLING TO PREDICT MECHANICAL PROPERTIES

In the past, the heat treatment of a new product was often done on a trial and error basis. This method is clearly time consuming and expensive. As a result, one of the early uses for modelling was to determine how a part should be heat treated in order to meet the property requirements.

As an example, take the case where a customer specified a minimum yield strength (at 500°C) of 1076 N/mm² in a superalloy forging. The first step in the process was to determine the cooling rate necessary to meet this requirement. This was achieved by quenching a small instrumented disk (122 mm diameter, by 51 mm thick) in different media to obtain different cooling rates. Disks of the same size and material were then quenched and mechanical testing carried out on specimens taken from locations where the cooling rate was known. This resulted in a relationship between cooling rate and yield strength, as shown in Figure 5. Thus, in order to obtain the specified yield strength of 1076 N/mm² it was known that the part must be cooled at a rate greater than about 125°C/min.

A finite element model of the forging was constructed, and used to determine the minimum cooling rate in the part as a function of the static air cool time prior to oil quenching (i.e., time from leaving the furnace to entering the oil tank)-see Figure 6. This analysis indicated that in order to meet the cooling rate/property requirement, the static air cool time should be less than 90 seconds. Stress analyses carried out showed that in order to avoid quench cracking, the static air cool time should not be less than 45 seconds. As a result, it was decided to heat treat the part with a 60 second static air cooling period prior to oil quenching.

Referring to Figure 6, it may be seen that, for location A, the model predicted a cooling rate of 135°C/min. and a yield strength of 1080 N/mm² for a 60 second static air cool-oil quench. One pre-production part was cut up after heat treatment, and the yield strength was found to be 1101 N/mm² which is close to the model prediction, and met the property specification.

5. REDUCTION OF DISTORTION/RESIDUAL STRESS PROBLEMS ASSOCIATED WITH HEAT TREATMENT

Forgings having thin cross sections or large differences in cross section can present distortion problems during heat treatment. For example, a thin disk made of a nickel based alloy was found to distort slightly during the oil quench. Although the distortion was within acceptable tolerances, subsequent machining proved to be extremely difficult due to the disk "springing" as it was being machined.

The quenching of the part was modelled and the temperatures shown in Figure 7 were predicted. It may be seen that during transfer from the furnace to the oil tank (0 to 0.75 minute) the surface temperature of the disk falls relatively slowly. As soon as the part is immersed in the oil tank, however, the temperatures fall very rapidly. Within 15 seconds of entering the oil tank, points A and C have fallen over 500°C. Point B does not cool down quite as quickly since it is located on the bottom surface of the disk (the heat extraction rate is lower on the bottom surface, see section 2), and at a point where the section size is relatively thick. The center of the disk, point D, cools much slower than the surface, and a temperature difference of over 550°C develops in the part shortly after entering the tank.

A thermal-stress analysis was carried out on the disk and, as shown in Figure 8, the effective (von Mises) surface stresses rise rapidly as soon as the disk enters the oil tank. Within seconds of entering the tank (at a time when the temperature difference in the part is increasing) stresses over 800 N/mm² develop. The stresses then slowly fall as the whole part cools down. Unfortunately, at the time of this investigation, data were not available to carry out a full elastic-plastic analysis, so the stresses shown are purely elastic. However, examination of elevated temperature tensile data indicated that just after the part entered the tank, when the stresses were rising rapidly, the elastic limit was exceeded at high temperature and plastic deformation took place. Hence, at the end of the quench there were residual stresses present in the part. Subsequently, when the part was being machined, and a surface layer of material removed, the part "sprung" on the machine in an attempt to attain stress equilibrium.

Previous work on this particular alloy revealed that the cooling rate attained by oil quenching was considerably quicker than needed to meet the property specification. Hence a simulation was carried out with the part being forced-air cooled. The model predicted that the cooling rate required to meet properties could be achieved by forced air cooling. The peak stresses generated during forced-air cooling, see Figure 9, were calculated to be around 350 N/mm², or half those developed during oil quenching. Furthermore, the rise in stresses was calculated to be much slower, resulting in lower stresses at any given temperature. It was therefore concluded that if plastic flow did occur during forced-air cooling, the residual stresses would be very much lower than those experienced from oil quenching.

Following the modelling work, a trial was carried out with a production disk using an experimental forced-air cooling system. A subsequent cut up test revealed that, as predicted, the property requirements could be met by forced-air cooling. A small number of parts were then similarly heat treated and these were machined without any distortion problems. A production cooling system was then designed, see Figure 10, to give the same heat extraction rates used on the test rig and in the model.

6. ELIMINATION OF QUENCH CRACKING PROBLEMS USING PROCESS MODELS

In the design of new engine components, alloys are being pushed closer to their strength limits. High strength is being attained, in part, by quenching forgings to give fast cooling rates. However, there is a limit to how fast a particular alloy can be quenched before it will crack. Today, we have reached this limit on several of the superalloys, and part geometry, which can influence cracking, is becoming an important factor in developing heat treatment practices.

As an example, consider the heat treatment of the superalloy turbine disk forging shown in Figure 11. In order to attain the desired mechanical properties the disk had to be rapidly quenched. Finite element models were used to determine the effect of part orientation on the stress levels attained during an oil quench. Figure 11 shows a plot of the stress developed at a certain point on the forging during the quench versus the temperature at which that stress occurs. With the part quenched in position 1 (see Figure 11), point 1 was found to be the critical location on the disk. It may be seen, however, that the stress never exceeds the ultimate tensile strength (UTS) of the material. Below about 790°C, the yield point of the material is exceeded which will lead to localised plastic deformation occurring and, hence, residual stresses will be present in the part after the quench. The local yielding does not mean that the part will crack at point 1, however, since the material has reasonable ductility over the temperature range at which it occurs.

The stresses developed in the disk when quenched in position 2 (upside down relative to position 1) is also given in Figure 11. In this case, point 2 becomes the critical location in the part, and it may be seen that the UTS of the material is exceeded over the 950 to 650°C temperature range. Thus, the disk would be expected to crack at point 2 when heat treated in the second position.

The accuracy of the models was verified when several disks were heat treated in position 1 without cracking. Three disks were heat treated in position 2 and all three cracked at the location indicated by the model.

7. CONCLUSIONS

Alloys for the aerospace industry are being pushed to their strength limits by aircraft engine builders. This translates into the processing window for heat treatment of forgings becoming narrow. The parts must be cooled rapidly in order to meet the required property specification, but quenching too fast can result in distortion problems both during quenching and subsequent machining. In extreme cases the parts may crack.

Process models are now available which allow the temperature and stress distribution within a part during quenching to be predicted. These are proving to be very accurate and hence extremely powerful tools that will enable the industry to get the most out of the existing superalloys. They will be a vital part of the current drive to produce near net shape forgings with reduced lead time from engine design to the production of useable hardware.

8. REFERENCES

1. J. V. Beck: Sandia National Laboratories, "Users Manual for CONTA - Program for Calculating Surface Heat Fluxes from Transient Temperatures Inside Solids", Report No. SAND83-7134, December 1983.

2. G. Stoltz, V. Paschkis, C. F. Bonilla, and G. Acevedo: "Thermal Considerations in Oil Quenching", Journal of the Iron and Steel Institute, October 1958, pp 116-123.

3. R. F. Price and A. J. Fletcher: "Determination of Surface Heat Transfer Coefficients during Quenching of Steel Plates", Metals Technology, May 1980, pp 203-211.

4. A. B. Shapiro: Lawrence Livermore National Laboratory, "TOPAZ2D - A Two-Dimensional Finite Element Code for Heat Transfer Analysis, Electrostatic, and Magnetostatic Problems", Report No. UCID-20824, July 1986.

5. J. O. Hallquist: Lawrence Livermore National Laboratory, "NIKE2D - A Vectorized, Implicit, Finite Deformation, Finite Element Code for Analyzing the Static and Dynamic Response of 2-D Solids", Report No. UCID-19677, Rev. 1, December 1986.

9. ACKNOWLEDGEMENT

The authors wish to thank the General Electric Company (Aircraft Engine Business Group) for support of projects in the process modelling area.

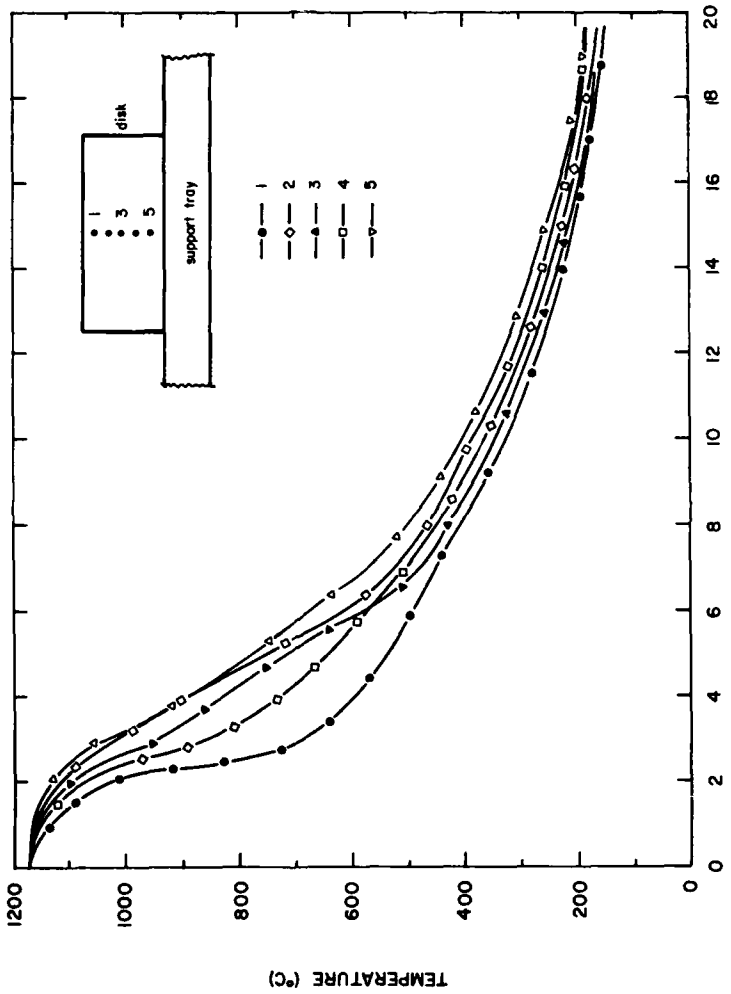

FIGURE 1, Cooling Curves from Oil Quenched Instrumented Disk

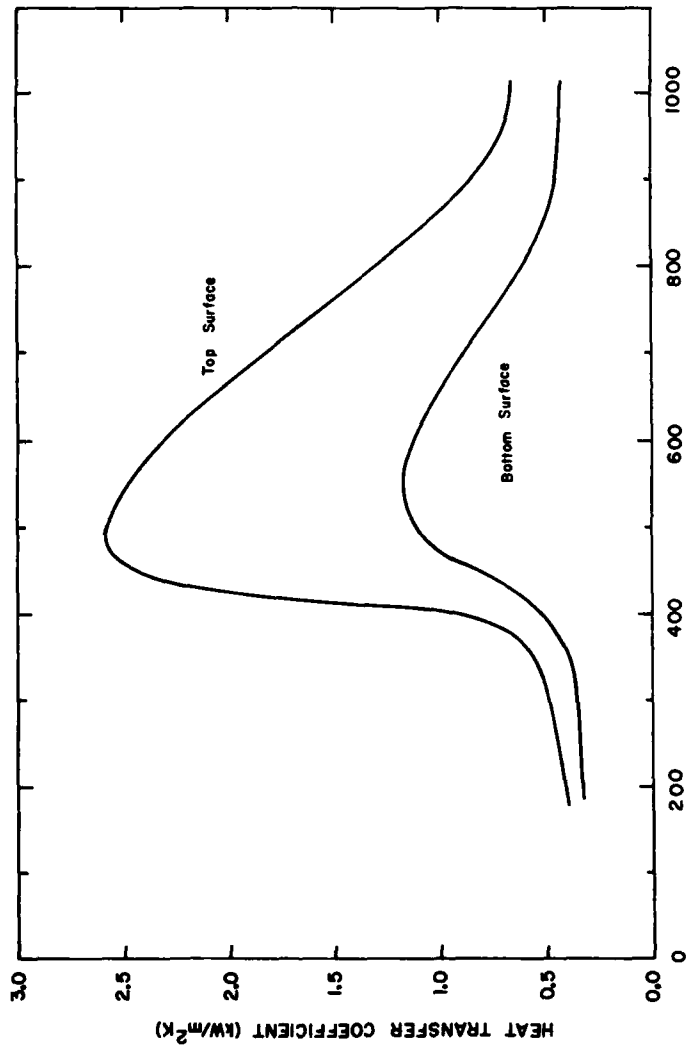

FIGURE 2, Effect of Temperature on Heat Transfer Coefficient During Oil Quench

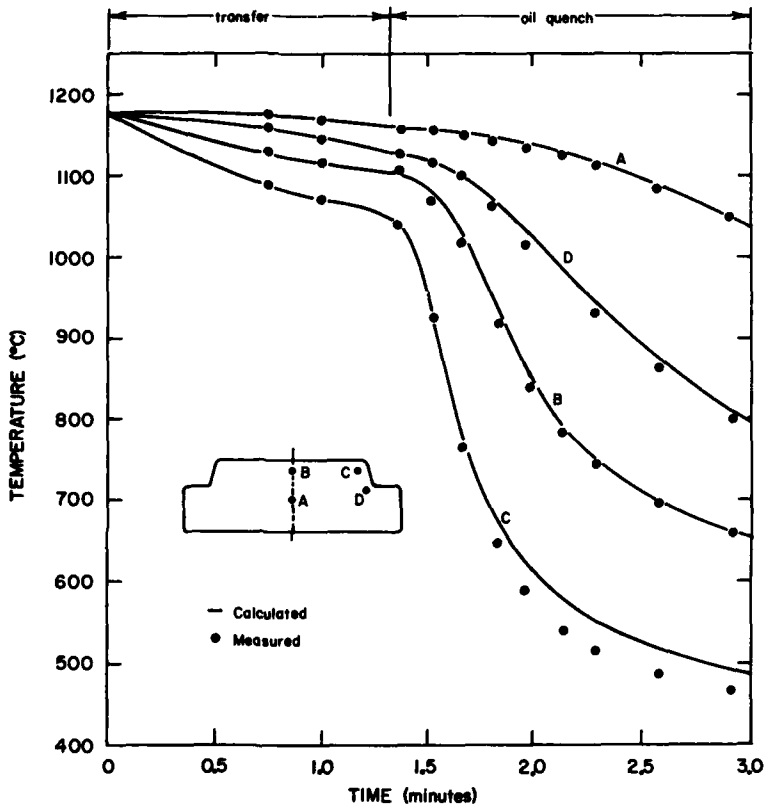

FIGURE 3, Comparison Between Calculated and Measured Temperatures During Oil Quenching of a Contour Forging

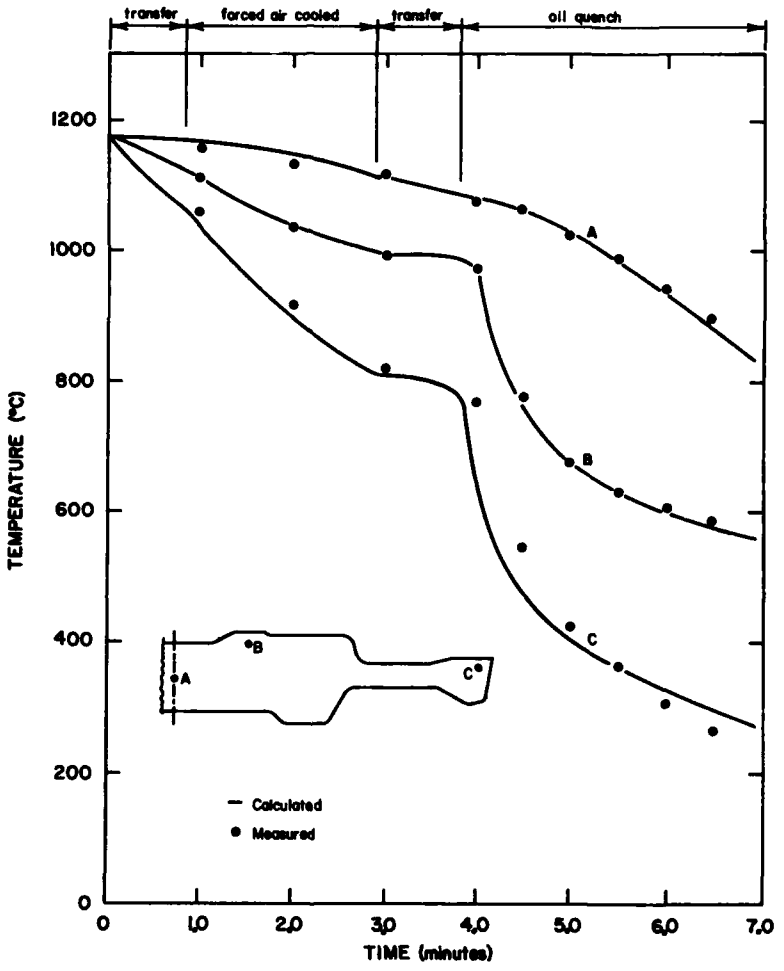

FIGURE 4, Comparison Between Calculated and Measured Temperatures During Heat Treatment of a Full Size Turbine Disk Forging

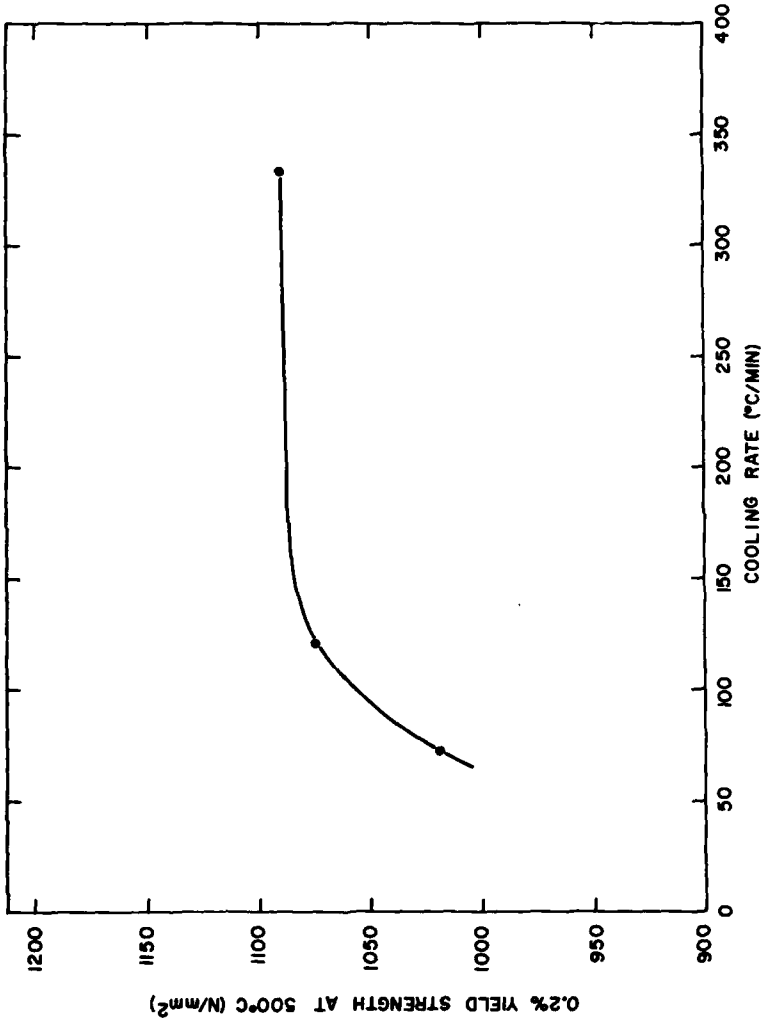

FIGURE 5, Effect of Cooling Rate on Yield Strength

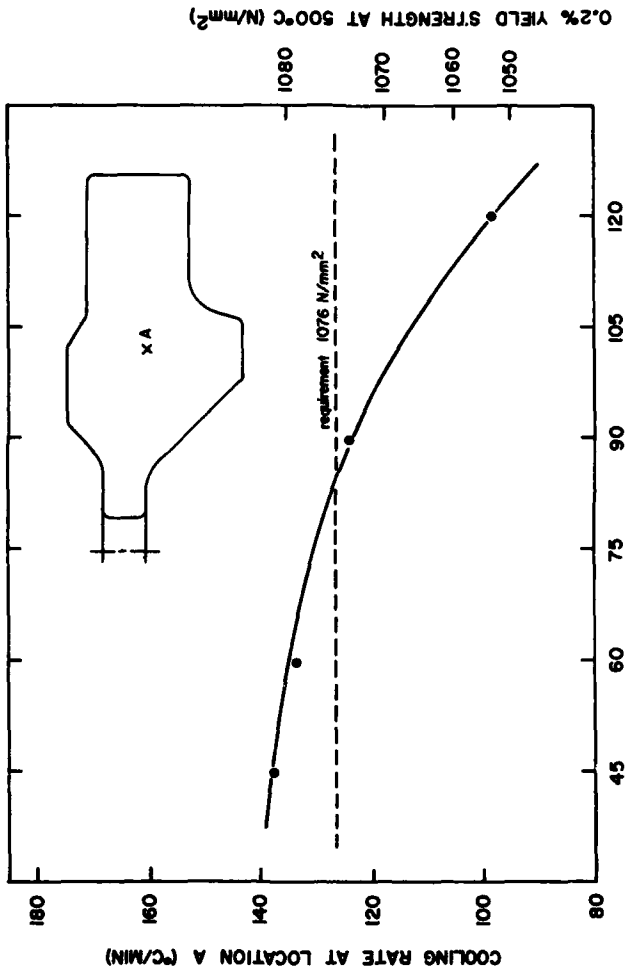

FIGURE 6, Effect of Static Air Cool Time Prior to Quenching on Cooling Rate and Properties

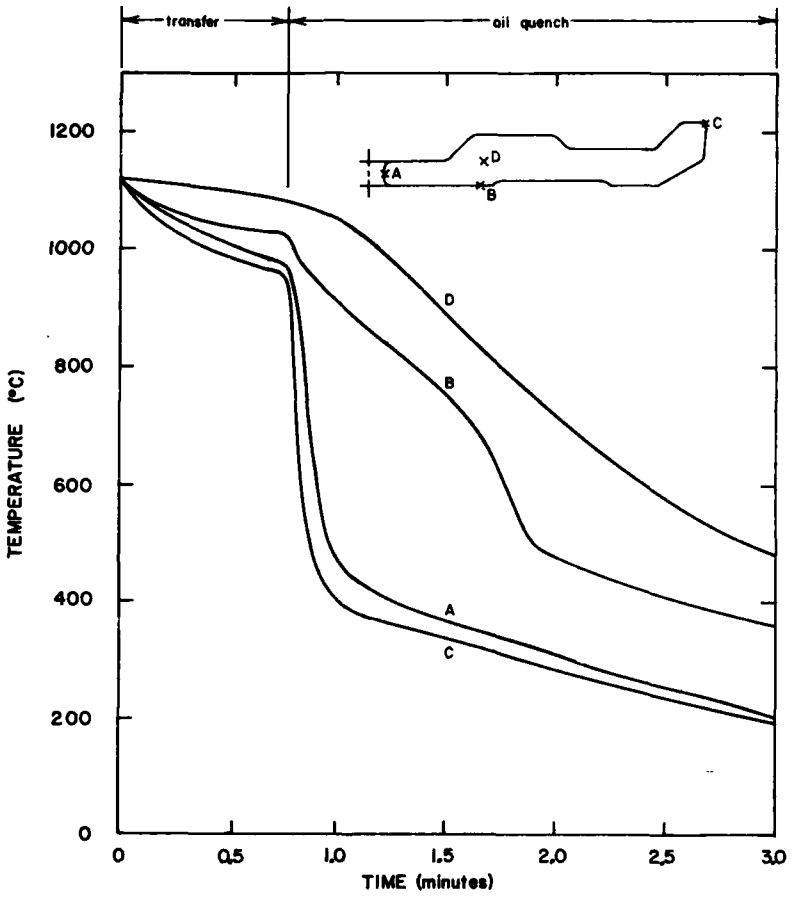

FIGURE 7, Temperature-Time Plot for Disk During Oil Quench

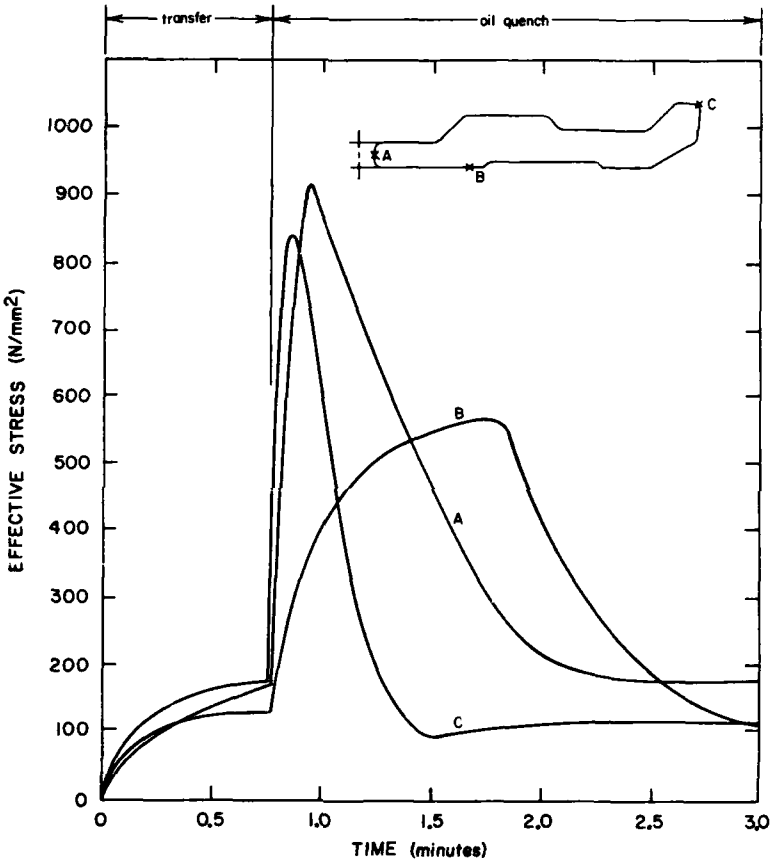

FIGURE 8, Stress-Time Plot for Disk During Oil Quench

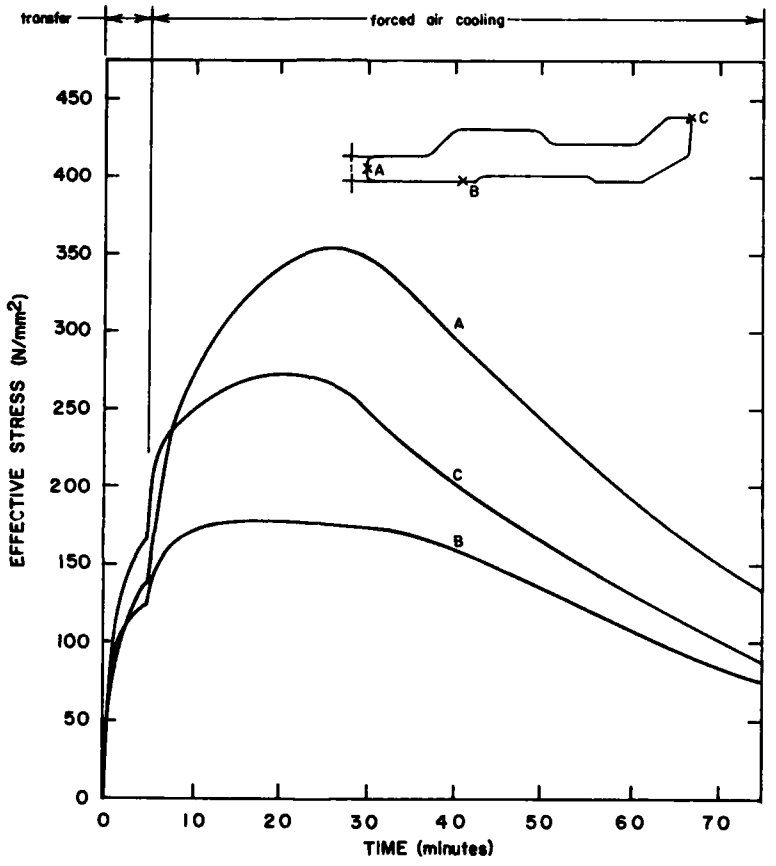

FIGURE 9, Stress-Time Plot for Disk During Forced Air Cooling

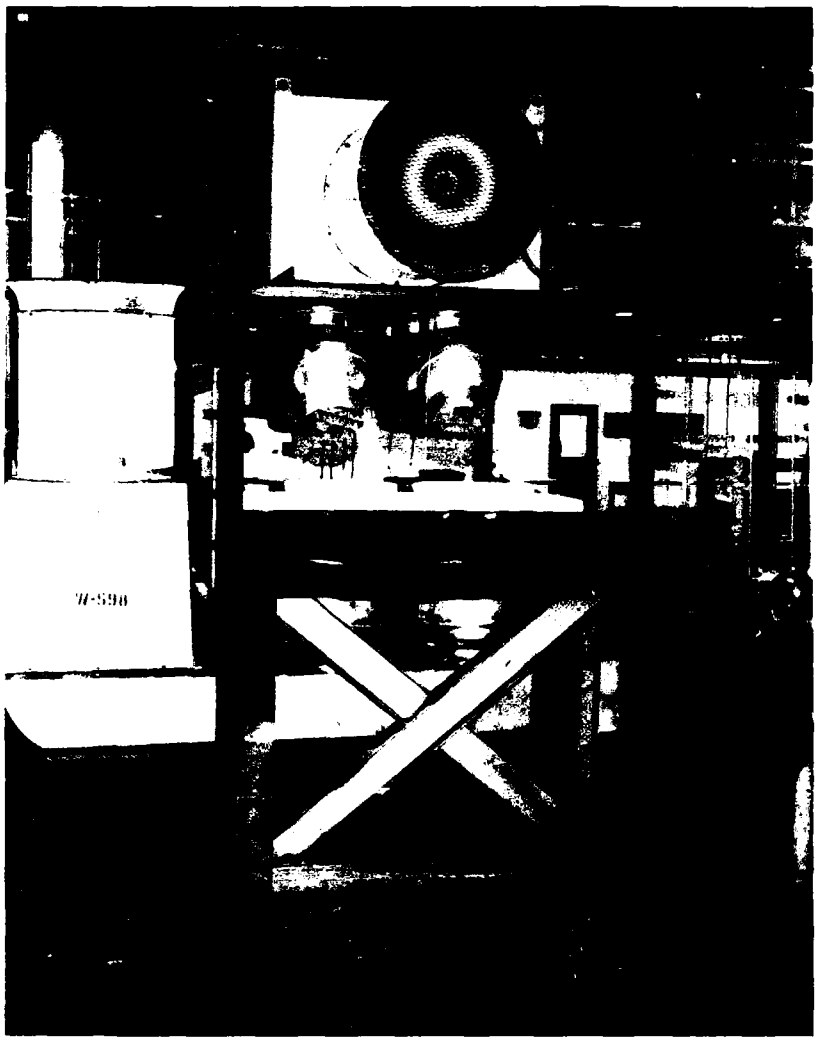

FIGURE 10, Production Forced-Air Cooling System

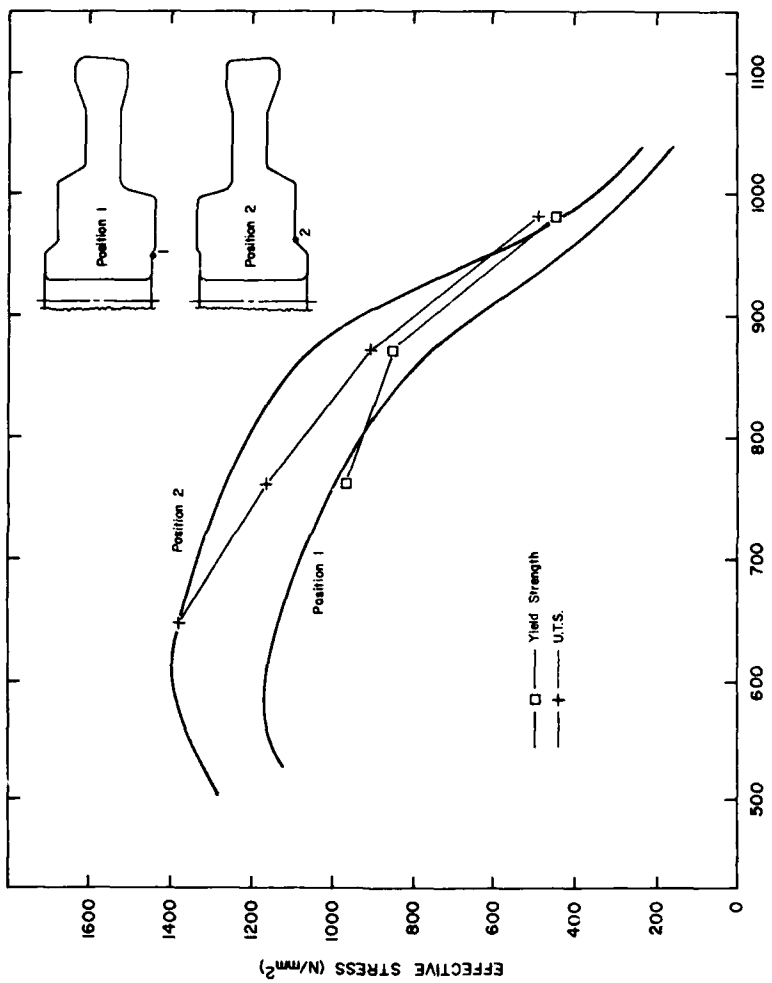

FIGURE 11, Stress-Temperature Plot for Turbine Disk During Quenching

REPORT DOCUMENTATION PAGE

1. Recipient's Reference	2. Originator's Reference	3. Further Reference	4. Security Classification of Document
	AGARD-CP-426	ISBN 92-835-0476-3	UNCLASSIFIED

5. Originator Advisory Group for Aerospace Research and Development
North Atlantic Treaty Organization
7 rue Ancelle, 92200 Neuilly sur Seine, France

6. Title

AEROSPACE MATERIALS PROCESS MODELLING

7. Presented at

the 65th Meeting of the Structures and Materials Panel of AGARD, held in Çeşme, Turkey, 2—4 October 1987.

8. Author(s)/Editor(s)	9. Date
Various	August 1988
10. Author's/Editor's Address	**11. Pages**
Various	270

12. Distribution Statement This document is distributed in accordance with AGARD policies and regulations, which are outlined on the Outside Back Covers of all AGARD publications.

13. Keywords/Descriptors

Castings
Forgings
Aerospace industry
Process control
Processing
Composite materials
Aluminum alloys
Titanium alloys
Ceramics
Manufacturing

14. Abstract

In recent years there has been a significant increase in the effort of developing process models for aerospace materials. Many factors have been responsible for this. Aerospace materials technology is changing very rapidly with the introduction of expensive and sophisticated materials. In addition the shorter life cycle from design to application is inconsistent with the traditional trial-and-error approaches formerly used.

The individual papers of the meeting cover developments on analytical process modelling to lower costs and increase reliability in manufacture of components.

The meeting concentrated on the modelling of the behaviour of metallic materials, particularly the forming of components such as castings and forgings.

AGARD Conference Proceedings No.426 Advisory Group for Aerospace Research and Development, NATO AEROSPACE MATERIALS PROCESS MODELLING Published August 1988 270 pages In recent years there has been a significant increase in the effort of developing process models for aerospace materials. Many factors have been responsible for this. Aerospace materials technology is changing very rapidly with the introduction of expensive and sophisticated materials. In addition the shorter life cycle from design to application is inconsistent with the traditional trial-and-error approaches formerly used. P.T.O	AGARD-CP-426 Castings Forgings Aerospace industry Process control Processing Composite materials Aluminum alloys Titanium alloys Ceramics Manufacturing	AGARD Conference Proceedings No.426 Advisory Group for Aerospace Research and Development, NATO AEROSPACE MATERIALS PROCESS MODELLING Published August 1988 270 pages In recent years there has been a significant increase in the effort of developing process models for aerospace materials. Many factors have been responsible for this. Aerospace materials technology is changing very rapidly with the introduction of expensive and sophisticated materials. In addition the shorter lif :le from design to application is inconsistent with the tradi onal trial-and-error approaches formerly used. P.T.O	AGARD-CP-426 Castings Forgings Aerospace industry Process control Processing Composite materials Aluminum alloys Titanium alloys Ceramics Manufacturing
AGARD Conference Proceedings No.426 Advisory Group for Aerospace Research and Development, NATO AEROSPACE MATERIALS PROCESS MODELLING Published August 1988 270 pages In recent years there has been a significant increase in the effort of developing process models for aerospace materials. Many factors have been responsible for this. Aerospace materials technology is changing very rapidly with the introduction of expensive and sophisticated materials. In addition the shorter life cycle from design to application is inconsistent with the traditional trial-and-error approaches formerly used. P.T.O	AGARD-CP-426 Castings Forgings Aerospace industry Process control Processing Composite materials Aluminum alloys Titanium alloys Ceramics Manufacturing	AGARD Conference Proceedings No.426 Advisory Group for Aerospace Research and Development, NATO AEROSPACE MATERIALS PROCESS MODELLING Published August 1988 270 pages In recent years there has been a significant increase in the effort of developing process models for aerospace materials. Many factors have been responsible for this. Aerospace materials technology is changing very rapidly with the introduction of expensive and sophisticated materials. In addition the shorter life cycle from design to application is inconsistent with the traditional trial-and-error approaches formerly used. P.T.O	AGARD-CP-426 Castings Forgings Aerospace industry Process control Processing Composite materials Aluminum alloys Titanium alloys Ceramics Manufacturing

The individual papers of the meeting cover developments on analytical process modelling to lower costs and increase reliability in manufacture of components.

The meeting concentrated on the modelling of the behaviour of metallic materials, particularly the forming of components such as castings and forgings.

Papers presented at the 65th Meeting of the Structures and Materials Panel of AGARD, held in Çeşme, Turkey, 2—4 October 1987.

ISBN 92-835-0476-3

The individual papers of the meeting cover developments on analytical process modelling to lower costs and increase reliability in manufacture of components.

The meeting concentrated on the modelling of the behaviour of metallic materials, particularly the forming of components such as castings and forgings.

Papers presented at the 65th Meeting of the Structures and Materials Panel of AGARD, held in Çeşme, Turkey, 2—4 October 1987.

ISBN 92-835-0476-3

The individual papers of the meeting cover developments on analytical process modelling to lower costs and increase reliability in manufacture of components.

The meeting concentrated on the modelling of the behaviour of metallic materials, particularly the forming of components such as castings and forgings.

Papers presented at the 65th Meeting of the Structures and Materials Panel of AGARD, held in Çeşme, Turkey, 2—4 October 1987.

ISBN 92-835-0476-3

The individual papers of the meeting cover developments on analytical process modelling to lower costs and increase reliability in manufacture of components.

The meeting concentrated on the modelling of the behaviour of metallic materials, particularly the forming of components such as castings and forgings.

Papers presented at the 65th Meeting of the Structures and Materials Panel of AGARD, held in Çeşme, Turkey, 2—4 October 1987.

ISBN 92-835-0476-3